UNIVERSITÄT BONN

Physikalisches Institut

Measurement of the Proton Structure Function F_2 at Very Low Q^2 at HERA

von

Christoph Amelung

aus

Detmold

Dieser Forschungsbericht wurde als Dissertation von der Mathematisch-Naturwissenschaftlichen Fakultät der Universität Bonn angenommen.

Angenommen am: 1.11.1999

1. Referent: Prof. Dr. E. Hilger
2. Referent: Prof. Dr. F. Klein

Contents

1 Introduction **5**

2 Theory **7**
2.1 The Standard Model (SM) . . . 7
2.2 Deep inelastic scattering (DIS) . . . 7
2.3 Kinematic variables . . . 8
2.4 The *ep* cross section and the proton structure functions . . . 11
2.5 Radiative corrections to the cross section . . . 12
2.6 The high-Q^2 regime . . . 13
2.6.1 The quark-parton model (QPM) . . . 13
2.6.2 Quantum Chromodynamics (QCD) . . . 15
2.6.2.1 Perturbative QCD (pQCD) . . . 15
2.6.2.2 The factorization theorems of QCD . . . 16
2.6.2.3 DGLAP equations . . . 17
2.6.2.4 The hadronic final state . . . 19
2.7 The low-Q^2 regime . . . 19
2.7.1 Longitudinal and transverse cross sections . . . 20
2.7.2 (Generalized) vector meson dominance model . . . 21
2.7.3 Regge theory . . . 22
2.7.3.1 Soft hadronic interactions . . . 24
2.7.3.2 Diffractive deep inelastic scattering . . . 24
2.8 Transition region . . . 25
2.9 Review of structure function data and parameterizations . . . 27
2.9.1 Structure function measurements . . . 27
2.9.2 Parton density parameterizations at high Q^2 . . . 28
2.9.2.1 MRST (Martin, Roberts, Stirling and Thorne) . . . 28
2.9.2.2 CTEQ (Coordinated Theoretical-Experimental Project on QCD) 31
2.9.2.3 GRV (Glück, Reya and Vogt) . . . 31
2.9.2.4 ZEUS QCD fit . . . 31
2.9.3 Cross section parameterizations at low Q^2 . . . 32
2.9.3.1 DL (Donnachie and Landshoff) . . . 32
2.9.3.2 ALLM (Abramowicz, Levy, Levin and Maor) . . . 33
2.9.3.3 CKMT (Capella, Kaidalov, Merino and Tran Thanh Van) . . . 33
2.9.3.4 ABY (Adel, Barreiro and Ynduráin) . . . 34
2.9.3.5 DLM (Desgrolard, Lengyel and Martynov) . . . 34
2.9.3.6 BK (Badełek and Kwieciński) . . . 34
2.9.3.7 MRS (Martin, Ryskin and Staśto) . . . 34
2.9.3.8 SS (Schildknecht and Spiesberger) . . . 34
2.9.3.9 H (Haidt) . . . 35
2.9.3.10 GBW (Golec-Biernat and Wüsthoff) . . . 35
2.9.3.11 ZEUS REGGE fit . . . 35
2.9.3.12 BKS (Badełek, Kwieciński and Staśto) model for R . . . 36

3 HERA and ZEUS **37**
3.1 HERA . . . 37
3.2 ZEUS . . . 38
3.2.1 Calorimeter (CAL) . . . 40
3.2.2 Central Tracking Detector (CTD) . . . 41
3.2.3 Luminosity measurement (LUMI) . . . 42
3.2.4 Trigger (FLT/SLT/TLT) and event reconstruction . . . 42

4 Beam Pipe Calorimeter and Tracker **45**
4.1 Small-angle detectors . . . 45
4.2 Beam Pipe Calorimeter (BPC) . . . 46
4.2.1 Concept of calorimetry . . . 46
4.2.1.1 Electromagnetic showers . . . 47
4.2.1.2 Hadronic showers . . . 48
4.2.2 The BPC of ZEUS . . . 48
4.3 Beam Pipe Tracker (BPT) . . . 50
4.3.1 Motivation for a tracking detector . . . 50
4.3.2 Concept of silicon detectors . . . 51
4.3.3 The BPT of ZEUS, fact and fiction . . . 52
4.4 Data taking and trigger . . . 54
4.5 Surveys . . . 56

5 Monte Carlo Simulation **57**
5.1 Concept of Monte Carlo Simulation . . . 57
5.2 ZEUS detector simulation . . . 58
5.2.1 BPC simulation . . . 58
5.2.2 BPT simulation . . . 59
5.3 Physics simulation . . . 61
5.3.1 Choice of event generators . . . 61
5.3.2 Event generation . . . 62
5.3.3 Preselection of events . . . 64

6 Reconstruction **65**
6.1 Reconstruction of BPC and BPT quantities . . . 65
6.1.1 BPC energy reconstruction and calibration . . . 65
6.1.2 BPC position reconstruction . . . 72
6.1.3 BPT track reconstruction and alignment . . . 74
6.1.3.1 Beam tilt . . . 79
6.1.4 BPT efficiency determination . . . 79
6.2 Reconstruction of hadronic final state quantities . . . 81
6.2.1 Noise suppression . . . 83
6.2.2 Reconstruction algorithm . . . 84
6.2.3 Global quantities of the hadronic final state . . . 84
6.3 Kinematic event reconstruction . . . 85
6.3.1 Electron method . . . 85
6.3.2 Double angle method . . . 85
6.3.3 Jacquet-Blondel method . . . 85
6.3.4 Sigma (Σ) method . . . 86
6.3.5 Mixed Sigma ($m\Sigma$) method . . . 86
6.3.6 Electron-Sigma ($e\Sigma$) method . . . 86
6.3.7 Resolutions . . . 86

7 Data Samples **89**
7.1 Event selection . . . 89
7.1.1 Online event selection . . . 89
7.1.2 Kinematic regions and reconstruction . . . 91
7.1.3 Offline event selection . . . 91
7.1.4 Using the BPT as a presampler . . . 95
7.2 Determination of the diffractive event fraction . . . 95
7.3 Backgrounds . . . 98
7.3.1 Non-ep background . . . 98
7.3.2 Photoproduction background . . . 99
7.4 Comparison of data and MC . . . 102
7.4.1 Scattered electron and hadronic final state . . . 102
7.4.2 The vertex distribution . . . 108

8 Results **111**
8.1 Measurement of the structure function . . . 111
8.1.1 Unfolding technique . . . 111
8.1.2 Binning of the data . . . 114
8.1.3 Estimate of the effect of F_L . . . 116
8.1.4 Estimate of systematic uncertainties . . . 118
8.1.5 Results of the measurement . . . 123
8.2 Interpretation of the results . . . 132
8.2.1 Extrapolation of the cross section to photoproduction . . . 132
8.2.2 Energy dependence of the photoproduction cross section . . . 134
8.2.3 The slope of F_2 . . . 137

9 Summary **139**

A A Simple Model for Diffraction **141**

B Measurement of the structure function using radiative events **143**
B.1 Event selection, reconstruction, and binning of the data . . . 143
B.2 Background . . . 145
B.3 Comparison of data and MC . . . 145
B.4 Results of the measurement . . . 145
B.5 Uncertainties from radiative corrections in the nominal analysis . . . 148

C Selection Cuts **151**
C.1 BPC energy calibration . . . 151
C.2 BPC position reconstruction . . . 152
C.3 BPC and BPT alignment . . . 152
C.4 BPT efficiency determination . . . 153
C.5 High-y region . . . 153
C.6 Medium-y region . . . 154
C.7 Low-y region . . . 154
C.8 Low-y prescaled region . . . 155
C.9 ISR analysis . . . 155

References **157**

Chapter 1

Introduction

The question "What is matter made of?" is one of the oldest questions of mankind. According to today's accepted scientific answer, formulated in the Standard Model of particle physics, matter is organized in hierarchies. It is composed of atoms, in which electrons surround a tiny core, the nucleus, which in turn consists of protons and neutrons. Protons and neutrons themselves are made of quarks, which are believed to be, like electrons, pointlike elementary particles.

Elementary particles interact with each other by exchanging shortlived virtual particles, which mediate the forces in the microscopic world, the strong, the electromagnetic and the weak force (the latter two being unified in the electroweak force). The properties of elementary and composite particles as well as of their interactions are explored in scattering experiments, where two particles are brought to collision. The interaction rate and the resulting final state of the interaction are used to draw conclusions on the nature of the interaction and of the participating particles.

Such scattering experiments are performed at the German electron synchrotron (Deutsches Elektronen-Synchrotron, DESY) laboratory in Hamburg, Germany. There, the storage ring HERA is used to collide electrons with protons, i.e. an elementary particle with a composite particle. The electrons are used as pointlike probes to explore the inner structure of the protons. This process is referred to as deep inelastic scattering, and the research work carries on a technique that was developed by Rutherford [1] in exploring the structure of atoms.

At HERA, the large detectors H1 and ZEUS are situated in the two interaction regions where the beams collide. They are massive devices, equipped with highly sophisticated electronics and detection components in order to reconstruct detailed information about the collision process.

The prime motivation for building HERA was the measurement of the proton structure functions, which contain information about the quarks inside the proton, as well as about their way of interacting with each other by exchanging the mediators of the strong force, the gluons. Theoretical models of the proton and the strong interaction are constructed to reproduce the structure functions, and can thus be tested by comparing their predictions to measurements.

This report is organized as follows: In chapter 2, the theoretical foundations of deep inelastic scattering are given. In chapter 3, the HERA storage ring and the ZEUS detector are presented, followed in chapter 4 by a more detailed description of two components of ZEUS that were of prime importance for this work. Chapters 5, 6 and 7 describe steps on the way from signals in the detectors to reconstructed final states emerging from electron-proton collisions. Chapter 8 presents the extraction technique and the results for the measurement of the proton structure function F_2, as well as a detailed interpretation and analysis of the obtained values.

Preliminary results of the analysis presented in this report have been published in a contributed paper to the EPS 99 conference [2] and two articles in conference proceedings [3, 4]. A ZEUS publication is in preparation. Figures and tables labelled by "ZEUS 1997 (Preliminary)" have been approved by the collaboration as official ZEUS results. According to the common policy of ZEUS, they will be declared final as soon as the publication of the results is ready.

Besides activities related to the subject of my thesis, I was responsible during my time as a doctoral candidate for the maintenance and further development of ELECPO [5–7], the algorithm for the reconstruction of the position of the scattered electron in the ZEUS detector, which is used in many of the analyses published by ZEUS. I also supervised two diploma theses [8, 9] during this time and contributed in discussions to further diploma and doctoral theses of ZEUS students in Bonn, as well as to analyses and publications of the "Structure Functions" working group in ZEUS. In Bonn, I was responsible for the system administration of the ZEUS cluster of Digital Unix workstations and Linux PC's, as well as for the WWW pages. At DESY, I participated, like all members of the experiment, in data taking shifts. As a member of the calorimeter group, I took over the task to adapt part of the calorimeter software to the operating system of a new readout computer.

Chapter 2

Theory

The first part of this chapter describes the theoretical foundations of deep inelastic electron-proton scattering, starting (after introducing the relevant variables and terms) from the parameterization of the cross section by structure functions, via the interpretation of structure function measurements as evidence for a substructure of the proton, i.e. the presence of quarks inside the proton, to the widely accepted picture of the strong interaction as a quantum field theory. In the second part of the chapter, the current status of structure function measurements and the contribution of HERA are discussed, together with models and parameterizations that serve to describe and interpret the measured data.

2.1 The Standard Model (SM)

The Standard Model (SM) of particle physics describes the subnuclear world in the framework of renormalizable quantum field theories with a certain group structure reflecting the nature of the forces that are governing this regime. The SM interprets interactions between pointlike fundamental particles, the quarks and leptons, as mediated by the exchange of virtual gauge bosons, the photon γ (electromagnetic interaction), the Z and $W^{\pm}$ (weak interaction), and the gluons g (strong interaction). These particles are listed in Table 2.1. Leptons and quarks are arranged in generations of lepton number respectively quark flavor. Only quarks participate in the strong interaction, charged leptons and quarks can interact electromagnetically, and all leptons and quarks feel the weak force.

	leptons		quarks	
charge	-1	0	$-1/3$	$+2/3$
1st gen.	electron e	e-neutrino ν_e	down d	up u
2nd gen.	muon μ	μ-neutrino ν_μ	strange s	charm c
3rd gen.	tau τ	τ-neutrino ν_τ	bottom b	top t

interaction	mediator
electromagnetic	photon γ
weak	$W^{\pm}$
	Z
strong	gluons g

Table 2.1: Fundamental fermions (left) and bosons (right) in the Standard Model.

While free leptons, like the electron, have been studied experimentally to great detail, quarks have never been observed directly. The existence of quarks can only be derived from the properties and interactions of the particles which they constitute, the hadrons. Two examples of hadrons are the proton and the neutron, which contain up (u) and down (d) quarks.

2.2 Deep inelastic scattering (DIS)

One of the means of collecting information about particles and their interactions are scattering experiments, where particles are accelerated to high energies and then brought to collision. From

the result of the interaction, conclusions can be drawn about the nature of the fundamental particles and the forces acting on them.

There are three approaches to study the fundamental lepton-quark interaction: lepton-quark elastic scattering, lepton-pair annihilation into quark pairs, and quark-pair annihilation into lepton pairs. These fundamental processes correspond to deep inelastic scattering (DIS), e^+e^- annihilation, and the Drell-Yan process, which are being investigated (for example) at HERA (DESY, Hamburg), LEP and SLC (CERN, Geneva and SLAC, Stanford) and the TEVATRON (FNAL, near Chicago), respectively (Fig. 2.1).

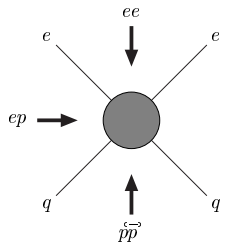

Fig. 2.1: The three approaches to study the fundamental lepton-quark interaction: ee colliders (LEP and SLC), ep colliders (HERA) and $\overleftarrow{p\bar{p}}$ colliders (TEVATRON).

Prior to 1960, elastic electron-proton scattering experiments had shown that the proton has a size of about 1 fm [10, 11]. Evidence for a substructure was found in the first deep inelastic scattering experiments that took place at the end of the 1960's at SLAC [12, 13], where electrons were brought to collision with a proton target at rest. Many other DIS experiments followed at increasing beam energies, until in 1992 the first deep inelastic scattering experiments with colliding beams, H1 and ZEUS, started to collect data.

2.3 Kinematic variables

Deep inelastic neutral current (NC) electron-proton scattering, $ep \to eX$, is viewed in lowest order as mediated by the exchange of a virtual photon or Z between the electron and the proton (Fig. 2.2). The charged current (CC) process $ep \to \nu X$, where the exchanged virtual boson $W^{\pm}$ carries electric charge and the outgoing lepton is a neutrino, will not be considered further in this report, and the discussion of neutral current scattering will be limited to photon exchange. This will be justified later.

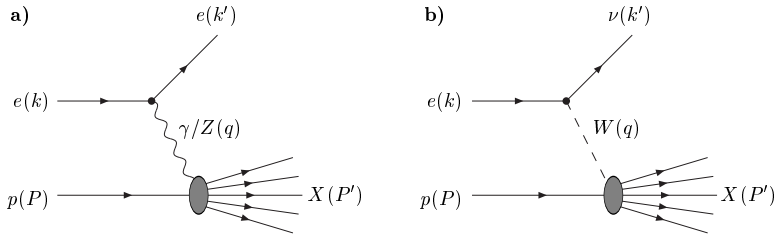

Fig. 2.2: Lowest-order Feynman diagrams describing a) neutral current and b) charged current deep inelastic electron-proton scattering.

The four-momenta of the incoming (outgoing) electron e are denoted by k (k'), those of the proton p and the hadronic final state X by P and P', and that of the exchanged photon by q. In the absence of initial and final state radiation, the kinematics of unpolarized electron-proton scattering can be described in a Lorentz-invariant way by the Mandelstam variables:

$$s = (k+P)^2 = (k'+P')^2 \quad (2.1)$$
$$t = (P-P')^2 = (k-k')^2 \quad (2.2)$$
$$u = (P-k')^2 = (P'-k)^2. \quad (2.3)$$

However, the following set of kinematic variables is more conventional:

$$Q^2 = -q^2 = -(k-k')^2 = -t \quad (2.4)$$
$$W^2 = (P+q)^2 = (P')^2 \quad (2.5)$$
$$x = Q^2/(2P\cdot q) \quad (2.6)$$
$$y = (P\cdot q)/(P\cdot k) \quad (2.7)$$
$$\nu = (P\cdot q)/m_p, \quad (2.8)$$

where m_p denotes the mass of the proton. At fixed s (the square of the electron-proton center-of-mass energy), only two Lorentz-invariants are independent; consequently, there are relations between them, given e.g. by

$$W^2 = s+t+u \quad (2.9)$$
$$W^2 = Q^2(1-x)/x \quad (2.10)$$
$$Q^2 = sxy \quad (2.11)$$
$$\nu = Q^2/(2xm_p). \quad (2.12)$$

Mass terms have been neglected. The common choice of two independent variables is x and Q^2 (or, occasionally, y and Q^2). In elastic electron-proton scattering, the kinematics are described by only one variable, as in this case $x = 1$.

The variable $\sqrt{s}$ represents the center-of-mass energy of the electron-proton system, which at HERA is $\sqrt{s} = 300\,\mathrm{GeV}$, about one order of magnitude higher than in all previous experiments.[1] This is an advantage of a collider experiment over a fixed-target experiment: at HERA, $s = 4E_eE_p$, while for protons at rest $s = 2E_em_p$.

The square of the four-momentum transfer, q^2, is usually replaced for convenience by its negative, Q^2, because Q^2 is positive for the photon being exchanged in the t-channel: the momentum transfer is spacelike. Q^2 represents the virtuality of the photon, which determines the hardness of the process: "hard" are processes where the exchanged boson has high virtuality, corresponding to a short distance between the interacting particles, while in "soft" processes the four-momentum transfer is small, and the particles are farther apart. Q^2 can be imagined as related to a resolving power, which is limited, in analogy to a microscope, by the wavelength of the virtual photon. This is given, in the proton rest frame, by

$$\lambda = \frac{1}{|\vec{q}|} = \frac{1}{\sqrt{Q^2+\nu^2}}, \quad (2.13)$$

which is approximately ($\nu^2 \gg Q^2$):

$$\lambda \approx \frac{1}{\nu} = \frac{2xm_p}{Q^2} = \frac{2m_p}{sy}. \quad (2.14)$$

A high resolution,[2] i.e. sensitivity to the structure of the proton, consequently requires to go to high squared four-momentum transfer Q^2, or to go to small values of x. The allowed range of Q^2 is given by $0 < Q^2 < s$.

[1] See footnote on page 37.

[2] Some authors quote instead $\lambda = 1/|q| = 1/\sqrt{Q^2}$ as resolution. In contrast to the de Broglie wavelength in the proton rest frame used above, this is a frame-independent quantity.

The cross section for the processes with Z or $W^{\pm}$ exchange is suppressed as compared to γ exchange by the propagator factor $[Q^2/(Q^2+M^2_{Z,W})]^2$, and the γ-Z interference term is suppressed by a factor $Q^2/(Q^2+M_Z^2)$, where $M_Z = 91.2\,\mathrm{GeV}$ and $M_W = 80.4\,\mathrm{GeV}$ [14] are the masses of the exchanged bosons, respectively. Consequently, it is justified to neglect these processes for $Q^2 \ll M^2_{Z,W}$, which is the case for the process studied in this report.

W^2 is the mass squared of the hadronic final state, or the center-of-mass energy squared of the photon-proton system. For $x \ll 1$, it can be approximated as

$$W^2 \approx \frac{Q^2}{x} = sy, \tag{2.15}$$

and the allowed values of W^2 lie in the range $0 < W^2 < s$.

The following variables can be understood most easily in the proton rest frame. There, the quantity ν is the energy of the intermediate photon, i.e. the energy transfer from the electron to the proton,

$$\nu = \tilde{E}_e - \tilde{E}'_e = \tilde{E}_\gamma \tag{2.16}$$

($\tilde{E}$ denotes an energy in the proton rest frame). The allowed range of ν is limited by the energy of the electron, $\tilde{E}_e = s/2m_p$, and thus ν can go up to the extremely large value $\tilde{E}_e = 48\,\mathrm{TeV}$ at HERA.

Closely related to ν is the relative energy transfer y, given by

$$y = \frac{\tilde{E}_e - \tilde{E}'_e}{\tilde{E}_e} = \frac{\nu}{\tilde{E}_e}, \tag{2.17}$$

and obviously $0 < y < 1$. The value of y determines the inelasticity of the event, and therefore the region where ep scattering becomes deep inelastic is at high values of y.

The Bjorken scaling variable x, for which also $0 < x < 1$, obtains its interpretation in the quark-parton model (section 2.6.1).

The Lorentz-invariant variables are not directly measured in an experiment; instead, one measures the energy E'_e of the scattered electron, and the angle θ of the outgoing relative to the incoming electron (for more sophisticated reconstruction methods see section 6.3). The following equations relate the Lorentz-invariant variables to those measured in the lab frame (E_e denotes the electron beam energy):

$$Q^2 = 2E_eE'_e(1-\cos\theta) \tag{2.18}$$

$$y = 1 - \frac{E'_e}{2E_e}(1+\cos\theta), \tag{2.19}$$

i.e. by selecting energy and angle of the emerging electron one can choose the value of y and Q^2. This allows to prepare a photon as a probe and use it to explore the structure of the proton. In this sense, the incoming electrons serve as a source of probes, and the outgoing electrons carry the information gathered by the probes.

For small scattering angles $\theta \ll 1$, $\cos\theta \approx 1 - \theta^2/2$, these relations simplify to

$$Q^2 \approx E_eE'_e\theta^2 \tag{2.20}$$

$$y \approx 1 - \frac{E'_e}{E_e}, \tag{2.21}$$

and it becomes obvious that in events at low values of Q^2 the scattered electron emerges at a small angle θ.

2.4 The ep cross section and the proton structure functions

Differential cross sections for the process $AB \to CD$ are calculated according to

$$d\sigma = \frac{|\mathcal{M}|^2}{F} dQ. \tag{2.22}$$

Here, dQ denotes the Lorentz-invariant phase space factor, related to the outgoing particles C and D (and ensuring four-momentum conservation),

$$dQ = (2\pi)^4\delta^{(4)}(p_C + p_D - p_A - p_B)\frac{d^3p_C}{(2\pi)^3 2E_C}\frac{d^3p_D}{(2\pi)^3 2E_D}, \tag{2.23}$$

and F is the flux of incoming particles A and B,

$$F = 4\sqrt{(p_A\cdot p_B)^2 - m_A^2 m_B^2}. \tag{2.24}$$

While dQ and F are merely "bookkeeping" factors related to the phase space and kinematics, the complete dynamics of the interaction are included in the matrix element $|\mathcal{M}|^2$, which is, in case spins are not measured, to be replaced by the spin-averaged matrix element, $\overline{|\mathcal{M}|^2}$.

Since ep scattering is mediated by the exchange of a photon, it falls into the domain of Quantum Electrodynamics (QED). For the most simple process described by QED, $e\mu \to e\mu$, the matrix element has the form

$$\overline{|\mathcal{M}|^2} = \frac{\alpha^2}{q^4} L^e_{\mu\nu} L^{\mu\nu}_\mu. \tag{2.25}$$

Here, α denotes the electromagnetic coupling constant, q the four-momentum of the exchanged photon, and $L^{\mu\nu}_e$ and $L^{\mu\nu}_\mu$ are Lorentz tensors describing the electron and the muon vertex, respectively. In QED, leptonic tensors are given by

$$L^{\mu\nu}_{e,\mu} = \frac{1}{2}\sum_{\text{spins}} \left[\bar{u}(k')\gamma^\mu u(k)\right]\left[\bar{u}(k')\gamma^\nu u(k)\right]^*. \tag{2.26}$$

In the process $ep \to eX$, the formalism is kept identical and one may write

$$\overline{|\mathcal{M}|^2} = \frac{\alpha^2}{q^4} L^e_{\mu\nu} W^{\mu\nu}_p, \tag{2.27}$$

where now the hadronic tensor $W^{\mu\nu}_p$ for the inelastic scattering off a proton has taken the place of the leptonic tensor $L^{\mu\nu}_\mu$ for the elastic scattering off a muon. Contrary to leptons, there is no simple formula like Eq. (2.26) for the hadronic tensor.

It can be shown, however, that for an electromagnetic interaction $W^{\mu\nu}_p$ may be written using the four-momenta of the proton and the exchanged photon, P and q, and two scalar structure functions depending on two variables, $W_{1,2}(x,Q^2)$. The structure functions carry the whole information about the interaction (or more precisely, about the deviation of the lepton-proton cross section from the lepton-lepton cross section):

$$W^{\mu\nu}_p = W_1(x,Q^2)\left(-g^{\mu\nu} + \frac{q^\mu q^\nu}{q^2}\right) + W_2(x,Q^2)\frac{1}{m_p^2}\left(P^\mu - \frac{P\cdot q}{q^2}q^\mu\right)\left(P^\nu - \frac{P\cdot q}{q^2}q^\nu\right). \tag{2.28}$$

In a more modern notation, these structure functions are replaced by $F_{1,2}(x,Q^2)$, to which they are related by

$$m_p W_1(x,Q^2) = F_1(x,Q^2) \tag{2.29}$$

$$\nu W_2(x,Q^2) = F_2(x,Q^2). \tag{2.30}$$

Yet another set of structure functions is in use, the helicity structure functions (the reason for their name will become clearer later), F_T and F_L, given by

$$F_L = F_2 - 2xF_1 \quad (2.31)$$
$$F_T = 2xF_1. \quad (2.32)$$

With one structure function from each of the latter two sets, the double-differential cross section for inelastic ep scattering may finally be expressed as

$$\frac{d^2\sigma}{dx\,dQ^2} = \frac{2\pi\alpha^2}{xQ^4}\left(Y_+F_2(x,Q^2) - y^2F_L(x,Q^2)\right), \quad (2.33)$$

where $Y_+ = 1+(1-y)^2$, and mass terms have been neglected. Note that the structure functions are explicitly defined with respect to the lowest order, i.e. the one-boson exchange or Born cross section, as used throughout this section.

2.5 Radiative corrections to the cross section

When measuring real-life cross sections, one has to take radiative corrections, i.e. effects of higher orders in QED, into account. The observed cross section will therefore have the form

$$\frac{d^2\sigma}{dx\,dQ^2} = \frac{2\pi\alpha^2}{xQ^4}\left(Y_+F_2(x,Q^2) - y^2F_L(x,Q^2)\right)(1+\delta_r), \quad (2.34)$$

i.e. the one-photon exchange cross section (the Born level $\mathcal{O}(\alpha^2)$), multiplied by a correction factor for QED radiative effects, $1+\delta_r$. The correction factor is a function of x and Q^2, but to a good approximation independent of F_2 and F_L.

There are two kinds of radiative corrections, those where real photons are emitted (and thus the final state is different from the Born level), and those where virtual photons (and possibly further particles) appear as additional internal lines (and the final state is unchanged, therefore such graphs contribute by interference). Real photon radiation can come from the electron or from the proton side or from both; the biggest contribution comes from radiation off the electron line.

In the next highest order above the Born level, $\mathcal{O}(\alpha^3)$, the electron may radiate a real photon before the interaction (initial state radiation, ISR), or after the interaction (final state radiation, FSR), or by the QED Compton process. More precisely, the radiative cross section can be separated into a sum of three parts, which are dominated by singularities arising, respectively, from the radiation of photons collinear with the incoming electron, of photons collinear with the outgoing electron, and of photons which shift Q^2 to small values. These three parts are denoted by ISR, FSR and QED Compton contribution.

In order $\mathcal{O}(\alpha^4)$, there are self-energy, vertex and loop corrections that by interference with the Born level graphs also contribute at level $\mathcal{O}(\alpha^3)$. The most important diagrams are shown in Fig. 2.3. Similar ones can be drawn for the proton side, and there are also graphs with radiation from both sides.

Radiative corrections leading to additional external lines affect the relations between energy and angle of the scattered electron and the kinematic variables. For example in the case of ISR collinear with the incoming electron, the ISR-corrected kinematic variables ($\hat{Q}^2$, $\hat{x}$, $\hat{y}$) can be derived from those calculated without taking ISR into account (Q^2, x, y) according to Eqs. (2.18) and (2.19). This is conveniently expressed in terms of a new variable $f = 1-z = E_\gamma/E_e$, with $0 < f < 1$ [15]:

$$\hat{Q}^2 = Q^2(1-f) \quad (2.35)$$
$$\hat{x} = xy(1-f)/(y-f) \quad (2.36)$$
$$\hat{y} = (y-f)/(1-f), \quad (2.37)$$

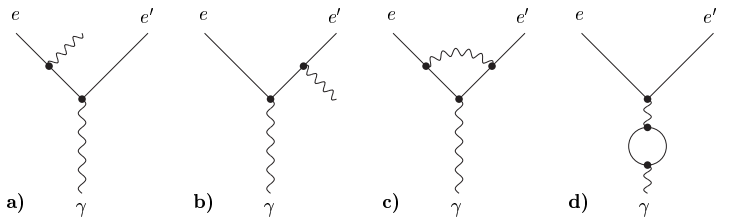

Fig. 2.3: The most important radiative corrections to ep scattering: a) ISR, b) FSR, c) vertex correction, d) virtual loop.

and similarly for FSR. The reduction of Q^2 by a factor $1-f$ can be exploited to extend the acceptance of an experiment toward lower Q^2 without making any changes to the detector (section 4.1).

2.6 The high-Q^2 regime

2.6.1 The quark-parton model (QPM)

The (so-called) naive quark-parton model was suggested by Feynman [16] in order to explain the early deep inelastic scattering experiments at SLAC. The proton is assumed to be composed of a number of pointlike, i.e. structureless, objects, the partons. Inelastic electron-proton scattering is then regarded as an incoherent sum over elastic electron-parton scattering processes (Fig. 2.4); the interactions of partons with each other are neglected in this picture.

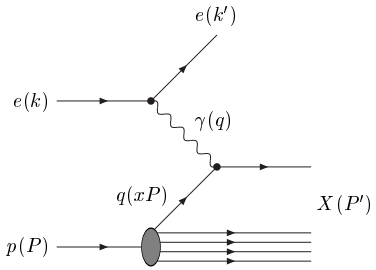

Fig. 2.4: Inelastic electron-proton scattering viewed as elastic electron-parton scattering: one of the partons q in the proton, carrying a momentum fraction x, interacts with the electron, while the other partons continue undisturbed.

The Bjorken scaling variable x can be interpreted in the parton model as the momentum fraction of the proton that is carried by the interacting parton. For the proof, one assumes that the photon is exchanged with a parton of four-momentum p inside the proton, carrying a momentum fraction ξ of the proton, $p = \xi P$, resulting in an emerging parton of four-momentum p'. Then, four-momentum conservation requires

$$p + q = \xi P + q = p' \quad \Longrightarrow \quad p^2 + 2\xi P\cdot q - Q^2 = {p'}^2. \quad (2.38)$$

Assuming equal (or negligibly small) masses for the initial and final state partons, $p^2 = {p'}^2$, yields $\xi = Q^2/(2P\cdot q) = x$. Note that this interpretation is compatible with the allowed range $0 < x < 1$.

In this picture, y obtains another interpretation. It is related to the scattering angle θ^* in

the electron-parton center-of-mass frame:

$$y = \frac{1}{2}(1 - \cos\theta^*). \tag{2.39}$$

It is convenient to neglect proton and parton masses, and also to neglect the intrinsic transverse momentum of the partons in the proton (which is of the order of the inverse of the proton size, $(1\,\mathrm{fm})^{-1} \approx 200\,\mathrm{MeV}$). This is done by invoking the infinite momentum frame, where the proton has a very large longitudinal momentum, which makes it appear to the photon as a Lorentz-contracted flat disc of partons. Due to time dilation, any interaction between the partons is retarded; the interaction of the electron and the proton can therefore be viewed as incoherent sum over single electron-parton interactions.

The momentum distribution of partons in the proton is described by parton density functions (PDF): $f_i(x, Q^2)\,dx$ denotes the number of partons of type i in the proton that carry a momentum fraction between x and $(x + dx)$, as observed when probing the proton with a photon of virtuality Q^2. The PDF's are believed to be universal, i.e. an intrinsic property of the proton, independent from the process being studied (e.g. pp or ep).

In the quark-parton model, the structure functions introduced in section 2.4 are related to the parton density functions f_i and the electrical charges of the partons e_i (in units of the electron charge e):

$$F_2(x, Q^2) = x \sum_i e_i^2 \cdot f_i(x, Q^2). \tag{2.40}$$

The relation for F_1 depends on the spin of the partons. For spin 1/2, the Callan-Gross relation [17] holds:

$$2xF_1 = F_2 \quad \Longrightarrow \quad F_L = 0, \tag{2.41}$$

while for partons of spin 0,

$$2xF_1 = 0 \quad \Longrightarrow \quad F_T = 0. \tag{2.42}$$

This can be understood from Fig. 2.5.

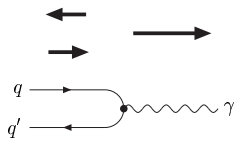

Fig. 2.5: Head-on collision of a parton and a photon. A virtual photon has three possible helicity states $\lambda = 0, \pm 1$. If the photon is transversely polarized, its spin points parallel or anti-parallel to its direction of movement, i.e. $\lambda = \pm 1$. Since in electromagnetic interactions helicity is conserved, the massless parton can absorb the photon only if it has spin 1/2. A similar argument shows that longitudinally polarized photons are needed if partons carry spin 0.

One of the key predictions of the quark-parton model is scaling [18]. The idea is that probing a pointlike object with increasing resolution cannot reveal any further structure (i.e. there is no length scale in the process); consequently, the structure functions should not depend on the scale parameter Q^2. Bjorken predicted that in the limit $Q^2 \to \infty$ and $\nu \to \infty$, but x constant:

$$F_1(x, Q^2) \;\to\; F_1(x) \tag{2.43}$$

$$F_2(x, Q^2) \;\to\; F_2(x). \tag{2.44}$$

The partons were identified [19] with the quarks [20–24], which had originally been introduced to explain the observed spectrum of hadrons. This implied that partons, like quarks, have spin 1/2, and indeed the Callan-Gross relation was confirmed by early SLAC data, as was Bjorken's hypothesis of scaling.

However, later measurements showed deviations from the Callan-Gross relation and violations of scaling. In addition, it was found that only about half of the proton momentum is carried by charged spin 1/2 partons [25]. These findings triggered the development of a quantum field theory of the strong interaction, Quantum Chromodynamics (QCD).

2.6.2 Quantum Chromodynamics (QCD)

QCD describes the strong interaction of quarks by the exchange of virtual gluons, in analogy to QED, where charged particles interact by exchanging virtual photons. Like QED, QCD is a renormalizable quantum field theory. The gluons mediate the force between the quarks in the proton and account for the missing fraction of the proton momentum.[3]

The place of electrical charge is taken in QCD by the attribute color, or "color charge" (having, of course, nothing to do with real colors). In contrast to electrical charge, which comes in only one type, namely the negative charge (and its anti-charge, the positive charge), there are three colors: red, green, and blue (and their respective anti-colors: cyan, magenta and yellow). This is reflected by the group structure of the theories, U(1) for QED and SU(3) for QCD. In QCD, also the mediators of the force, the gluons, carry color. This is characteristic for a non-Abelian gauge theory, in contrast to the Abelian QED, where the photon is uncharged. Consequently, gluons do not only mediate the force between quarks, but they can also interact with each other. There are eight gluons in QCD, each carrying color plus anti-color.

In the static quark model, all hadrons are made of quarks, and they are composed such that the sum of quark colors is white: either in a $|qqq\rangle$ state (a baryon) with one red, one green, and one blue quark, or in a $|q\bar{q}\rangle$ state (a meson), with one quark carrying the anti-color of the other (to be more rigorous: all hadrons are color singlet states). These quarks are referred to as valence quarks. In QCD, a state $|X\rangle$ can fluctuate for a short time e.g. into a $|Xg\rangle$ or a $|Xq\bar{q}\rangle$ state, yielding in the latter case a dynamically originated pair of sea quarks.[4]

For the structure functions of the proton, QCD introduces corrections to the picture of QPM: a quark in the proton can e.g. radiate a gluon before the interaction with the probing photon (the QCD Compton process, QCDC) and thus acquire transverse momentum, which renders the argument of Fig. 2.5 obsolete: spin 1/2 quarks can also couple to longitudinally polarized photons, and the Callan-Gross relation no longer holds.

In the same way, the existence of gluons leads to scaling violations: the quarks continuously radiate and absorb gluons, forming a cloud of gluons and quark-antiquark pairs (from pair production of gluons) around the bare quarks. By increasing the resolution Q^2 of the probe, one can look deeper into the cloud (which has, in contrast to the pointlike quark, a structure); this obviously constitutes a resolution-dependent effect. One observes a logarithmic dependence of the structure functions on Q^2, which is exactly what is predicted by QCD. Two graphs leading to scaling violations, the boson-gluon fusion process (BGF) and the QCD Compton (QCDC) process, are shown in Fig. 2.6.

2.6.2.1 Perturbative QCD (pQCD)

When calculating cross sections in a quantum field theory like QED, Feynman graphs representing matrix elements are calculated up to a certain order, i.e. number of involved vertices, and the contribution from the missing higher orders is assumed to be small, due to the small coupling constant of QED, $\alpha = 1/137$. The cross section is thus expanded in a perturbation series, of which only the dominant contributions are calculated.

Unfortunately, there are contributions from higher orders, like loop diagrams, that result in logarithmically diverging integrals over the momenta of the circulating particles. This problem is solved by a calculation technique called renormalization, where the divergences are absorbed order by order into a redefinition of the electron charge, mass, and wave function. In addition, the coupling constant is no longer constant, but becomes scale dependent, by the introduction of an effective reference scale μ, the renormalization scale. In practice, α remains small over the whole region accessible to experiments.

[3] In the following, the term partons will be used to denote both quarks and gluons.

[4] At this point, there is in general no way to tell a valence from a sea quark any more. Valence and sea quarks do, however, have different characteristical parton density functions.

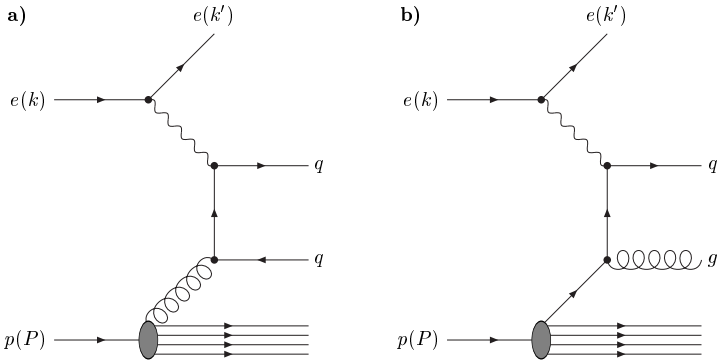

Fig. 2.6: Two graphs leading to scaling violations. a) The boson-gluon fusion (BGF) process. The exchanged photon and a gluon from the proton produce a quark-antiquark pair. This is also the most important process leading to the production of heavy quarks c and b. b) The QCD-Compton (QCDC) process. A quark from the proton radiates a gluon before interacting with the photon.

In QCD the perturbative expansion technique runs into a severe problem: the coupling strength of QCD, α_s, is not small in general, not even everywhere in the limited region accessible to experiments where one would like to apply perturbative QCD (pQCD). Its scale dependence is given by

$$\alpha_s(\mu^2) = \frac{12\pi}{(11n - 2n_f)\ln(\mu^2/\Lambda^2)}, \tag{2.45}$$

where $n = 3$ is the number of colors, $n_f = n_f(\mu^2)$ is the number of active quark flavors (at HERA, $n_f = 3 \ldots 5$), and $\Lambda \approx 100 \ldots 300\,\mathrm{MeV}$ is a parameter of QCD. A usual choice for the renormalization scale is $\mu^2 = Q^2$.

As can easily be seen, $\alpha_s \to 0$ for $\mu \to \infty$ and $\alpha_s \to \infty$ for $\mu \to \Lambda$. This asymptotic behavior of the strong coupling constant has two consequences: at high Q^2, corresponding to small distances, the strong interaction becomes weak, and consequently the partons in the proton do not interact with each other. This is the situation that had to be postulated in the quark-parton model, and is referred to as asymptotic freedom of the quarks: as long as they are close together, they do not notice each other.[5]

At the other end, at low Q^2, or large distances, the force between quarks becomes so large that it is not possible to observe free quarks outside bound states. This property is known as confinement of the quarks in the hadrons.

Consequently, pQCD calculations can only be made for large Q^2, where α_s is small. At low Q^2, α_s is forbiddingly large.

2.6.2.2 The factorization theorems of QCD

The factorization theorems[6] of QCD [26] specify the problem of the nonapplicability of perturbative calculation techniques, by reducing it to only part of the interaction. They state that

[5] This is in contrast to the situation in QED, where the scale dependence of the coupling strength is explained by charges in a surrounding cloud of virtual particles screening the charge of the bare particle; in QCD, the self-interaction of gluons leads to anti-screening of color.

[6] There is one factorization theorem for each interaction known to factorize.

an interaction involving hadrons factorizes into short-distance and long-distance contributions. This introduces a new scale μ_F, the factorization scale, which separates what is understood by "long" and "short". Short-distance interactions are calculable in perturbative QCD, while long-distance interactions are not. For the case of structure functions, this means that F_2, for example, can be written as

$$F_2(x, Q^2) = \sum_{i=q,\bar{q},g} \int_x^1 dx' C_i\left(\frac{x}{x'}, \alpha_s(\mu_F^2), \frac{Q^2}{\mu_F^2}\right) f_i(x', \mu_F^2), \tag{2.46}$$

where C_i denote the coefficient functions, responsible for the short-range interaction, and f_i are the parton density functions, parameterizing the long-range part. The factorization theorem for the $ep \to eX$ process is illustrated in Fig. 2.7.

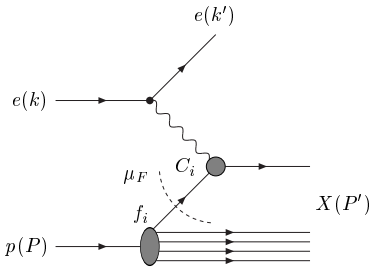

Fig. 2.7: Illustration of the QCD factorization theorem for the $ep \to eX$ process. The factorization scale μ_F separates long-range and short-range contributions, which are absorbed into parton densities f_i and coefficient functions C_i, respectively.

In leading order perturbation theory, the C_i are simply the squared parton charges, times a delta function:

$$C_q(x) = e_q^2\delta(1-x) \tag{2.47}$$
$$C_{\bar{q}}(x) = e_{\bar{q}}^2\delta(1-x) = C_q(x) \tag{2.48}$$
$$C_g(x) = 0, \tag{2.49}$$

and thus one retrieves again the familiar QPM form in Eq. (2.40) for the structure function F_2.

In higher orders, this is no longer true and there is some freedom whether to absorb corrections into the coefficient or into the parton density functions. This has to be specified by the choice of a renormalization scheme. The DIS scheme [27] is defined such that all corrections go into the parton densities, such that the coefficient functions and the relation between F_2 and the parton densities keep their simple form. For theoretical calculations, however, the $\overline{\mathrm{MS}}$ scheme (modified minimal subtraction) [28] is preferred.

It should be noted here that parton densities are not directly observable, and therefore are allowed to depend on an (arbitrary) parameter like the factorization scale. Structure functions, however, are observables, and must not depend on the choice of μ_F. The choice of absorbing corrections into coefficient functions or into parton densities does therefore not affect the resulting F_2, but only the relation between F_2 and the parton densities.

2.6.2.3 DGLAP equations

Parton density functions cannot be derived from first principles. What (p)QCD can predict, however, is the Q^2 dependence of parton densities, their evolution with Q^2. This means that, given the parton densities at one scale Q^2, a prediction can be derived for any different scale. Qualitatively, the origin of the scale dependence has already been mentioned above: if the resolving power is increased, an object, carrying a quark charge and a momentum fraction x',

which looked pointlike before, may be resolved as consisting rather e.g. of a radiated gluon and a quark, carrying momentum fractions x and $(x' - x)$, respectively. When looking deeper into it, the gluon may e.g. further split into two quarks of even smaller momentum fraction. Thus, it is intuitive that with increasing resolving power Q^2, the parton densities and thus the structure functions increase at low x, while simultaneously they decrease at high x.

The evolution equations quantitatively describing this phenomenon are known as DGLAP (or Altarelli-Parisi) equations [29–32]:

$$\frac{dg}{d\ln Q^2} = \frac{\alpha_s(Q^2)}{2\pi}\left(\sum_j P_{gg}\otimes g + P_{gq_j}\otimes q_j\right) \tag{2.50}$$

$$\frac{dq_i}{d\ln Q^2} = \frac{\alpha_s(Q^2)}{2\pi}\left(\sum_j P_{q_ig}\otimes g + P_{q_iq_j}\otimes q_j\right), \tag{2.51}$$

where $P_{ij}(\xi)$ denote the splitting functions with $\xi = x/x'$, $0 < \xi < 1$, and $g(x, Q^2)$ and $q_i(x, Q^2)$ are the gluon and quark densities. The quantity $\alpha_s(Q^2)P_{ij}(x/x')$ is a measure of the probability that a parton i of momentum fraction x is radiated from a parton j of momentum fraction $x' > x$, $j(x') \to i(x)k(x' - x)$, when the scale changes by $+d\ln Q^2$. The basic diagrams are shown in Fig. 2.8. Note that one fundamental vertex of QCD has been neglected, namely the four-gluon vertex, $g \to ggg$. This is, however, a higher order graph. Also, recombination processes like $q\bar{q} \to g$ are not taken into account.

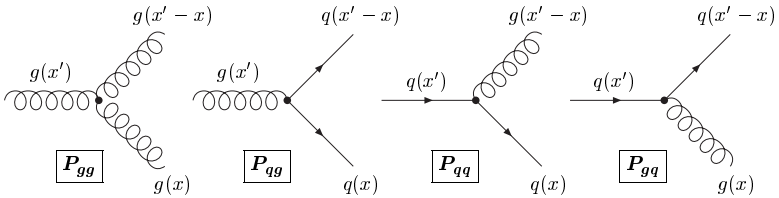

Fig. 2.8: The lowest order parton splittings: the $\alpha_s(Q^2)P_{ij}(x/x')$ are a measure of the probability for the shown vertices of QCD.

The prescription for convoluting $P \otimes f$ is given by

$$P \otimes f = \int_x^1 \frac{dx'}{x'} f(x', Q^2) P\left(\frac{x}{x'}\right), \tag{2.52}$$

i.e. for a parton at momentum fraction x one integrates over all allowed, that is all higher, values of x' of possible mother partons. There are symmetry relations between the splitting functions, easily obtained by flipping the diagrams about the horizontal axis:

$$P_{qq}(x) = P_{gg}(1 - x) \tag{2.53}$$

$$P_{qg}(x) = P_{qg}(1 - x) \tag{2.54}$$

$$P_{gg}(x) = P_{gg}(1 - x). \tag{2.55}$$

The relation between quark densities, the structure function and the gluon density is exploited by [33] to directly correlate F_2 and xg at low x:

$$\frac{dF_2(x, Q^2)}{d\ln Q^2} \approx \frac{5\alpha_s(Q^2)}{9\pi}\frac{2}{3}xg(2x, Q^2). \tag{2.56}$$

This follows from the DGLAP equations by neglecting the contribution from the quark densities, which are small compared to the gluon density.

2.6.2.4 The hadronic final state

Due to the confinement of quarks (and gluons) in hadrons, they can never be observed outside of bound states. If one attempts to remove a single quark from a hadron (e.g. by transferring a large momentum to it), a massive exchange of gluons, and gluons splitting into quark-antiquark pairs, sets in and finally leads merely to the formation of new, colorless hadrons (Fig. 2.9). This process is called fragmentation or hadronization.

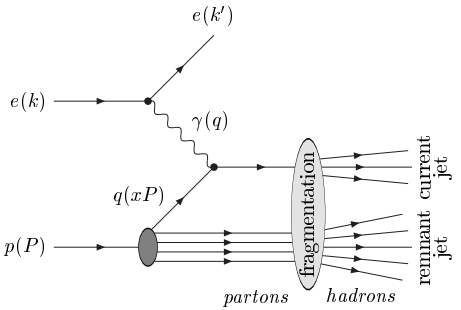

Fig. 2.9: Resulting from the subsequent interactions between the struck quark and the proton remnant (fragmentation), two jets of hadrons emerge from the reaction: the current jet in the direction of the struck quark, and the remnant jet in proton direction.

However, at sufficiently high energies, a correlation between the products of the fragmentation process and the original quarks remains observable: the hadrons are collimated in jets, emerging approximately at the same angle as the quarks. In lowest order, a DIS process exhibits two jets, the current jet and the proton remnant jet, correlated to the struck quark and the remaining quarks of the proton, respectively. In higher orders, processes like BGF and QCDC (Fig. 2.6) lead to events with more than two jets.

2.7 The low-Q^2 regime

At low Q^2, the transition from deep inelastic scattering to photoproduction ($Q^2 = 0$) occurs, i.e. the transition from a virtual to a real photon being exchanged.

Strictly speaking, a photoproduction experiment requires a beam of real photons colliding with protons. However, one can exploit that at very small Q^2 the scattering angle of the electron is small, and so is the angle of the virtual photon with respect to the electron (and the proton). In this case, ep scattering can be viewed as $\gamma^* p$ scattering where a quasireal γ collides head-on with the proton.

The kinematic separation between photoproduction and deep inelastic scattering at HERA is relatively arbitrary, and has been based on the acceptance of the detectors. In the beginning the detector acceptance for scattered electrons was limited to about $Q^2 > 4\,\mathrm{GeV}^2$, and a photoproduction event was defined to be an event where no scattered electron was found in the main detector [34]. With the installation of new detector components and the modification of old ones, this limit was continuously pushed to lower Q^2 values.[7]

The idea of a separation between the emission of a photon by the electron and the subsequent interaction of the photon with the proton allows to introduce some new concepts and models.

[7] The average virtuality of the photon is $\langle Q^2 \rangle \approx 10^{-5}\,\mathrm{GeV}^2$ if the electron is not scattered into the main detectors. This is the consequence of a rapid decrease of the cross section with Q^2, and it is helpful because measurements in photoproduction do thus not depend very much on the definition of photoproduction.

2.7.1 Longitudinal and transverse cross sections

If the lifetime of the exchanged photon in an electron-proton interaction is long compared to its interaction time with the proton (given by the diameter of the proton and the velocity of the photon), it is appropriate to factorize the interaction into the emission of a photon by the electron, and the subsequent interaction of the photon with the proton [35]. This condition is met if

$$x \ll \frac{1}{2r_p m_p} \cdot \sqrt{1 + \frac{4m_p^2 x^2}{Q^2}}, \tag{2.57}$$

i.e. for small x and/or large Q^2 ($r_p \approx 1\,\mathrm{fm}$ is the proton radius). The electron is treated as source of the photon flux, and the interaction is described by the total photon-proton cross section. This is illustrated in Fig. 2.10.

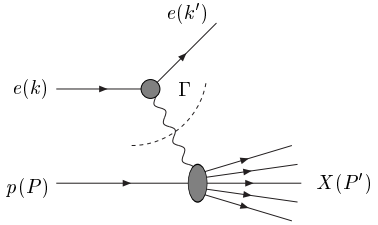

Fig. 2.10: Illustration of the factorization into virtual photon flux Γ and subsequent $\gamma^* p$ interaction.

A virtual photon has three possible helicity states $\lambda = 0, \pm 1$ (in contrast to a real photon with only two helicity states, $\lambda = \pm 1$). For unpolarized protons, parity conservation requires the cross sections for $\lambda = +1$ and $\lambda = -1$ to be equal. Consequently there are only two potentially different cross sections, those for the absorption of transversely ($\lambda = \pm 1$) and longitudinally ($\lambda = 0$) polarized photons:

$$\sigma_T^{\gamma^* p} = \frac{1}{2}(\sigma_+ + \sigma_-) \tag{2.58}$$

$$\sigma_L^{\gamma^* p} = \sigma_0. \tag{2.59}$$

For $x \ll 1$, the cross sections can be related to the structure functions by

$$\sigma_{\mathrm{tot}}^{\gamma^* p} = \sigma_T^{\gamma^* p} + \sigma_L^{\gamma^* p} = \frac{4\pi^2\alpha}{Q^2} F_2 \tag{2.60}$$

$$\sigma_L^{\gamma^* p} = \frac{4\pi^2\alpha}{Q^2} F_L \tag{2.61}$$

$$\sigma_T^{\gamma^* p} = \frac{4\pi^2\alpha}{Q^2} F_T, \tag{2.62}$$

(motivating to call F_T and F_L the transverse and longitudinal structure functions), and the double differential ep cross section from Eq. (2.34) can be expressed in terms of the total $\gamma^* p$ cross sections,

$$\frac{d^2\sigma}{dy\, dQ^2} = \Gamma\left(\sigma_T^{\gamma^* p} + \epsilon\, \sigma_L^{\gamma^* p}\right)(1 + \delta_r), \tag{2.63}$$

where $\Gamma = \alpha Y_+/(2\pi y Q^2)$ denotes the flux of virtual photons (in the convention of [36], see also [37]), and $\epsilon = 2(1-y)/Y_+$ is the polarization of the virtual photon.

In the limit $Q^2 \to 0$, the contribution to $\sigma_{\mathrm{tot}}^{\gamma^* p}$ from the transverse cross sections must remain finite, while that from the longitudinal cross section has to vanish because the photon loses the

$\lambda = 0$ degree of freedom. This leads to the following asymptotic behavior for the structure functions at $Q^2 \to 0$:

$$F_2 \propto Q^2 \quad \text{and} \quad F_L \propto Q^4 \tag{2.64}$$

(which represents another manifest violation of scaling, in addition to the logarithmic scaling violations arising from parton dynamics). The quantity $R = \sigma_L/\sigma_T = F_L/(F_2 - F_L)$ is the ratio of the longitudinal to the transverse cross sections; from the above limits it follows that $R \propto Q^2$ for $Q^2 \to 0$. Using R, one can rewrite the cross section from Eq. (2.63) as

$$\frac{d^2\sigma}{dy\, dQ^2} = \Gamma\sigma_T^{\gamma^* p}\,(1 + \epsilon\, R)\,(1 + \delta_r). \tag{2.65}$$

2.7.2 (Generalized) vector meson dominance model

Before interacting with the proton, the photon can fluctuate into a $q\bar{q}$ pair. If the lifetime of this fluctuation is long enough, it can form a bound state with the quantum numbers of the photon. The lowest-mass particles in question are the vector mesons ρ, ω and ϕ, having $J^{PC} = 1^{--}$ like the photon.

If the formation of a vector meson precedes the interaction with the proton, this can be viewed as a hadron-hadron interaction, and in fact the observed real photon-proton cross section shows striking similarities to hadron-hadron cross sections (section 2.7.3.1), justifying the approach taken in the vector meson dominance model (VDM) [38]. One makes the ansatz that the photon is a superposition of the bare photon and of vector-meson-like states: $|\gamma\rangle = |\gamma_{\mathrm{bare}}\rangle + \sum |V\rangle$, where $V = \rho, \omega, \phi$. Consequently, the photon can interact with the proton either directly, as a bare photon, or indirectly, first fluctuating into a vector meson. The VDM predicts for the transverse and longitudinal cross-sections that

$$\sigma_T^{\gamma^* p}(W^2, Q^2) = \sum_{V=\rho,\omega,\phi} r_V \left(\frac{m_V^2}{m_V^2 + Q^2}\right)^2 \sigma_{\mathrm{tot}}^{\gamma p}(W^2) \tag{2.66}$$

$$\sigma_L^{\gamma^* p}(W^2, Q^2) = \sum_{V=\rho,\omega,\phi} \xi_V r_V \left(\frac{m_V^2}{m_V^2 + Q^2}\right)^2 \frac{Q^2}{m_V^2} \sigma_{\mathrm{tot}}^{\gamma p}(W^2), \tag{2.67}$$

where the coefficient $r_V = (4\pi\alpha/f_V^2)\sigma_{\mathrm{tot}}^{Vp,\lambda=\pm1}/\sigma_{\mathrm{tot}}^{\gamma p}$ depends on the fluctuation probability of the photon into the vector meson V, and $\xi_V = \sigma_{\mathrm{tot}}^{Vp,\lambda=0}/\sigma_{\mathrm{tot}}^{Vp,\lambda=\pm1}$ is a parameter describing the ratio of longitudinal and transverse cross sections.

One observes that VDM is in agreement with experimental data only at low Q^2. It has therefore been extended to GVDM [39], the generalized vector meson dominance model (which is, however, not an unambiguous generalization, see e.g. also [40]). The idea of GVDM is to extend the set of ρ, ω and ϕ by a mass continuum of heavier vector meson states.

The relative contribution of the continuum states is fixed by the normalization condition at $Q^2 = 0$, where $r_\rho + r_\omega + r_\phi = 0.78 = 1 - r_C$. The cross section formulae obtain additional terms for the mass continuum, with a Q^2 behavior compatible with the data:

$$\sigma_T^{\gamma^* p}(W^2, Q^2) = \left[\sum_{V=\rho,\omega,\phi} r_V \left(\frac{m_V^2}{m_V^2 + Q^2}\right)^2 + r_C \left(\frac{m_0^2}{m_0^2 + Q^2}\right)\right] \sigma_{\mathrm{tot}}^{\gamma p}(W^2) \tag{2.68}$$

$$\sigma_L^{\gamma^* p}(W^2, Q^2) = \left[\sum_{V=\rho,\omega,\phi} \xi_V r_V \left(\frac{m_V^2}{m_V^2 + Q^2}\right)^2 \frac{Q^2}{m_V^2} + \xi_C r_C \left(\frac{m_0^2}{Q^2} \ln\left(\frac{Q^2 + m_0^2}{m_0^2}\right) - \left(\frac{m_0^2}{m_0^2 + Q^2}\right)\right)\right] \sigma_{\mathrm{tot}}^{\gamma p}(W^2). \tag{2.69}$$

2.7.3 Regge theory

Regge theory provided a successful description of soft hadronic cross sections, as well as of elastic and diffractive scattering, in the early days of the strong interaction. As usual in scattering processes, the interaction of two hadrons is viewed as mediated by the exchange of particles. In the beginning, the strong interaction could be well described by one-pion exchange; however, there is no justification not to allow the exchange of other mesons with higher spin J. This would unfortunately violate the Froissart bound [41, 42] (an upper limit for cross sections at $60\,\mathrm{mb} \cdot (\ln^2 s)$, with s being the center-of-mass energy of the process) for $J \geq 1$, since the cross section for the exchange of a particle with spin J rises like $\propto s^{2J-1}$.

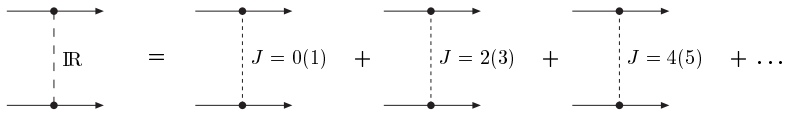

Fig. 2.11: The exchange of a Regge trajectory (a reggeon) is equivalent to the exchange of all particles on the trajectory.

Regge theory solves this problem by introducing the concept of the exchange of a trajectory of particles (a reggeon), corresponding to the exchange of many particles with different spin, $J = 0, 2, 4 \ldots$ or $J = 1, 3, 5 \ldots$, and otherwise identical quantum numbers (Fig. 2.11). A trajectory is made up by a group of particles that lie on a straight line in the Chew-Frautschi plot [43] of spin versus mass squared. That is, for $t = m^2$, $J = \alpha(t) = \alpha_0 + \alpha' t$. $\alpha_0 = \alpha(0)$ is the intercept of the trajectory. Experimentally, one finds $\alpha(0) \approx 0.0 \ldots 0.5$ and $\alpha' \approx 1\,\mathrm{GeV}^{-2}$ for all trajectories. Figure 2.12 shows an example of a Chew-Frautschi plot.

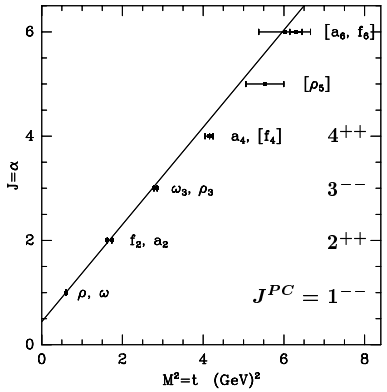

Fig. 2.12: Chew-Frautschi plot of the ρ/ω and f_2/a_2 trajectories (reproduced from [44]).

Regge theory predicts that each trajectory i that can be exchanged contributes to the total cross section an additive term such that

$$\sigma_{\mathrm{tot}} = \sum_i \sigma_i = \sum_i \beta_i \left(\frac{s}{s_0}\right)^{\alpha_i(0)-1}, \tag{2.70}$$

with $\alpha_i(0)$ being the intercept of that trajectory, β_i an unknown residue function, and s_0 an arbitrary normalization constant which is often set to $s_0 = 1\,\mathrm{GeV}^2$. In the limit of high energies, one of the (possibly many) trajectories will dominate, namely that with the highest of all

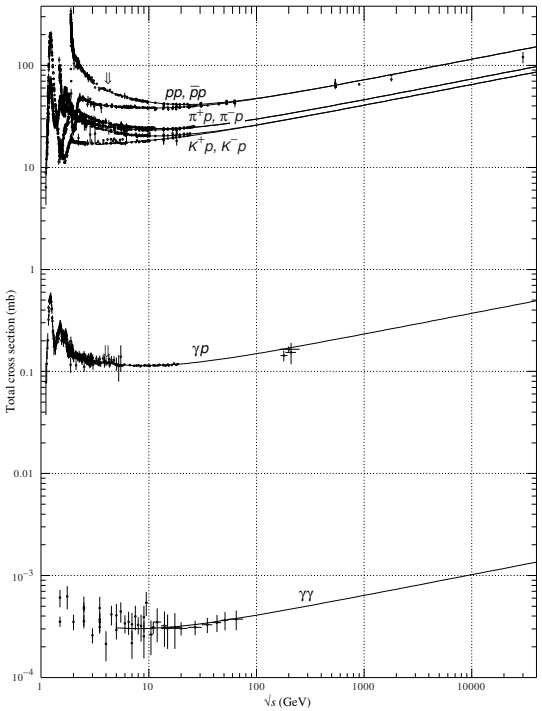

Fig. 2.13: Various total hadron-hadron cross sections versus energy, together with the total photon-proton and photon-photon cross sections. Overlaid are fits inspired by Regge theory, made by the PDG (reproduced from [14]).

intercepts. The asymptotic behavior of the cross section is then determined by the intercept of the dominating trajectory, $\alpha(0)$, to be

$$\sigma_{\mathrm{tot}} \propto \left(\frac{s}{s_0}\right)^{\alpha(0)-1}. \tag{2.71}$$

It comes as a puzzle that all trajectories of known particles have an intercept of at most $\alpha(0) \approx 0.5$, i.e. below unity, implying decreasing cross sections at high center-of-mass energies. In vast contrast, hadronic cross sections rise, however slowly, with energy (Fig. 2.13). Consequently, one needs to postulate an additional trajectory with $\alpha(0)$ slightly above 1, which was named "pomeron" after Pomeranchuk.[8] No particles on the pomeron trajectory were found so far; they would have to have the quantum numbers of the vacuum, $J^{PC} = 0^{++}$. Glueballs, bound states of two gluons, would be possible candidates. Since it has the largest of all intercepts, the pomeron trajectory always dominates at high energies. In contrast to all other reggeons, the pomeron has $\alpha' \approx 0.25\,\mathrm{GeV}^{-2}$.

In the following time, the interest in Regge theory decreased, because it was unable to

[8] Actually, at that time it was widely believed that cross sections would become flat at high energies and would not rise again, therefore the postulated trajectory had $\alpha(0) = 1$.

describe hard hadronic processes, and attempts to make the theory more rigorous proved problematic. QCD emerged as a successful qualitative description of the strong interaction, but its region of quantitative applicability has remained limited to hard processes up to now. Regge theory was partly resurrected when processes interpreted as hard scattering off a pomeron were observed [45,46], and when at HERA a significant fraction of similar events was found, viewed as diffractive deep inelastic scattering, or deep inelastic scattering on the pomeron [47,48].

2.7.3.1 Soft hadronic interactions

Total hadron-hadron cross sections can be described by a two-component parameterization inspired by Regge theory, consisting of a pomeron and a reggeon term[9] [44]:

$$\sigma_{\text{tot}} = X s^{\epsilon} + Y s^{-\eta}, \tag{2.72}$$

where the first term is identified to arise from pomeron exchange, and the second from the ρ/ω and f_2/a_2 trajectories, and $1+\epsilon$ and $1-\eta$ are the effective pomeron and reggeon intercepts, with numerical values $\epsilon = 0.0808$ and $\eta = 0.4525$. A more careful analysis of the same data [49] yielded $\epsilon = 0.096^{+0.012}_{-0.009}$. Introducing different reggeon intercepts for C-odd and C-even exchanges, which contribute differently to AB and $A\bar{B}$ scattering according to [14]

$$\sigma_{\text{tot}}^{AB} = X s^{\epsilon} + Y_1 s^{-\eta_1} + Y_2 s^{-\eta_2} \tag{2.73}$$

$$\sigma_{\text{tot}}^{A\bar{B}} = X s^{\epsilon} + Y_1 s^{-\eta_1} - Y_2 s^{-\eta_2}, \tag{2.74}$$

results in $\epsilon = 0.095 \pm 0.02$, $\eta_1 = 0.34 \pm 0.02$ and $\eta_2 = 0.55 \pm 0.02$.

The pomeron trajectory appearing in this context, with an intercept of 1.095 ± 0.02, is referred to as the soft pomeron.

Also photon-photon and photon-proton cross sections can be described by such a form, the latter of which are accessible at HERA.[10] Experimentally, one finds that while $\sigma_{\text{tot}}^{\gamma p}$ can be well described by a soft pomeron at high energies, $\sigma_{\text{tot}}^{\gamma^* p}$ for Q^2 greater than about $1\,\text{GeV}^2$ rises more steeply as a function of W^2. This has been interpreted by some people as evidence for the existence of an additional, so-called hard, pomeron, with an intercept of about 1.4 ± 0.1.

2.7.3.2 Diffractive deep inelastic scattering

In diffractive deep inelastic scattering, interpreted as DIS on the pomeron, the differential cross section is (in analogy to inclusive deep inelastic scattering) given by

$$\frac{d^4\sigma}{dx_{\mathbb{P}}\, d|t|\, d\beta\, dQ^2} = \frac{2\pi\alpha^2}{\beta Q^4}\left(Y_+ F_2^{D(4)}(x_{\mathbb{P}}, t, \beta, Q^2) - y^2 F_L^{D(4)}(x_{\mathbb{P}}, t, \beta, Q^2)\right), \tag{2.75}$$

where the diffractive structure functions $F_2^{D(4)}(x_{\mathbb{P}}, t, \beta, Q^2)$ and $F_L^{D(4)}(x_{\mathbb{P}}, t, \beta, Q^2)$, which replace the inclusive structure functions $F_2(x, Q^2)$ and $F_L(x, Q^2)$, depend on four instead of two variables, and have unit GeV^{-2} instead of being bare numbers. The three new variables are defined as

$$t = (P - P'_p)^2, \tag{2.76}$$

the four momentum transfer at the proton vertex, where the proton is scattered quasi-elastically,

$$x_{\mathbb{P}} = (P_{\mathbb{P}} \cdot q)/(P \cdot q), \tag{2.77}$$

[9] Technically, the pomeron is a reggeon. It has become customary, however, to speak of pomerons and reggeons as distinct objects, "reggeon" meaning "any reggeon except the pomeron".

[10] In describing photon-proton cross sections, s is of course replaced by W^2, the photon-proton center-of-mass energy squared.

the momentum fraction of the proton carried by the pomeron, and

$$\beta = Q^2/(2P_{\mathbb{P}} \cdot q). \tag{2.78}$$

In addition to the variables introduced in section 2.3, P'_p and $P_{\mathbb{P}}$ denote the four momenta of the scattered proton and of the incoming pomeron, respectively. Note that the definition of t in diffractive events according to Eq. (2.76) differs from that in Eq. (2.2).

The interpretation of $F_2^{D(4)}(x_{\mathbb{P}}, t, \beta, Q^2)$ in terms of parton densities is unclear. One possible approach is to assume factorization of the diffractive structure function into a pomeron flux $f_{\mathbb{P}/p}(x_{\mathbb{P}}, t)$ (the probability for finding a pomeron in the proton) and a pomeron structure function $F_2^{\mathbb{P}}(\beta, Q^2)$ (which is then related to parton densities in the pomeron in the usual way):

$$F_2^{D(4)}(x_{\mathbb{P}}, t, \beta, Q^2) = f_{\mathbb{P}/p}(x_{\mathbb{P}}, t) \cdot F_2^{\mathbb{P}}(\beta, Q^2). \tag{2.79}$$

In this case, β can be interpreted as the momentum fraction of the pomeron carried by the struck parton in the pomeron, and $x = \beta \cdot x_{\mathbb{P}}$.

Since inclusive event samples by definition include diffractive events, diffractive and inclusive structure functions are related. One can define the diffractive contribution to F_2, F_2^{diff}, by integration over the additional variables t and $x_{\mathbb{P}}$ according to

$$F_2^{\text{diff}}(x, Q^2) = \int F_2^{D(4)}(x_{\mathbb{P}}, t, \beta, Q^2)\delta(\beta \cdot x_{\mathbb{P}} - x)\, dx_{\mathbb{P}}\, d\beta\, dt. \tag{2.80}$$

Consequently, since any event is either diffractive or non-diffractive, $F_2 = F_2^{\text{diff}} + F_2^{\text{non-diff}}$, where $F_2^{\text{non-diff}}$ denotes the non-diffractive contribution to F_2.

At HERA, diffractive events have characteristic signatures. They contain a quasi-elastically scattered outgoing proton (i.e. with a measured momentum close to the incoming one), the mass of the observed hadronic system (excluding the outgoing proton), M_X, is small, and the hadronic final state exhibits a rapidity[11] gap, a cone around the scattered proton where no other scattered particles are observed (in contrast to non-diffractive events, where the hadronic final state particles are on average evenly distributed in rapidity). The quantity $\eta_{\max}$ is introduced, which denotes the pseudorapidity of the most forward (i.e. in proton direction) observed hadronic final state particle (except the proton itself). Diffractive events are concentrated at small values of $\eta_{\max}$.

Each of these three signatures can be used to characterize and select diffractive events. They were found at HERA to contribute about 10% of the observed cross section at Q^2 values of 10–100 GeV^2 [47,48], and about 35% at $Q^2 = 0$ [50,51].

Since the subject of this report is the measurement of the inclusive structure function, diffraction and diffractive structure functions are beyond its scope. However, due to their distinct hadronic final state, diffractive events turn out to be important for a technical detail of the analysis (section 5.3.2).

2.8 Transition region

Since the DGLAP equations have been derived in perturbative QCD, they cannot be expected to hold when α_s becomes large, equivalent to Q^2 becoming small. For example, at $Q^2 = 1\,\text{GeV}^2$, $\alpha_s \approx 0.5$ (Fig. 2.14). Going from high to low Q^2, it is important to see where pQCD breaks down, i.e. where it predicts a Q^2 dependence of the structure functions that is incompatible with the data.

Another limitation of the DGLAP formalism becomes obvious when considering the terms that have been neglected: there is no recombination mechanism for quarks and gluons, i.e.

[11] The rapidity of a particle, $y = (E - p_Z)/(E + p_Z)$, is, neglecting mass terms, approximated by its pseudorapidity. The pseudorapidity is related to the polar angle via $\eta = -\ln\tan(\theta/2)$.

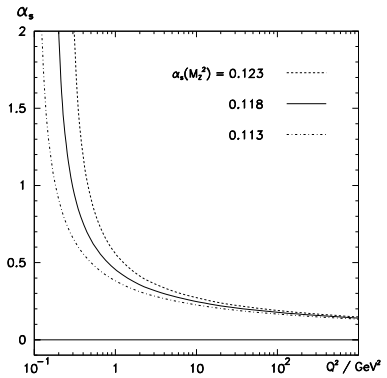

Fig. 2.14: The evolution of α_s in NLO in the $\overline{\text{MS}}$ scheme starting from $\alpha_s(M_Z^2) = 0.118$ (full curve), 0.123 (dashed curve) and 0.113 (dash-dotted curve) (reproduced from [52]).

the process $q\bar{q} \to g$, and thus their number grows unlimited toward lower x for increasing Q^2. This, however, in the end violates unitarity (an upper bound for the cross section, where the probability of anything happening becomes greater than 100%), because it means that F_2 and thus the cross section grows beyond any limits. The search for signs of recombination is one of the motivations of measuring structure functions at small values of x.

At low Q^2, the dominant processes are of nonperturbative nature, while with increasing Q^2 perturbative contributions become more important. It is of fundamental interest to understand this interplay of soft and hard processes theoretically, and to identify experimentally where in Q^2 the transition takes place, and if it happens sudden or smooth.

It should be pointed out at this point that the different languages applied to the high-Q^2 and the low-Q^2 regions are closely related. When viewing electron-proton interactions as the exchange of a photon between the electron and a quark in the proton, the appropriate variables to describe the process are x and Q^2. Regge theory instead, regarding the interaction as the exchange of a Regge trajectory between the photon and the proton, describes it in terms of four-momentum transfer squared t and center-of-mass energy squared W^2. These are related to the deep inelastic scattering variables by $W^2 = Q^2(1-x)/x$.

Consequently, predictions made by Regge theory can readily be translated into the deep inelastic scattering language. For example, the rise of the cross section at high energies like $(W^2)^{\alpha_{\mathbb{P}}-1}$ is equivalent to a rise of F_2 at low x like $(1/x)^{\alpha_{\mathbb{P}}-1}$ (at fixed Q^2), and thus both of them violate unitarity (although only at unaccessibly high energies).

In applying the DGLAP formalism, one usually defines flavor singlet and nonsinglet parton distributions,

$$q_S = \sum_i (q_i + \bar{q}_i) \quad \text{and} \quad q_{NS} = \text{`}\vec{q}_i - \text{`}\vec{q}_j, \tag{2.81}$$

parameterizing the sea quark and the valence quark content of the proton, respectively.[12] In the Regge language, the pomeron dominates in interactions with sea quarks at low x (high W^2), and is thus related to the singlet quark density, while the other reggeons contribute in reactions with valence quarks at high x (low W^2), and are therefore related to the nonsinglet density.

In order to have a working definition of the terms high and low Q^2, it seems reasonable to identify them with the perturbative and the nonperturbative region of QCD, i.e. high Q^2 is where the value of α_s is small enough to safely apply the DGLAP evolution equations, without significant corrections from higher orders. At low Q^2, this description is expected to fail, and phenomenological models like Regge theory and GVDM become important.

[12] Actually, there is only one flavor singlet distribution, defined as above; there are, however, many nonsinglet distributions. Those parameterizing the valence content of the proton are $q_i - \bar{q}_i$. When speaking of "the" nonsinglet distribution, one usually refers to $\sum(q_i - \bar{q}_i)$.

2.9 Review of structure function data and parameterizations

2.9.1 Structure function measurements

Deep inelastic scattering experiments apart from ZEUS and H1 are all fixed target experiments. They differ in both the type of the incoming lepton (electron, muon, neutrino) and the target (hydrogen, deuterium, heavy nuclei). The range in the kinematic plane (Q^2 vs. x) covered by various fixed target experiments and by ZEUS is shown in Fig. 2.15.

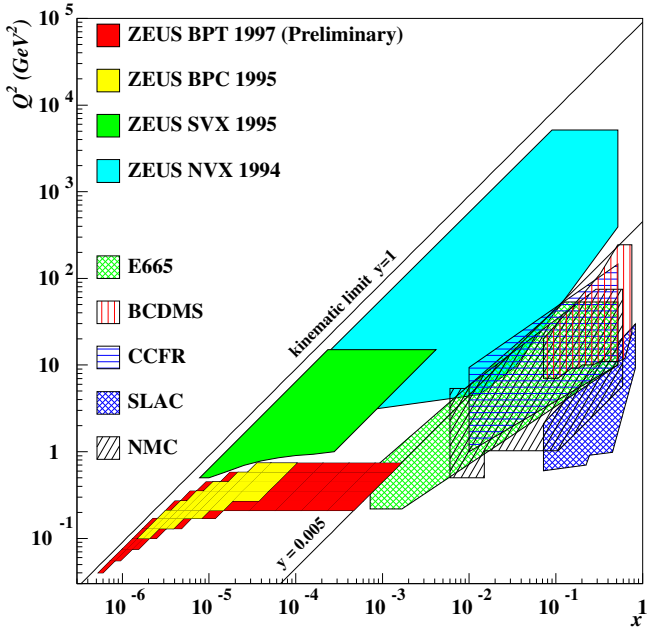

Fig. 2.15: The coverage of the kinematic plane (Q^2 versus x) by various fixed target experiments and by ZEUS. The direction of "technical progress" points to the upper left corner, i.e. future deep inelastic scattering experiments will cover the region above the HERA kinematic limit (indicated by the $y = 1$ line). The range covered by H1 until 1995 is similar to that of ZEUS NVX 1994 and ZEUS SVX 1995. The measurement of F_2 in the range indicated by "ZEUS BPT 1997 (Preliminary)" is the subject of this report.

SLAC experiments scattered electrons ($2.65\,\text{GeV} < E_e < 20\,\text{GeV}$) on hydrogen and deuterium. The CERN experiments EMC, NMC and BCDMS used muons ($100\,\text{GeV} < E_\mu < 280\,\text{GeV}$). In the FNAL experiments CCFR and E665, the scattering of (anti-)neutrinos ($30\,\text{GeV} < E_\nu < 600\,\text{GeV}$) respectively muons ($400\,\text{GeV} < E_\mu < 500\,\text{GeV}$) was studied.

The highest lepton-nucleon center-of-mass energy achieved in fixed target experiments is around $\sqrt{s} = 35\,\text{GeV}$, in contrast to the HERA value of $\sqrt{s} = 300\,\text{GeV}$. HERA therefore allows to reach a value of Q^2 that is two orders of magnitude higher than before for fixed x, or to go down by two orders in magnitude in x for fixed Q^2.

The HERA experiments have contributed a lot to the world knowledge of structure functions, mostly due to the exploration of a kinematic domain that was unaccessible before, where

predictions of models could be tested. While typical statistical and systematic errors of fixed-target experiments are 1–3%, the precision of ZEUS and H1 measurements from data of the years 1992–95 is of the order of 5–10%. For reviews of HERA results, see e.g. [53] and [54].

The present-day ZEUS contribution to structure function data stems from three data sets: NVX (nominal vertex) 1994 [55], SVX (shifted vertex) 1995 [56] and BPC (Beam Pipe Calorimeter) 1995 [57] (the notation will be explained in section 4.1). They cover the ranges $3.5\,\mathrm{GeV}^2 < Q^2 < 5000\,\mathrm{GeV}^2$, $0.6\,\mathrm{GeV}^2 < Q^2 < 17\,\mathrm{GeV}^2$ and $0.11\,\mathrm{GeV}^2 < Q^2 < 0.65\,\mathrm{GeV}^2$, respectively. Only the NVX data set extends down to low values of y around 0.005, while the SVX and BPC data sets are limited to $y > 0.05$ respectively $y > 0.08$. Consequently, there is a considerable gap between ZEUS and fixed-target experiments at low Q^2, while at high Q^2 some overlap has been achieved. Two key conclusions can be drawn from the data so far [56]:

- The evolution of F_2 with x:

  The value of F_2 for fixed Q^2 rises toward small values of x. This has been seen at HERA for the first time, and the steepness of the rise came somewhat surprising when the first HERA data were analyzed. At low values of x, approximately $x < 0.01$, F_2 can be well described by the form $F_2 \propto x^{-\lambda_{\mathrm{eff}}}$. At high Q^2, one finds a rise in F_2 that is substantially larger than that expected from Regge theory: $1 + \lambda_{\mathrm{eff}}$ increases from a value near the soft pomeron intercept (approximately $1.11 \ldots 1.14$ below $Q^2 < 1\,\mathrm{GeV}^2$) to around $1.3 \ldots 1.4$ at $Q^2 \approx 200\,\mathrm{GeV}^2$ (Fig. 2.16). However, the precision of the λ_{eff} extraction from 1994/95 data is relatively low, and therefore the nature of the transition cannot be investigated in detail.

- The evolution of F_2 with Q^2:

  The measured F_2 data are found to be well described by DGLAP-inspired parameterizations (Fig. 2.17; for the technicalities of such fits see section 2.9.2). Surprisingly, the quality of this description does not degrade even down to values of Q^2 around $1.0\,\mathrm{GeV}^2$, where perturbation theory is not seriously assumed to be applicable. With the current precision of the data it is not possible to identify a Q^2-value below which pQCD breaks down, at least this is not indicated by a degradation of DGLAP fits.

2.9.2 Parton density parameterizations at high Q^2

In global analyses, the parton densities are determined from a fit to a wide range of experimental data (mostly DIS). The philosophy is to parameterize the parton densities as a function of x by a suited form at a low scale Q_0^2, and to evolve them to higher Q^2 using the DGLAP equations. The result is fitted to data above a lower cutoff scale Q^2_{min}, where perturbative QCD is believed to be applicable.[13]

The choice of Q_0^2 has no direct physical impact, because the DGLAP equations allow an evolution both to higher and lower Q^2. It can therefore be adapted such that the chosen parametric forms for the parton densities at the scale Q_0^2 lead to a good fit.

2.9.2.1 MRST (Martin, Roberts, Stirling and Thorne)

Martin, Roberts, Stirling and Thorne [58] parameterize the starting parton distributions at $Q_0^2 = 1\,\mathrm{GeV}^2$ in the $\overline{\mathrm{MS}}$ scheme. $Q^2_{\mathrm{min}} = 1.5\,\mathrm{GeV}^2$ is chosen as the lower cutoff for the fit, above

[13] No functional form has been found that is a solution of the DGLAP equations. The described strategy is therefore sort of a "poor man's solution", which has the undesirable feature of introducing many free parameters.

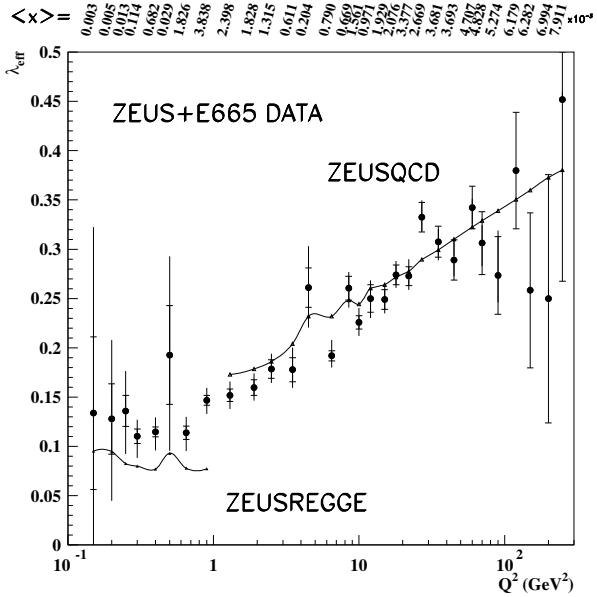

Fig. 2.16: The effective parameter λ_{eff} in $F_2 \propto x^{-\lambda_{\mathrm{eff}}}$ as extracted from ZEUS 1994 and 1995 data. At low values of Q^2, results from the E665 experiment were also used, because the ZEUS data alone cover too small a region in x for fixed Q^2. On top, the mean x is given where λ_{eff} was extracted. Small triangles linked by lines are values extracted from a ZEUS REGGE and a ZEUS QCD fit to the data (sections 2.9.2.4 and 2.9.3.11).

which indeed a satisfactory description of the data is achieved. MRST use the forms

$$xu_v = A_u x^{\eta_1}(1-x)^{\eta_2}(1+\epsilon_u\sqrt{x}+\gamma_u x) \quad (2.82)$$

$$xd_v = A_d x^{\eta_3}(1-x)^{\eta_4}(1+\epsilon_d\sqrt{x}+\gamma_d x) \quad (2.83)$$

$$xS = A_S x^{-\lambda_S}(1-x)^{\eta_S}(1+\epsilon_S\sqrt{x}+\gamma_S x) \quad (2.84)$$

$$xg = A_g x^{-\lambda_g}(1-x)^{\eta_g}(1+\epsilon_g\sqrt{x}+\gamma_g x), \quad (2.85)$$

where the A_i, η_i, ϵ_i, λ_i and γ_i are free parameters to be determined from the fit. The functions u_v and d_v denote the u and d valence quark distributions, g is the gluon distribution, and S is the summed sea distribution, which makes up the u, d, s sea quark distributions according to

$$x(u_s + \bar{u}_s) = 2x\bar{u} = 0.4xS - x\Delta \quad (2.86)$$

$$x(d_s + \bar{d}_s) = 2x\bar{d} = 0.4xS + x\Delta \quad (2.87)$$

$$x(s_s + \bar{u}_s) = 2x\bar{s} = 0.2xS \quad (2.88)$$

(this suppression of the strange sea compared to up and down sea quarks is suggested by data, and not a priori obvious). The function Δ parameterizes the difference between u and d sea distributions:

$$x\Delta = x(\bar{d} - \bar{u}) = A_\Delta x^{\eta_\Delta}(1-x)^{\eta_S+2}(1+\gamma_\Delta x + \delta_\Delta x^2). \quad (2.89)$$

Normalization conditions like the momentum sum rule and quark counting rules are imposed to fix some of the free parameters.

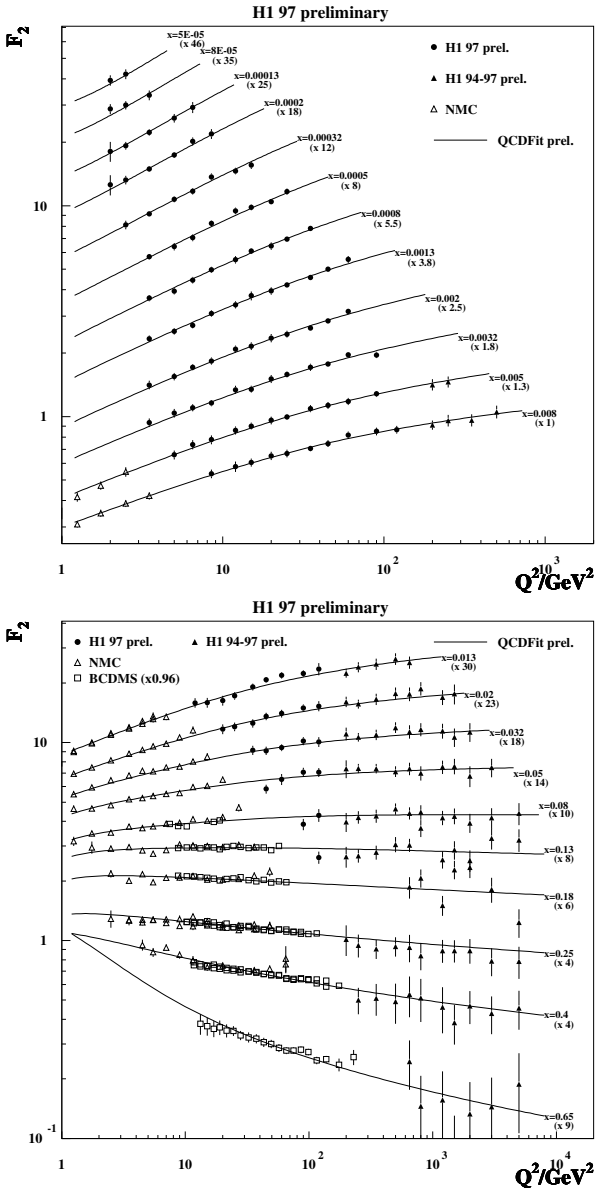

Fig. 2.17: The scaling violations of F_2 as measured by H1 from preliminary 1994–97 data, and by the fixed-target experiments NMC and BCDMS. F_2 can can be described by a DGLAP fit over the whole range $Q^2 > 1\,\mathrm{GeV}^2$.

The treatment of heavy quarks is notoriously nontrivial. MRST implement it such that at very low Q^2 heavy quarks are generated exclusively by the boson-gluon fusion (BGF) process $\gamma g \to q\bar{q}$ ($q = c, b$). Only at higher $Q^2 \approx m_{c,b}^2$ heavy quark densities turn on.

This parameterization was updated several times, the last time in 1998 (MRST). There is an older version still being used (MRSA), which has the advantage of being, at least formally, valid down to $Q^2 = 0.625\,\mathrm{GeV}^2$.

2.9.2.2 CTEQ (Coordinated Theoretical-Experimental Project on QCD)

The CTEQ collaboration [59] uses a technique very similar to that of MRST, differing mainly in the treatment of heavy quarks.

2.9.2.3 GRV (Glück, Reya and Vogt)

Glück, Reya and Vogt [60] (updated in [61]) start from a different ansatz. They parameterize the valence quark, sea quark and gluon densities with a form similar to that of MRST, but at a very low scale, $Q_0^2 = 0.4\,\mathrm{GeV}^2$ (which is a fitted parameter in their case), where these distributions turn out to have a valence-like shape. The whole sea contribution to the parton densities at low x then arises as a consequence of the Q^2 evolution, which leads to the term "dynamical parton distributions". The lower cutoff for fitting is chosen as $Q_{\min}^2 = 2\,\mathrm{GeV}^2$. Close to the scale Q_0^2, the authors characterize their parton distributions to be meaningless.

2.9.2.4 ZEUS QCD fit

The parameteric form of the parton densities in the ZEUS QCD fit [56] is similar to that of MRST. The focus of the fit is primarily to extract the gluon density from the measured F_2 with a realistic estimate of the uncertainty, and to study the behavior of DGLAP-based fits at low Q^2, rather than to obtain a perfect description of a wide variety of world data.

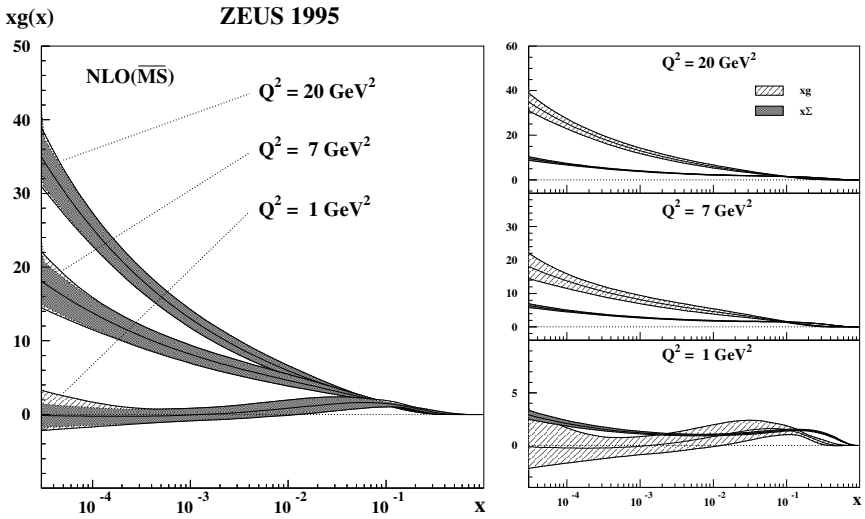

Fig. 2.18: The gluon and sea quark densities resulting from the ZEUS QCD fit.

The gluon density has been extracted with an error of about 15% over a range from $3 \cdot 10^{-4}$ to $1 \cdot 10^{-1}$ in x (Fig. 2.18). Two rather unexpected observations are made when extending the fit to low values of Q^2: Firstly, such a fit describes well the measured F_2 down to $Q^2_{\min} = 1\,\mathrm{GeV}^2$. Secondly, there is apparently a price to pay for the good agreement of the fit with data at low Q^2: while the sea distribution remains sea-like, i.e. increasing toward small x, the gluon density becomes valence-like, i.e. compatible with zero below $x \approx 10^{-2}$ (Fig. 2.18). This is clearly counter-intuitive, because quarks at low x are believed to originate from the splitting of gluons (and do originate that way in the DGLAP formalism), which will be suppressed, however, if the gluon density at low x is zero.

This observation may indicate that the breakdown of pQCD does not necessarily have to manifest itself as the unability of a fit to describe the data, because the formalism might be flexible enough to absorb nonperturbative effects into the many free parameters. On the other hand, the gluon density is not a directly observable quantity, and does not necessarily have to have an easily interpretable value.

2.9.3 Cross section parameterizations at low Q^2

Cross-section parameterizations based on Regge theory or generalized vector dominance do not use the concept of parton distributions at all. Instead, they directly assume a functional form for F_2 or $\sigma_{\mathrm{tot}}^{\gamma^* p}$, and adjust the free parameters of the model to fit the data.

2.9.3.1 DL (Donnachie and Landshoff)

Donnachie and Landshoff [62] (updated and improved in [63]) extended their parameterization of real photon-proton cross sections [44] to accomodate also virtual photon-proton cross sections. Their fit to F_2 has the form

$$F_2(x,Q^2) = \sum_i f_i(Q^2) \left(\frac{1}{x}\right)^{\epsilon_i}, \tag{2.90}$$

with coefficient functions

$$f_1(Q^2) = A_1 \left(\frac{Q^2}{Q^2+a_1}\right)^{1+\epsilon_1} \tag{2.91}$$

$$f_2(Q^2) = A_2 \left(\frac{Q^2}{Q^2+a_2}\right)^{1+\epsilon_2}. \tag{2.92}$$

The parameters $\epsilon_1 = 0.0808 = \epsilon$ and $\epsilon_2 = -0.4525 = -\eta$ are fixed to the same values as found in hadron-hadron interactions. This simple form is further refined, without changing the result very much.

It fails to describe the data already at relatively low Q^2, and is improved by adding to the reggeon and soft pomeron term a third, hard pomeron term. The hard pomeron has $\epsilon_0 = 0.418$, and the coefficient functions become more complicated:

$$f_0(Q^2) = A_0 \left(\frac{Q^2}{Q^2+a_0}\right)^{1+\epsilon_0} \left(1 + X \log\left(1+\frac{Q^2}{Q_0^2}\right)\right) \tag{2.93}$$

$$f_1(Q^2) = A_1 \left(\frac{Q^2}{Q^2+a_1}\right)^{1+\epsilon_1} \frac{1}{1+\sqrt{Q^2/Q_1^2}} \tag{2.94}$$

$$f_2(Q^2) = A_2 \left(\frac{Q^2}{Q^2+a_2}\right)^{1+\epsilon_2}. \tag{2.95}$$

The authors point out that, since Regge theory makes no statement about the coefficient functions $f_i(Q^2)$, they have been chosen to fit the data, without claiming that the form of their parameterization has any physical meaning.

2.9.3.2 ALLM (Abramowicz, Levy, Levin and Maor)

The aim of the parameterization given by Abramowicz, Levy, Levin and Maor [64] (updated in [65]) is to provide a phenomenological description of available structure function data for all values of Q^2, with the emphasis on a good fit rather than on a small number of parameters with a clear physical meaning. The fit is inspired by Regge theory at low Q^2 and smoothly extended to high Q^2 in a way compatible with perturbative QCD. The total cross section is parameterized as

$$\sigma_{\mathrm{tot}}^{\gamma^* p} = \frac{4\pi^2\alpha}{Q^2+m_0^2} \frac{1}{1-x} \left(1 + \frac{4m_p^2 Q^2}{(Q^2+W^2-m_p^2)^2}\right) \cdot \left(F_2^{\mathbb{P}} + F_2^{\mathbb{R}}\right) \tag{2.96}$$

with

$$F_2^{\mathbb{P}} = C_{\mathbb{P}}(\tau) x_{\mathbb{P}}^{\alpha_{\mathbb{P}}(\tau)} (1-x)^{b_{\mathbb{P}}(\tau)} \tag{2.97}$$

$$F_2^{\mathbb{R}} = C_{\mathbb{R}}(\tau) x_{\mathbb{R}}^{\alpha_{\mathbb{R}}(\tau)} (1-x)^{b_{\mathbb{R}}(\tau)} \tag{2.98}$$

and

$$\tau = \ln\left(\frac{\ln[(Q^2+Q_0^2)/\Lambda^2]}{\ln[Q_0^2/\Lambda^2]}\right), \tag{2.99}$$

yielding a total of 23 parameters.

2.9.3.3 CKMT (Capella, Kaidalov, Merino and Tran Thanh Van)

Capella, Kaidalov, Merino and Tran Thanh Van [66] (updated in [67]) propose a parameterization of F_2 at low and moderate values of Q^2 of the form

$$F_2(x,Q^2) = F_{\mathrm{S}}(x,Q^2) + F_{\mathrm{NS}}(x,Q^2), \tag{2.100}$$

splitting up F_2 into singlet and nonsinglet parts. The former corresponds to the pomeron contribution:

$$F_{\mathrm{S}}(x,Q^2) = A x^{-\Delta(Q^2)} (1-x)^{n(Q^2)+4} \left(\frac{Q^2}{Q^2+a}\right)^{1+\Delta(Q^2)}, \tag{2.101}$$

where $1+\Delta$ denotes an effective pomeron intercept, which depends on Q^2:

$$\Delta(Q^2) = \Delta_0 \cdot \left(1 + \frac{\Delta_1 Q^2}{Q^2+\Delta_2}\right). \tag{2.102}$$

CKMT assume that at low Q^2, the soft pomeron of DL is not the "bare" but a "shadowed" pomeron. Thus, Δ approaches the soft pomeron value at low Q^2, while at higher Q^2 the shadowing gradually disappears and Δ takes the bare pomeron value, $\Delta \approx 0.2 \ldots 0.25$. The nonsinglet term, corresponding to reggeon exchange, is parameterized as

$$F_{\mathrm{NS}}(x,Q^2) = B x^{1-\alpha_{\mathbb{R}}} (1-x)^{n(Q^2)} \left(\frac{Q^2}{Q^2+b}\right)^{\alpha_{\mathbb{R}}}. \tag{2.103}$$

The valence quark contribution is separated into a sum of u and d valence quarks according to

$$B(1-x)^{n(Q^2)} = B_u (1-x)^{n(Q^2)} + B_d (1-x)^{n(Q^2)+1} \tag{2.104}$$

with

$$n(Q^2) = \frac{3}{2} \cdot \left(1 + \frac{Q^2}{Q^2+c}\right). \tag{2.105}$$

The authors suggest to use the parameterization at low Q^2 as a theoretically motivated starting point for a DGLAP evolution to higher Q^2.

2.9.3.4 ABY (Adel, Barreiro and Ynduráin)

Adel, Barreiro and Ynduráin [68] obtain a description of F_2 at small x over the whole range in Q^2 with two contributions, corresponding to a soft and a hard pomeron. They assume the applicability of perturbative QCD evolution down to the lowest Q^2, but need to make the assumption that α_s saturates at the QCD scale Λ,

$$\alpha_s(Q^2) = \frac{4\pi}{\beta_0 \log[Q^2/\Lambda^2]} \quad \longrightarrow \quad \alpha_s(Q^2) = \frac{4\pi}{\beta_0 \log[(Q^2+\Lambda^2)/\Lambda^2]}, \tag{2.106}$$

i.e. α_s remains finite at $Q^2 = \Lambda^2$ (and approaches infinity only at $Q^2 \to 0$).

2.9.3.5 DLM (Desgrolard, Lengyel and Martynov)

Desgrolard, Lengyel and Martynov [69] propose a dipole pomeron model with a Q^2-independent intercept of exactly unity. A good description of the data is obtained by a suitable Q^2 dependence of the residue function, rather than by introducing a hard pomeron or a Q^2-dependent pomeron intercept. Theoretically, such a model has the desirable feature of respecting unitarity, which cannot be achieved with a pomeron intercept above unity.

2.9.3.6 BK (Badełek and Kwieciński)

Badełek and Kwieciński [70] use GVDM to describe F_2, which is separated into a vector meson part and a partonic part:

$$F_2(x,Q^2) = F_2^{\mathrm{V}}(x,Q^2) + F_2^{\mathrm{par}}(x,Q^2). \tag{2.107}$$

The vector meson part F_2^{V}, dominating at low Q^2, is represented by the contribution of low-mass vector mesons (ρ, ω, ϕ) coupling to the virtual photon. At higher Q^2, the form of the higher mass term F_2^{par} is derived from the asymptotic structure function F_2^{AS}, which is assumed to be known and taken in this parameterization from the result of a DGLAP fit (GRV) at a scale of $Q_0^2 = 1.2\,\mathrm{GeV}^2$:

$$F_2^{\mathrm{par}}(x,Q^2) = \frac{Q^2}{Q^2+Q_0^2} F_2^{\mathrm{AS}}(\bar{x}, Q^2+Q_0^2) \quad \text{with} \quad \bar{x} = \frac{Q^2+Q_0^2}{W^2+Q^2+Q_0^2}. \tag{2.108}$$

2.9.3.7 MRS (Martin, Ryskin and Staśto)

Martin, Ryskin and Staśto [71] follow the method of BK. They describe $\sigma_{\mathrm{tot}}^{\gamma^* p}$ over the entire Q^2 range in terms of perturbative and nonperturbative contributions, separated by a boundary value Q_0^2. The region below Q_0^2 is described by the vector meson dominance model at low masses, and at higher masses by the additive quark model and the impulse approximation (i.e. only one quark of the $q\bar{q}$ pair which the photon fluctuated into interacts with the proton, and the quark-proton cross section is approximated by 1/3 of the proton-proton cross section). The region above Q_0^2 is described by perturbative QCD, using known parton distributions from DGLAP fits.

2.9.3.8 SS (Schildknecht and Spiesberger)

Schildknecht and Spiesberger [72] base their model for F_2 at $x < 0.05$ and the whole Q^2 range on generalized vector meson dominance. They obtain

$$\sigma_T^{\gamma^* p}(W^2,Q^2) = N\left[\frac{1}{Q^2+m_0^2}\ln\frac{W^2}{am_0^2} - \frac{1}{Q^2}\ln\left(1+\frac{Q^2}{m_0^2}\right)\right] \tag{2.109}$$

$$\sigma_L^{\gamma^* p}(W^2,Q^2) = N\xi\left[\left(\frac{1}{Q^2}\ln\left(1+\frac{Q^2}{m_0^2}\right) - \frac{1}{Q^2+m_0^2}\right)\ln\frac{W^2}{am_0^2} + \frac{1}{Q^2}\left(\ln\left(1+\frac{Q^2}{m_0^2}\right) + \mathrm{Li}_2\left(-\frac{Q^2}{m_0^2}\right)\right)\right], \tag{2.110}$$

where Li_2 denotes the dilogarithm, $N = 0.0548$ is a normalization constant,[14] $\xi = 0.171$ is related to the ratio of longitudinal and transverse cross sections, the parameter $a = 15.1$ describes the hadron-like energy dependence of photoproduction, and $m_0^2 = 0.89\,\mathrm{GeV}^2$.

2.9.3.9 H (Haidt)

Haidt [74] reports the observation that all available F_2 data for $x < 0.005$ and the whole range of Q^2 can be parameterized in a very simple way as

$$F_2(x,Q^2) = c\log_{10}\left(1+\frac{Q^2}{Q_0^2}\right)\log_{10}\left(\frac{x_0}{x}\right), \tag{2.111}$$

with $c = 0.41$, $Q_0^2 = 0.5\,\mathrm{GeV}^2$ and $x_0 = 0.04$. An interesting aspect of the success of this parameterization (and of that of Schildknecht and Spiesberger) would be that apparently the data cannot discriminate between a logarithmic and a power-law behavior in x.

2.9.3.10 GBW (Golec-Biernat and Wüsthoff)

Golec-Biernat and Wüsthoff [75] propose a model based on the concept of saturation at small x and Q^2. They obtain a good description of F_2 for $x < 0.01$ and all values of Q^2 with only three free parameters. An approximation of the cross section parameterization is given by

$$\sigma_{\mathrm{tot}}^{\gamma^* p}(x,Q^2) = \sigma_0\left[\ln\left(\left(\frac{x_0}{x}\right)^\lambda\frac{Q_0^2}{Q^2}+1\right) + \left(\frac{x_0}{x}\right)^\lambda\frac{Q_0^2}{Q^2}\ln\left(\left(\frac{x}{x_0}\right)^\lambda\frac{Q^2}{Q_0^2}+1\right)\right], \tag{2.112}$$

where $Q_0^2 = 1\,\mathrm{GeV}^2$ (fixed), and σ_0, x_0, λ are obtained from a fit to the data.

2.9.3.11 ZEUS REGGE fit

The idea of the ZEUS REGGE fit [56] is to combine the Q^2 dependence predicted by GVDM with the W^2 dependence of Regge theory.

At low Q^2, GVDM predicts approximate factorization of the Q^2 and the W^2 dependences of the photon-proton cross section (and Regge theory does so, independent of Q^2, too). For the Q^2 dependence, the explicit prediction from GVDM is used, taking only the continuum part into account:

$$\sigma_T^{\gamma^* p}(W^2,Q^2) = \left(\frac{m_0^2}{m_0^2+Q^2}\right)\sigma_{\mathrm{tot}}^{\gamma p}(W^2) \tag{2.113}$$

$$\sigma_L^{\gamma^* p}(W^2,Q^2) = \xi\left(\frac{m_0^2}{Q^2}\ln\frac{m_0^2+Q^2}{m_0^2} - \frac{m_0^2}{m_0^2+Q^2}\right)\sigma_{\mathrm{tot}}^{\gamma p}(W^2), \tag{2.114}$$

where m_0 is the lower mass cutoff of the continuum, and $\xi = 0.171$ is related to the ratio of longitudinal and transverse cross sections. Since fluctuations of the photon to a ρ meson are the dominant contribution at low Q^2, and the light vector meson contribution has been neglected in the above derivation, one expects $m_0 \approx m_\rho$.

[14] Reference [72] quotes a wrong value for the normalization, $N = 1.48$ [73].

Using Regge theory, the W^2 dependence of $\sigma_{\rm tot}^{\gamma p}(W^2)$ is parameterized as the sum of a reggeon and a pomeron term, following the approach of [44]:

$$\sigma_{\rm tot}^{\gamma p}(W^2) = A_{\rm I\!R} \cdot (W^2)^{\alpha_{\rm I\!R}-1} + A_{\rm I\!P} \cdot (W^2)^{\alpha_{\rm I\!P}-1}, \tag{2.115}$$

where $A_{\rm I\!R}$ and $A_{\rm I\!P}$ are normalization constants and $\alpha_{\rm I\!R}$ and $\alpha_{\rm I\!P}$ denote the intercepts of the reggeon and the pomeron trajectories. Combining the Q^2 and the W^2 dependence yields the form of the ZEUS REGGE fit:

$$\sigma_{\rm tot}^{\gamma^* p}(W^2, Q^2) = \left(\frac{m_0^2}{m_0^2 + Q^2}\right) \left(A_{\rm I\!R} \cdot (W^2)^{\alpha_{\rm I\!R}-1} + A_{\rm I\!P} \cdot (W^2)^{\alpha_{\rm I\!P}-1}\right). \tag{2.116}$$

2.9.3.12 BKS (Badełek, Kwieciński and Staśto) model for R

Badełek, Kwieciński and Staśto [76] present a model for the longitudinal structure function F_L and $R = F_L/(F_2 - F_L)$ at low Q^2. It is based on the photon-gluon fusion mechanism, which is the dominant mechanism contributing to F_L at low x, extrapolated to the low Q^2 region. Contributions of quarks with low and high transverse momenta are treated separately; the former are described by a soft pomeron exchange mechanism. The model embodies the constraint $F_L \propto Q^4$ for $Q^2 \to 0$.

Chapter 3

HERA and ZEUS

ZEUS is the name of an international collaboration of more than 400 physicists from currently 50 institutes in 12 countries. ZEUS also is the name of the sophisticated system of particle detectors, built, maintained and continuously improved by this collaboration at the HERA collider at DESY in Hamburg. In this chapter, an overview of the HERA machine and the ZEUS detector is given.

3.1 HERA

The electron-proton accelerator HERA (Hadron-Elektron-Ring-Anlage) [77, 78] at the research laboratory DESY (Deutsches Elektronen-Synchrotron) in Hamburg, Germany, is the only collider in the world that operates with particles of different masses. HERA occupies a 6.3 km long tunnel, located 10–15 m under ground (Fig. 3.1). It has begun routine operation in 1992, and the running is scheduled to continue at least until 2005. For the year 2000, an upgrade of HERA is planned to significantly increase its luminosity.

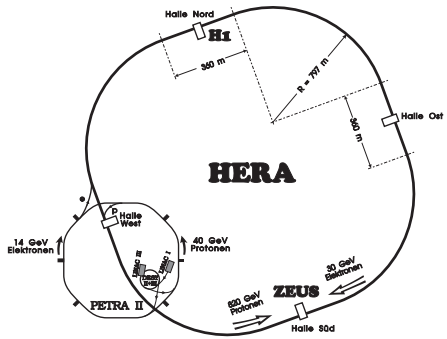

Fig. 3.1: The storage ring HERA, together with the pre-accelerator system and the location of the detectors ZEUS (south hall) and H1 (north hall). In the east hall, the experiment HERMES is located, in the west hall HERA-B is being assembled.

In two separate and interlaced rings, electrons (protons) are injected at energies of 12 GeV (40 GeV), accelerated to 27.5 GeV (820 GeV), and stored for the colliding mode.[1] The proton ring has super-conducting dipole and quadrupole magnets, providing the high magnetic field

[1] In 1992 and 1993, the electron energy was 26.7 GeV. Since 1998, the proton energy is 920 GeV. Consequently, the center-of-mass energy $\sqrt{s}$ increased from 296 GeV in 1992–93 and 300 GeV in 1994–97 to 318 GeV in 1998–. From 1994 to 1997, HERA accelerated positrons (e^+) rather than electrons (e^-). In this report, "electron" is used as a generic term for both electrons and positrons.

with the bending power needed to keep the protons on a circular orbit, while the accelerating cavities are normal-conducting. The electron ring has normal-conducting bending magnets, but super-conducting cavities to compensate for the high energy loss that electrons suffer from synchrotron radiation.

HERA has four interaction regions. Only in two of them the beams are brought to collision. There the detectors H1 and ZEUS are located. The other two interaction regions house the experiments HERMES and HERA-B, which are operated in fixed-target mode, using only the electron or the proton beam, respectively.

Both particle beams are structured in up to 210 bunches,[2] leading to a beam crossing every 96 ns, or at a rate of 10.4 MHz.

In 1997, HERA delivered an integrated luminosity of $36\,\mathrm{pb}^{-1}$, of which $28\,\mathrm{pb}^{-1}$ were recorded by ZEUS as usable for analysis purposes. The maximum instantaneous luminosity was $1.4 \cdot 10^{31}\,\mathrm{cm}^{-2}\,\mathrm{s}^{-1}$. The proton current was typically 90–100 mA, the electron current between 30–40 mA at the beginning of a fill and 10–15 mA at the end. HERA stored 175 colliding bunches, 5 unpaired proton and 17 unpaired electron bunches, thus leaving 23 buckets empty. Unpaired and empty bunches are used for background studies. The mean proton (electron) bunch length was of the order of 20 cm (1 cm), yielding a length of the interaction region of about 10 cm.

3.2 ZEUS

The purpose of the ZEUS detector [79] is to detect the final state particles of the electron-proton interactions. Consequently, it surrounds the interaction point nearly hermetically. Obviously, two holes at opposite sides are needed to accomodate the beam pipe.[3]

The ZEUS coordinate system is defined as a right-handed cartesian system with the origin in the nominal interaction point, the Z axis pointing along the proton beam direction (referred to as the forward direction), and the X axis pointing horizontally to the center of HERA. The angles ϑ and ϕ are defined in the usual way: ϑ is the angle with respect to to the Z axis, ϕ the angle with respect to the X axis in the X-Y plane. Therefore, $\vartheta = 0$ for the incoming proton and $\vartheta = \pi$ for the incoming electron. $R = \sqrt{X^2 + Y^2}$ denotes the distance from the Z axis. It is convenient to define also $\theta = \pi - \vartheta$.

The ZEUS detector is asymmetric and thus adapted to the special kinematic situation at HERA. Due to the asymmetry in the energies of the colliding particles, the ep center-of-mass system is boosted with $\beta = 0.94$ in proton direction. Consequently, most of the components in forward direction have a finer segmentation and instrumentation in order to account for the higher particle multiplicities and energies that are expected in this direction in the laboratory frame.

Since the start-up the ZEUS detector has seen almost yearly upgrades by adding new components to the original configuration. Here, the status as of the 1997 running period is described. Proceeding inside out, ZEUS consists of the following detector components (Fig. 3.2): The beam pipe is surrounded by a cylindrical drift chamber (Central Tracking Detector, CTD) that serves to measure momentum and direction of charged particles, as well as their specific energy loss. In forward direction, there are three additional planar drift chambers (Forward Tracking Detector, FTD1/2/3) which are intended to improve the track reconstruction at small angles with respect to the beam axis. In the gaps between FTD1/2 and FTD2/3, transition radiation detectors (TRD1/2 and TRD3/4) are located, which are to be used for particle identification purposes. FTD and TRD together are referred to as Forward Detector (FDET). In backward direction,

[2] There are 220 buckets due to the high-frequency structure of HERA, 210 of which can be filled with bunches at the same time, the gap being necessary to allow a controlled dumping of the beams.

[3] Unfortunately, most of the products of a typical ep reaction have a tendency to escape detection through exactly these holes; among them the particles of the proton remnant jet, as well as the scattered electron in reactions at very low Q^2, the predominant process at HERA. "Nearly hermetic" is therefore true in terms of the fraction of the solid angle covered, but not in terms of the fraction of final state particles detected.

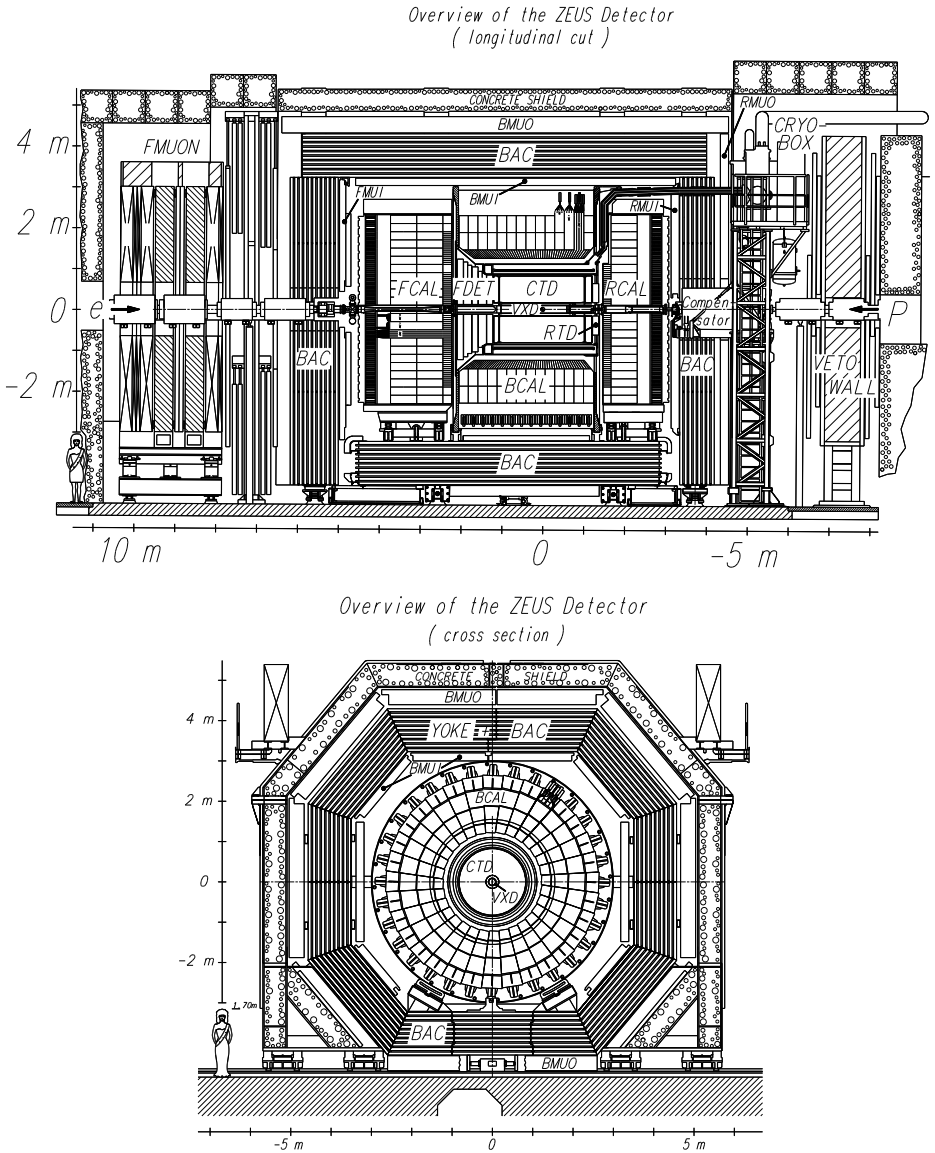

Fig. 3.2: The ZEUS detector. Top: cut in the Y-Z plane at $X = 0$. Bottom: cut in the X-Y plane at $Z = 0$. The vertex detector (VXD) was removed in 1996. Not shown or not indicated in the figures are SRTD (between RTD and RCAL), the magnet (surrounding the CTD), PRT1 (between FCAL and BAC), BPC and BPT (between RCAL and compensator magnet), PRT2, LPS, FNC, luminosity system and taggers (outside the range).

there are one planar drift chamber (Rear Tracking Detector, RTD) and a scintillator hodoscope (Small Angle Rear Tracking Detector, SRTD). In order to measure the track momentum from the track curvature in a magnetic field, the tracking detectors are located in the field of a superconducting solenoid magnet, which provides a magnetic field of 1.43 T. This part of ZEUS is called the inner detector.

The inner detector is surrounded by the uranium-scintillator calorimeter (CAL), consisting of three parts (F/B/RCAL), which is used to measure the kinetic energy of both charged and neutral particles.[4] The CAL is surrounded by a backing calorimeter (BAC) that also provides the return yoke for the solenoid magnet, and by a number of muon chambers (F/B/RMUON). A veto wall detector serves to reject reactions of the proton beam with gas molecules in the beam pipe. These components, including the inner detector, are together referred to as the central detector.

Close to the beam line, further detector components are installed up- and downstream. In forward direction, scintillator strip detectors (Proton Remnant Tagger, PRT1/2) serve to detect fragments of the dissociated proton, further away from the central detector the Leading Proton Spectrometer (LPS) is installed in gaps between HERA beam magnets to measure longitudinal and transverse momentum of quasi-elastically forward scattered protons, and the Forward Neutron Calorimeter (FNC) can detect forward scattered neutrons. In the rear direction, the Beam Pipe Calorimeter (BPC) and Beam Pipe Tracker (BPT) serve to measure energy and angle of electrons emerging under small angles. At different positions further away from the central detector (8 m, 35 m, 44 m), three small taggers (electromagnetic calorimeters) detect electrons under even smaller scattering angles, and finally a calorimeter 107 m away from the interaction point detects photons from the Bethe-Heitler bremsstrahlung process [80] to measure the luminosity. A compensator magnet compensates the effect of the ZEUS solenoid magnet on the beams in HERA.

In the following sections, CAL and CTD as well as the luminosity system and the trigger and event reconstruction chain will be described. The two detectors of central importance in this report, BPC and BPT, will be presented in detail in chapter 4, together with some material about particle detection techniques. All the other detector components have not been used.

3.2.1 Calorimeter (CAL)

The ZEUS calorimeter [81] is a compensating uranium-scintillator sandwich sampling calorimeter (for the concept of calorimetric energy measurement see section 4.2.1). The passive absorber layers are made of 3.3 mm thick depleted uranium plates, encapsulated in 0.2 mm (EMC) respectively 0.4 mm (HAC) thick stainless steel sheets. The active detector layers consist of 2.6 mm thick organic scintillators. The light from the scintillators is read out by photomultipliers, which are attached to the scintillators by wavelength shifters. Each calorimeter cell is read out independently on two sides, thus allowing to reconstruct the transverse position of a shower from the imbalance between both signals. Having a redundant readout also renders the calorimeter less sensitive to the failure of the readout system on one side.

Under test beam conditions, the energy resolution of the calorimeter is $\sigma(E)/E = 18\%/\sqrt{E\,[\mathrm{GeV}]} \oplus 1\%$ for electromagnetic and $\sigma(E)/E = 35\%/\sqrt{E\,[\mathrm{GeV}]} \oplus 2\%$ for hadronic showers.[5] These resolutions result from the design goal of compensation, i.e. equal detector responses for electrons and hadrons of the same energy, which dictates a specific ratio for the thickness of absorber and scintillator layers. This yields the best hadronic energy resolution, but at the same time compromises the electromagnetic energy resolution.

The time resolution is $\sigma(t) = 1.5\,\mathrm{ns}/\sqrt{E\,[\mathrm{GeV}]} \oplus 0.5\,\mathrm{ns}$ for energy deposits above 3 GeV [82]. This allows a reliable rejection of beam-related background events (beam-gas events) that did not occur inside the detector, but further up- or downstream.

[4] Except neutrinos and muons.

[5] The symbol $\oplus$ denotes addition in quadrature.

The ZEUS calorimeter consists of the planar forward (FCAL) and rear (RCAL) calorimeters, as well as of the cylindrical barrel (BCAL) calorimeter. Each of the parts is divided longitudinally into one electromagnetic (EMC) and one (RCAL) or two (B/FCAL) hadronic sections (HAC). Transversely, the calorimeter is organized in modules consisting of towers which are further subdivided into cells.

Both FCAL and RCAL have 23 modules, each consisting of a stack of up to 23 towers. In FCAL (RCAL), a tower has the transverse dimensions $20 \times 20\,\mathrm{cm}^2$ and a depth of $7(4)\lambda$, $4(2)$ electromagnetic cells, 1λ deep, 5(10) cm high and 20 cm wide, as well as 2(1) hadronic cells of $20 \times 20\,\mathrm{cm}^2$ and 3λ depth each. This structure is illustrated in Fig. 3.3.

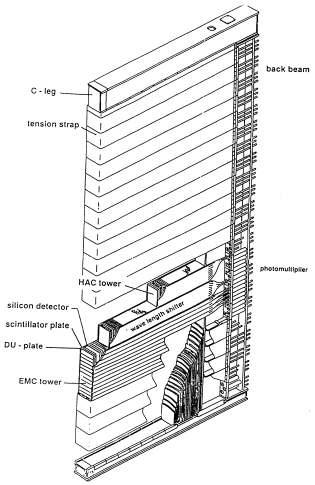

Fig. 3.3: Isometric view of an FCAL module.

The BCAL consists of 32 wedge-shaped modules, 5λ deep, with 14 towers each, having the approximate front face dimensions $24 \times 5\,\mathrm{cm}^2$. The modules are rotated by 2.5° around a Z-parallel axis in order to prevent neutral particles from escaping undetected through the gaps between modules.[6]

The natural radioactivity of the depleted uranium in the CAL provides a very precise and perfectly stable reference point for the energy calibration. The uncertainty of the electromagnetic energy scale of the CAL is 1–2% in RCAL, 1% in BCAL, and 3% in FCAL. The uncertainty of the hadronic energy scale is 3% in RCAL, and 2% in BCAL and FCAL.

3.2.2 Central Tracking Detector (CTD)

The CTD is a cylindrical drift chamber with signal and potential wires parallel to the beam axis. The signal wires are arranged in 9 super-layers with 8 layers each, in between the signal wires are the potential wires. This structure is shown in Fig. 3.4.

As a consequence of the wire orientation, the X and Y coordinates of points on a track (hits) can be measured with high precision. In order to also measure Z, the super-layers 2, 4, 6, 8 are inclined by a small angle ($\approx \pm 5°$) with respect to the beam axis (Z-by-stereo) and to the super-layers 1, 3, 5, 7. Mostly for trigger purposes, some layers also have a Z-by-timing system

[6] The sign of this rotation was determined by requiring that the curvature of the track of the scattered electron (e^-) should not allow it to disappear in the gap, independent of its energy. This cannot, without exorbitant mechanical modifications, be ensured also for HERA running with positrons (e^+).

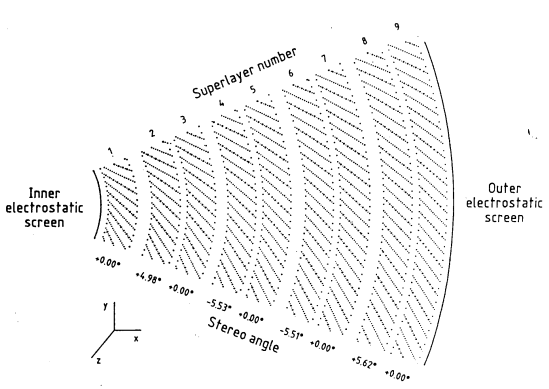

Fig. 3.4: Cross section of an octant of the central tracking detector, indicating the structure of super-layers and drift cells. Big circles denote signal wires, small circles potential wires.

that exploits signal arrival time differences between the wire ends to measure the coordinate along the wire.

The curvature of tracks in the magnetic field serves to measure their transverse momentum:

$$p_T\,[\mathrm{GeV}] = 0.2998 \cdot B\,[\mathrm{T}] \cdot r\,[\mathrm{m}], \tag{3.1}$$

yielding, together with the Z information, the momentum $p = p_T/\sin\theta$. The resolution of the measurement depends on the number and precision of hits on the track, and on the contribution of multiple scattering. For full-length tracks, it is given by [83]

$$\frac{\Delta p_T}{p_T} = 0.58\% \cdot p_T\,[\mathrm{GeV}] \oplus 0.65\% \oplus 0.14\%/p_T\,[\mathrm{GeV}]. \tag{3.2}$$

The first term accounts for the position resolution of the hits, the second one for multiple scattering inside the CTD, and the third term for multiple scattering before the particle enters the CTD.

From the reconstructed tracks, the primary interaction vertex can be derived with a typical resolution of 0.4 (0.1) cm along (transverse) to the beam direction. However, the vertex position in transverse direction is better known from the beam profile, to a resolution of 330 μm in X and 90 μm in Y.

From the signal height, the specific energy loss dE/dx of particles can be measured and used for particle identification.

3.2.3 Luminosity measurement (LUMI)

The luminosity is measured via the Bethe-Heitler process [80] $ep \to ep\gamma$, using a separate lead-scintillator calorimeter (LUMI-γ) positioned at $Z = -107$ m, detecting photons with scattering angles less than 0.5 mrad. The uncertainty of the luminosity measurement for the data sample used in this analysis is 1.8%. A second electromagnetic calorimeter (LUMI-e), positioned at $Z = -35$ m, is used for tagging electrons in background studies.

3.2.4 Trigger (FLT/SLT/TLT) and event reconstruction

During data taking, the predominant task is to find the interesting signal ep events in a far greater number of uninteresting background events. Due to the large amounts of data to be processed and stored, this decision has to be taken online, during the process of data taking. This is the purpose of triggers.

At a luminosity of $2{\cdot}10^{31}\ \mathrm{cm}^{-2}\,\mathrm{s}^{-1}$, DIS events with $Q^2 > 100\,\mathrm{GeV}^2$ occur at a rate of 0.11 Hz, soft photoproduction events at 240 Hz [79]. Background events have rates that are higher by several orders of magnitude, like cosmic muons traversing the detector at some 1000 Hz, and collisions of beam particles with gas molecules inside the beam pipe (beam-gas events) occurring with about 10000 Hz (depending on the beam and vacuum conditions).

The data measured by the components of ZEUS are analyzed by a three-level trigger system. Each trigger level has the task to reduce the input event rate such that its output rate is low enough as input rate for the next level. The complexity of the decisions and the data they are based on increases for each level.

The first level trigger (FLT) is based predominantly on energy deposits in the CAL and hits in the CTD. Enforced by the beam crossing rate of 10.4 MHz, it has to deliver a decision every 96 ns. Calculation speed at these orders of magnitude is achievable only by hard-wired electronic logic circuits, but even these are too slow. Consequently, as one wants to avoid dead time, the data from the different detector components have to be stored in pipelines and are evaluated by the trigger during the passage through the pipeline. The first level trigger decision then has to be available after 5 μs.[7] Each component participating in the FLT has its own local FLT, which sends its decision to the global first level trigger (GFLT). The output rate of the GFLT must be below 1 kHz. In the case of a positive GFLT decision the pipelines are stopped, and the data are read out for further processing in the subsequent levels.

The second level trigger (SLT) consists of a programmable transputer network. It is predominantly used to filter out beam-gas events by exploiting the energy and timing information from the calorimeter that becomes available at this stage. As in the previous level, the SLT decisions of the participating components are collected and evaluated by the global second level trigger (GSLT). The output rate of the GSLT must be below 100 Hz.

The event builder (EVB) collects the complete information from the components and brings them into the data format used by the third level trigger (TLT) and by the offline reconstruction and analysis software. In a farm of Silicon Graphics processors, reconstructed physics quantities like kinematic event variables, global quantities of the hadronic final state, output from algorithms like electron finders, reconstructed shortlived particles etc. are available for event selection and classification. The software running on the TLT processors is similar to parts of the offline reconstruction software, and operates on the same raw data, though partly simplified in order to save processing time. The TLT output rate amounts to a few Hz, which is, given an average event size of 100 KB, sufficiently low to send all the event data over a network to mass storage facilities on the DESY site.

The trigger system is completed by a logic that (acting as a pseudo fourth-level trigger) classifies events by assigning DST (data summary tape) bits to them according to certain physics conditions.

If logical conditions are not sufficient to reduce the rate of a certain trigger slot, it can be prescaled by a factor n, which means that only each n-th accepted event is taken, i.e. written to tape or handed to the next higher trigger level. This, of course, effectively reduces the available luminosity by a factor n, and is therefore regarded only as the last measure to reduce trigger rates.

The ZEUS offline reconstruction software is written predominantly in FORTRAN (plus some pieces written in C/C++) and organized in many separate packages, among them CCRECON (calorimeter reconstruction [84]), VCTRAK (CTD reconstruction [85, 86]), BPRECON (BPC reconstruction [87]) and BPTRECON (BPT reconstruction [88]). There are also numerous collections of utilities and algorithms available, like the PHANTOM [89] and RUNLIB [90] libraries. The reconstructed quantities are stored in the relational database format ADAMO

[7] This number is determined by the component with the shortest pipeline, having 56 entries.

(Aleph Data Model [91]) that is interfaced to the FORTRAN language.

Since the collected data from ZEUS would occupy far more hard disk space than the budget permits, only a reasonable selection of reconstructed quantities (omitting nearly all raw detector data) is collected in MDST (mini data summary tape) files that are stored on hard disks for quick access by many users, while the complete data are only accessible from tapes and typically only needed for dedicated reconstruction runs. The events are classified with DST bits, allowing selective access to those events that are interesting in a certain analysis, thus speeding up the processing time when analyzing events.

For the individual analysis, a further data reduction step is performed by the user in creating Ntuples, summary files of event variables, based on the HBOOK [92] package. The Ntuples are produced by a FORTRAN program running on the central computing facility ZARAH [93], while the further analysis of Ntuples is mostly performed at the home institutes. At this stage, the amount of data has been reduced to roughly a few GB.

Many of the analysis tools commonly used in particle physics have been developed at CERN, like HBOOK, the collection of mathematical routines CERNLIB [94], the minimization package MINUIT [95], and the data analysis and visualization program PAW [96].

Chapter 4

Beam Pipe Calorimeter and Tracker

In this chapter, the two key detectors for the analysis are presented: the Beam Pipe Calorimeter (BPC) and the Beam Pipe Tracker (BPT) of ZEUS. The chapter starts with the motivation why detectors at small angles are necessary for low-Q^2 physics, and continues with a description of the BPC and BPT hardware concept, and of the operating conditions in the year 1997.

4.1 Small-angle detectors

The reason why detectors at very small angles are desirable in an electron-proton scattering experiment has already been pointed out: a large fraction of particles typically emerges at low angles with respect to the beam axis. For DIS reactions, detecting the scattered electron at small scattering angles is equivalent to measuring events at low Q^2 (section 2.3). This is the key to studying the transition region from deep inelastic scattering to photoproduction.

On the detector side, there are two complementary possibilities to achieve this goal. For a given detector configuration, the acceptance at low scattering angles can be increased by either moving detectors closer to the beam line, or by moving the event (i.e. the primary vertex) further away from the detectors, along the beam line.

On the physics side, one can make use of events where the incoming electron has radiated a collinear photon before interacting with the proton (initial state radiation, ISR). This leads to an effective reduction of the incoming electron energy and thus of the center-of-mass energy available for the electron-proton interaction, which translates into larger scattering angles for the same Q^2 (section 2.5), or an extension of the acceptance toward lower Q^2.

Since 1994, when the interest in low-Q^2 structure functions at HERA arised, all of these possibilities have been exploited: In 1995, the two halves of the central RCAL module, above and below the beam pipe, were shifted closer together, leaving a rectangular instead of a quadratic hole. During some periods in 1994 and 1995, data were taken with the nominal interaction point shifted from $Z = 0\,\mathrm{cm}$ to $Z = +70\,\mathrm{cm}$, i.e. away from the rear detectors (shifted vertex (SVX), [56, 97]). With 1994–97 data, analyses of ISR events were performed [97–100]. As a result, the lower acceptance limit in Q^2 was pushed from $4\,\mathrm{GeV}^2$ down to about $1\,\mathrm{GeV}^2$.

However, it became clear that one needed additional acceptance at low Q^2. Therefore, a completely new detector was designed to reach Q^2 values well below $1\,\mathrm{GeV}^2$. It came in two parts: In 1995, the Beam Pipe Calorimeter (BPC) was installed close to the rear beam pipe behind the RCAL hole, and the ZEUS collaboration published a first measurement of F_2 in the range $0.11\,\mathrm{GeV}^2 < Q^2 < 0.65\,\mathrm{GeV}^2$ with the BPC [57]. In 1997, the BPC was upgraded by the installation of a tracking detector in front of it, the Beam Pipe Tracker (BPT) (Fig. 4.1). This report presents a new and improved measurement of F_2 using BPC and BPT in the range $0.045\,\mathrm{GeV}^2 < Q^2 < 0.65\,\mathrm{GeV}^2$.

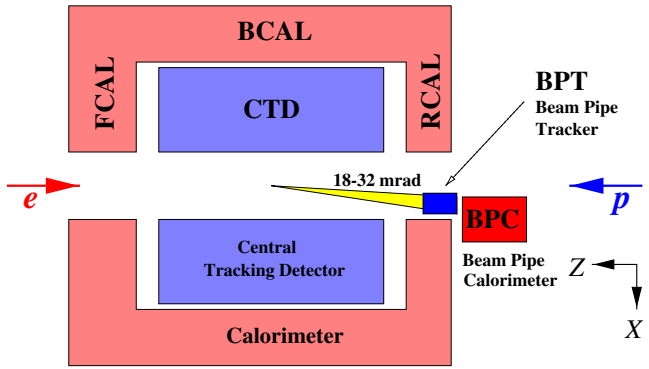

Fig. 4.1: Schematic view of the ZEUS detector, indicating the position and angular acceptance of BPC and BPT (not to scale).

4.2 Beam Pipe Calorimeter (BPC)

4.2.1 Concept of calorimetry

Calorimeters in high-energy physics are massive devices used to measure the kinetic energy of high-energetic particles by absorption. In interactions with the calorimeter material, a primary particle produces lower-energetic secondary particles, thus developing a particle shower. In order to stimulate the showering process, calorimeter materials have a high density. A popular class of calorimeters are scintillator sandwich or sampling calorimeters, where tiles of a dense absorber material (passive layers) alternate with tiles of scintillator material (active layers). The actually measured quantity is the total amount of light produced in the scintillators by the passage of charged shower particles, which is proportional to the kinetic energy that the primary particle had before entering the calorimeter.

Calorimeters have a number of properties that make them suited for high-energy physics experiments; besides energy, they can measure also time and position, and they can be used for particle identification:

- energy resolution: the energy resolution usually behaves like $\sigma(E)/E \propto 1/\sqrt{E\,[\mathrm{GeV}]}$, i.e. the relative resolution improves with increasing particle energy,[1] in contrast to e.g. tracking chambers, where particle momenta are measured from the curvature in a magnetic field, yielding a resolution that worsens with increasing momentum.

- time resolution: the production and detection of light is a very fast process (in well-suited scintillators and photodetectors) and thus allows the measurement of the arrival time of particles with a resolution improving with energy as $\sigma(t) \propto 1/\sqrt{E\,[\mathrm{GeV}]}$.

- position resolution: in the case of a transverse segmentation of the calorimeter, or of a light detection system reading out on opposite sides, a position measurement is possible, with the position resolution behaving like $\sigma(X) \propto 1/\sqrt{E\,[\mathrm{GeV}]}$. If position reconstruction is the main focus, however, there are other detector concepts better suited for position measurement than calorimeters, like e.g. tracking detectors.

- particle identification: in the case of a transverse (longitudinal) segmentation of the calorimeter, the shower width (depth) can be measured. Due to the significantly different behavior of electromagnetic and hadronic showers (see below), this can be used for electron-hadron separation.

- dimensions: the calorimeter dimension that is needed to fully contain a particle shower increases only logarithmically with the particle energy, both in transverse and longitudinal direction, thus allowing relatively compact detectors even in experiments at highest energies.

[1] More precisely, the energy resolution in a calorimeter can be approximated as $\sigma(E)/E = A/\sqrt{E\,[\mathrm{GeV}]} \oplus B \oplus C \ln E\,[\mathrm{GeV}]$, where the first term is caused by sampling fluctuations, the second term by the readout system, and the third one by longitudinal leakage. For well-designed calorimeters, however, B and C are small. The time and position resolutions have similar additional terms.

Although the measurement principle is the same for all particle kinds, the physical processes behind the shower development depend on its type. Electrons and photons initiate electromagnetic showers, while hadrons develop hadronic showers.

4.2.1.1 Electromagnetic showers

Electromagnetic showers are quite well-understood and calculable, since only QED processes are involved (in contrast to hadronic showers, which are governed by the strong interaction). When a high-energetic electron or photon enters a massive absorber material, it starts an electromagnetic cascade, developing predominantly by bremsstrahlung and pair production in the vicinity of atomic nuclei. After the produced particles fall below the critical energy, $E_c \approx 800\,\mathrm{MeV}/(Z+1.2)$ (Z being the atomic number of the absorber), they dissipate their remaining energy by ionization and excitation.

The characteristic longitudinal length scale for electromagnetic showers is the radiation length X_0, defined as the mean distance after which a high-energy electron has lost all but $1/e$ of its original energy by bremsstrahlung processes. Figure 4.2 shows the longitudinal profile of an electromagnetic shower in a simulation.

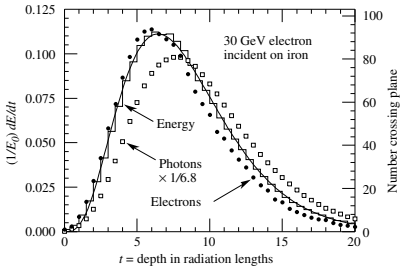

Fig. 4.2: Simulation of a 30 GeV electromagnetic shower in iron. The histogram shows the fractional energy deposition per unit radiation length, the curve is a fit to the distribution. Circles indicate the number of electrons, squares the number of photons above 1.5 MeV at the given depth (reproduced from [14]).

For a sandwich calorimeter, or more generally for a compound of n different materials with fractions w_i (by weight), the effective radiation length is approximately given by

$$1/X_0 = \sum_{i=1}^{n} w_i/X_i. \tag{4.1}$$

The characteristic transverse length scale is the Molière radius

$$R_M = X_0 \frac{E_s}{E_c}, \tag{4.2}$$

where $E_s = 21.2052\,\mathrm{MeV}$. On average, 90% of the shower energy are deposited inside a cylinder with radius R_M, and 95% in a radius of $2R_M$. The transverse shower distribution is often parameterized as a sum of two gaussians.

4.2.1.2 Hadronic showers

For particles other than electrons and photons, the dominating energy loss mechanism is by ionization. The average energy loss rate dE/dx is then approximately given by the Bethe-Bloch formula as illustrated in Fig. 4.3. For hadrons, the development of the shower, i.e. the production of secondary particles, occurs by strong interaction of the hadrons with the absorber material. Muons, which are not subject to the strong interaction, consequently interact with absorbers by ionization only and can traverse long distances before coming to rest.

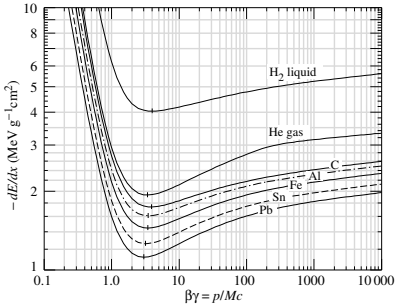

Fig. 4.3: Average energy loss rate dE/dx in liquid hydrogen, gaseous helium, carbon, aluminum, iron, tin, and lead (reproduced from [14]). A particle at the minimum dE/dx is called a minimum-ionizing particle (MIP).

Hadronic showers have a much larger transverse and longitudinal size than electromagnetic showers of the same energy. The characteristic scale is the hadronic interaction length λ, defined as the traversed distance after which all but $1/e$ of a large number of hadrons have undergone at least one interaction, which is typically much larger than the electromagnetic radiation length X_0 (e.g. $\lambda \approx 25\,X_0$ for the ZEUS uranium-scintillator calorimeter).

4.2.2 The BPC of ZEUS

The BPC has been installed in ZEUS in 1995, together with a specially designed new rear beam pipe. It is a tungsten-scintillator sampling calorimeter with the front face located at $Z = -293.7$ cm, the Y-center at $Y = 0$ cm and the inner edge of the active part at $X = 4.4$ cm, as close as possible to the beam pipe. Its active dimensions are $12.0 \times 12.8\,\mathrm{cm}^2$ in $X \times Y$ (Fig. 4.4).

The little available space in the rear part of ZEUS made this very compact design necessary. Tungsten was chosen as absorber material because of its short radiation length and particularly because of its small Molière radius, which determines how close to the calorimeter edge the energy measurement works reliably, and therefore limits the angular acceptance.

Actually, there are two BPC modules, named BPC north and south according to their geographical location at positive respectively negative X coordinates on either side of the rear beam pipe, at a distance precisely defined by a spacer bar. Only BPC north is used for physics analysis, because the usable part of the active area of BPC south is very small. BPC south was used in 1995 for alignment purposes. In the following, "BPC" always means "BPC north". In Fig. 4.1 only BPC north is shown.

The BPC is composed of alternating layers of tungsten alloy (DENSIMET D18K) and scintillator plates (SCSN-38), in total 26 layers of each kind. The absorber plates have a thickness of 0.35 cm each, the scintillators of 0.26 cm. The resulting depth of $24\,X_0$ is sufficient to contain electromagnetic showers of up to about 30 GeV in longitudinal direction.[2] The energy resolution as determined in test beam measurements at 3–6 GeV is $\sigma(E)/E = 17\%/\sqrt{E\,[\mathrm{GeV}]}$.

[2] For kinematic reasons, the scattered electron energy cannot exceed the incoming electron energy at small scattering angles.

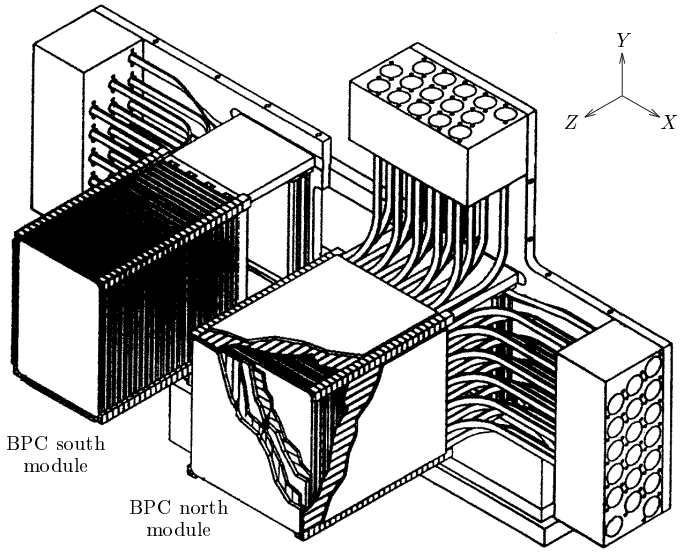

Fig. 4.4: The BPC of ZEUS. On the left side the south module, on the right side the north module, together with the light guides and photomultipliers of the readout system, and parts of the support structure. Not shown is the rear beam pipe, which runs between the two modules. Only the north module is used for physics analysis, and is referred to as "the" BPC.

The scintillators are alternatingly subdivided in horizontal and vertical strips (7.9 mm wide, each separately wrapped in aluminum foil, with a 0.1 mm gap between adjacent strips). Between each scintillator layer and the beam pipe, a 0.5 cm wide tungsten strip is glued to the adjacent tungsten layer, to keep the scintillators in position. Groups of 13 $X(Y)$-measuring scintillator strips in a stack (longitudinally) are referred to as an $X(Y)$ finger. They are connected and read out on one side by a wavelength shifter (30 ppm Y7 in PMMA), transporting the light to a photomultiplier (Hamamatsu R5600-03). This construction principle allows to reconstruct the transverse shower position in the BPC with a resolution of approximately $\sigma(X) = \sigma(Y) = 0.22\,\mathrm{cm}/\sqrt{E\,[\mathrm{GeV}]}$. BPC north has 15 X fingers and 16 Y fingers. There is no readout segmentation in longitudinal direction. More details about the BPC hardware can be found in [101].

Scattered electrons travel most of their way from the interaction point toward the BPC inside the beam pipe. At $Z = -249.8$ cm, the beam pipe has a 1.5 mm thick aluminum exit window, which allows the electrons to leave the beam pipe by crossing only 1.6% X_0 of inactive material. The D-shaped projection of the exit window onto the BPC surface is referred to as the fiducial area, covering roughly the region $4\,\mathrm{cm} < X < 10\,\mathrm{cm}$ and $-3\,\mathrm{cm} < Y < 3\,\mathrm{cm}$. Only electrons scattered into the fiducial area are used for the analysis, and some additional constraints reduce the usable part of the fiducial area in 1997 to $5.2\,\mathrm{cm} < X < 9.3\,\mathrm{cm}$ and $-2.3\,\mathrm{cm} < Y < 2.8\,\mathrm{cm}$. The acceptance of the BPC is therefore limited to scattering angles of $18\,\mathrm{mrad} < \theta < 32\,\mathrm{mrad}$ (i.e. $178.1^\circ < \vartheta < 178.9^\circ$) for particles emerging at the nominal interaction point (the effective geometrical acceptance is slightly larger due to the spread in the Z vertex distribution).

The positioning of the BPC as close as possible to the rear beam pipe implies that it is

exposed to high radiation doses, caused by beam-related background. The BPC therefore has to be radiation-hard, and its operating parameters, e.g. calibration constants, have to be checked and eventually corrected for time dependences.

4.3 Beam Pipe Tracker (BPT)

4.3.1 Motivation for a tracking detector

During the analysis of the 1995 BPC data, it became clear that there are several reasons why tracking information, in addition to the energy, timing and position information provided by the BPC, is desirable. The motivation for building the BPT has been summarized in [102]:

- Improved measurement of the scattered electron:

  The energy and the angle of the scattered electron are the basic ingredients for the reconstruction of kinematic variables in an event (section 6.3). Using the BPC, the angle is derived from the impact position of the electron in the BPC, and from the event vertex as reconstructed by the CTD. Since the angle of the scattered electron is far too small to leave a track in the CTD, the vertex is reconstructed exclusively from the hadronic final state. The longitudinal vertex resolution is typically $\sigma(Z) = 0.4\,\text{cm}$, the transverse resolution is given by the size of the beams, $\sigma(X) = 330\,\mu\text{m}$ and $\sigma(Y) = 90\,\mu\text{m}$ in 1997. However, if none of the hadrons leaves a reconstructable track in the CTD, the vertex is set to a default value (the nominal interaction point), which deteriorates the longitudinal resolution to the width of the vertex distribution, around $\sigma(Z) = 10\,\text{cm}$. The probability for this to happen is a function of the event topology, which is correlated with the kinematic variables. There are also cases where the vertex reconstructed by the CTD is significantly wrong, because a secondary vertex (typically from the interaction of a hadronic particle in the beam pipe wall) is erroneously picked as the primary vertex.

  It turns out (section 6.3.7) that for events with a proper CTD vertex the resolution of kinematic variables is dominated by the BPC energy resolution; consequently, additional tracking information is of minor use here. However, in events without a CTD vertex, the kinematic resolution is dominated by the angular resolution and therefore improves by a better determination of the angle using a tracking detector. In addition, possible systematic effects caused by a missing or misreconstructed CTD vertex are avoided with an independent tracking detector.

- Better control of systematic effects:

  The position reconstructed by the BPC enters directly into the angular reconstruction, and indirectly also into the energy reconstruction algorithm, which corrects for position-dependent effects (section 6.1.1).

  Position reconstruction from a segmented calorimeter is known to introduce position-dependent systematic shifts, no matter how sophisticated the algorithm may be. Consequently, both the angular reconstruction and the energy calibration gain in precision from the use of a tracking detector, providing an unbiased angular measurement.[3]

- Background rejection:

  The sort of background most difficult to handle in the BPC are events where one or more particles of the hadronic final state, usually photons from a π^0 decay, fake an electron signal in the BPC. Due to the $1/Q^4$ dependence of the ep cross section, these are usually events at much lower Q^2 than the typical Q^2 of the analysis, and the real scattered electron escapes undetected in the beam pipe ("photoproduction events"). In addition, photons from ISR/FSR may fake an electron signal.

  By requiring a track that extrapolates to the shower position in the BPC, i.e. a neutral particle veto, this background can be strongly suppressed.

  Another, though less serious, source of background are electrons from interactions of the electron beam with gas molecules in the beam pipe, and off-momentum electrons that get deflected by the beam optics into the BPC.

  Such events can be recognized by their apparent event vertex as reconstructed from a tracking detector, which is far outside the ZEUS detector (and cannot be reconstructed by the CTD). They usually come in time with normal ep interactions and can therefore not be suppressed by requiring a proper arrival time at the BPC.

[3] Another, yet later abandoned, motivation was the plan to replace the current BPC by $PbWO_4$ crystals with a much better energy resolution of $\sigma(E)/E = 5\%/\sqrt{E\,[\text{GeV}]}$, but a much worse position resolution.

In anticipation of the experience gained during the analysis of 1997 data, all of the above design considerations turned out to be justified. However, their relative importance was slightly misjudged: while the above list was originally assumed to be ordered by decreasing importance, it turns out to be in fact ordered by increasing importance. Some additional benefits of a tracking detector showed up during the analysis:

- Better knowledge of detector position:

  Although the presence of an additional position detector introduces new and a priori unknown parameters (describing its position in ZEUS coordinates) into the problem, it turns out that the absolute position of a tracking detector in front of the BPC can be determined to a higher precision than that of the BPC, and as a consequence also the BPC position itself is known more precisely.

- Tuning of the position reconstruction algorithm:

  Using the tracking detector to obtain an independent prediction of the impact point of a particle in the BPC, it is possible to develop a good position reconstruction algorithm for the BPC using measured data.

Given the above considerations, silicon microstrip detectors were the most appropriate solution.

4.3.2 Concept of silicon detectors

Thin silicon detectors are used (not only) in high-energy physics as position-sensitive devices. Operating several of them together forms a tracking detector, providing both position and direction information.

A thin silicon detector is a semiconductor diode operated in reverse-biased mode. Ionizing particles traversing the diode create electron-hole pairs along their track. Due to the applied depletion voltage, electrons and holes do not recombine, but rather drift in the electric field to opposite sides, approaching the n^+ respectively p^+ doped electrodes. In order to localize the charge, one of the electrodes is subdivided in strips or pixels, thus providing a measurement of one respectively two space coordinates (Fig. 4.5). Contrary to calorimetric measurements, a thin silicon detector permits a nondestructive measurement.

Silicon detectors have many properties that make them increasingly popular in high-energy physics experiments:

- The position resolution can be chosen from a relatively wide range according to the needs of the experiment, and is in practice usually limited by the number of possible readout channels, and by the ability to provide the microscopically small connections to the detector strips or pixels, rather than by effects related to the transverse dimensions of the energy deposition in the detector itself.

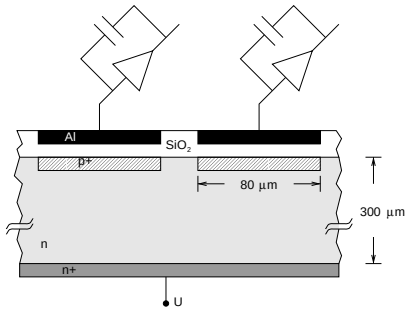

Fig. 4.5: Schematic cross section of a silicon detector. The dimensions and materials given are those of the detectors used in the BPT.

- The detector readout can be either analog or binary (i.e. the signal height is read out, or only the result of comparing it to a threshold value), where in the former case an energy-weighting algorithm can be used to further improve the position resolution over the binary-readout case.
- Silicon detectors can be made radiation-hard, allowing to install them in places with high particle flux, e.g. very close to the beam line.
- Compared to other tracking detector concepts, they provide a high signal-to-noise ratio and thus allow to set low signal thresholds, typically yielding a detection efficiency close to 100%.

4.3.3 The BPT of ZEUS, fact and fiction

The BPT has been designed as a telescope with five silicon microstrip detectors (Figs. 4.6 and 4.7). The detectors (single-sided, 576 channels, 80 µm strip width, 100 µm pitch, dimensions $6 \times 6 \times 0.03\,\mathrm{cm}^3$) were manufactured by EURISYS. The signal strips are grounded by a surrounding bias ring. They are covered by a thin (some 100 nm) layer of insulating SiO_2, on top of which aluminum contact strips serve to connect to the readout system.[4] The depletion voltage is 40 V.

The strips are connected to kapton cables, passing the signals to the front-end readout electronics. Groups of 64 channels each are read out by an analog amplifier and comparator chip (TEKZ), followed by a digital chip with pipeline and event buffering (DTSC). The readout is thus binary. The subsequent readout chain is implemented as part of the LPS [103]. The total number of readout channels per detector plane was limited for technical reasons to 512; therefore, 128 strips at one edge of a plane are read out in pairs, yielding an effective pitch of 200 µm there.

The detector planes and hybrids are fixed in a support structure of carbon fiber composite. It has the dimensions $6.3 \times 7.0 \times 41.0\,\mathrm{cm}^3$ in $X \times Y \times Z$, and is attached with two screws to a support that has been glued to the BPC front face. The whole BPT is wrapped in a number of metal and plastic foils in order to screen it optically and magnetically. Its center is located at $X = 6.85$ cm and $Y = 0$ cm in the ZEUS coordinate system.

The planes are glued to the readout hybrids in a precisely defined spatial relation, and the hybrids are fixed by screws to holes provided in the support frame. This setup was intended to be used for a precise alignment of the BPT planes relative to each other. However, in practice, the obtained accuracy turned out to be insufficient.

[4] This AC-coupling (alternating current, i.e. capacitive connection of the signal electrodes to the readout electronics) has an important advantage compared to DC-coupling (direct current, i.e. direct connection): the leakage current, which is quite high when operating the BPT at normal temperatures and high radiation doses, is decoupled from the pre-amplifier.

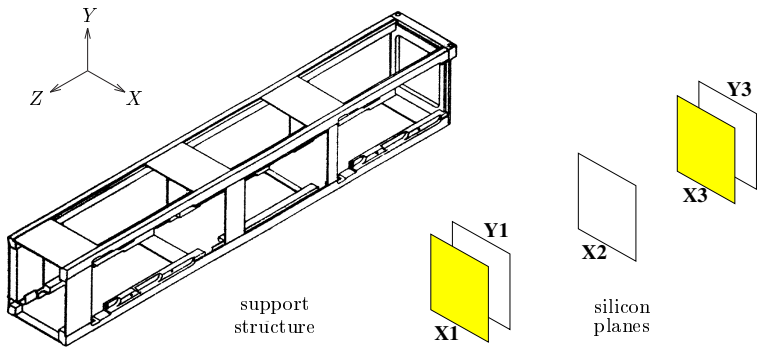

Fig. 4.6: The BPT of ZEUS. Left: the support structure of carbon fiber composite. Right: the five silicon microstrip detectors as foreseen in the original design. Dark shaded are the detector planes that were installed in 1997. The scale is the same as in Fig. 4.4.

In its 1997 configuration, the BPT consists of two silicon microstrip detectors, which both measure the X coordinate. In the design configuration, one additional X-measuring and two Y-measuring planes were foreseen. According to the coordinate they measure, the BPT planes are named X1, Y1, X2, X3, Y3, where X1 and X3 are the two planes of 1997. Each BPT plane adds 0.32% X_0 to the material between interaction point and BPC.

Fortunately, with two X planes the performance of the BPT is already close to its expected peak performance with five planes. This is mainly because, at the position of BPC and BPT, measuring X is essentially equivalent to measuring θ, while Y corresponds to ϕ. The unpolarized ep scattering cross section is ϕ-independent, and the relevant angle θ can essentially be measured with two X planes. A third X plane would increase slightly the angular resolution, and decrease the sensitivity to noise (i.e. the fraction of events where a noise hit is picked to reconstruct a BPT track, which is anyway small). Y planes are not very interesting for the measurement, since the precision of the Y measurement from the BPC is sufficient. They might be of use for detector studies.

As the readout is binary, the position resolution (for perpendicular incidence) of each plane is given by $\sigma(X) = d/\sqrt{12} \approx 30(60)$ µm, where $d = 100(200)$ µm is the effective strip pitch. The planes are oriented such that the strips read out in pairs are located at high values of X (corresponding to high θ), thus keeping the maximum relative angular resolution[5] $\sigma(\theta_X)/\theta_X$ small. The distance between X1 and X3 is $\Delta Z = 26.4$ cm, yielding the angular resolution in the X-Z plane, $\sigma(\theta_X) = \sqrt{2}\,\sigma(X)/\Delta Z = 0.15$ mrad. The relative angular resolution, $\sigma(\theta_X)/\theta_X$, varies between 0.9% and 0.5% for θ_X between 18 mrad and 32 mrad. Both resolutions increase by a factor of $\sqrt{2}$ (2) if one (two) strips read out in pairs are involved, which is the case in only a tiny border part of the fiducial area.

Anticipating the alignment result (section 6.1.3), the absolute position of BPC and BPT in the ZEUS coordinate system can be determined to an accuracy of 200 µm. The relative alignment of the BPT planes to each other and to the BPC is determined to a much higher precision (a few µm). The tracking efficiency is limited by a few percent of dead channels and by high threshold settings to a level of about 95% for each plane, yielding an overall tracking efficiency of $90.4\% \pm 1.5\%$.

[5] This is a fairly peculiar quantity. It makes sense, however, for small angles, where $\sin\theta \approx \tan\theta \approx \theta$. In this case it appears naturally in the formulae for $\sigma(Q^2)/Q^2$ and $\sigma(y)/y$.

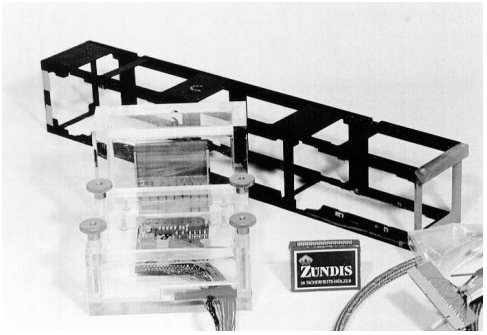

Fig. 4.7: Photo of the BPT support structure. In the foreground, a silicon plane bonded to a readout hybrid is displayed (kept in a perspex box).

4.4 Data taking and trigger

The BPT has been installed in front of the BPC at the end of July 1997 (Figs. 4.8 and 4.9). The commissioning took a couple of weeks, and useful data were taken between beginning of September and mid October. The collected events correspond to an integrated luminosity of $3.9\,\mathrm{pb}^{-1}$. A special trigger configuration with enabled BPC trigger slots was used (during the rest of 1997, most of these triggers had been switched off).

Trigger decisions based on BPC information are made at all three levels of the ZEUS trigger system. Due to the high background rate close to the beam line, an effective background reduction is necessary already at an early stage.

On the first trigger level, hard-wired analog summing circuits provide sums of energies in different groups of fingers. The sums are converted to four-bit numbers by a flash analog-to-digital converter (FADC) module and sent to the GFLT. The available sums for BPC north are (E^i_X, E^i_Y denote the energy in the i-th X respectively Y finger):

1. X fingers inside fiducial area: $\sum_{i=2}^{10} E^i_X$
2. Y fingers inside fiducial area: $\sum_{i=3}^{14} E^i_Y$
3. X and Y fingers outside fiducial area: $E^1_Y + E^2_Y + E^{15}_Y + E^{16}_Y + \sum_{i=11}^{15} E^i_X$
4. innermost X finger: E^1_X.

Only the second (rather than the first) of these sums is used in the trigger, because all Y fingers are expected to be likewise damaged by radiation, while the inner X fingers suffer much more than the outer ones. This would introduce a position-dependent bias, which furthermore changes with time. Since the trigger rate obtained using this sum alone is already acceptable, further requirements, e.g. vetoes based on the third and the fourth sum, are not implemented. In addition to the summed energies, also a timing signal is derived from the BPC and provided to the GFLT.

At the second and third trigger level, individual finger energies and time measurements are available. This provides a more precise energy measurement than at the first level, and it allows to base decisions on the shower position and width, and a more sophisticated background rejection. The BPC DST bits are just copies of the BPC TLT bits. SLT information from the BPT was not available in 1997; TLT information was available but not used. No time-dependent effects of the BPT performance were observed that could be attributed to radiation damage.

Fig. 4.8: Photo taken during the installation of the BPT in ZEUS. The position of the photographer was behind the opened RCAL, above the beam pipe (1), which runs from the upper left to the lower right corner. The interaction point is outside the picture (to the upper left). Also shown are the exit window (2) in front of the BPT (3) and some photomultiplier housings at the back of the upper half (4) and the lower half (5) of the central RCAL module. The BPC north (6) and south (7) modules are better visible on the next photo.

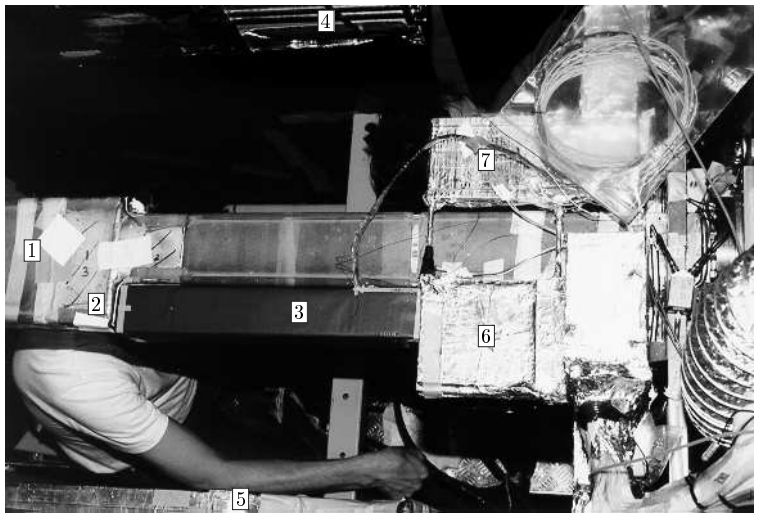

Fig. 4.9: Same as above. The photo was taken from above the BPC and BPT. The beam pipe runs from left to right, the interaction point is outside the picture (to the left).

4.5 Surveys

Two different surveys related to BPC and BPT were performed, in order to determine their position in space. An "absolute" survey, that was primarily intended to determine the position of BPC and BPT in the ZEUS coordinate system, as well as a "relative" survey, that concentrated on a precise determination of the position of BPC and BPT with respect to each other.

The method of the absolute survey was identical to 1995. With optical devices, the BPC position was determined relative to the compensator magnet, the position of which in turn needs to be determined relative to the ZEUS coordinate system. This survey was performed in two steps in 1997:

1. In October 1997, directly after the end of the running period, the position of BPC and BPT relative to the compensator magnet was surveyed. At that time, the position of the compensator itself could not be determined (because needed reference points were hidden behind other detector components). So, the position from a previous survey was assumed in the calculations. The result was [104]:

   $$X_{\mathrm{BPC}} = 4.33\,\mathrm{cm} \quad Y_{\mathrm{BPC}} = 0.02\,\mathrm{cm} \quad Z_{\mathrm{BPC}} = -293.7\,\mathrm{cm}.$$

   In X, the numbers refer to the position of the inner edge of the first X finger, in Y to the edge between the 8th and 9th Y finger, and in Z to the BPC front face. The overall precision is estimated to be at best $\pm 0.05\,\mathrm{cm}$. The angles of the BPC edges with respect to the ZEUS coordinate system were also determined. They are negligibly small for the purpose of position reconstruction.

   After this survey, BPC and BPT were removed from ZEUS, in order to protect them from radiation damage during the subsequent HERA machine study time.

2. In December 1997, the detectors obstructing the reference points had been removed. The compensator position was determined and it turned out to deviate significantly from the previous survey, by about $0.1\,\mathrm{cm}$ in X. Unfortunately, there was no way to find out if it moved before or after the October survey, and BPC and BPT had already been removed. Assuming the new compensator position, the result for the BPC changes to [104]:

   $$X_{\mathrm{BPC}} = 4.43\,\mathrm{cm} \quad Y_{\mathrm{BPC}} = 0.00\,\mathrm{cm} \quad Z_{\mathrm{BPC}} = -293.9\,\mathrm{cm}.$$

The relative survey was performed after the removal of BPC and BPT from ZEUS, using an opto-electronical surveying machine. In order to avoid possible damage to the detectors, BPC and BPT were taken out of ZEUS separately and put together again afterwards. Although some care was taken, it is not clear to what precision their relative position in X and Y could be reproduced; in Z, it should have succeeded fairly well with the desired accuracy of a few $100\,\mu\mathrm{m}$. Consequently, only the result for Z from this survey is considered further [105]:

$$Z_{\mathrm{X1}} = -252.67\,\mathrm{cm} \quad Z_{\mathrm{X3}} = -279.05\,\mathrm{cm}.$$

The accuracy of the determination of $\Delta Z = Z_{\mathrm{X3}} - Z_{\mathrm{X1}}$ is estimated to be $\pm 300\,\mu\mathrm{m}$. This is not the precision of the surveying machine, which is much better, but a number derived from the measured tilt of the two planes around the X and Y axes. For simplicity, this tilt is assumed to be zero in reconstruction and alignment, and accounted for by assuming an uncertainty for ΔZ.

The remaining positions in X are determined directly from measured data (section 6.1.3). The results are given here for comparison:

$$\begin{aligned} X_{\mathrm{BPC}} &= 4.33\,\mathrm{cm} \pm 0.01\,\mathrm{cm}\,(\mathrm{stat}) \pm 0.02\,\mathrm{cm}\,(\mathrm{sys}) \quad \text{(before access)} \\ X_{\mathrm{BPC}} &= 4.36\,\mathrm{cm} \pm 0.01\,\mathrm{cm}\,(\mathrm{stat}) \pm 0.02\,\mathrm{cm}\,(\mathrm{sys}) \quad \text{(after access)} \end{aligned}$$

which are in better agreement with the first survey result. "Before/after access" refers to a maintenance access to the ZEUS detector during the BPT data taking period, after which a movement of the CTD was observed.

Chapter 5

Monte Carlo Simulation

5.1 Concept of Monte Carlo Simulation

Monte Carlo simulations (MC) are used in high-energy physics experiments to determine the acceptance for selecting events, to study the resolution of reconstruction algorithms, and to estimate background rates. In historical times, detectors were simple enough to determine all these quantities analytically or by measurements, but in an experiment of the complexity of ZEUS this is virtually impossible. Monte Carlo simulations consist of two distinct ingredients:

- Physics simulation:

  A physics simulation implements the best knowledge about the reaction to be analyzed. Ideally, all necessary ingredients for the process, like cross sections, particle life times, masses, decay branching ratios etc., are known. Values that are not known precisely can be given as variable input parameters. Where a calculable theory is not available (like e.g. for fragmentation), phenomenological models (typically also depending on free parameters) are used. If simulated events are generated with certain input parameters that later turn out not to represent the experimental data, weights can be assigned to the events to reproduce the effect of different input parameters.

  The input to the physics simulation consists of the colliding initial state particles and their four-vectors, and of the free parameters needed for the simulation process. The output is a number of events, where for each event a list of final-state particles and their four-vectors is given.

- Detector simulation:

  Here, the interaction of the detector with the final state particles of the events is simulated. For this purpose, the detector simulation contains a description of the geometry and the materials of the detector, in order to be able to simulate the interaction of primary and secondary particles with matter, like formation of showers, energy loss by ionization etc. The decays of unstable particles inside the detector are as well simulated. This is the passive part of the detector simulation.

  The MC also implements algorithms that simulate the response of the active detector components to the particles, i.e. the data are generated that would be read out by the detector readout. This is the active part of the simulation. For example, in a calorimeter the amount of energy deposited in the simulated scintillator plates could be taken as a measure of the amount of light that would have been created in the real detector.

  The output from the detector simulation is reconstructed with the same algorithms as the real data (although for some aspects separate branches exist, implementing a slightly different treatment of data and MC), and the output has the same format as the output from the real detector, plus some additional information about the true particles.

5.2 ZEUS detector simulation

The ZEUS detector simulation program MOZART is based on the GEANT 3.13 [106] package which was developed at CERN. GEANT implements a vast amount of processes and is the standard tool for this purpose in high-energy physics.

5.2.1 BPC simulation

The BPC implementation in MOZART (Fig. 5.1) has been described in detail in [107]. It was tuned according to knowledge gained in the analysis of 1995 data and has been left untouched since then. This means that the position of the BPC in MOZART is the one that was obtained from the optical survey in 1995, and the energy resolution matches that resulting from the energy calibration process of the 1995 data. Both of these features cannot a priori be assumed to match the state of 1997, and it will be shown in chapter 6 that they indeed do not. However, the differences between 1995 and 1997 will turn out to be small enough to justify the use of the unmodified 1995 simulation of the BPC for the analysis of 1997 data. Of course, the parameters that are different between data and MC (like the position of the detector) have to be taken properly into account by the reconstruction and event selection.

For comparison with the survey results from section 4.5, the BPC north position used in the

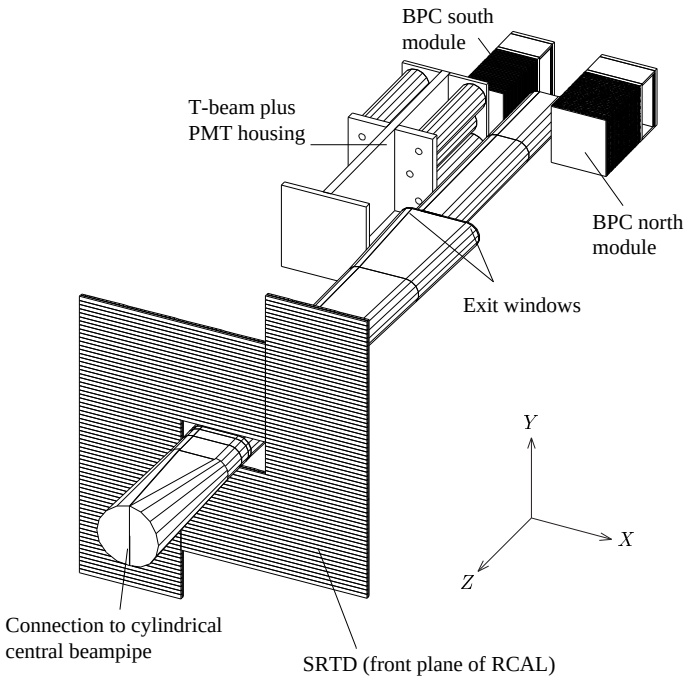

Fig. 5.1: View of the BPC geometry implementation in MOZART, shown together with the rear beam pipe and the SRTD, indicating the front face of RCAL (reproduced from [107]).

Monte Carlo simulation is

$$X_{\mathrm{BPC}} = 4.37\,\mathrm{cm} \quad Y_{\mathrm{BPC}} = 0.18\,\mathrm{cm} \quad Z_{\mathrm{BPC}} = -293.7\,\mathrm{cm}.$$

5.2.2 BPT simulation

Since MOZART is an extremely large and complicated piece of software, the development and testing of the BPT simulation was done in the framework of a small standalone program that was set up on the basis of an existing simulation for the BPC [108].

The main parts of the support structure and the readout hybrids are implemented in simplified shape as (partly overlapping) volumes of carbon, copper and epoxy, respectively. The detector planes are modelled as thin boxes of silicon, subdivided into 576 subvolumes each and having an inactive area at the edges. The details of the geometry definition are shown in Figs. 5.2 and 5.3. Figure 5.4 shows an event simulated by MOZART.

Energy deposits in the active subvolumes of the detector planes are taken to be hits in the corresponding strip if the energy is above a threshold of 30 keV. No attempt was made to tune the fraction of charged-particle passages that create hits in more than one strip per plane (i.e. clusters of two or more adjacent strips).

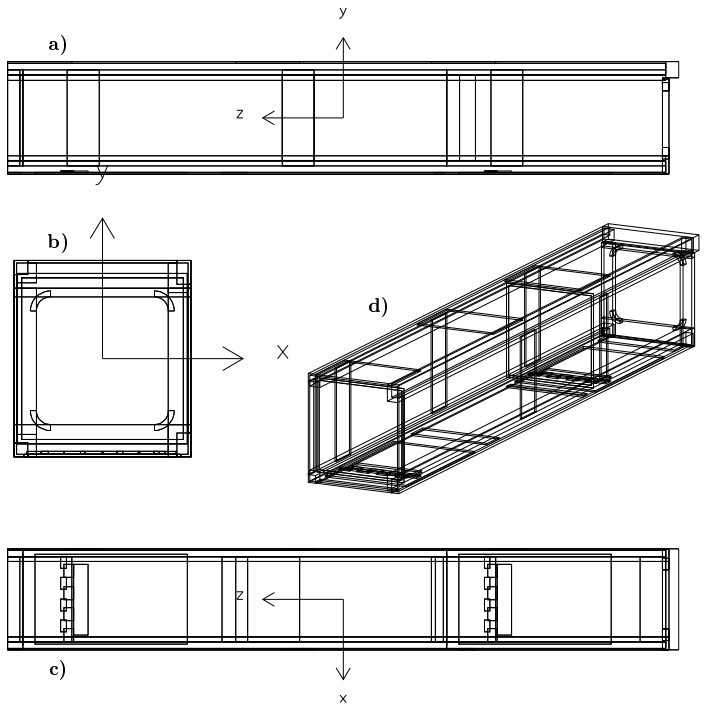

Fig. 5.2: Different views of the BPT geometry as implemented in the simulation (in the 1997 configuration with two silicon planes). Shown are: a) side view; b) front view; c) top view; d) isometric projection.

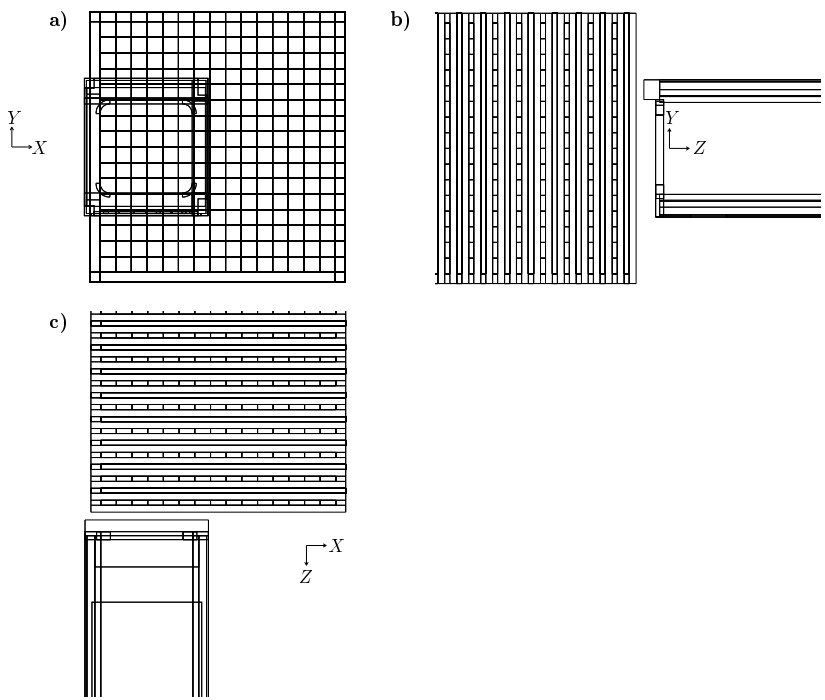

Fig. 5.3: Different views of the BPC and BPT geometry in the interface region as implemented in the simulation. Shown are a) front view; b) side view; c) top view.

The median of the Landau-distributed energy deposits in a 300 µm thick silicon plane is at 90 keV; the distribution has its peak at 85 keV and a width (FWHM) of 30 keV. The simulation was tuned to reproduce these values, which were determined from phenomenological parameterizations [109]. The chosen energy threshold of 30 keV then roughly corresponds to a charge threshold of 1.5 fC as originally foreseen for the operation of the BPT.

One problem occurred at the stage of implementing the geometry definition in MOZART: the position in space where the BPT is situated was already occupied by a different volume.[1] This problem was circumvented by shifting the whole BPT such that its Z position in MC differs from the real position by about 1 cm. The effect of this mismatch on the present analysis is negligible (if the different Z positions in data and MC are taken properly into account). The position of the BPT plane centers in MOZART is:

$$Z_{\mathrm{X1}} = -251.65\,\mathrm{cm} \quad Z_{\mathrm{X3}} = -278.05\,\mathrm{cm} \quad X_{\mathrm{X1}} = X_{\mathrm{X3}} = 6.85\,\mathrm{cm} \quad Y_{\mathrm{X1}} = Y_{\mathrm{X3}} = 0.0\,\mathrm{cm}.$$

[1] Although this volume only contains air, GEANT 3.13 does not allow overlapping volumes (however, the overlap of volumes containing the same material is believed to be safe). The problem occurs in the algorithm that determines from a given point in space the volume containing that point: this algorithm returns the first matching volume that does not have subvolumes. If a point is contained in two different volumes, none being a subvolume of the other one, it is unpredictable which of them the algorithm will choose and hence, which material GEANT will assume at that point.

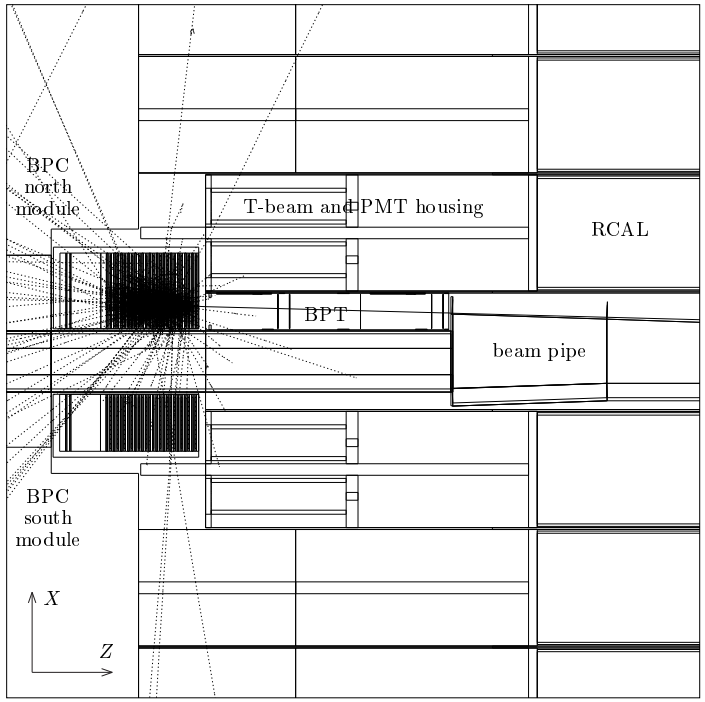

Fig. 5.4: Display (projection into the X-Z plane) of an event with electron in BPC and BPT as simulated by MOZART. Shown as solid line is the primary electron, the dotted lines denote secondary particle trajectories.

From the survey of BPC and BPT (section 4.5), the shifts in Z between data and MC positions were determined to be $\Delta Z_{\mathrm{X1}} = -1.02\,\mathrm{cm}$ and $\Delta Z_{\mathrm{X3}} = -1.00\,\mathrm{cm}$, with an accuracy of 300 µm.

5.3 Physics simulation

5.3.1 Choice of event generators

The subject of this report is to study the transition region between photoproduction and deep inelastic scattering. For these two regimes, the development of event generators has taken two different paths.

Photoproduction generators concentrate on the photon-proton interaction, and expect the flux of photons to be given as input by the user. This is historically motivated: photoproduction experiments were usually performed such that a beam of real photons was produced, which then interacted with the target (and in addition the flux of photons could be measured). At HERA, the production of the (quasi-)real photons does not happen until the electron reaches the immediate vicinity of the proton, rendering a direct measurement of the photon flux impossible, which therefore can only be calculated theoretically in the von-Weizsäcker-Williams approximation [110–112].

Furthermore, the picture of the electron as a source of photons hides some underlying problems, like for example radiative processes, where the electron emits a hard real photon before interacting with the proton. Correcting the output from a photoproduction generator that does not implement radiative processes is rather nontrivial.

Deep inelastic scattering generators, on the other hand, concentrate on the modelling of the electron-proton (or electron-quark) interaction. One-photon radiative corrections are routinely implemented, two-photon corrections are available as routines performing analytical calculations, but not yet in the form of event generators. The scattering process is modelled in two parts, the lepton vertex which is purely QED (including radiative corrections), and the hadronic vertex with the subsequent fragmentation process.

Since the precise measurement of the ep cross section is the aim, it was decided to use DIS generators, rather than photoproduction generators, for the simulation of signal events.

Two programs were used for the generation of the signal event sample: DJANGOH 1.1 [113] and RAPGAP 2.06/51 [114], which have been designed to simulate non-diffractive and diffractive hadronic final states, respectively. Both of them use HERACLES 4.6 [115] to generate the lepton vertex, while the interaction of the photon with the constituents of the proton differs between the two of them. The fragmentation is taken care of in both cases by ARIADNE [116] and JETSET [117–119].[2] While for structure function analyses DJANGO is the standard tool, using RAPGAP for this purpose is novel (at least for ZEUS). From the variety of diffractive event generators RAPGAP was chosen because it uses HERACLES, which makes it relatively straightforward to run RAPGAP with the same parameters as DJANGO for the lepton side of the event.

The generator PYTHIA 5.724 [121] is used for the production of events at very low Q^2 values (i.e. from the photoproduction regime), which are expected to constitute the main source of background.

5.3.2 Event generation

The basic idea of the following procedure is to generate non-diffractive events with DJANGO, diffractive events with RAPGAP, and to mix them according to a prescription determined from the data.[3] This method is expected to give the best possible description of the hadronic final state. The concept is similar to what is done in measurements of the real photon-proton cross section $\sigma_{\rm tot}^{\gamma p}$ at HERA [50, 51].

The following parameters and cuts are used for event generation: MRSA PDF parameterizations; $F_L = 0$; $Q_e^2 > 0.03\,\mathrm{GeV}^2$;[4] $W > 3\,\mathrm{GeV}$; no additional y cut. The MRSA parameterization is valid only for $Q^2 > 0.625\,\mathrm{GeV}^2$ and $x > 10^{-6}$. Below these values, the implementation of PDFLIB 7.09 [122] returns constant values. Therefore, the MC sets are reweighted later to the ALLM97 parameterization, which is known to give a good description of F_2 at low Q^2.

The official ZEUS implementation of DJANGO in the AMADEUS [123] framework was fully adequate for the needs of this analysis, while the RAPGAP implementation had to be modified in a few aspects.

For the F_2 unfolding procedure, the structure function parameterization $F_2(x,Q^2)$ used in the generation of MC events is needed as an input, and must therefore be known precisely. As RAPGAP was primarily designed to generate diffractive events, its normal running mode allows to specify $F_2^{D(4)}(x_{I\!P},t,\beta,Q^2)$, from which the corresponding $F_2^{\rm diff}(x,Q^2)$ has to be calculated by

[2] DJANGO and RAPGAP optionally allow to use the MEPS option of LEPTO [120] for the fragmentation instead of ARIADNE, which was not used here.

[3] Exclusive vector meson production, $ep \to epV$, where $V = \rho,\omega,\phi$, is included in RAPGAP, therefore no attempt was made to generate such events separately.

[4] This is Q^2 as "reconstructed" from true variables of the outgoing electron with the electron method; the true Q^2 can be much smaller in case of ISR.

numerical integration and subsequent interpolation on an x-Q^2 grid [114]:

$$F_2^{\rm diff}(x,Q^2) = \int F_2^{D(4)}(x_{I\!P},t,\beta,Q^2)\,\delta(\beta\cdot x_{I\!P}-x)\,dx_{I\!P}\,d\beta\,dt. \qquad (5.1)$$

Such a procedure was found to be not precise enough. Fortunately, RAPGAP also offers a mixed running mode, generating a mixed sample of diffractive and non-diffractive events, where both the overall $F_2(x,Q^2)$ and the $F_2^{D(4)}(x_{I\!P},t,\beta,Q^2)$ for the diffractive part can be specified by the user. The distribution of events in x and Q^2 is then generated according to $F_2(x,Q^2)$, while the probability for an event at a certain x and Q^2 to become a diffractive event is $F_2^{\rm diff}(x,Q^2)/F_2(x,Q^2)$. RAPGAP was modified such that this probability is artificially set to unity, which results in the desired feature of generating diffractive events that are distributed in x and Q^2 in a precisely defined way. It has been explicitly checked that the generated distributions from DJANGO and RAPGAP are identical (Fig. 5.5).

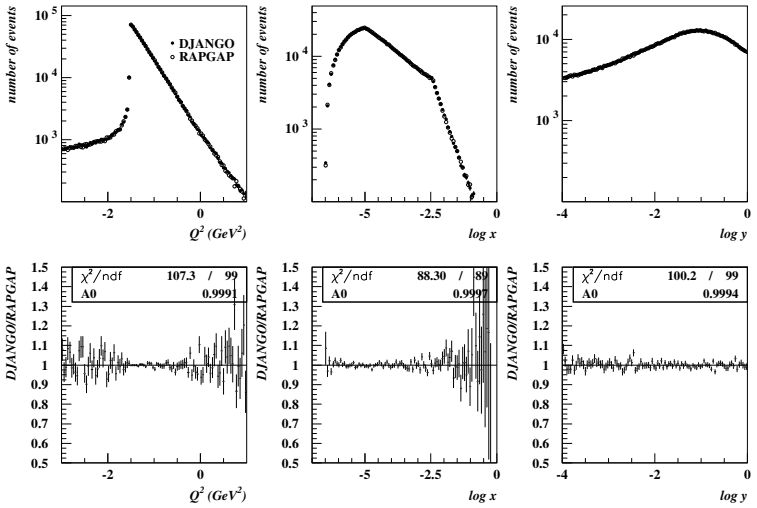

Fig. 5.5: Comparison of distributions of generated kinematic variables for the DJANGO and RAPGAP samples (upper plots) and the ratio of them (lower plots). All distributions are identical within statistical errors.

The function $F_2^{D(4)}(x_{I\!P},t,\beta,Q^2)$ does not only determine the probability for an event to become a diffractive event (which has been set to unity), but it also determines the distribution of events in the variables $x_{I\!P}$ and t. It has to be provided by the user in the form of diffractive parton distributions, i.e. parton distributions for diffractive events. Here, they are chosen to be the PDF's of the proton (according to the MRSA parameterization, i.e. the same set as used in DJANGO, using the relation $x = \beta\cdot x_{I\!P}$), multiplied by a factor $e^{-6|t|}/x_{I\!P}^n$. A value of $n = 1.3$ is found to give a satisfactory description of the M_X and $\eta_{\rm max}$ distributions in data. It has been checked that the simple model for diffraction which is implicitly used here gives a good description of diffractive structure functions as measured by ZEUS at higher Q^2 (appendix A).

The mixing fractions of diffractive and non-diffractive events are determined from data. For this purpose, histograms of certain hadronic variables are generated in different ranges of x and Q^2 for data and the two Monte Carlo samples separately. In each range the diffractive fraction

$f(x,Q^2)$ is determined from a fit of the form

$$n(x,Q^2)\cdot\text{Data} = f(x,Q^2)\cdot\text{RAPGAP} + [1-f(x,Q^2)]\cdot\text{DJANGO} \tag{5.2}$$

where n is a normalization factor. The details of the procedure are described in section 7.2.

For the justification of this method, it is not necessary to claim that the whole business of dealing with diffractive events here has anything to do with diffraction. The prime objective is to obtain a good description of the hadronic final state, which could in principle be achieved by any mechanism that is able to produce the low M_X and low $\eta_{\max}$ hadronic final states missing in DJANGO.[5] Therefore, calling the above procedure a measurement of the fraction of diffractive events is avoided. Consequently, it is also not clear whether it would be appropriate to obtain $f(x,Q^2)$ from measurements or theoretical predictions about the fraction of diffractive events.

5.3.3 Preselection of events

Given that the geometrical acceptance of the BPC is below 15% even in that kinematic range where it is highest, it would be not very efficient to pass all the events generated by DJANGO and RAPGAP through the detector simulation managed by FUNNEL [124], the Monte Carlo production facility of ZEUS. Actually, about 80 million events have been generated, which would have blocked the entire FUNNEL system for one year.

Therefore, a preselection is applied before feeding the events into the detector simulation. The Z event vertex is sampled from an unbiased estimate of the true vertex distribution (section 7.4.2), X and Y are randomly chosen from gaussian distributions with widths of $\sigma_X = 330\,\mu\text{m}$ and $\sigma_Y = 90\,\mu\text{m}$. Using true vertex and angle of the outgoing electron, its impact position on the BPC front face is predicted (neglecting the magnetic field and multiple scattering). The event is accepted only if this position satisfies the conditions $4.4\,\text{cm} < X < 10.8\,\text{cm}$ and $-3.3\,\text{cm} < Y < 4.0\,\text{cm}$. These cuts on true variables are sufficiently far away from the fiducial area cuts that are applied later in the analysis on reconstructed variables. It was checked (using a small test sample) that none of the discarded events would have passed the final event selection cuts. In the end, only 2.5% of the generated events pass the preselection, which leaves about 2 million events to be fed into the detector simulation.

This sample of simulated events represents the basis for both the following detector studies and the subsequent measurement of the structure function F_2.

[5] For example, MEPS (including soft color interactions) can generate events at lower masses and lower $\eta_{\max}$ than ARIADNE (but still fails to describe the whole distribution of $\eta_{\max}$).

Chapter 6

Reconstruction

The key ingredient for a measurement of the structure function $F_2(x,Q^2)$ is the good reconstruction of the kinematic variables x, y and Q^2. In the experiment, these quantities are not directly measured; instead, they are derived from measured quantities of the final state particles as observed in the detector. The main focus is on the scattered electron, which is in principle sufficient to reconstruct the kinematic variables; however, in practice the applicability of this approach is limited to only a part of the kinematic plane. Information from the hadronic final state is needed in addition to the electron variables.

In the first part of this chapter, the algorithms used to reconstruct energy and angle of the scattered electron in BPC and BPT are discussed. The second part describes the reconstruction of the hadronic final state variables. The third part is dedicated to a discussion of the different reconstruction methods that can be used to derive the kinematics from the measured variables.

6.1 Reconstruction of BPC and BPT quantities

Although no major modifications were made to the BPC after the 1995 running, it was removed from ZEUS, taken apart, checked for radiation damage, rebuilt (with exchanged scintillators where necessary) and re-installed twice since then. Therefore, its 1995 energy calibration and position alignment could not be assumed to be still valid in 1997 and had to be determined again. In addition, the reconstruction algorithms that were developed in 1995 have been improved in order to make best use of the high-precision data from the BPT.

For the BPT, being a completely new detector, all operating parameters had to be determined for 1997, and new reconstruction techniques were developed and tested.

6.1.1 BPC energy reconstruction and calibration

The energy deposited in the BPC is calculated as the sum over all 15 X and 16 Y fingers. Usually, 3–5 fingers of each orientation exhibit a signal. Since there is no online calibration of the BPC, calibration factors for individual fingers have to be determined offline. In addition, transverse shower leakage at the low-X side of the BPC, light attenuation in the scintillator fingers and nonuniformities caused by the 0.1 mm gap between adjacent fingers have to be corrected for.

The 1995 calibration algorithm, as implemented in the BPC reconstruction package BPRECON [87], used the position reconstructed by the BPC as input for the energy reconstruction. This was improved for this analysis using instead the position provided by the BPT.[1]

Using a large sample of kinematic peak electrons,[2] the new BPC energy calibration is deter-

[1] There are indications that checks performed in 1995 might have given too optimistic results on the BPC uniformity, due to a conspiracy with the intrinsic bias of the BPC-based position reconstruction algorithm.

[2] A cut $y_{\text{JB}} < 0.04$ selects events for which the true energy of the scattered electron sharply peaks within 2% of the beam energy, providing a good calibration source (kinematic peak electrons). The complete list of selection cuts is given in appendix C.1.

mined from a fit of all relevant parameters using MINUIT. The calibrated energy is calculated in the following steps. A first estimate of the energy is obtained by

$$E_X^{(0)} = \sum_{i=1}^{15} c_X^i E_X^i \quad (6.1)$$

$$E_Y^{(0)} = \sum_{i=1}^{16} c_Y^i E_Y^i, \quad (6.2)$$

where c_X^i and c_Y^i are calibration constants for the BPC fingers. Then, corrections for leakage, attenuation and nonuniformity are applied:

$$E_X = \frac{E_X^{(0)}}{L_X(X) \cdot A_X(Y) \cdot N_X(X)} \quad (6.3)$$

$$E_Y = \frac{E_Y^{(0)}}{L_Y(X) \cdot A_Y(X) \cdot N_Y(Y)}. \quad (6.4)$$

The transverse leakage correction functions are parameterized as

$$L_X(X) = \int_{-\infty}^{l_X(X-l_X^0)} \frac{1}{\sqrt{2\pi}} \exp\left(-\frac{1}{2}t^2\right) dt \quad (6.5)$$

$$L_Y(X) = \int_{-\infty}^{l_Y(X-l_Y^0)} \frac{1}{\sqrt{2\pi}} \exp\left(-\frac{1}{2}t^2\right) dt, \quad (6.6)$$

and the attenuation correction functions are given by

$$A_Y(X) = \exp\left(\frac{X - X_R}{\lambda_Y}\right) \quad (6.7)$$

$$A_X(Y) = \exp\left(\frac{Y - Y_R}{\lambda_X}\right), \quad (6.8)$$

where X_R (Y_R) are the end points of the scintillator fingers in X (Y), where they are read out by wavelength shifters. Finally, the nonuniformity correction is parameterized as

$$N_X(X) = 1 - n \cdot |\mathrm{mod}(X - X_0, d) - d/2| \quad (6.9)$$

$$N_Y(Y) = 1 - n \cdot |\mathrm{mod}(Y - Y_0, d) - d/2|, \quad (6.10)$$

with X_0 (Y_0) denoting the lower edge of the active BPC volume in X (Y), and $d = 0.8\,\mathrm{cm}$ being the width of a BPC finger.

Only the calibration constants c_X^i and c_Y^i of fingers inside or close to the fiducial area can be determined (i.e. $i = 1 \ldots 8$ in X and $i = 4 \ldots 13$ in Y); the constants outside the area have negligible effects on the result and are fixed at the mean value of 1.0 (data) respectively 0.72 (MC). X is measured by the BPT, Y still has to be taken from the BPC.

The leakage correction functions are derived assuming a gaussian transverse shower profile (i.e. $l_X^0 = l_Y^0 = X_0$ would be expected as result of the fit), neglecting that real-life showers look rather like the sum of two gaussian distributions. Also the exponential attenuation correction is a simplification of the real situation, in which scintillation light can travel either the direct way to the wavelength shifter, or start to travel in the opposite direction and be reflected at the far end of the scintillator bar, in which case it travels a much longer way to the wavelength shifter; this would suggest an attenuation correction being the sum of two exponential functions rather than only one. However, it turns out that the combination of leakage and attenuation correction as used here is sufficiently flexible to describe both the leakage and the attenuation satisfactorily. The price to pay is that l_X^0 and l_Y^0 cannot be interpreted any more as the point in space where the leakage starts, and λ_X and λ_Y become effective attenuation lengths. The nonuniformity correction has a sawtooth-like shape, rising linearly from zero between fingers to n in the center of each finger.

The fit has 25 free parameters: $c_X^1 \ldots c_X^8$, $c_Y^4 \ldots c_Y^{13}$, l_X^0, l_X, l_Y^0, l_Y, λ_X, λ_Y, n. The χ^2 to be minimized is defined as

$$\chi^2 = \frac{1}{2}\left(\frac{E_X\,[\mathrm{GeV}] - 13.75}{0.18 \cdot \sqrt{13.75}}\right)^2 + \frac{1}{2}\left(\frac{E_Y\,[\mathrm{GeV}] - 13.75}{0.18 \cdot \sqrt{13.75}}\right)^2 + \left(\frac{E_X + E_Y\,[\mathrm{GeV}] - 27.5}{0.18 \cdot \sqrt{27.5}}\right)^2. \quad (6.11)$$

It consists of three terms in order to ensure that the energy in X and Y fingers separately as well as their sum yields the expected values. MC studies show that the energy in X and Y fingers should be equal on average. The energy resolution is tentatively assumed to be $\sigma(E)/E = 18\%\sqrt{E\,[\mathrm{GeV}]}$, and the weight of the separate energy measurements is chosen to be half of that of their sum.

The procedure is applied to both data and MC. The resulting parameters are listed in Table 6.1 and illustrated in Fig. 6.1.

Data

no.	name	unit	value	error
1	c_X^1		1.0760	0.0074
2	c_X^2		1.0629	0.0012
3	c_X^3		1.0806	0.0008
4	c_X^4		1.0647	0.0008
5	c_X^5		1.0943	0.0009
6	c_X^6		1.0441	0.0010
7	c_X^7		1.0650	0.0020
8	c_X^8		0.9264	0.0056
9	c_Y^4		0.8355	0.0211
10	c_Y^5		1.0211	0.0037
11	c_Y^6		0.8853	0.0018
12	c_Y^7		0.7608	0.0014
13	c_Y^8		0.8930	0.0017
14	c_Y^9		1.0194	0.0019
15	c_Y^{10}		1.0615	0.0020
16	c_Y^{11}		1.0112	0.0020
17	c_Y^{12}		0.9643	0.0026
18	c_Y^{13}		0.8600	0.0109
19	l_X^0	(cm)	4.52	0.01
20	l_X	(cm^{-1})	2.38	0.03
21	l_Y^0	(cm)	2.85	0.02
22	l_Y	(cm^{-1})	0.61	0.01
23	λ_X	(cm)	94.58	0.75
24	λ_Y	(cm)	81.18	1.48
25	n		0.0405	0.0007

Monte Carlo

no.	name	unit	value	error
1	c_X^1		0.7709	0.0023
2	c_X^2		0.7597	0.0007
3	c_X^3		0.7485	0.0005
4	c_X^4		0.7423	0.0005
5	c_X^5		0.7388	0.0006
6	c_X^6		0.7395	0.0007
7	c_X^7		0.7397	0.0010
8	c_X^8		0.7459	0.0034
9	c_Y^4		0.5462	0.0158
10	c_Y^5		0.7406	0.0020
11	c_Y^6		0.7244	0.0015
12	c_Y^7		0.7210	0.0015
13	c_Y^8		0.7208	0.0014
14	c_Y^9		0.7207	0.0014
15	c_Y^{10}		0.7201	0.0014
16	c_Y^{11}		0.7201	0.0015
17	c_Y^{12}		0.7228	0.0018
18	c_Y^{13}		0.7931	0.0097
19	l_X^0	(cm)	3.77	0.03
20	l_X	(cm^{-1})	1.35	0.04
21	l_Y^0	(cm)	3.39	0.02
22	l_Y	(cm^{-1})	0.88	0.01
23	λ_X	(cm)	71.81	0.43
24	λ_Y	(cm)	58.18	0.79
25	n		−0.0146	0.0007

Table 6.1: Energy calibration parameters determined for data (left) and Monte Carlo (right) from a global fit using MINUIT.

One possible means of checking the quality of the method and the fit result are the finger calibration constants for MC. They are in good approximation uniform, as expected due to the absence of calibration differences between individual fingers in the simulation. This is a nontrivial result, because one could imagine wrong fit results for the calibration constants to be absorbable into the leakage and attenuation correction.

The best fit yields $\chi^2/\mathrm{ndf} = 4.0$ (data) and $\chi^2/\mathrm{ndf} = 4.2$ (MC). From the above definition, one would expect a value of χ^2/ndf slightly below 2 (due to the correlation between E_X, E_Y

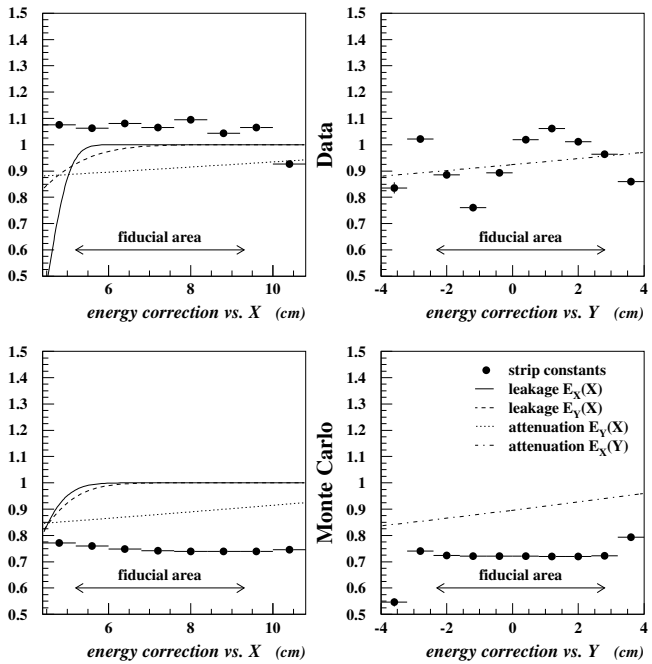

Fig. 6.1: Illustration of the calibration constants and of the position-dependent correction functions that are used in the energy reconstruction algorithm as a result of the calibration procedure. The fluctuations of c_Y^i in data are larger than expected; the calibration performed before the beginning of data taking is assumed to be good to about 10%.

and $(E_X + E_Y)$), if the assumed resolution of $\sigma(E)/E = 18\%\sqrt{E\,[\mathrm{GeV}]}$ were correct. However, this ignores that for events selected by $y_{\mathrm{JB}} < 0.04$ the true electron energy is not identical to 27.5 GeV, but has a spread due to the nonzero value of y and due to radiative corrections.

The uniformity (i.e. position-independence) of the mean BPC energy response is found to be good to 0.3% (Fig. 6.2). As a check, the uniformity was also checked for subsamples of data and MC (which will be called the "low-y" and "low-y prescaled" samples later in the analysis). For both of them, the uniformity was as well found to be good within 0.3%.

Comparing data and MC in the "low-y" and "low-y prescaled" samples, it is found that also the absolute energy scales of data and MC agree to 0.3% (Figs. 6.3 and 6.4). The energy resolution in data is slightly better (!) than in MC; therefore the measured energy in data is smeared to match that of the MC.[3]

A comparison of the mean reconstructed to the mean true energy in MC shows that the absolute scale determined this way is too high by about 2.3% (by construction, since the fit

[3]Of course, it would have been more appropriate to modify the MC such that the resolution matches that of the data; however, since there is no reliably unbiased "unsmearing" algorithm, this would have meant to make potentially very complicated changes to the MOZART code of the BPC, and it would have meant to rerun the detector simulation over all the events for the analysis. Given that the mismatch in resolution is small, the simpler way chosen here appears to be justified. The smearing is done by multiplying the reconstructed energy with a random number sampled from a gaussian distribution around 1 with $\sigma = 0.0144$.

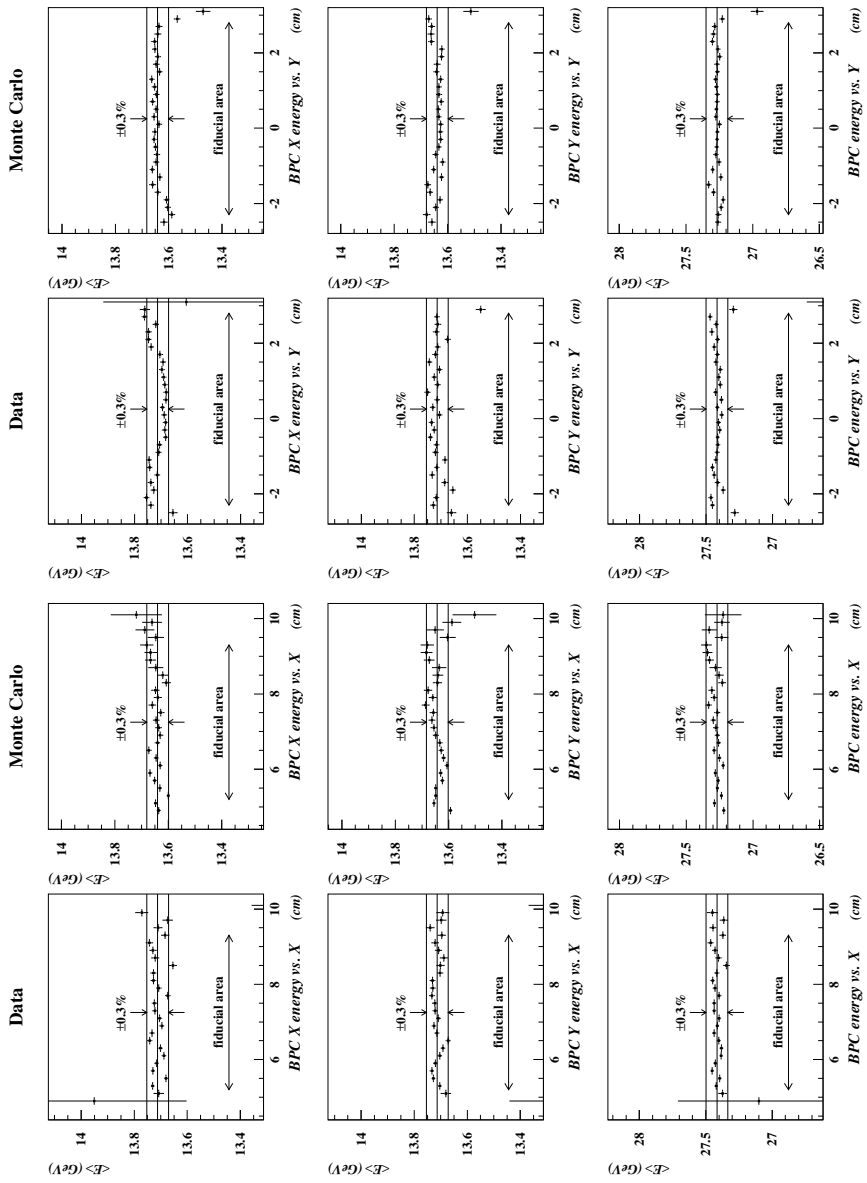

Fig. 6.2: The mean energy response as a function of horizontal and vertical position after the calibration, for data and MC. Uniformity has been achieved at the level of ±0.3% for both the energies in X and Y fingers separately as well as for the sum of the two. The correction of the scale by 2.3% has not been applied yet.

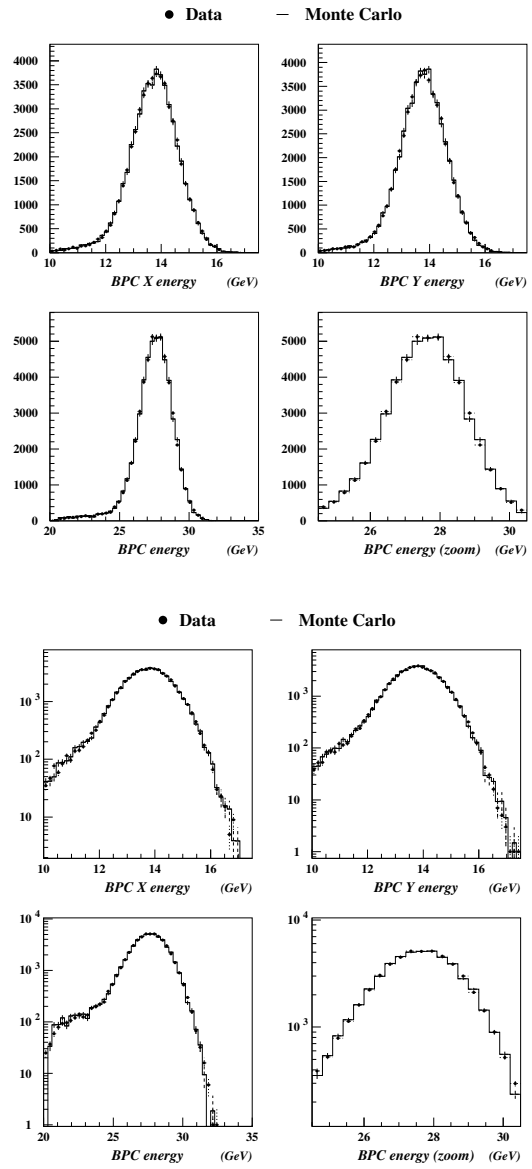

Fig. 6.3: Low-y sample. Energy scale and resolution, compared between data and MC. The agreement in the scale is better than 0.3%, while reasonable agreement in the resolution has been achieved by artificially smearing the energy reconstructed in the data. The correction of the scale by 2.3% has not been applied yet.

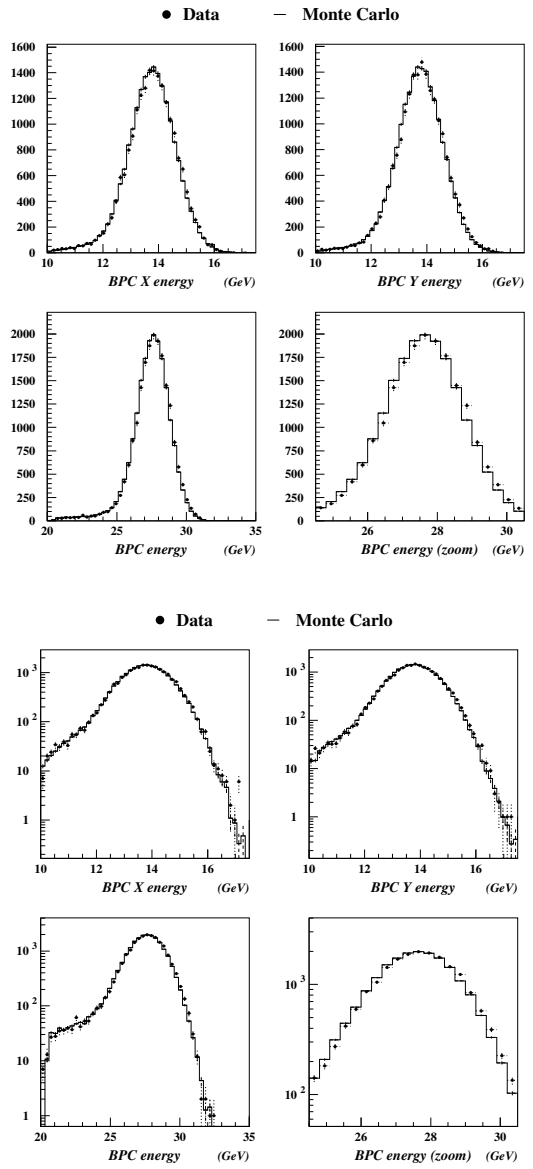

Fig. 6.4: Low-y prescaled sample. Energy scale and resolution, compared between data and MC. The agreement in the scale is better than 0.3%, while reasonable agreement in the resolution has been achieved by artificially smearing the energy reconstructed in the data. The correction of the scale by 2.3% has not been applied yet.

procedure forced the reconstructed kinematic peak energy to be 27.5 GeV). Therefore data and MC are corrected back to the correct scale. It should be noted that this has no net effect on the measurement of F_2, because the unfolding procedure takes a shifted energy scale properly into account if the shift is simulated in the MC (at least for small shifts up to a few percent). Therefore, the important point is to have the same energy scale in data and MC, not to have the correct one.

A long-scale time dependence of the mean reconstructed BPC energy of the order of $-160\,\mathrm{MeV/month}$ for kinematic peak energies is observed, corresponding to a shift of about 1% between beginning and end of the BPT data taking. The effect is attributed to radiation damage of the scintillators. It is corrected for by a run-number dependent linear function, and the fit is repeated. As a check, the data sample was divided in two halves and the fit was run separately for them. The only parameter that changed significantly was the calibration constant for the first X finger, c_X^1 (by 2%). This was expected since radiation damage is known to affect predominantly the low X edge of the BPC. Still, this variation was small enough to justify the use of only one set of calibration constants (plus the linear correction for time dependence) throughout the whole BPT running period.

Having fixed the BPC energy scale at the kinematic peak energy, it has to be checked if the assumed linear correlation between the signal and the electron energy is given over the whole energy range. A possible nonlinearity of the BPC energy response has been explored in [125], using an EGS4 [126] simulation of the BPC together with the results of a Co^{60} scan of the BPC after the data taking. The nonlinearity was found to be less than 1% at 4 GeV, and is assumed to decrease linearly toward 27.5 GeV.

Concluding, a few points should be addressed why this procedure is believed to be superior to what was done in the 1995 analysis: firstly, also events falling outside the fiducial area by a few mm are included in the calibration procedure. This results in a calibration that is stable in the vicinity of the fiducial area boundaries. Secondly, when comparing data and MC below a certain y_{JB}, it has been ignored in past analyses that the samples did not agree in normalization, since events below certain thresholds of W or y are not simulated in the MC. This mismatch has been avoided here by choosing a region in y where data and MC are found to be in good agreement ($0.005 < y_{\mathrm{JB}} < 0.04$). Finally, when checking the success of a tuning procedure, it has to be done using a statistically independent event sample. This was attempted here by using two "very different" subsamples of the sample used for the tuning (they differ in number of events and distribution over X and Y of the BPC).

6.1.2 BPC position reconstruction

Although the BPT provides a very precise and unbiased X position reconstruction of the scattered electron, it is still necessary to also calculate its position from the BPC. This is needed for track matching, and, of course, because the BPT cannot measure Y in its 1997 configuration.

Since there is no longitudinal segmentation of the BPC readout, the longitudinal position of the center of gravity of the shower can only be derived on average from the measured energy:

$$Z = Z_{\mathrm{BPC}} - 0.7\left[\log_{10}\left(\frac{E\,[\mathrm{MeV}]}{10.6}\right) - 0.5\right]\ \mathrm{cm} \tag{6.12}$$

($Z_{\mathrm{BPC}} = -293.7\,\mathrm{cm}$ denotes the position of the BPC front face in Z).

In 1995, the transverse position in the BPC was reconstructed using a logarithmically weighted average [101, 107]. The dependence of the resolution of this method on the energy in the BPC can be approximated by $\Delta X = 0.33\,\mathrm{cm}/\sqrt{E\,[\mathrm{GeV}]}$ (there are, however, deviations from this form both at high and low energies). The one free parameter in the reconstruction method was chosen to be the same for data and MC. Knowing that the shower behavior is not perfectly simulated in the BPC simulation, this procedure is expected to cause systematic differences between data and MC.

The new position reconstruction in the BPC uses a method inspired by ELECPO [5–7], the position reconstruction routine for the CAL. The following description applies to X fingers, although it works exactly the same way for Y fingers (or would work, if the BPT had Y planes).

In the first step, an imbalance function is defined using three fingers: the one with the highest energy deposit, and its two neighbors. The energy deposits in these are denoted by E_2, E_1 and E_3, respectively. They are calibrated with the finger calibration constants, but the position-dependent corrections are not applied. The imbalance is then defined as

$$\mathrm{imbal} = \frac{p_1(E_3 - E_1) + p_2E_2}{p_3E_2 - p_4(E_3 + E_1)}\,, \tag{6.13}$$

where $p_1 \ldots p_4$ are parameters to be optimized later. In a second step, the imbalance is converted into a position relative to the center of the most energetic finger:

$$\Delta X = 0.4\,\mathrm{cm} \cdot \frac{\arctan(p_5 \cdot \mathrm{imbal})}{\arctan(p_5)} - p_6. \tag{6.14}$$

The parameter p_5 determines the shape of the conversion function, while p_6 takes into account a possible misalignment of the BPT relative to the BPC at the stage of optimizing this algorithm. Later, for position reconstruction and alignment of BPC and BPT, p_6 is set to zero.

Using electrons in a broad energy range,[4] the parameters $p_2 \ldots p_6$ (with p_1 fixed at 1, without loss of generality) are determined from a global fit using MINUIT. The fit is performed for data and MC separately. The χ^2 to be minimized is defined as

$$\chi^2 = \left(\frac{X_{\mathrm{BPC}} - X_{\mathrm{BPT}}}{0.22\,\mathrm{cm}/\sqrt{E\,[\mathrm{GeV}]}}\right)^2. \tag{6.15}$$

Though the need for it may be not a priori obvious, it turns out that p_2 is a necessary parameter in order to obtain a symmetric distribution of $\Delta X = X_{\mathrm{BPC}} - X_{\mathrm{BPT}}$. The complete list of parameters is given in Table 6.2. The obtained value of $\chi^2/\mathrm{ndf} = 1.1$ is the same for data and MC.

Data

no.	name	value
1	p_1	1
2	p_2	−0.02
3	p_3	−2.02
4	p_4	3.24
5	p_5	10.18

Monte Carlo

no.	name	value
1	p_1	1
2	p_2	−0.02
3	p_3	−2.52
4	p_4	4.08
5	p_5	17.72

Table 6.2: Position reconstruction parameters determined for data (left) and Monte Carlo (right) from a global fit using MINUIT.

The same parameters as for the X reconstruction are also used for the Y reconstruction. This is mainly due to a lack of alternatives; on the other hand, there is no good reason to assume that the parameter sets should be very different. Figure 6.5 shows that the position reconstruction works indeed well in both coordinates. The (nearly) complete absence of structures of the size of a BPC finger (0.8 cm) indicates the quality of the position reconstruction algorithm.

The energy dependence of the position resolution can on average be described by $\Delta X = 0.22\,\mathrm{cm}/\sqrt{E\,[\mathrm{GeV}]}$ (Fig. 6.6), which is better by a factor 1.5 than the resolution of the old algorithm.

Another advantage of this reconstruction method is that it is possible to compare all features between data and MC. The position-dependence of the bias is found to follow a sinusoidal shape

[4] The complete list of selection cuts is given in appendix C.2.

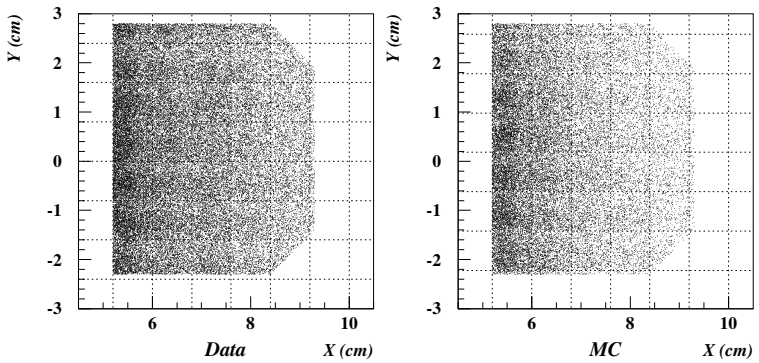

Fig. 6.5: Reconstructed position of scattered electrons in the BPC for data (left) and MC (right).

with zeroes between fingers and in their center and amplitudes of $\pm 300\,\mu m$ in between. The position resolution improves with energy. It is best close to the finger edges and worsens toward the finger centers, varying by about a factor of two (Fig. 6.7). The shower widths, σ_X and σ_Y, are calculated as the second moments of the logarithmic energy weighted sum in the BPC fingers.

6.1.3 BPT track reconstruction and alignment

At the beginning of BPT data taking, the reconstruction package BPTRECON [88] existed already, and it was expected that it would only have to be adapted to the (unexpected) situation of having two instead of five planes, and to the beforehand unknown alignment parameters [8, 127, 128]. Unfortunately, it turned out that BPTRECON is (at least for the situation of having only two X planes, and for the purpose of determining alignment parameters) more complicated and less flexible than necessary.[5]

Therefore, for this analysis the simplest possible track reconstruction algorithm was used: the 2-dimensional projection of a track in the X-Z plane is taken to be the straight line joining two hits in the BPT. If there is more than one hit in a BPT plane, the combination which fits best with the shower position in the BPC and with an assumed event vertex at the nominal interaction point is chosen. It has been checked [8] that the influence of the magnetic field, which is neglected in this method, is very small (Fig. 6.8). Anyway it should be simulated (at least to some extent) in MOZART, and therefore possible systematic effects due to neglecting it are simulated in the MC and have thus no net effect on the F_2 analysis.

Having reconstructed the BPT track, it can easily be extrapolated to the Z position of the front face of the BPC, the center of gravity in Z of the shower inside the BPC, and the mean X vertex of the run. The latter point of extrapolation provides the BPT-measured vertex in Z, while the former are used to apply the fiducial area and track matching cuts in the analysis. An example of a reconstructed event with an electron in the BPC and BPT is shown in Fig. 6.9.

Using a large sample of medium to high energy electrons[6] with a gold-plated hit pattern in the BPT (one hit per plane) and a well-reconstructed CTD vertex (from at least three tracks

[5] It was also found (although never investigated in detail) that BPTRECON gives a slightly worse (!) resolution and bias of reconstructed electron angle and event vertex than the simple straight-line reconstruction, even for MC where one would not expect to see effects related to possibly wrong alignment parameters.

[6] The complete list of selection cuts is given in appendix C.3.

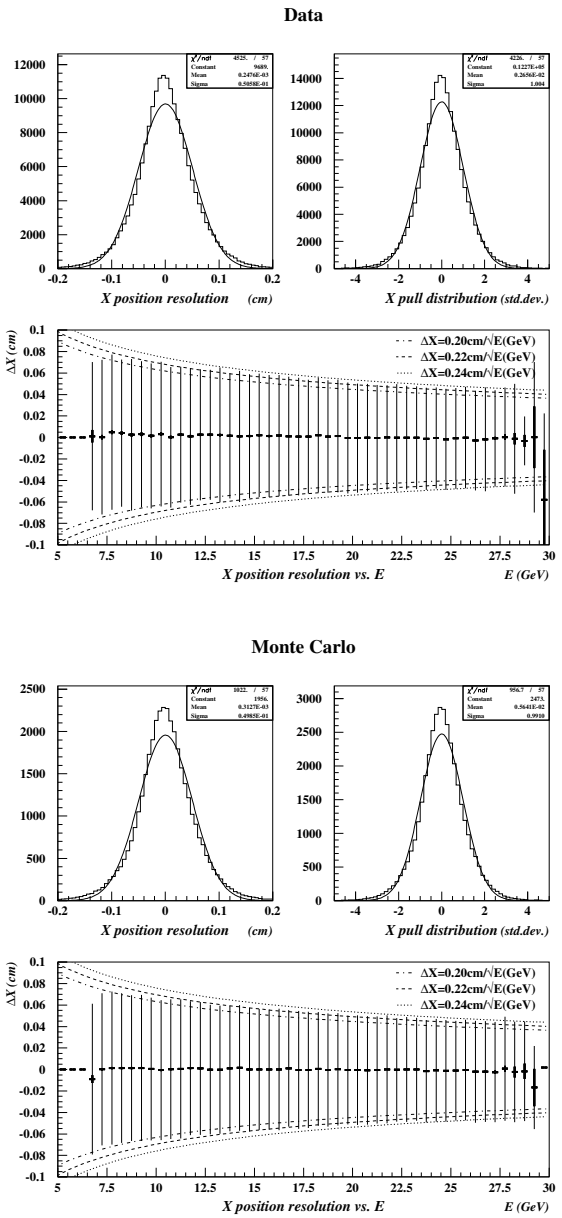

Fig. 6.6: Resolution $X_{\mathrm{BPC}} - X_{\mathrm{BPT}}$, pull $(X_{\mathrm{BPC}} - X_{\mathrm{BPT}})/(0.22\,\mathrm{cm}/\sqrt{E\,[\mathrm{GeV}]})$ and energy dependence of the resolution for data (top) and Monte Carlo (bottom).

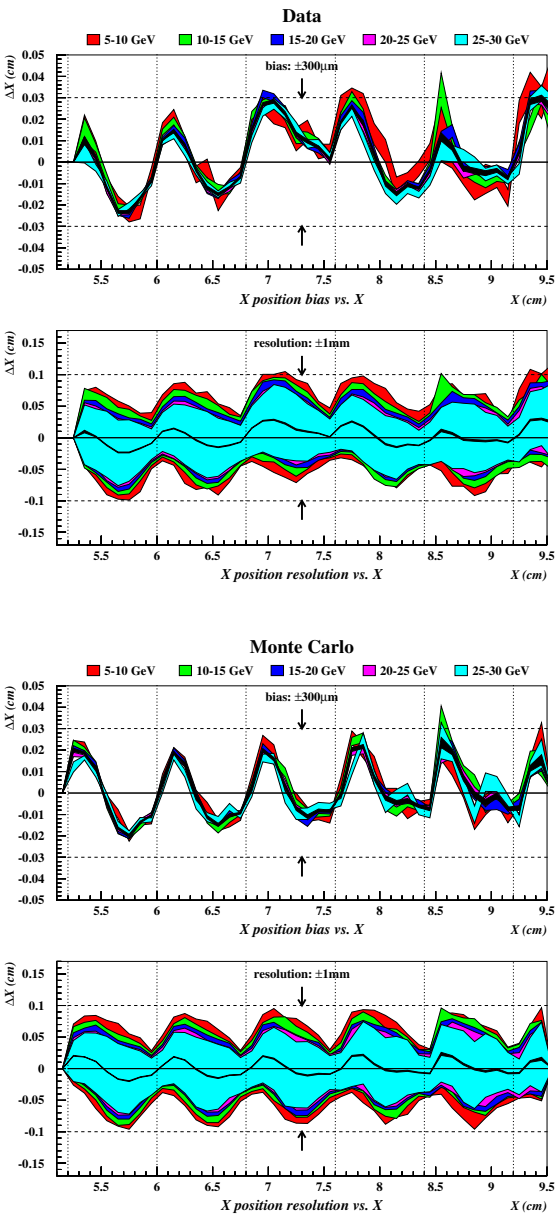

Fig. 6.7: Energy and position dependence of bias and resolution of the position reconstruction for data (top) and Monte Carlo (bottom).

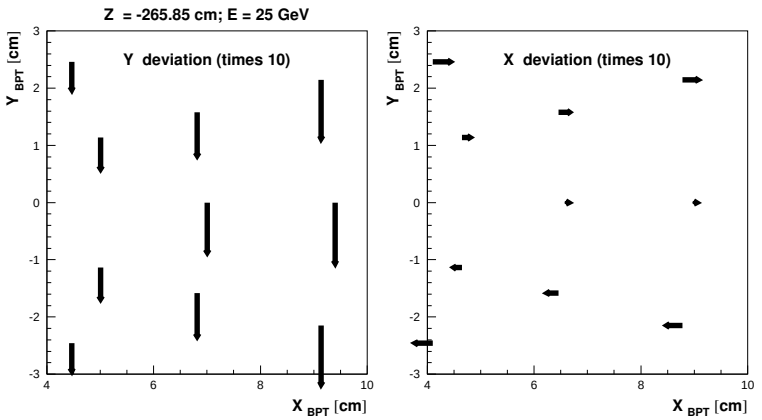

Fig. 6.8: The effect of the magnetic field on the impact point of a 25 GeV electron on the (nonexisting) BPT plane X2. Shown are the deviations in Y (left) and X (right) from the trajectory without magnetic field, scaled by a factor of ten.

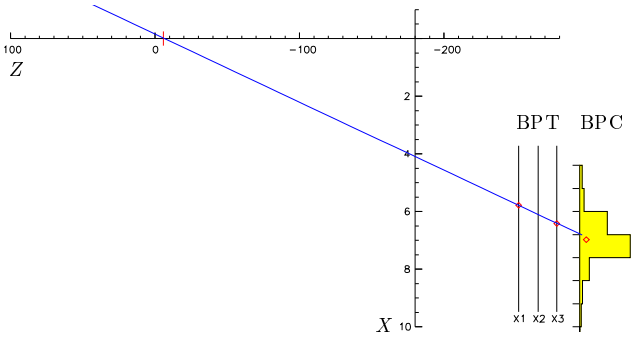

Fig. 6.9: Reconstructed track in a real BPC/BPT event (projection into the X-Z plane). The BPT track joining the hits in X1 and X3 extrapolates nicely to the center of gravity of the energy deposits in the BPC and to the vertex measured by the CTD.

and with a good χ^2), the determination of the alignment of BPT and BPC with respect to the ZEUS coordinate system (which is defined by the CTD) is performed as a fit of the alignment parameters using MINUIT.

The idea of the alignment procedure is to compare on an event-by-event basis the vertex reconstructed by the CTD to that from the BPT. In case of a misalignment of the planes relative to each other or to the CTD, one observes a systematic deviation, which is exploited by the χ^2 minimization. The simultaneous alignment of the BPC is needed due to the missing Y planes in the BPT, because possible rotations of the BPT planes around the Z axis cannot be recognized without an independent Y measurement.

The relevant alignment parameters are: shifts of the planes in X (ΔX_1, ΔX_3), rotations

of the planes around the Z axis ($\Delta\phi_1$, $\Delta\phi_3$), shift of the BPC in X ($\Delta X_{\rm BPC}$). Since it was found that the CTD moved in an access during the BPT data taking period (September 16, 1997, around run #27500), the shift of the CTD between the times before and after the access is introduced as a sixth parameter: $\Delta X_{\rm CTD}$.[7] The fit parameters are defined as deviations from the Monte Carlo values, i.e. they are zero for MC. All Y and Z parameters are taken from the survey for data, and fixed at the known true values in MC. The tilts of the BPT planes around the X and Y axes are set to zero. The alignment procedure as well as the analysis are fairly insensitive to their values.

Relative distances and rotations can be determined with much higher precision than absolute ones, therefore the set of fit parameters actually used in the fit is ΔX_1, $\Delta X_3 - \Delta X_1$, $\Delta\phi_1$, $\Delta\phi_3 - \Delta\phi_1$, $\Delta X_{\rm BPC}$, $\Delta X_{\rm CTD}$. The χ^2 to be minimized is defined as

$$\chi^2 = \sum_{j=1}^{n}\sum_{i=1}^{2} \frac{(X_i - c_j - m_j Z_i)^2}{\sigma_{c_j}^2 + \sigma_{X_i}^2 + Z_i^2\sigma_{m_j}^2 + m_j^2\sigma_{Z_i}^2 + 2Z_i\mathrm{cov}(c_j, m_j) - 2m_j\mathrm{cov}(X_i, Z_i)}, \qquad (6.16)$$

where c_j and m_j are intercept and slope of the reconstructed BPT track in event j for a certain combination of alignment parameters, the first sum runs over all n events and the second sum over the CTD-measured ($i = 1$) and BPC-measured ($i = 2$) points (X_i, Z_i) on the BPT track.

Events whose individual contribution to χ^2 is greater than 20 are rejected, in order to become insensitive to the tails of the χ^2 distribution. Such events are mostly misreconstructed, e.g. because the real hit of the electron was not recorded due to an inefficient BPT strip, and a noise hit picked instead (section 6.1.4).

Six fits are made altogether: data before the access, data after the access, all data with the CTD shift as additional free parameter, all Monte Carlo events, first half of the Monte Carlo sample, second half of the Monte Carlo sample. For these fits, the results are given in Table 6.3.

Data

no.	name	unit	value	error
1	ΔX_1	(μm)	−295	87
2	$\Delta X_3 - \Delta X_1$	(μm)	711	9
3	$\Delta X_{\rm BPC}$	(μm)	−186	103
4	$\Delta\phi_1$	(mrad)	−1.93	0.26
5	$\Delta\phi_3 - \Delta\phi_1$	(mrad)	13.15	0.06
1	ΔX_1	(μm)	−14	50
2	$\Delta X_3 - \Delta X_1$	(μm)	713	5
3	$\Delta X_{\rm BPC}$	(μm)	106	59
4	$\Delta\phi_1$	(mrad)	−2.04	0.17
5	$\Delta\phi_3 - \Delta\phi_1$	(mrad)	13.25	0.04
1	ΔX_1	(μm)	−11	43
2	$\Delta X_3 - \Delta X_1$	(μm)	713	4
3	$\Delta X_{\rm BPC}$	(μm)	107	51
4	$\Delta\phi_1$	(mrad)	−2.01	0.14
5	$\Delta\phi_3 - \Delta\phi_1$	(mrad)	13.22	0.03
6	$\Delta X_{\rm CTD}$	(μm)	259	8

Monte Carlo

no.	name	unit	value	error
1	ΔX_1	(μm)	−8	36
2	$\Delta X_3 - \Delta X_1$	(μm)	−1	3
3	$\Delta X_{\rm BPC}$	(μm)	180	43
4	$\Delta\phi_1$	(mrad)	−0.01	0.13
5	$\Delta\phi_3 - \Delta\phi_1$	(mrad)	−0.23	0.03
1	ΔX_1	(μm)	−44	49
2	$\Delta X_3 - \Delta X_1$	(μm)	−5	5
3	$\Delta X_{\rm BPC}$	(μm)	134	59
4	$\Delta\phi_1$	(mrad)	−0.03	0.18
5	$\Delta\phi_3 - \Delta\phi_1$	(mrad)	−0.23	0.04
1	ΔX_1	(μm)	36	54
2	$\Delta X_3 - \Delta X_1$	(μm)	4	5
3	$\Delta X_{\rm BPC}$	(μm)	236	65
4	$\Delta\phi_1$	(mrad)	0.02	0.20
5	$\Delta\phi_3 - \Delta\phi_1$	(mrad)	−0.24	0.04

Table 6.3: Alignment parameters as determined for different combinations of data (left) and MC (right) samples. From top to bottom: data: before the access, after the access, combined with the CTD shift as additional free parameter. MC: all events, first half of the sample, second half of the sample.

The third fit, all data with the CTD shift as additional free parameter, is chosen as the BPT alignment in this analysis. The χ^2/ndf of the fit is 2.2 (data) respectively 2.3 (MC). From the definition of χ^2 one expects a value of 2, neglecting that events with a very high contribution to χ^2 have been excluded.

[7] As the CTD defines the ZEUS coordinate system, by definition it cannot move. $\Delta X_{\rm CTD}$ is therefore taken to be a virtual shift of BPC and BPT after the access.

The check of the alignment procedure in the MC simulation yields the expected results, i.e. the alignment parameters are zero within their statistical errors. The only exception is the relative rotation of the two planes which comes out to be nonzero (also $X_{\rm BPC}$ is nonzero; this, however, is an artefact (or a feature) of the intrinsic bias of the BPC position reconstruction algorithm and not really an information about the BPC detector position). The nonzero relative rotation of the planes is assumed to be an (and probably the only visible) effect of neglecting the magnetic field in the track reconstruction. By dividing the MC sample in two halves, it is checked that also the statistical errors given by MINUIT are reasonable.

These checks indicate that the alignment procedure produces reliable results. Several systematic studies were performed to investigate the stability of the results. The largest contribution to the systematic error comes from the uncertainty in the relative distance of the BPT planes, which is taken from the survey of BPC and BPT to be ±300 μm. The resulting total systematic uncertainty of the absolute BPC and BPT X positions is less than ±200 μm (compared to ±500 μm in 1995 for the BPC).

6.1.3.1 Beam tilt

The beam tilt is the inclination of the electron beam with respect to the Z axis of the ZEUS coordinate system. It is measured using the LUMI-γ detector, where impact positions of collinearly radiated photons, mainly from bremsstrahlung events, are averaged run-wise. The beam tilt in the X-Z plane is then determined as $\theta_{X,\rm beam} = \langle X\rangle / Z_{\rm LUMI-\gamma}$ (the tilt in the Y-Z plane and its contribution to θ are neglected).

The coordinate system chosen in the LUMI reconstruction routines for giving X in the LUMI-γ detector is not the ZEUS coordinate system [129]. Instead, it is the nominal proton orbit frame,[8] which is tilted by 0.405 mrad with respect to the ZEUS coordinate system (and shifted by about 500 μm, which is neglected here). So, the correct electron scattering angle θ_X reconstructed using BPC or BPT is $\theta_X = \theta_{X,\rm BPC/BPT} - \theta_{X,\rm beam} + 0.405\,\mathrm{mrad}$.

6.1.4 BPT efficiency determination

There are two possible sources of BPT inefficiency: dead strips and signals below charge thresholds. The latter effect is possibly nonnegligible, as for the 1997 data taking unexpectedly high thresholds (significantly higher than the foreseen 1.5 fC) had to be chosen in order to reach a reasonable noise suppression. The reason for this is unclear, since such behavior had not been observed at the BPT test setup in the laboratory before.

Dead strips are identified in a "wire map" (Fig. 6.10), a histogram of the frequency distribution with which BPT strips recorded hits in BPC-triggered events. The distribution should be smooth for a fully efficient BPT. Dead strips exhibit no (or very few) entries; noisy strips have a much higher rate than their neighbors.

Those strips that were identified as dead strips in data are masked out in MC events before running the track reconstruction routine. The results of the alignment are taken into account, i.e. strips are masked according to their position in ZEUS, rather than according to their position on the silicon detector. Some dead strips in data have one or two neighbors with higher-than-expected rates. It is believed that either by capacitive coupling of the strips, or by cross talk effects at the damaged bonding, the neighboring strip(s) signal(s) the hits in the dead strip, thereby compensating fully or partly for its inefficiency. Such not-really-dead strips are not masked in the MC, and no attempt is made to simulate them. No special treatment for noisy strips is applied for the analysis, but they are masked out in data and MC for the purpose of the following overall efficiency determination.

[8] Which, needless to say, has nothing to do with the real proton orbit.

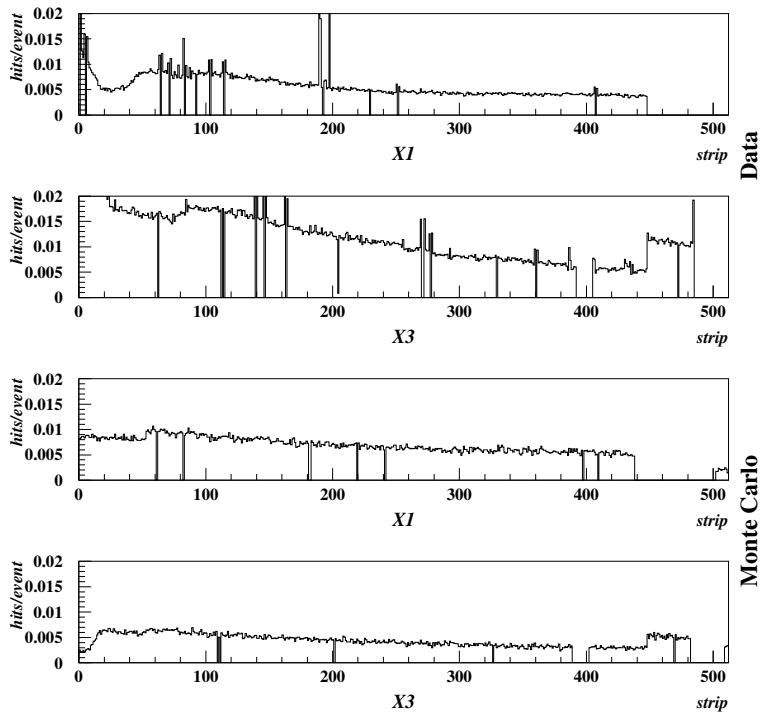

Fig. 6.10: Histogram of BPT strips that recorded hits in BPC-triggered events ("wire map"). No further event selection has been applied. High strip numbers correspond to high X, and above strip #448 starts the region of strips read out in pairs (the corresponding readout chip in X1 is not working). Top: data; bottom: Monte Carlo. Dead strips exhibit no (or very few) entries; noisy strips have a much higher rate than their neighbors. In MC, dead strips have already been implemented. The higher rate in X3 is not fully understood; it might be due to background events.

It is assumed that by masking dead strips all relevant position-dependent effects affecting the efficiency are removed (i.e. simulated correctly in the MC). What remains are overall effects that might be caused by the high threshold settings mentioned above.

The overall efficiency is measured using the CTD vertex and the BPC position of scattered electrons.[9] A hit that is reasonably close to the straight line CTD-BPC (distance less than $2\Delta X_{\rm cut}$, where $\Delta X_{\rm cut}$ is a variable parameter) is searched in each of the BPT planes. If such a hit is found in plane X1, a refined prediction is made for plane X3 using the CTD vertex and the hit in plane X1. Plane X3 is counted as efficient if a hit is found within $\Delta X_{\rm cut}$, and inefficient otherwise. If, because no hit was found in plane X1, there was no refined prediction at all for X3, the event does not count for plane X3. This takes into account that also neutral particles can fake an electron signal in the BPC. In such events one would not want to claim the BPT to be inefficient. Therefore, a hit in one plane is implicitly used as a trigger for expecting a signal

[9]The complete list of selection cuts is given in appendix C.4.

in the other plane. The same algorithm is performed with the roles of X1 and X3 exchanged.

In the same procedure, also the noise in the BPT can be measured, simply by counting all hits outside the search range in the efficiency determination as unexpected hits, and therefore defined as hits produced by noise. As a result of this study, a small number of randomly distributed artificial noise hits (0.15 hits per plane and event on average, sampled from a poisson distribution) is added to the hits recorded in the MC before the track reconstruction.

The results are shown in Fig. 6.12. The artificial noise has already been added. $\Delta X_{\rm cut}$ is at its nominal value in this study (500 µm). For the noise distribution, one would expect a triangular shape (plotted is essentially the difference of two random numbers, if the noise is not correlated to the passage of the electron). Comparing the efficiency results for data and MC, the difference in the measured efficiency between data and MC of plane X3 is higher than that of X1. This is consistent with the fact that the threshold for X3 was chosen to be higher than that for X1. Simulated events are weighted by a factor $\epsilon_{\rm Data}/\epsilon_{\rm MC}$, where $\epsilon = \epsilon_{\rm X1} \cdot \epsilon_{\rm X3}$, in order to account for the different overall efficiency in data and MC.

It has been checked that the result for $\epsilon_{\rm Data}/\epsilon_{\rm MC}$ is independent of the choice of $\Delta X_{\rm cut}$. Figure 6.11a shows the efficiency correction factor $\epsilon_{\rm Data}/\epsilon_{\rm MC}$ as a function of $\Delta X_{\rm cut}$. It becomes stable for $\Delta X_{\rm cut} > 200$ µm, i.e. twice the strip pitch, or about $3-4\sigma$ of the width of the residuals. This proves that the tails of the residuals are very well described by the MC.

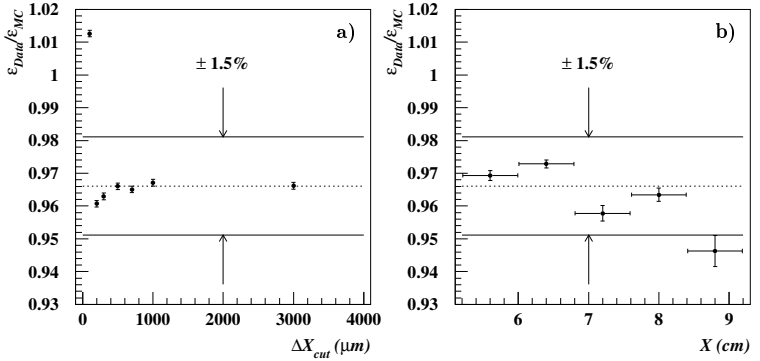

Fig. 6.11: Systematic checks of the efficiency determination procedure. a) Efficiency correction factor $\epsilon_{\rm Data}/\epsilon_{\rm MC}$ vs. $\Delta X_{\rm cut}$. b) Efficiency correction factor vs. BPC X position.

The assumption that one overall correction factor is sufficient to bring the efficiency in data and MC into agreement has also been checked. Figure 6.11b shows the correction factor as a function of the X position as measured by the BPC. Within their errors, the results in all bins agree to ±1.5%. For the bin at the highest X, the efficiency of X3 is very low (≈ 75%) due to a large cluster of dead strips. As systematic uncertainty, an error of ±1.5% is assigned to each measured F_2 bin individually, rather than adding it to the overall normalization error. This takes into account possible remaining position-dependent efficiency variations.

6.2 Reconstruction of hadronic final state quantities

For global variables of the hadronic final state, one sums over all final state particles. In an experiment like ZEUS, where not all particles can be observed, and where no particle identification is performed, "particles" has to be replaced by a suitable definition of "reconstructed objects". The CTD and the CAL are the detectors used to detect the hadronic final state particles.

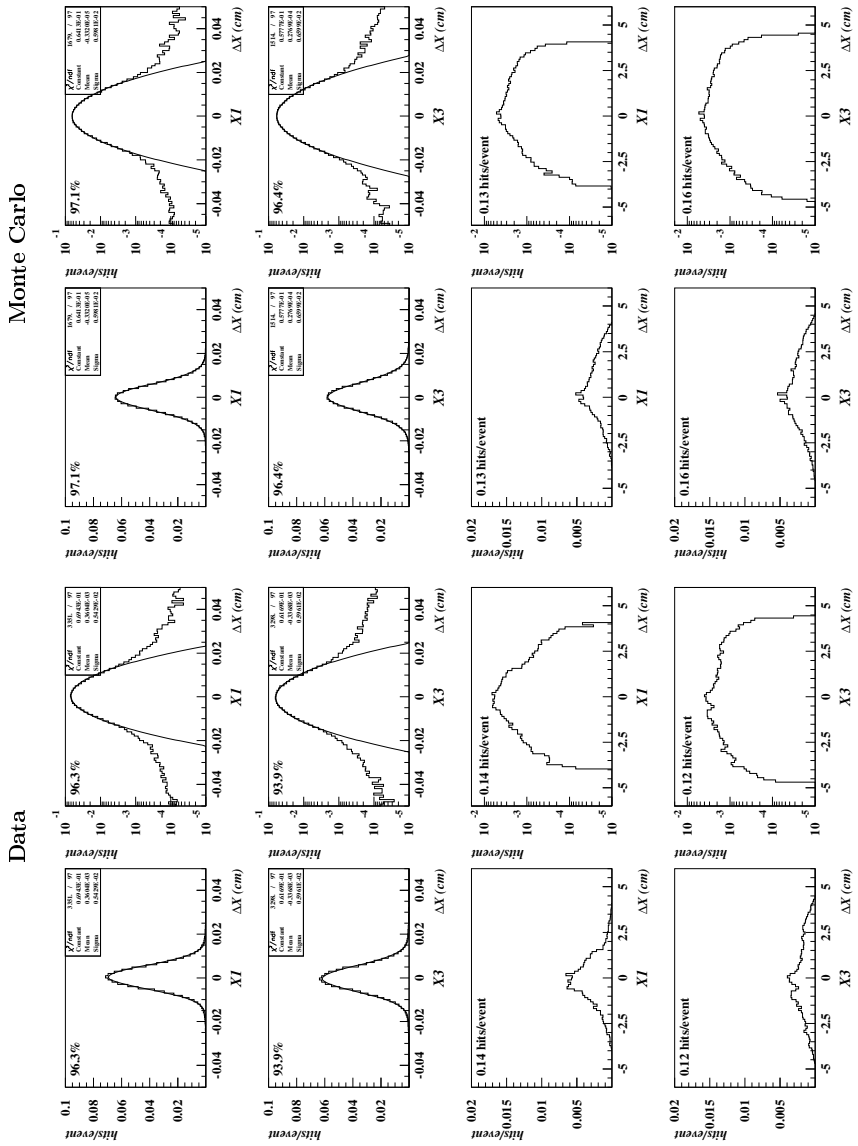

Fig. 6.12: Efficiency (left) and noise (right) determination in the BPT for data (bottom) and Monte Carlo (top), displayed both in linear and logarithmic scale. Shown is the difference ΔX between the predicted and the measured hit position in the BPT; efficiency and noise have been obtained by integrating these distributions. Note the different scale of the efficiency and the noise plots: the width of the former is less than one bin of the latter.

6.2.1 Noise suppression

The natural radioactivity of the depleted uranium in the ZEUS calorimeter provides a good calibration source, but it also creates a certain level of low-energetic noise.

At the standard ZEUS reconstruction level, energy deposits are required to be above 60 MeV (EMC cells) respectively 110 MeV (HAC cells). A more sophisticated algorithm (NOISE96) was used to further suppress noise [130]. It implements a special treatment for cells that are known to frequently exhibit noise signals, and it removes very asymmetric signals, where one photomultiplier signal in a cell differs by so much from that of the other photomultiplier that one must assume a malfunction. Finally, isolated cells are required to have $E > 120$ MeV (EMC) or $E > 160$ MeV (HAC).

The latter cuts are typically chosen in analyses of diffractive events, where the hadronic activity is low, as is also the case in the events analyzed here. The default cuts of the NOISE96 routine (80/140 MeV), as well as the cuts used in previous years for F_2 analyses at higher Q^2 (100/150 MeV) [55–57], were found to be unable to reduce CAL noise to a satisfactory level for this measurement. This has been studied using empty events in data and MC. The reconstructed $y_{\rm JB}$ for empty events in data and MC is shown in Fig. 6.13. For low noise cuts (80/140 MeV), there are empty events with a $y_{\rm JB}$ as large as the lower limit of the analysis (0.005), consequently events from $y \approx 0$ could migrate into the lowest y bins just by the contribution of noise. For higher noise cuts (120/160 MeV), this source of misreconstruction is very effectively suppressed.

In principle, if noise was properly simulated in the MC, and if the physics simulation would simulate events down to extremely low y, this would be less of a problem. Unfortunately, neither of these conditions is met. The physics simulation has a lower cutoff at $W = 3$ GeV, which is approximately equivalent to $y > 10^{-5}$, and due to next-higher-order corrections of QED, HERACLES is recommended not to be used below $y < 0.004$ [115]. The detector simulation seems to reasonably describe the shape of the $y_{\rm JB}$ spectrum of noise, but not its normalization, i.e. its rate. This can be seen from the reduction in number of events when going from low to high noise cuts in Fig. 6.13: the change in data is by a factor of ten, but in the MC only by a factor of five. Consequently, the optimum choice is to impose such cuts that, on the one hand, noise is suppressed below a level where it might significantly influence the result, but on the

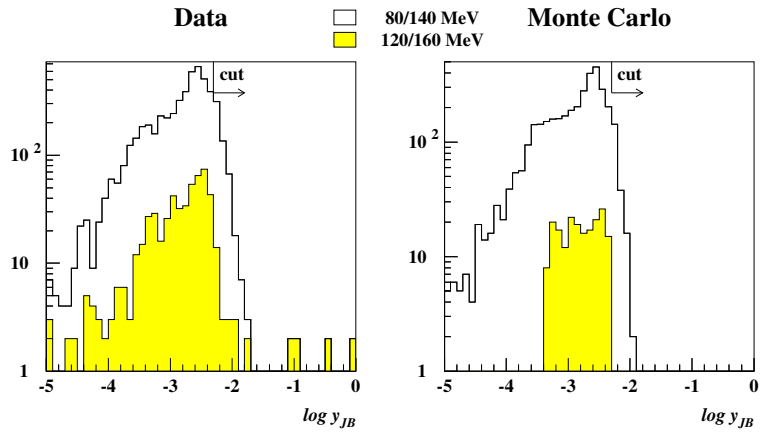

Fig. 6.13: The reconstructed $y_{\rm JB}$ for empty events in data and MC. The lowest y in the analysis is 0.005, as indicated in the figure by "cut".

other hand, not too many energy deposits from real particles are removed, in order not to spoil the reconstruction of hadronic final-state quantities. The effect of lowering the noise cuts on the F_2 analysis is discussed in section 8.1.4.

6.2.2 Reconstruction algorithm

The simplest choice of final state objects are calorimeter cells. The calorimeter detects both neutral and charged particles and measures their energy,[10] however with a resolution degrading at small energies. This algorithm has been the standard method in the past years in ZEUS.

In the context of diffractive physics analyses, the ZUFO[11] [131, 132] algorithm has been developed. ZUFO's combine CTD and CAL measurements, by assigning tracks to energy deposits and inferring the relevant quantities of the combined objects from either CTD or CAL, depending on certain quality criteria and the trade-off between the differently energy-dependent resolutions of CAL and CTD. Special care is taken in order to avoid double-counting of particles.

For analyses in high-Q^2 physics, the CORANDCUT [133] algorithm has been proposed, which aims at removing backsplash, i.e. energy deposits from backscattered or deflected particles which mimick energy flow in directions into which no particles have emerged from the primary vertex. After this cleaning step, either a cell-based or a ZUFO reconstruction can be performed. Since the hadronic activity in events at low Q^2 is typically small, backsplash is no significant problem in such events.

All reconstruction methods were studied for this analysis. ZUFO's were found to give the best resolution and also the best agreement between data and MC; this reconstruction method is therefore used.

6.2.3 Global quantities of the hadronic final state

The most important quantity of the hadronic final state entering in the analysis is

$$\delta_{\rm had} = \sum_i E_i(1-\cos\vartheta_i), \tag{6.17}$$

where the sum runs over all hadronic final state objects with energy E_i reconstructed at a polar angle θ_i (taking into account the event vertex as reconstructed by the BPT). $\delta_{\rm had}$ is closely related to

$$y_{\rm JB} = \frac{\delta_{\rm had}}{2E_e}. \tag{6.18}$$

One also defines

$$p_{X,\rm had} = \sum_i E_i \sin\vartheta_i \cos\phi_i \tag{6.19}$$

$$p_{Y,\rm had} = \sum_i E_i \sin\vartheta_i \sin\phi_i \tag{6.20}$$

$$p_{Z,\rm had} = \sum_i E_i \cos\vartheta_i \tag{6.21}$$

$$p_{T,\rm had} = \sqrt{p^2_{X,\rm had}+p^2_{Y,\rm had}}, \tag{6.22}$$

and, together with the scattered electron energy E'_e and angle ϑ,

$$\delta = \delta_{\rm had} + E'_e(1-\cos\vartheta). \tag{6.23}$$

[10] Except neutrinos and muons.
[11] "ZEUS unidentified flying object", also EFO ("energy flow object").

Longitudinal momentum conservation requires $\delta = 2E_e = 55\,\text{GeV}$ for fully contained and perfectly measured events. For the analysis of ISR events, it is convenient to replace δ by

$$\delta' = \delta + 2E_{\rm LUMI-\gamma}, \tag{6.24}$$

where $E_{\rm LUMI-\gamma}$ is the energy of the radiated photon as measured in the photon calorimeter of the LUMI system. The polar angle of the hadronic system, which in the quark-parton model coincides with the angle of the struck quark, is calculated as

$$\cos\gamma_{\rm had} = \frac{p^2_{T,\rm had}-\delta^2_{\rm had}}{p^2_{T,\rm had}+\delta^2_{\rm had}}. \tag{6.25}$$

6.3 Kinematic event reconstruction

From the scattered electron and the hadronic final state, four independent measured quantities can be derived in total. These can be chosen, for example, to be energy E'_e and angle ϑ of the electron, and $\delta_{\rm had}$ and $p_{T,\rm had}$) of the hadrons. The choice of hadronic variables is motivated by the desire to be independent of particle loss in longitudinal (forward) direction.

From these four quantities, two independent Lorentz-invariant quantities are to be calculated, which are usually chosen to be x and Q^2 (or y and Q^2). Consequently, the system is overdetermined and there are different possibilities to choose two out of the four measured quantities to reconstruct the Lorentz-invariants. One can also choose more than two of them and mix them. Not all combinations are particularly useful; the following ones are in widespread use.

6.3.1 Electron method

With the electron method [134], the kinematic variables are reconstructed from measured quantities of the scattered electron only. This method was traditionally used in fixed target experiments and has the unique advantage of being totally independent of the hadronic final state. Its resolution is good above $y \approx 0.1$, but deteriorates for lower y. In this analysis, the electron method is used at $y > 0.08$. The formulae are, of course, identical to Eqs. (2.18) and (2.19). E_e and E'_e denote the energy of the incoming and scattered electron, ϑ its scattering angle with respect to the forward direction.

$$Q^2_e = 2E_eE'_e(1+\cos\vartheta) \tag{6.26}$$

$$y_e = 1-\frac{E'_e}{2E_e}(1-\cos\vartheta). \tag{6.27}$$

6.3.2 Double angle method

The double angle method [134] uses the angle of the scattered electron and the angle γ of the scattered quark (reconstructed from the final state hadrons).

$$Q^2_{\rm DA} = 4E_e^2\cdot\frac{\sin\gamma(1+\cos\vartheta)}{\sin\gamma+\sin\vartheta-\sin(\vartheta+\gamma)} \tag{6.28}$$

$$y_{\rm DA} = \frac{\sin\vartheta(1-\cos\gamma)}{\sin\gamma+\sin\vartheta-\sin(\vartheta+\gamma)}. \tag{6.29}$$

6.3.3 Jacquet-Blondel method

This method, proposed by Jacquet and Blondel [135], uses only the hadronic final state to reconstruct the kinematics. In structure function analyses, $y_{\rm JB}$ is often used to reduce event

migration from low y, where it has a good resolution.

$$Q^2_{\mathrm{JB}} = \frac{p^2_{T,\mathrm{had}}}{1-y_{\mathrm{JB}}} \quad (6.30)$$

$$y_{\mathrm{JB}} = \frac{\delta_{\mathrm{had}}}{2E_e}. \quad (6.31)$$

6.3.4 Sigma (Σ) method

The Σ method [136] tries to unite the very good resolution of the electron method at high y and the superior resolution of the Jacquet-Blondel method at low y. In addition, the variables y_Σ and Q^2_Σ are constructed such that they are insensitive to initial state radiation, i.e. in contrast to other reconstruction methods, the equations do not change in case of ISR.

$$Q^2_\Sigma = \frac{(E'_e \sin\vartheta)^2}{1-y_\Sigma} \quad (6.32)$$

$$y_\Sigma = \frac{\delta_{\mathrm{had}}}{\delta}. \quad (6.33)$$

6.3.5 Mixed Sigma ($m\Sigma$) method

The $m\Sigma$ method [136] is a mixture of the electron and the Σ method. It uses Q^2_e and y_Σ, thus making optimum use of the available resolution, but giving up the insensitivity to ISR in Q^2.

$$Q^2_{m\Sigma} = Q^2_e \quad (6.34)$$

$$y_{m\Sigma} = y_\Sigma. \quad (6.35)$$

6.3.6 Electron-Sigma ($e\Sigma$) method

Like the $m\Sigma$ method, the $e\Sigma$ method [136] is a mixture of the electron and the Σ method. It additionally rescales y_Σ.

$$Q^2_{e\Sigma} = Q^2_e \quad (6.36)$$

$$y_{e\Sigma} = y_\Sigma \frac{Q^2_e}{Q^2_\Sigma}. \quad (6.37)$$

At low y, the $m\Sigma$ and $e\Sigma$ methods become indistinguishable. At high y, the resolution of the $e\Sigma$ is superior to that of the $m\Sigma$ method. In this analysis, the $e\Sigma$ method is used at $y < 0.08$.

6.3.7 Resolutions

The errors of the reconstructed kinematic variables due to resolutions or systematic uncertainties of the reconstructed variables E'_e, $\theta = \pi - \vartheta$ and δ_{had} are given (for small scattering angles θ) by

$$\frac{\sigma(Q^2_e)}{Q^2_e} = \left(\frac{\sigma(E'_e)}{E'_e}\right) \oplus 2\left(\frac{\sigma(\theta)}{\theta}\right) \quad (6.38)$$

$$\frac{\sigma(y_e)}{y_e} = (1-1/y_e)\left(\frac{\sigma(E'_e)}{E'_e}\right) \oplus (1-1/y_e)\left(\frac{\theta^2}{2}\right)\cdot\left(\frac{\sigma(\theta)}{\theta}\right) \quad (6.39)$$

$$\frac{\sigma(Q^2_{e\Sigma})}{Q^2_{e\Sigma}} = \left(\frac{\sigma(E'_e)}{E'_e}\right) \oplus 2\left(\frac{\sigma(\theta)}{\theta}\right) \quad (6.40)$$

$$\frac{\sigma(y_{e\Sigma})}{y_{e\Sigma}} = 2(y_{e\Sigma}-1)\left(\frac{\sigma(E'_e)}{E'_e}\right) \oplus 4(y_{e\Sigma}-1)\left(\frac{\sigma(\theta)}{\theta}\right) \oplus (1-2y_{e\Sigma})\left(\frac{\sigma(\delta_{\mathrm{had}})}{\delta_{\mathrm{had}}}\right) \quad (6.41)$$

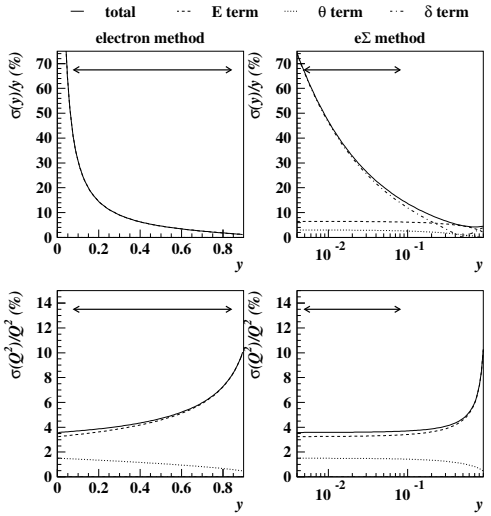

Fig. 6.14: Contributions to the resolutions of Q^2 and y from the resolution of energy, angle and hadronic final state reconstruction, for the electron and the $e\Sigma$ method as functions of y. Note the change from linear to logarithmic y scale. Arrows indicate the region where the respective method is used.

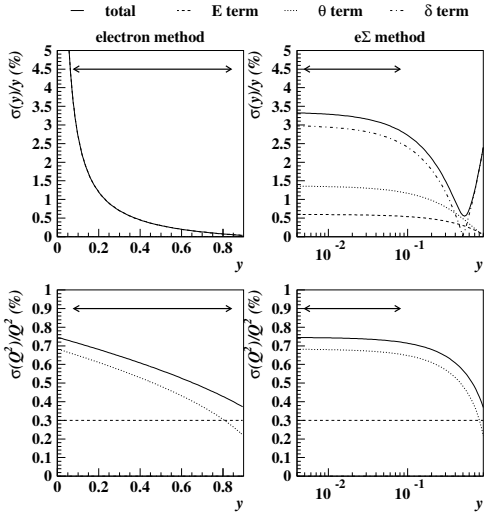

Fig. 6.15: Same as Fig. 6.14, now contributions to the systematic uncertainty in Q^2 and y from energy calibration and alignment.

for the electron and the $e\Sigma$ method (for a complete listing of resolution formulae see [136]). Note that Q^2_e and $Q^2_{e\Sigma}$ are identical. In Fig. 6.14 a comparison is shown based on the following approximations of detector resolutions:

$$\frac{\sigma(E)}{E} = 17\%/\sqrt{E\,[\mathrm{GeV}]} \qquad \frac{\sigma(\theta)}{\theta} = 0.15\,\mathrm{mrad}/\theta \qquad \frac{\sigma(\delta_{\mathrm{had}})}{\delta_{\mathrm{had}}} = 35\%/\sqrt{\delta_{\mathrm{had}}\,[\mathrm{GeV}]}.$$

These values represent design resolutions, but the following considerations will essentially remain the same in a more careful approach.

The contribution of the energy resolution to both the Q^2 and y_e resolution is by far dominating over the whole y range. $y_{e\Sigma}$ is dominated by the δ_{had} resolution. The contribution of the angular resolution is negligible in both methods.

At high y, y_e has the best resolution, but it deteriorates rapidly toward lower y, where $y_{e\Sigma}$ becomes superior. The point where y_e and $y_{e\Sigma}$ have equal resolutions is about at $y = 0.5$. In the analysis a lower y_{JB} cut is applied, which effectively improves the y_e resolution at low y and allows to use the electron method down to $y = 0.08$ (which is helpful due to the trigger configuration, see section 7.1.1). There is also a Q^2 dependence of the resolutions, which is not shown here because it does not affect the conclusions significantly.

For events where the primary interaction vertex could not be reconstructed (which happens sometimes when reconstructing it using the CTD), it is known only to a precision that corresponds to the width of the vertex distribution of about 10 cm. In this case, $\sigma(\theta)/\theta$ increases by about a factor of four and becomes the dominating contribution to the Q^2 resolution.

The same considerations can be made for possible systematic shifts in reconstructed kinematic variables. The alignment and energy calibration of BPT, BPC and CAL have a precision of

$$\frac{\delta(E)}{E} = 0.3\% \qquad \frac{\delta(\theta)}{\theta} = 0.07\,\mathrm{mrad}/\theta \qquad \frac{\delta(\delta_{\mathrm{had}})}{\delta_{\mathrm{had}}} = 3\%.$$

The results are shown in Fig. 6.15. The absolute scale in Q^2 is known to better than 1%, and the scale in y to better than 4%. The Q^2 scale is dominated by the alignment precision, while the quality of the y reconstruction depends on the BPC energy calibration in the electron method, and on the CAL energy calibration in the $e\Sigma$ method.

Chapter 7

Data Samples

For the measurement of the structure function F_2, a sample of events with an identified and well-measured electron in the BPC and BPT is needed. In the first part of this chapter, the method of selecting such a sample is explained. In the second part, the mixing fractions of non-diffractive and diffractive Monte Carlo samples are extracted from data. In the third part, the background contamination is discussed and its magnitude is estimated. Finally, the quality of the simulation is verified by comparing distributions of reconstructed variables between data and MC.

7.1 Event selection

Events are selected online, during data taking, by the three-level trigger of ZEUS. The purpose of the trigger is to preserve all interesting events while rejecting as many background events as possible. Offline, at the stage of analyzing the data, a tighter event selection is made. Here, it is important to obtain a well-reconstructed event sample, and to control the selection efficiency and purity.

The event selection is based on those 1997 ZEUS data taking runs in which the low luminosity trigger configuration was activated (see below). The first run (#27305) represents the start of BPT data taking, when the detector readout was functioning and all parameters were set to their final values; the last run (#27889) coincides with the end of ZEUS data taking in 1997. The total integrated luminosity for these runs amounts to $3.9\,\mathrm{pb}^{-1}$, with an uncertainty of $\pm 1.8\%$.

7.1.1 Online event selection

The high ep cross section at low Q^2 places stringent requirements on the design of the BPC triggers, in order not to exceed the maximum rate that FLT/SLT/TLT are able to handle. The following BPC-related trigger slots are of importance in the analysis:

- First level trigger:

  FLT 52: Standard trigger for electrons in the BPC.
  Requires good BPC timing and $E'_e > 6\,\mathrm{GeV}$.

  FLT 50: Trigger for low energy electrons in the BPC. Prescaled by a factor of 2.
  Requires good BPC timing, $E'_e > 2\,\mathrm{GeV}$, and a minimum energy deposit in RCAL.[1]
  The requirement of some energy in RCAL is necessary to keep the trigger rate at an acceptable level. In high-y, low-Q^2 events, for which this slot is intended, the hadronic angle γ_{had} always points in the backward direction, thus some hadronic activity is expected in the RCAL.

[1] RCAL_EMC_E > 0.464 GeV or RCAL_EMC_th > 1.250 GeV.

FLT 32: Combined trigger for BPC-ISR events and for elastic vector-meson production.
Requires good BPC timing, $E'_e > 6\,\text{GeV}$, and a track in the CTD or $E_{\text{LUMI}-\gamma} > 3.5\,\text{GeV}$.

- Second level trigger:

SLT DIS 2: Standard trigger for BPC events.
Implements a primitive electron finder by requiring that at least 35% of the total BPC energy be deposited in three adjacent X fingers. To reject beam-related background (section 7.3.1), the X finger with the largest signal must not the be the one closest to the beam line. This implicitly rejects scattered electrons in the first X finger, thus imposing the cut $X > 5.2\,\text{cm}$, which determines the lower limit of the geometrical acceptance in θ.
Cuts on $\delta > 25\,\text{GeV}$ (FLT 52) respectively $\delta' > 10$ (FLT 50) (!), below the corresponding condition imposed by the TLT.

- Third level trigger and DST bits:

TLT DIS 17 "BPC F_2" (DST 121): Requires FLT 52, SLT DIS 2, $y_{\text{JB}} > 0.02$, $E'_e > 6\,\text{GeV}$, $25\,\text{GeV} < \delta < 65\,\text{GeV}$, BPC timing (corrected for a possible offset) compatible with an ep interaction: $|t - \bar{t}| < 5\,\text{ns}$.
Used for events in the kinematic region of the 1995 measurement. There was an additional requirement of some energy deposit in RCAL in 1995, which was removed because it relies on a good simulation of the hadronic final state and therefore introduces systematic uncertainties.

TLT DIS 18 "BPC only" (DST 122): Requires SLT DIS 2 or 3. The latter is a passthrough trigger, prescaled by a factor of 18, which is not used.
Used to save the events discarded by TLT DIS 23 at low y and $X_{\text{BPC}} < 7.0\,\text{cm}$ (see below). Prescaled by a factor of 12, except for the first runs (#27305–#27322) of the BPT data taking period.

TLT DIS 19 "QED Compton" (DST 123): not used.
QED Compton events served in 1995 for alignment purposes. In 1997, a different method was used for alignment.

TLT DIS 20 "LPS" (DST 124): not used.
There were some ideas to use diffractive events with the scattered electron in the BPC/BPT and the proton in the LPS for alignment purposes; later abandoned due to statistical and systematic limitations.

TLT DIS 21 "BPC ISR" (DST 125): Requires FLT 32 or 52, SLT DIS 2, $30\,\text{GeV} < \delta' < 65\,\text{GeV}$, $E_{\text{LUMI}-\gamma} > 3.5\,\text{GeV}$, $E_{\text{LUMI}-e} < 4\,\text{GeV}$, $y_{\text{JB}} > 0.04$ (not corrected for ISR). No timing cut.
Used in the ISR analysis (appendix B).

TLT DIS 22 "BPC LowE" (DST 126): Requires FLT 50, SLT DIS 2, $\delta' > 20\,\text{GeV}$, $|t - \bar{t}| < 5\,\text{ns}$.
Used for events at high y.

TLT DIS 23 "BPC KP" (DST 127): Requires FLT 52, SLT DIS 2, $y_{\text{JB}} < 0.1$, $E'_e > 17\,\text{GeV}$, $|t - \bar{t}| < 5\,\text{ns}$. For unknown reasons, this trigger implements a cut $X_{\text{BPC}} > 7.0\,\text{cm}$.
Together with TLT DIS 18, it covers the low-y region.

Depending on the instantaneous luminosity and the beam-related background conditions, ZEUS took data in two different trigger configurations, named "low luminosity" and "high luminosity" configuration. In the high luminosity configuration, the BPC triggers were prescaled, therefore for the analysis only runs with the low luminosity configuration were used. Adding the high luminosity runs would decrease the statistical error only by a negligible amount, at the price of introducing some bookkeeping complications.

7.1.2 Kinematic regions and reconstruction

In order to account for the complicated trigger design, the kinematic range has to be subdivided into four regions (Figs. 7.1 and 7.2), each of which corresponds to a different BPC trigger path:

- low y (FLT 52 → SLT DIS 2 → TLT DIS 23):
  $0.005 < y < 0.08$, $0.45 < Q^2 < 0.78\,\text{GeV}^2$.
- low y prescaled (FLT 52 → SLT DIS 2 → TLT DIS 18):
  $0.005 < y < 0.08$, $0.21 < Q^2 < 0.45\,\text{GeV}^2$.
- medium y (FLT 52 → SLT DIS 2 → TLT DIS 17):
  $0.08 < y < 0.74$, $0.04 < Q^2 < 0.78\,\text{GeV}^2$.
- high y (FLT 50 → SLT DIS 2 → TLT DIS 22):
  $0.74 < y < 0.84$, $0.04 < Q^2 < 0.17\,\text{GeV}^2$.

Because BPC and BPT have been designed as devices for measuring the scattered electron with high precision, the electron method (section 6.3.1) is used to reconstruct the event kinematics where it gives the best resolution. This is the case in the medium-y and high-y regions. At low y, the $e\Sigma$ method (section 6.3.6) is employed instead, which still only uses BPC and BPT for the reconstruction of Q^2, but drastically improves the y resolution by also considering the hadronic final state. The choice of two different reconstruction methods is another reason for subdividing the kinematic region.

Technically, the four regions are treated as four single measurements, i.e. the F_2 determination procedure is run for each region separately, with the event kinematics reconstructed according to the respective method.

It is important to note that the BPC energy calibration has been performed using low-y events, for which the measured electron energy has only a small impact on the reconstructed kinematic variables, since here the $e\Sigma$ method relies predominantly on δ_{had}. Otherwise, the strong correlation between the event samples used in calibration and measurement would induce systematic effects which are hard to control.

7.1.3 Offline event selection

Since the BPC trigger is not simulated in the ZEUS Monte Carlo, the offline event selection is designed such that all conditions imposed on the trigger level are superseded by tighter offline cuts. This requirement implies that the triggers are fully efficient for the selected event sample (see below), in which case no correction for trigger inefficiency has to be applied to the MC.

Selected events must not belong to runs that are tagged as problematic or unusable by the routines EVTAKE [90] and XSECTAKE II [90], e.g. because one of the main detector components was switched off or not working properly.[2]

[2] EVTAKE additionally rejects the small number of events that were taken after the last update of the integrated luminosity measurement in a run, thereby ensuring that the accepted events correspond exactly to the quoted luminosity value.

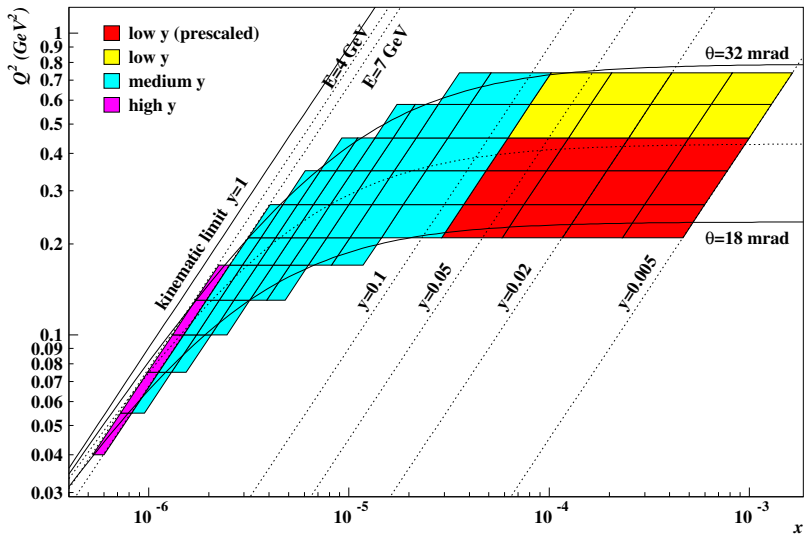

Fig. 7.1: The kinematic region covered by this analysis. The four regions and the bins used for the F_2 analysis are indicated, together with some relevant iso-E'_e, iso-y and iso-θ lines.

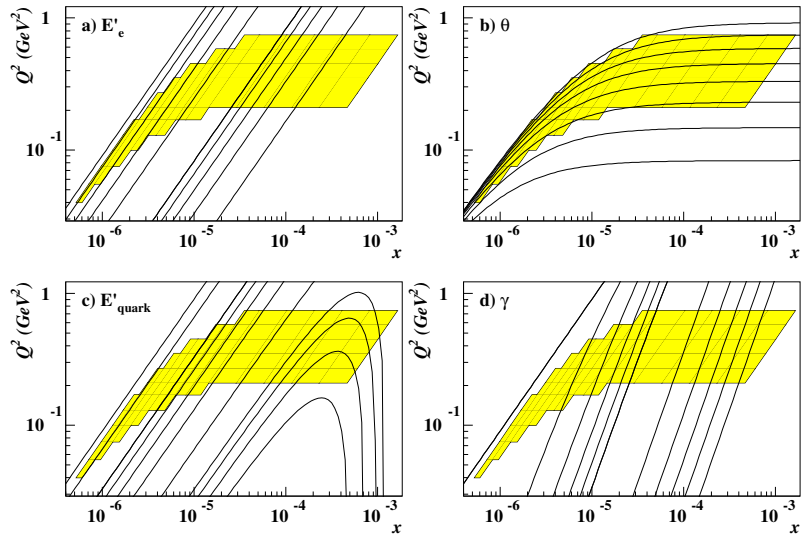

Fig. 7.2: Isolines of a) scattered electron energy (left to right: 0, 5, 10, 15, 20, 25, 25.5, 26, 26.5, 27 GeV), b) electron scattering angle (2.0°, 1.8°, 1.6°, 1.4°, 1.2°, 1.0°, 0.8°, 0.6°), c) scattered quark energy (27.5, 20, 10, 8, 6, 4, 2, 1, 0.8, 0.6, 0.4 GeV), d) quark scattering angle (180°, 178°, 176°, 174°, 172°, 170°, 150°, 130°, 110°, 90°, 70°).

The following cuts are made in the offline event selection. Some of them differ for the different kinematic regions. If not indicated otherwise, "low y" applies to both "low y" and "low y prescaled". The cuts fall into two classes, cuts on the scattered electron and cuts on the hadronic final state:

- The offline electron energy cut is higher than the cut on the trigger level, in order to be well above the trigger threshold; in addition this is also necessary because the trigger uses "a bit calibrated" energy values, and the final calibrated energy is typically higher than the uncalibrated value:
  - ◇ high y: $4.4\,\text{GeV} < E'_e < 7.2\,\text{GeV}$
  - ◇ medium y: $E'_e > 7\,\text{GeV}$
  - ◇ low y: $E'_e > 20\,\text{GeV}$.
- The scattered electron position on the BPC front face has to be inside the fiducial area (see also section 7.1.4). First, the center of gravity of the shower in X is reconstructed by the BPT, Y and Z by the BPC. Then, X and Y are projected to the BPC front face at $Z = -293.7\,\text{cm}$, along the BPT track, and corrected for the beam position. The usable fiducial area is D-shaped; it is approximated by a polygon composed of a rectangle and a trapezoid:
  - ◇ $5.2\,\text{cm} < X < 9.3\,\text{cm}$ (for low y only: $7.2\,\text{cm} < X < 9.3\,\text{cm}$)
  - ◇ $-2.3\,\text{cm} < Y < 2.8\,\text{cm}$
  - ◇ $X - Y < 10.7\,\text{cm}$
  - ◇ $X + Y < 11.2\,\text{cm}$.
- The transverse shower size is limited to a value well above the typical size of electromagnetic showers in the BPC, but below that of hadronic showers:
  - ◇ $\sqrt{(\sigma_X^2 + \sigma_Y^2)/2} < 0.8\,\text{cm}$.
- Requiring a matching track in the BPT suppresses neutral particles faking an electron in the BPC (photoproduction background, see section 7.3.2):
  - ◇ $|X_{\text{BPT}} - X_{\text{BPC}}| < 5\sigma$, where $\sigma = 0.22\,\text{cm}/\sqrt{E\,[\text{GeV}]}$.
- The event vertex as measured by the BPT is required to be compatible with the nominal interaction region:
  - ◇ $-90\,\text{cm} < Z_{\text{BPT}}^{\text{vertex}} < 90\,\text{cm}$.

  This cut serves to suppress beam-related background, where the apparent event vertex is typically far outside the ZEUS detector (section 7.3.1).
- The reconstructed value of the quantity δ is limited to
  - ◇ $30\,\text{GeV} < \delta < 65\,\text{GeV}$.

  This cut ensures the longitudinal containment of the event. The loss of particles through the rear beam pipe hole decreases δ. Lost particles can be e.g. a hard photon from ISR, or the true scattered electron, while a signal in the BPC is faked by some other particles. The cut therefore reduces photoproduction background and the sensitivity to radiative

corrections (appendix B.5). Background events that are partially or completely caused by other sources than ep interactions can also have a too low or too high δ.

Usually, the lower cut is placed at 35 GeV in F_2 analyses [55–57]. It was reduced to 30 GeV in order to be less sensitive to the properties of the hadronic final state at high y. The price to pay are a slightly higher background contamination and a higher sensitivity to radiative corrections.

Note that in the low-y region the lower cut on δ has no effect, since the contribution of the electron alone is already above the cut.

- In order to suppress migrations from low y, especially in the regions where the electron method is used, y_{JB} is required to lie above a cutoff value which is sufficiently far below the lowest y bin boundary. This cut also removes QED-Compton events, where the "hadronic" final state only consists of a photon (that is typically not detected at all):
  - ◇ medium y and high y: $y_{\mathrm{JB}} > 0.06$
  - ◇ low y: $0.004 < y_{\mathrm{JB}} < 0.1$.
- In data, the BPC and CAL timing is required to be compatible with an ep interaction. In MC, the timing is poorly simulated, therefore this cut is not made (and would have no reasonable effect if made). Systematic run-by-run variations of the BPC-measured time are corrected for by subtracting the mean reconstructed BPC time for the run:
  - ◇ $|t - \bar{t}| < 3\,\mathrm{ns}$.
- Trigger bits as described in section 7.1.2 are required for data only, because the BPC trigger bits are not simulated in MC. Instead, cuts made at the trigger level on other than BPC quantities are also made offline, in the variables used by the trigger, which are simulated in MC. This accounts for most of the missing trigger bit simulation.

Applying these offline cuts, the efficiency of the BPC triggers, defined as

$$\text{trigger efficiency} \;=\; \frac{\#\text{ accepted by trigger \& passing offline cuts}}{\#\text{ passing offline cuts}}, \tag{7.1}$$

is checked using an independently triggered event sample. The definition of this sample is quite arbitrary; the important point is to choose trigger slots that are unrelated to the BPC trigger slots used in the analysis.[3] The BPC trigger inefficiency is found to be less than 0.5% in all bins and is neglected.

An important consistency check is to look at time variations of the measured cross section. Obviously, the value of a physical observable should not depend on the date. If it does, this is an indication that some time-dependent effects have not been properly taken into account, like e.g. the beam position or background conditions in HERA varying between fills. Figure 7.3 shows the number of accepted events per luminosity, plotted versus the run number (representing the time axis). The rate of accepted events is flat, and the fluctuations around the mean value have exactly the expected magnitude, as shown in the perfect pull distribution, centered at zero with unit width. Apart from being a consistency check, this already indicates that beam-related background (which can strongly fluctuate between HERA fills) is a negligible effect.

[3] The independent trigger used is a logical OR of DST bit 9 and the FLT slots 18, 30, 33, 40, 41, 42, 43, 44, 45. DST bit 9, an OR of five electron finders in the CAL, does not require or veto any of the BPC FLT/SLT/TLT triggers. None of the BPC SLT or TLT slots requires any of the listed FLT slots; events finally accepted by the trigger therefore have to pass some other (not specified) SLT and TLT slots. Consequently, these conditions indeed define an independently triggered sample.

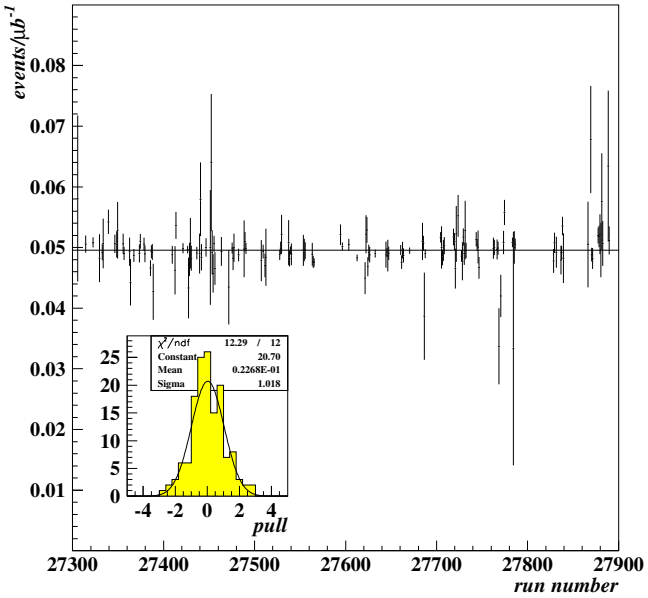

Fig. 7.3: Medium-y region. Number of events per unit luminosity passing the offline selection, plotted versus run number. The inset shows the pull distribution.

7.1.4 Using the BPT as a presampler

The fiducial area cuts can be checked using the BPT as a presampler, i.e. by measuring the mean number of hits in a BPT plane vs. the shower position as reconstructed by the BPC (Figs. 7.4 and 7.5). The result is a projection of the beam pipe exit window onto the BPC surface: Where electrons pass the exit window, the mean number of hits per BPT plane is scarcely greater than one, while outside it increases dramatically due to the showering of electrons that have had to cross much more beam pipe material. Only hits in a region around a predicted electron trajectory are counted, the prediction being derived from the CTD vertex and the BPC position.

There is a slight mismatch of the nearly material-free regions in Y between data and MC. In order to select the overlap region between them, the fiducial area cuts as made in 1995 were tightened in 1997. It is not clear whether the data-MC mismatch is due to a misalignment of the BPC in Y in 1997, or if it is a feature that already existed in 1995 and affected the measurement. This check has been made possible only by the installation of the BPT.

7.2 Determination of the diffractive event fraction

The reason why it is important to correctly simulate diffractive and non-diffractive events is that at high y and low Q^2 the contributions of diffractive and non-diffractive events to the "invisible" cross section (i.e. events that were not triggered or do not pass the offline cuts) are significantly different. This can be understood in the following way: at high y, the angle of the hadronic system γ_{had} is close to π, i.e. at least part of the hadronic system tends to escape through the rear beam pipe hole, which lowers the measured quantities δ_{had} and y_{JB}. The loss depends on

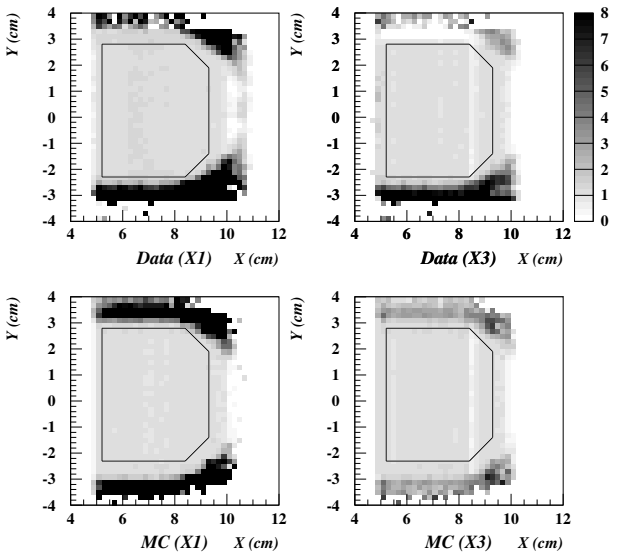

Fig. 7.4: The amount of material in front of the BPC is scanned and compared between data and MC. Indicated in gray scale is the mean number of hits in a BPT plane on a straight line from the vertex to the BPC shower, plotted versus the shower position.

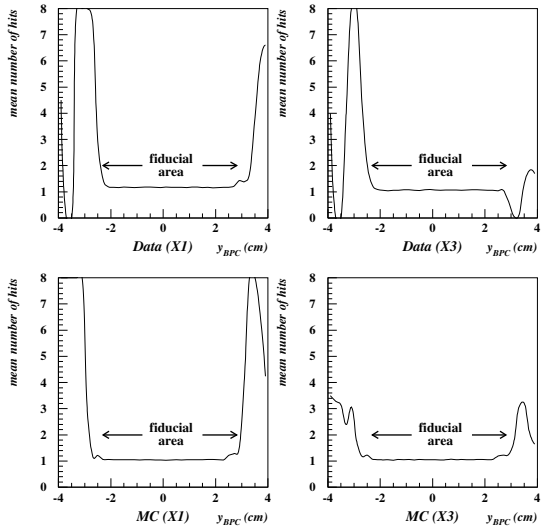

Fig. 7.5: One-dimensional projection of the previous plots on the Y-axis. The slight shift of the material-free region between data and MC is taken into account in the fiducial area cuts. The drop of the number of hits in X3 outside the fiducial area (in data) is not understood.

the event shape; cuts on $\delta_{\rm had}$ and $y_{\rm JB}$ will consequently discard different fractions of diffractive and non-diffractive events.

Clearly, in an ideal measurement one would rely on the scattered electron only; in this case, the acceptance would not depend on the hadronic final state. From a puristic point of view, any dependence on the hadronic final state is also in contradiction to the definition of an inclusive $ep \to eX$ cross section measurement. However, at least at HERA some cuts on the hadronic final state are unavoidable, and it is only by using the hadronic final state in the kinematic reconstruction that the range at low y can be covered at all.

The key ingredient in the determination of the acceptance of the event selection cuts is the Monte Carlo simulation. As described in section 5.3.2, it has one free parameter left to be extracted from data, the mixing fraction of DJANGO and RAPGAP samples. For this purpose, histograms of certain hadronic variables are generated in different ranges in x and Q^2 for data and the two Monte Carlo samples separately. In each range the diffractive fraction $f(x,Q^2)$ is determined from a fit of the form

$$n(x,Q^2) \cdot \text{Data} = f(x,Q^2) \cdot \text{RAPGAP} + [1 - f(x,Q^2)] \cdot \text{DJANGO}, \tag{7.2}$$

where n is a normalization factor. For the case that $F_2^{\rm data} = F_2^{\rm MC}$, which is true after a few iterations in the F_2 measurement procedure, the normalization factor is expected to be equal to unity.

The diffractive fraction is parameterized in a polynomial form and allowed to depend on x and Q^2. It turns out that it can be satisfyingly parameterized as a function of x only, which may be partially attributed to the feature that x and Q^2 are correlated due to the limited geometrical acceptance of the BPC. The parameterization as a function of x is used thereafter to reweight the two MC samples, assigning each RAPGAP event a weight $f(x,Q^2)$ and each DJANGO event a weight $1 - f(x,Q^2)$, where x and Q^2 are the true event variables. This procedure ensures that the distribution of events in the generated variables x and Q^2 in the mixed sample is identical to that in the pure DJANGO and RAPGAP samples (which also were likewise distributed): the kinematic distributions of the sample (i.e. the electron side of the events) are not changed, only some non-diffractive hadronic final states are replaced by diffractive ones.

The parameterization is determined in bins of measured variables, but has to be applied as a function of true variables. Therefore, the determination of $f(x,Q^2)$ is iterated, with the two MC samples reweighted to the mixing fraction determined in the previous step. After a few iterations the process converges, yielding the desired parameterization as a function of true variables.

The choice of hadronic variables for the $f(x,Q^2)$ determination is quite nontrivial. A natural choice would seem to be $\eta_{\rm max}$ or $\ln(M_X^2)$; these variables are known to provide a good separation between diffractive and non-diffractive events, and have been successfully used for this purpose in previous analyses of diffractive events by ZEUS and H1. However, there is also a good argument for choosing instead the variables $\delta_{\rm had}$ and $p_{T,{\rm had}}$. These variables are closely correlated to the kinematic variables, and $\delta_{\rm had}$ is even directly used for cuts in the analysis. Therefore it is of prime importance to achieve a good data-MC agreement for the distributions of these two variables.

From both groups of hadronic final state variables diffractive fractions are extracted and compared (for $\delta_{\rm had}$ and $p_{T,{\rm had}}$, a combined fit to the two histograms is made to enhance the sensitivity). The results for $\eta_{\rm max}$ and $\ln(M_X^2)$ are quite similar; only $\eta_{\rm max}$ is further considered, because the general agreement between data and MC is better than for $\ln(M_X^2)$. However, while the diffractive fraction determined by $\delta_{\rm had}$ and $p_{T,{\rm had}}$ is in good agreement with that from $\eta_{\rm max}$ at medium x, they differ at the borders of the kinematic region, most significantly at the lowest x (Fig. 7.6). The reason for this discrepancy remains unclear even after detailed studies. It is believed to be due to a poor description of the hadronic final state (or, rather, the correlations between different aspects of it) at the lowest x by both DJANGO and RAPGAP, or rather by

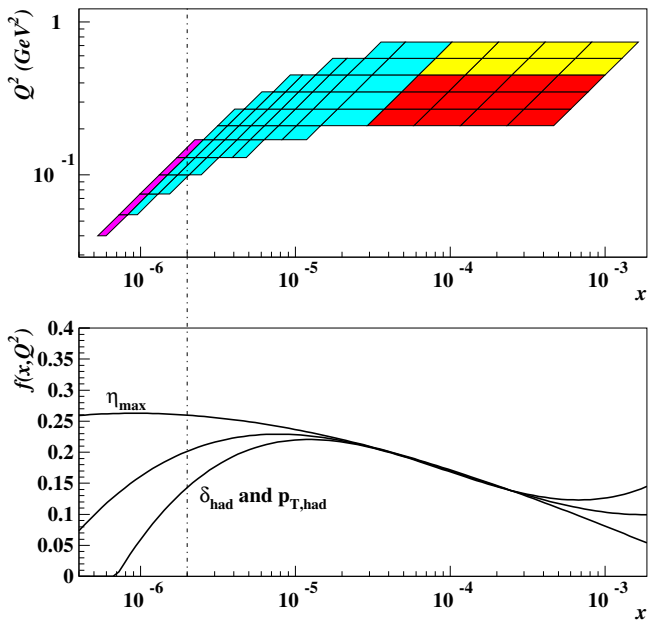

Fig. 7.6: Bottom: Diffractive fraction $f(x,Q^2)$ as a function of x, determined from fitting $\eta_{\max}$ respectively $\delta_{\rm had}$ and $p_{T,\rm had}$. For the analysis, the average of the two curves (the central solid line) is used, and the difference between the methods is included in the systematic error. Where the difference is small, the diffractive fraction is varied by $\pm 15\%$ (relative) instead as systematic check. Top (for orientation): the bins used for the F_2 analysis. The region where the systematic error of F_2 is dominated by the uncertainty of the diffractive fraction (below $x \approx 2 \cdot 10^{-6}$) corresponds to only a small number of bins at the lowest x and Q^2.

the ARIADNE and JETSET packages used by both generators for fragmentation. Lacking a better idea, the average of the diffractive fractions determined by the two methods is used in the F_2 analysis, while the difference between them is included in the systematic error calculation. Note that the two curves represent two extreme assumptions about the fraction of diffractive events at low x, i.e. essentially zero or as high as 25%, whence is expected that the true curve lies in between. Where the two methods yield similar diffractive fractions, $f(x,Q^2)$ is instead varied by $\pm 15\%$ (relative) in order to estimate the sensitivity of the result to the contribution of diffractive events. This value represents the typical statistical fluctuation of extracted diffractive fractions between adjacent bins.

7.3 Backgrounds

7.3.1 Non-*ep* background

Background that is not related to ep interactions inside the ZEUS detector comes predominantly from interactions of the electron beam with gas molecules in the beam pipe, and from off-momentum electrons that have reduced their energy by bremsstrahlung and are deflected into

the BPC by the beam optics. Also interactions of the proton beam with gas molecules, and cosmic muons traversing the detector can possibly fake signal events; however, they typically do not pass the requirement of a track in the BPT and an electromagnetic shower in the BPC.

For most off-momentum beam electrons which have a track in the BPT and a shower in the BPC the vertex resolution of the BPT is sufficient to recognize that the (virtual) event vertex is far outside the ZEUS detector, typically around $Z = 400 \ldots 600$ cm, where the C4 collimator of HERA is located, which serves to scrape off-momentum and background particles from the beam. Apparently, the remaining background electrons are those that just manage to pass the collimator edge.[4] Electron beam-gas interactions have a flat event vertex distribution in Z, and are therefore suppressed by limiting the accepted vertex range.

The background from all non-ep sources can be statistically estimated from the assignment of events to bunch crossing types, which can be any one of ep, e only ("e pilot"), p only ("p pilot"), or empty (Fig. 7.7). Events recorded at a time when there was no ep beam crossing in ZEUS must obviously be background events.[5] The fraction of events observed in unpaired or empty bunches is scaled by the ratio of currents in paired and unpaired bunches [137]. The total non-ep background is found to be below 0.5% and is neglected.

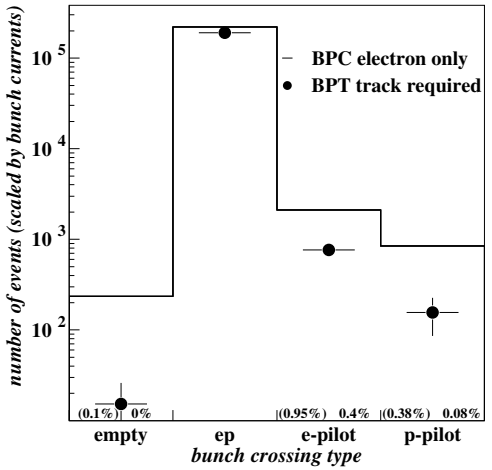

Fig. 7.7: Medium-y region. The improvement in background suppression achieved by requiring a BPT track, illustrated in the distribution of bunch crossing types. The numbers at the bottom denote the fraction of events in unpaired ("pilot") bunches respectively in empty bunches after (before) requiring a BPT track.

7.3.2 Photoproduction background

A more dangerous source of background are events where one or more particles of the hadronic final state, usually photons from a π^0 decay, fake an electron signal in the BPC which passes all selection cuts, and the true scattered electron is missed, usually because it escapes through the rear beam pipe hole. Due to the increasing cross section toward lower Q^2, these are mostly events at lower Q^2 than relevant for the analysis ("photoproduction background"). In events at higher Q^2, the scattered electron is found in the CAL. Also photons from ISR/FSR can produce a fake electron signal. Since the fake signals are energy deposits in the BPC, which usually have a much lower energy than the incoming electron, this background occurs predominantly at high

[4] This class of background also is the reason why the SLT DIS 2 trigger rejects events with the electron in the first BPC X finger, which constitutes the overwhelming contribution. Only BPT information at the FLT (which is not available) would possibly allow to raise this condition.

[5] The result will still be an overestimation of the true rate, because "empty bunch" is defined by HERA as "below a threshold", i.e. for technical reasons there do exist some beam particles in empty bunches.

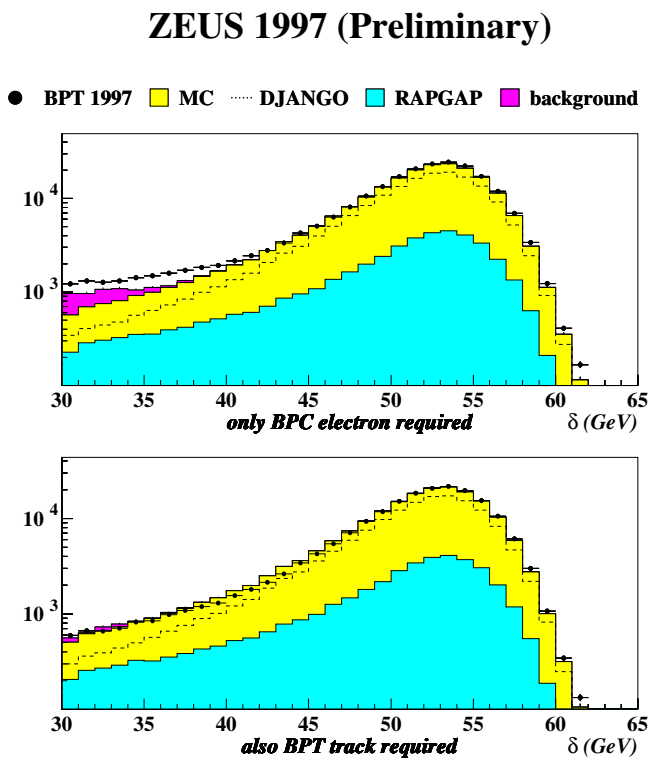

Fig. 7.8: Medium-y region. The improvement in background suppression achieved by requiring a BPT track, illustrated in the distribution of δ. The points denote measured data, the light-shaded histogram is the sum of non-diffractive (DJANGO) and diffractive (RAPGAP) MC, the medium-shaded histogram is RAPGAP alone, the dashed line is DJANGO alone, and the dark shaded histogram is the sum of MC and background. Photoproduction background is expected predominantly at low δ. The background is estimated using LUMI-tagged photoproduction events. For the analysis, a cut is made at $30\,\text{GeV} < \delta < 65\,\text{GeV}$.

(apparent) y_e. The longitudinal momentum carried away by the undetected true electron in rear direction decreases δ; consequently, a δ cut can remove a large fraction of photoproduction background events.

By requiring a track in the BPT that matches the shower position in the BPC, photoproduction background is strongly suppressed compared to the situation without the BPT (Fig. 7.8). Note that, although an estimate of the background has been added to the signal Monte Carlo events (see below), the agreement with data is not very good at low δ in the BPC-only analysis, while in the BPC+BPT analysis it is excellent over the whole δ range.

To study the photoproduction background, 109 K events with direct interaction and 115 K events with resolved interaction were generated with the PYTHIA generator. The corresponding integrated luminosities are $300\,\text{nb}^{-1}$ and $30\,\text{nb}^{-1}$, respectively, i.e. a factor of 13 (6.5) and 130 (65) less than the luminosities in data for the medium (high)-y region. The negation of the cut

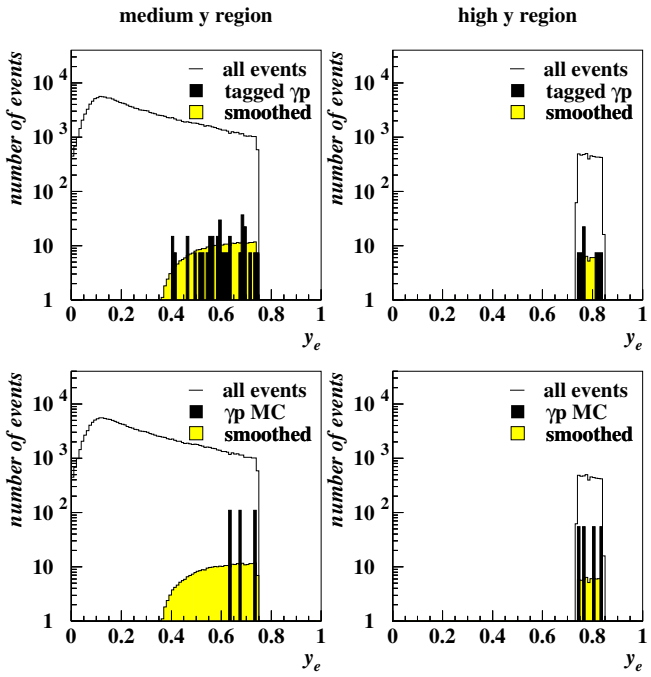

Fig. 7.9: Top: Estimate of photoproduction background from LUMI-tagged events as a function of reconstructed y_e, for the medium-y and the high-y regions. The distribution of tagged events is parameterized as a smoothed function of y and then used to correct F_2 for background contamination. Bottom: same as above, but background estimated using a photoproduction Monte Carlo. The smoothed distribution is the same as in the upper plots. For the medium-y region, the agreement between the two methods is reasonably good, while for the high y region they differ. This is taken into account in the systematic error.

for the preselection of signal events (section 5.3.3) was applied, in order to reject those events where the true scattered electron itself leaves the signal in the BPC.

Two methods of estimating the remaining photoproduction background in the data sample are studied and compared. The first, straightforward method is to count the events from the photoproduction MC that pass all selection cuts. The disadvantage of this method is, however, that one has to rely on a good simulation of the hadronic final state, which is responsible for the fake electron signal.

The second method uses LUMI-tagged photoproduction events. These are data events where the true scattered electron is detected in the electron calorimeter of the luminosity system. This calorimeter has a reasonably high acceptance for about $0.2 < y < 0.6$ and $Q^2 < 0.01\,\text{GeV}^2$.[6] In this method, the photoproduction Monte Carlo is used only to determine the tagging efficiency of the LUMI-e detector as a function of δ. This efficiency is found to be 13.5% in the region of interest between 25 GeV and 40 GeV, where photoproduction background is concentrated. The

[6] Note that this is the acceptance for the true scattered electron; since the apparent y of a background event is calculated from a fake energy deposit in the BPC, LUMI-tagged events contribute to the background also at higher y.

number of accepted events in data with a signal in LUMI-e is scaled by the inverse of the tagging efficiency and taken as the background estimate.

There is also a background contribution to the LUMI-tagged background events themselves, which originates from overlay events with the $e\gamma$ pair from a Bethe-Heitler (BH) process, $ep \to ep\gamma$. In such events the BH electron is mistakenly assumed to be the LUMI-tagged true scattered electron in the event, which would lead to an overestimation of the background. However, since the photon from the overlay event is detected with an acceptance of about 90% in the LUMI-γ detector, this class of events can be effectively suppressed by imposing the additional constraints that $\delta + 2E_{\mathrm{LUMI}-e} < 65\,\mathrm{GeV}$ and $E_{\mathrm{LUMI}-\gamma} < 3\,\mathrm{GeV}$, i.e. the electron in LUMI-e must fit in the assumption that it belongs to the event, and no photon should be observed in LUMI-γ.

The resulting distribution of background events in y_e is shown in Fig. 7.9 and compared between the two methods.

The agreement between the two methods is good in the medium-y region, but they differ slightly in the high-y region. Here, tagged photoproduction events predict a background contamination of $1.3^{+1.1}_{-0.6}\%$, while the photoproduction MC predicts $4.8^{+3.8}_{-2.3}\%$. Therefore, as a systematic check, the normalization of the background parameterization is varied by $+200\%$ and -100%.

The result from LUMI-tagged events is chosen for background subtraction, because it depends only on the simulation of LUMI-e tagging efficiency, but not on the hadronic final state simulation in the photoproduction MC, and because it has a higher statistical precision (38 real events, compared to 3 events in the medium-y region). Since the statistical accuracy is too low for a statistical subtraction in each bin of the F_2 analysis, the distribution of LUMI-tagged background events is smoothed and parameterized as a function of y, rising linearly from zero at $y = 0.35$ to 1.35% at $y = 0.8$. This parameterization is used to correct the measured F_2 for contamination from photoproduction background.

7.4 Comparison of data and MC

In order to check the overall quality of the description of the data by the Monte Carlo simulation, distributions of reconstructed variables interesting for the analysis are compared between data and MC. The results are shown in Figs. 7.10, 7.11, 7.12, 7.13 and 7.14. DJANGO and RAPGAP have been mixed as described in section 7.2. No background subtraction (section 7.3) was made. The MC was reweighted to the structure function as measured in the data (section 8.1.1).

7.4.1 Scattered electron and hadronic final state

Generally speaking, the agreement of data and MC is close to perfect for the medium-y and low-y regions in those quantities that are used for the reconstruction of kinematics, like angle and energy of the scattered electron, and δ_{had}, as well as in the quantities $p_{T,\mathrm{had}}$, γ_{had} and y_{JB}. This is partly a trivial consequence of reweighting the MC to the structure function as measured in data; however, the agreement in many variables proves that also correlations between variables are well simulated, which is nontrivial.

The distributions of $\eta_{\max}$ and $\ln(M_X^2)$ agree reasonably well, too, although the latter appears to be slightly shifted between data and MC. The agreement is still reasonable on a qualitative level when comparing quantities that are not directly correlated to kinematics, like total or transverse energy in the CAL or parts of it, numbers of cells, tracks, ZUFO's etc. (not shown). These variables depend on details of the fragmentation process. Here, the general structure is always reproduced by the MC, but the distributions often differ slightly in mean and spread.

In the high-y region, the agreement between data and MC becomes less good, reflecting the uncertainty about the fraction of diffractive events. Here the problem with mixing the two MC samples at low x, or high y, is strikingly illustrated: the $\eta_{\max}$ distributions would match better

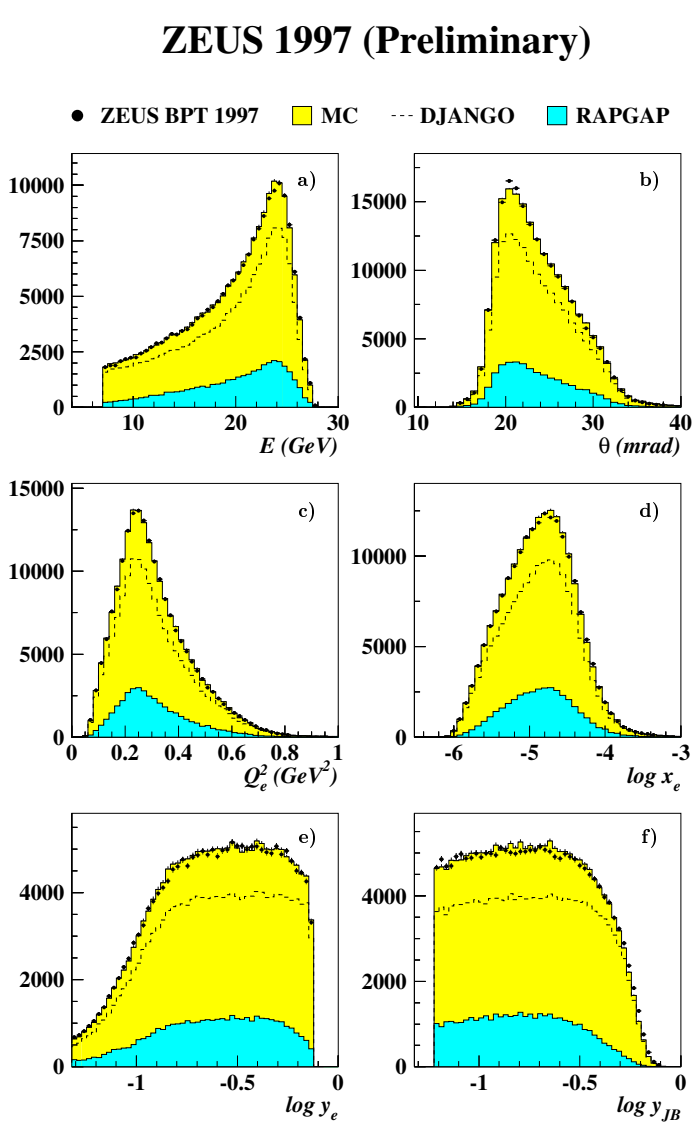

Fig. 7.10: Medium-y region (part one). Distributions of reconstructed quantities for data and Monte Carlo simulation. The points denote measured data, the light-shaded histogram is the sum of non-diffractive (DJANGO) and diffractive (RAPGAP) MC, the dark-shaded histogram is RAPGAP alone, and the dashed line is DJANGO alone. Shown are: a) electron energy E'_e, measured in the BPC; b) electron scattering angle θ, measured in the BPT; c)–e) Q^2, x and y reconstructed with the electron method; and f) y_{JB}.

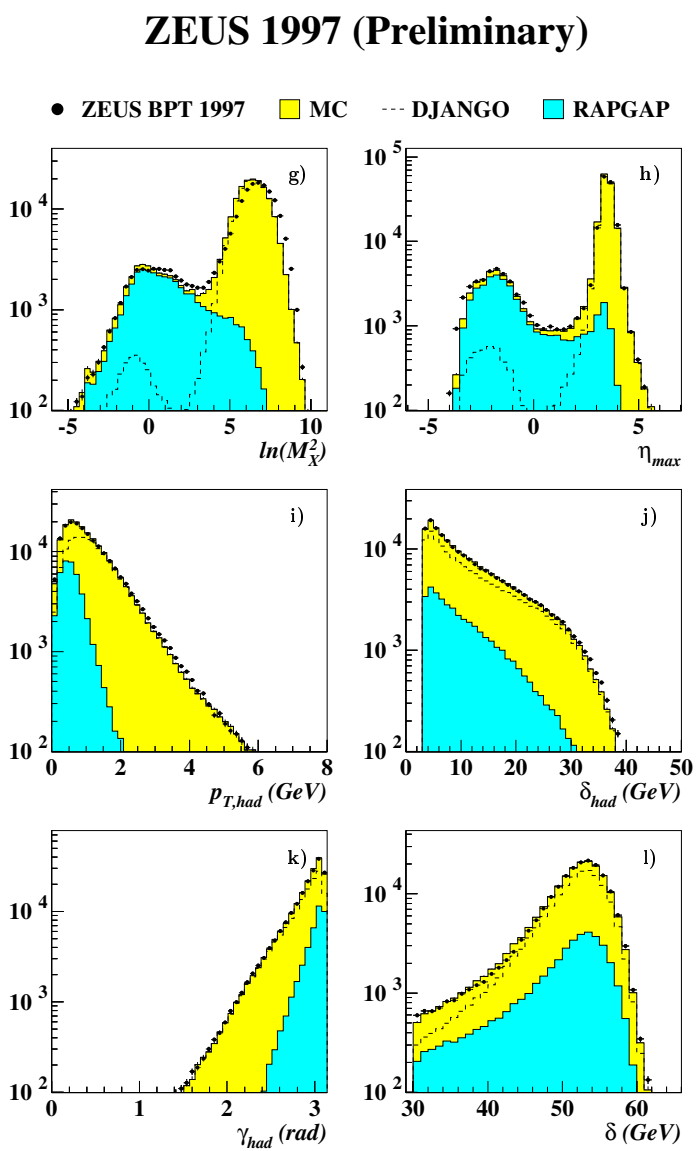

Fig. 7.11: Medium-y region (part two). Distributions of reconstructed quantities for data and Monte Carlo simulation. Shown are: g) $\ln(M_X^2)$, the logarithm of the invariant mass squared of the hadronic final state observed in the detector; h) $\eta_{\max}$, the pseudorapidity of the most forward energy deposit or track seen in the detector; i) hadronic transverse momentum $p_{T,\mathrm{had}}$; j) δ_{had}; k) γ_{had}; and l) δ.

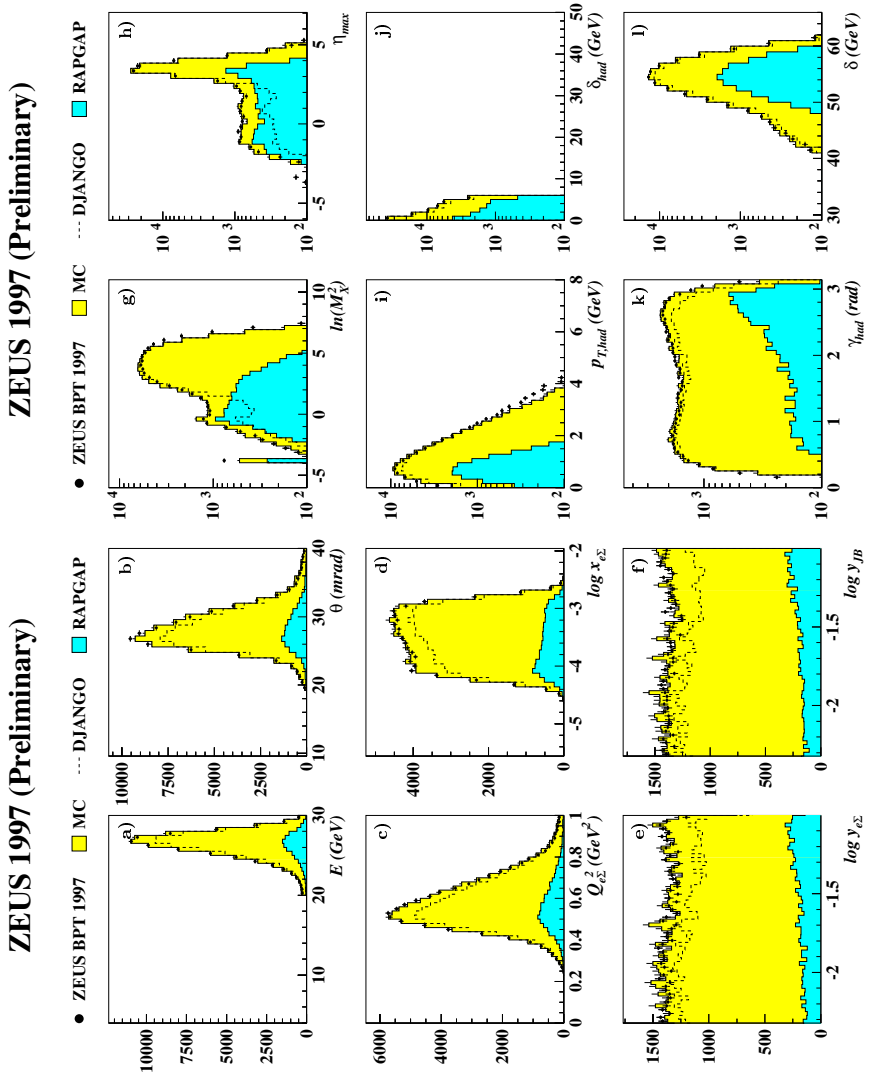

Fig. 7.12: Low-y region. Distributions of reconstructed quantities for data and Monte Carlo simulation. The points denote measured data, the light-shaded histogram is the sum of non-diffractive (DJANGO) and diffractive (RAPGAP) MC, the dark-shaded histogram is RAPGAP alone, and the dashed line is DJANGO alone. The plots a)–l) show the same quantities as in Figs. 7.10 and 7.11. Q^2, x and y have been reconstructed with the $e\Sigma$ method.

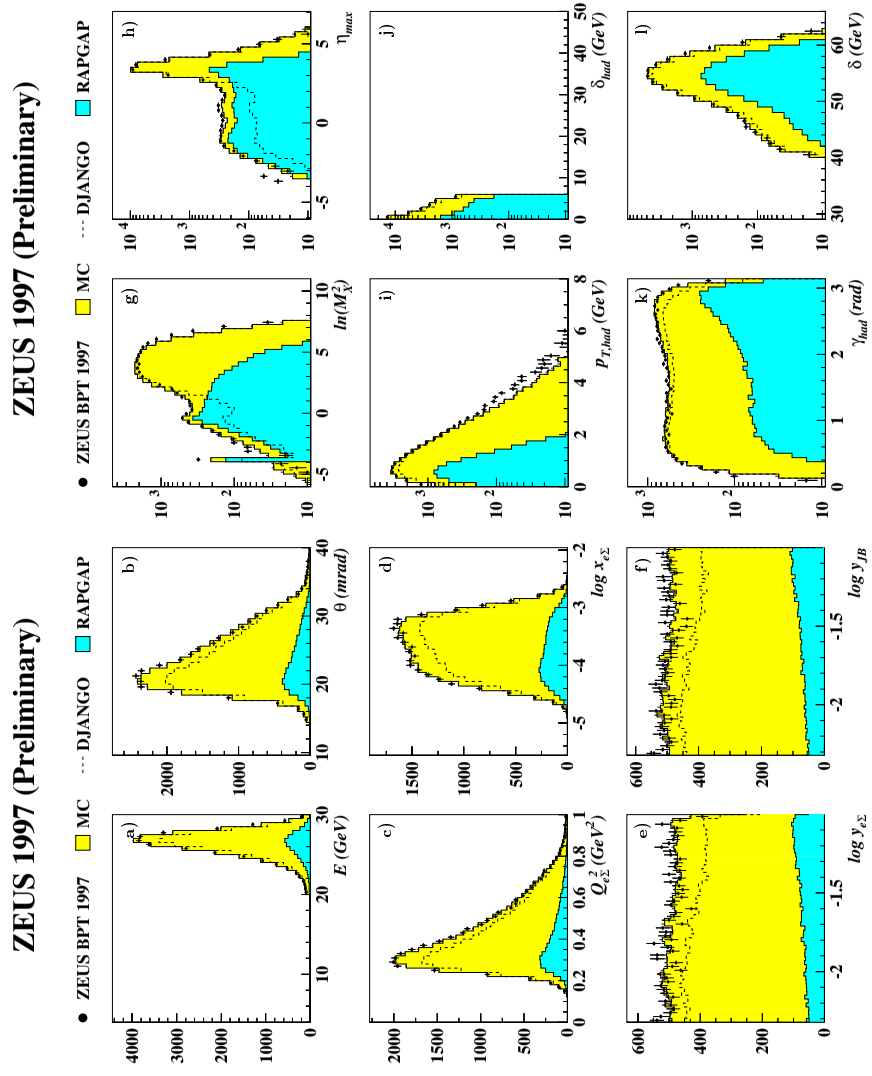

Fig. 7.13: Low-y prescaled region. Distributions of reconstructed quantities for data and Monte Carlo simulation. The points denote measured data, the light-shaded histogram is the sum of non-diffractive (DJANGO) and diffractive (RAPGAP) MC, the dark-shaded histogram is RAPGAP alone, and the dashed line is DJANGO alone. The plots a)–l) show the same quantities as in Figs. 7.10 and 7.11. Q^2, x and y have been reconstructed with the $e\Sigma$ method.

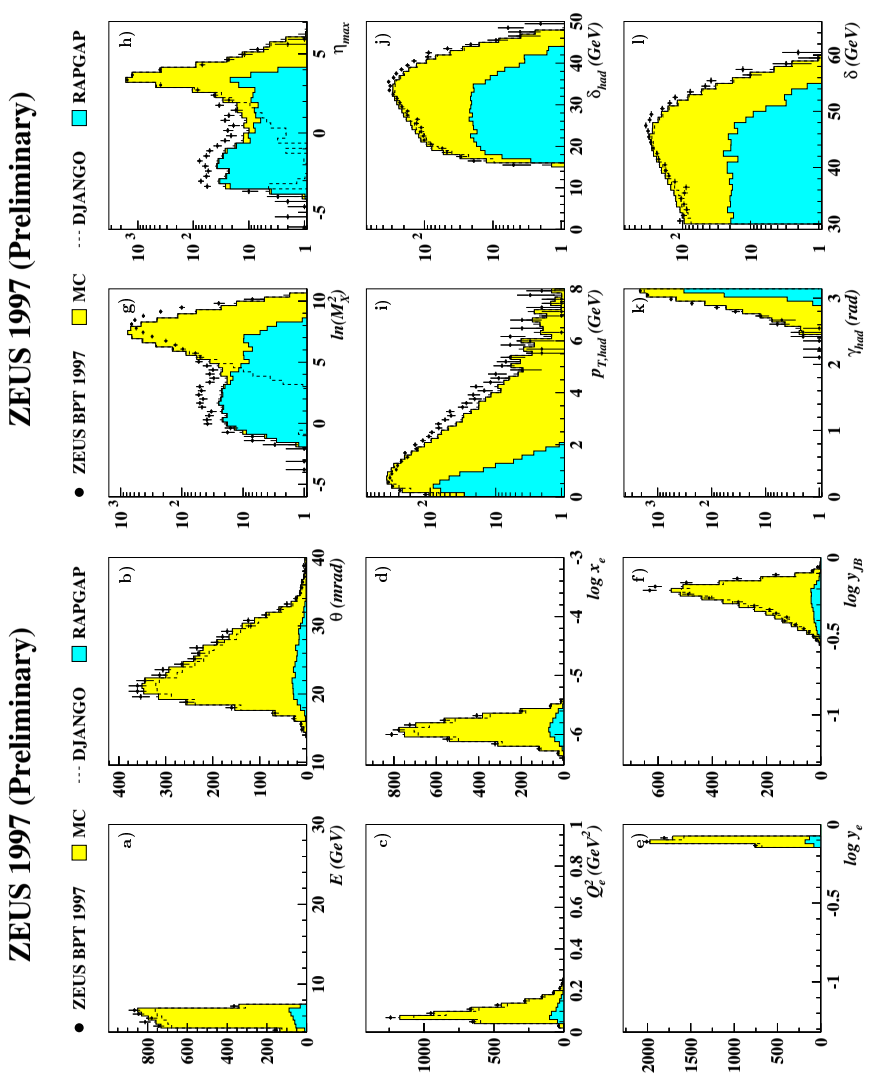

Fig. 7.14: High-y region. Distributions of reconstructed quantities for data and Monte Carlo simulation. The points denote measured data, the light-shaded histogram is the sum of non-diffractive (DJANGO) and diffractive (RAPGAP) MC, the dark-shaded histogram is RAPGAP alone, and the dashed line is DJANGO alone. The plots a)–l) show the same quantities as in Figs. 7.10 and 7.11.

with a higher fraction of diffractive events, while $\delta_{\rm had}$ would prefer an even lower fraction. The mixing fraction therefore reflects a compromise.

7.4.2 The vertex distribution

The distribution of Z of the vertex is an important ingredient for the structure function analysis, because the geometrical acceptance of the BPC depends on it. An incorrect vertex distribution in the Monte Carlo sample would therefore affect the measured structure function.

A "true" vertex distribution is needed as input for the MC generation. Due to the limited acceptance of the BPC, this distribution is expected to be significantly different from the vertex distribution as later measured by the BPT. Therefore, the true vertex distribution had to be determined independently. This was done using an unbiased sample of DIS events, where a scattered electron in the CAL was taken as a trigger condition, and the angle of the hadronic final state was limited such that the reconstructed vertex distribution was not biased [138]. The authors of [138] provided a special true vertex distribution for the 1997 BPT data taking period [139] (shown in Fig. 7.15), which was used in the event generation for this analysis.

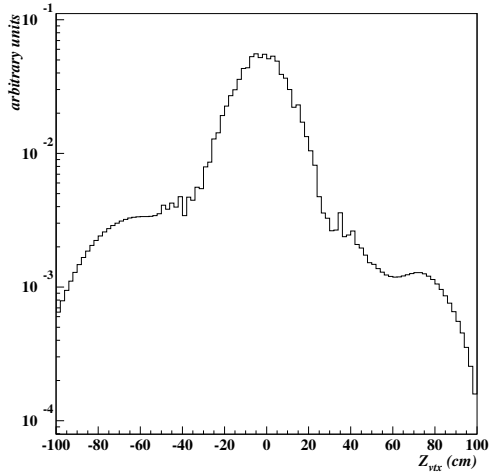

Fig. 7.15: Unbiased estimate of the Z vertex distribution from [139] for the 1997 BPT running period. The distribution has been smoothed outside ± 50 cm, because the statistical fluctuations in this region were too high for event generation purposes.

From a comparison of reconstructed vertex distributions in data and Monte Carlo (Fig. 7.16), it can be seen that the procedure worked fine, except in the region below $Z < -50$ cm, where the agreement of data and MC is not perfect. This is presumably due to a low statistical accuracy of the unbiased event sample in this region. In order not to sample from a wildly fluctuating vertex distribution, the original distribution was smoothed outside ± 50 cm. Anyway, only 3.3% of all events lie in the region below $Z < -50$ cm. The effect of this discrepancy is taken into account in the systematic error, by varying the cut on the reconstructed Z vertex, and turns out to be small.

The fraction of events where the CTD could not reconstruct a vertex used to be a problematic quantity in ZEUS structure function analyses. Such events show up in the CTD-reconstructed vertex distribution at the mean value for the run, around $Z \approx 0$. Since the resolution in kinematic variables is deteriorated for these events, their fraction affects the average resolution, which therefore is not correctly modelled by an MC that has a wrong fraction of "vertexless" events.

Also in this analysis, the number of vertexless events is not perfectly reproduced by the Monte Carlo, although it is better than e.g. in the previous BPC analysis, where the discrepancy was

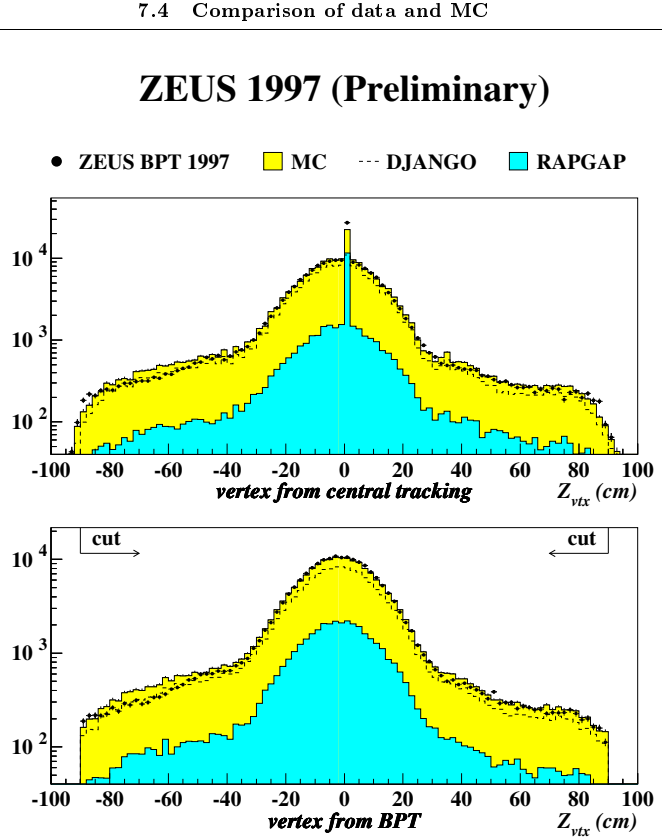

Fig. 7.16: Medium-y region. The event vertex as reconstructed by the CTD (top) and the BPT (bottom). The number of events without a CTD vertex is reproduced to better than 20% by the MC, but has anyway no effect on the analysis.

as large as a factor of two. The improvement is attributed to the effort put into the simulation of the hadronic final state, because the fraction of vertexless events depends predominantly on the energy and multiplicity of the hadronic final state, being quite different in diffractive and non-diffractive events. Anyway, nowhere in this analysis the reconstructed vertex from the CTD is used. All the problems related to the CTD vertexing efficiency are thus avoided.

Chapter 8

Results

In the first part of this chapter, the method and the results of the extraction of the proton structure function F_2 and of the total virtual photon-proton cross section $\sigma_{\text{tot}}^{\gamma^* p}$ are presented in detail. In the second part, the results are interpreted in the framework of phenomenological models, and further quantities of interest, like the total real photon-proton cross section, the effective intercept of the soft pomeron trajectory, $\alpha_{\mathbb{P}}$, and the parameter describing the rise of F_2, λ_{eff}, are extracted from fits to the data.

8.1 Measurement of the structure function

8.1.1 Unfolding technique

The quantity that needs to be measured in deep inelastic scattering for an extraction of the structure function F_2 is the double differential cross section for the reaction $ep \to eX$,

$$\frac{d^2\sigma}{dx\, dQ^2}(x, Q^2), \tag{8.1}$$

which is a function of x and Q^2. Measuring a cross section means to count the number of observed events, normalized to the integrated luminosity. Since in an experiment the cross section can only be measured by counting a finite number of events, one has to determine the observed number of events in a reasonable range in x and Q^2, a bin, yielding the observable quantity

$$\frac{\Delta^2\sigma}{\Delta x\, \Delta Q^2}(x, Q^2) = \frac{1}{\Delta x\, \Delta Q^2} \int_{\Delta x} \int_{\Delta Q^2} \frac{d^2\sigma}{dx\, dQ^2}(x', Q^{2\prime})\, dx'\, dQ^{2\prime}. \tag{8.2}$$

In principle, the point in x and Q^2 where the observed cross section is quoted can be chosen anywhere inside the bin. However, there is a special choice: The mean value theorem predicts that if a function is continuous in the interval Δx, there is a value ξ inside the interval Δx for which

$$\frac{1}{\Delta x} \int_{\Delta x} f(x)\, dx = f(\xi). \tag{8.3}$$

So, there is a point in x and Q^2 for which the averaged cross section value in the bin is equal to the actual cross section value at x and Q^2, which allows to identify the averaged and the actual cross section. If x' and Q'^2 are chosen to be different from this point, a bin-centering correction $c(x, x', Q^2, Q'^2)$ has to be applied according to

$$\frac{d^2\sigma}{dx\, dQ^2}(x', Q'^2) = c(x, x', Q^2, Q'^2) \frac{d^2\sigma}{dx\, dQ^2}(x, Q^2). \tag{8.4}$$

It will be shown later how this problem is avoided completely, by using a technique where all bin-centering corrections cancel.

As a further complication, the number of events M_i that are observed in a bin is, in practice, not equal to the true number of events N_i that would have been observed in a perfect measurement. Instead, they are related via

$$M_i = \sum_j T_{ij} N_j, \tag{8.5}$$

where T_{ij} is the transfer or smearing matrix, and $T_{ij} \neq \delta_{ij}$. Three ingredients enter in T_{ij}:

- Detector effects:

  Detectors have a finite resolution, determining how well quantities like x and Q^2 can be reconstructed, i.e. how close the reconstructed value is to the true one. By imperfect reconstruction, events can migrate out of their true bin and get reconstructed in a different bin. Good reconstruction algorithms have a good resolution, such that the nondiagonal elements of T_{ij} remain small. Obviously, the nondiagonal elements in T_{ij} can also be reduced by choosing larger bins; however, large bins yield less information about the shape of the function to be measured. The chosen bin width therefore is always a compromise, and a width between $\pm 1\sigma$ and $\pm 2\sigma$ is commonly used.

- Physics effects:

  There are also physics processes leading to migration of events. Radiative effects, like the radiation of a hard real photon in the initial state (ISR), let events migrate to a different x and Q^2, if the photon is not detected or not taken into account in the reconstruction.

- Event selection efficiency:

  Cuts made to suppress background events or to ensure well-reconstructed events are usually not fully efficient for signal events. While migration effects lead to non-diagonal elements in the transfer matrix, the selection efficiency can be separated as a diagonal matrix (with elements smaller than unity).

The matrix T_{ij} is determined from a Monte Carlo Simulation which includes both detector effects (calculated in the detector simulation) and physics effects (calculated in the event simulation). The efficiency of selection cuts is also extracted from the Monte Carlo.

The purpose of an unfolding method is to retrieve the true from the measured values.[1] Different unfolding techniques differ in how much they rely on the transfer matrix calculated from Monte Carlo as an approximation of the transfer matrix in data. Only the simplest unfolding technique will be discussed and used here, the bin-by-bin unfolding.

The bin-by-bin unfolding method approximates the transfer matrix by a diagonal matrix. This means that it takes into account only the net migrations out of and into a bin, but not the correlations between bins, i.e. the information where migrating events come from and go to:

$$T_{ij} = \delta_{ij} T_i, \tag{8.6}$$

the diagonal elements of which are given by

$$T_i = \frac{M_i^{\mathrm{MC}}}{N_i^{\mathrm{MC}}}. \tag{8.7}$$

This leads to

$$M_i^{\mathrm{data}} = \frac{M_i^{\mathrm{MC}}}{N_i^{\mathrm{MC}}} N_i^{\mathrm{data}}. \tag{8.8}$$

[1] Which is, in principle, the task to invert the transfer matrix. In practice, it becomes more complicated, e.g. by statistical fluctuations that tend to make the matrix inversion unstable.

Cross sections are related to the numbers of true events via the luminosity $\mathcal{L}$:

$$\sigma = \frac{N}{\mathcal{L}}. \tag{8.9}$$

Consequently, the double-differential cross section can be written as

$$\left(\frac{d^2\sigma}{dx\,dQ^2}(x,Q^2)\right)_i = \frac{N_i}{\mathcal{L}}, \tag{8.10}$$

and, applying Eq. (8.10) for data and MC to eliminate the true numbers of events N_i from Eq. (8.8),

$$\left(\frac{d^2\sigma}{dx\,dQ^2}(x,Q^2)\right)_i^{\mathrm{data}} = \frac{\mathcal{L}^{\mathrm{MC}}}{\mathcal{L}^{\mathrm{data}}} \cdot \frac{M_i^{\mathrm{data}}}{M_i^{\mathrm{MC}}} \cdot \left(\frac{d^2\sigma}{dx\,dQ^2}(x,Q^2)\right)_i^{\mathrm{MC}}. \tag{8.11}$$

In this form, it becomes obvious that bin-centering corrections automatically cancel when using the same x and Q^2 values in the data and the MC term. This means that x and Q^2 can be chosen as convenient numbers anywhere in the bin i, without complicating the procedure. Usually, they are chosen close to the bin center. As a last step, Eq. (8.11) can be written in terms of structure functions:

$$\Big((Y_+F_2 - y^2F_L)(1+\delta_r)\Big)_i^{\mathrm{data}} = \frac{\mathcal{L}^{\mathrm{MC}}}{\mathcal{L}^{\mathrm{data}}} \cdot \frac{M_i^{\mathrm{data}}}{M_i^{\mathrm{MC}}} \cdot \Big((Y_+F_2 - y^2F_L)(1+\delta_r)\Big)_i^{\mathrm{MC}}. \tag{8.12}$$

It is assumed that $F_L = 0$ (the effect of F_L is discussed in section 8.1.3), and that radiative corrections are described correctly by the Monte Carlo simulation (the uncertainty of radiative corrections is estimated in appendix B.5). Then, the double differential cross section is simply proportional to F_2, and the result is:

$$\Big(F_2(x,Q^2)\Big)_i^{\mathrm{data}} = \frac{\mathcal{L}^{\mathrm{MC}}}{\mathcal{L}^{\mathrm{data}}} \cdot \frac{M_i^{\mathrm{data}}}{M_i^{\mathrm{MC}}} \cdot \Big(F_2(x,Q^2)\Big)_i^{\mathrm{MC}}. \tag{8.13}$$

There are, however, some issues to be aware of. In bin-by-bin unfolding, the MC simulation describes migrations correctly only if the structure function in MC is the same as in data. If it is different, the unfolding tends to bias the resulting measured structure function toward the one in the Monte Carlo. To avoid this, the MC events are reweighted to match the structure function as measured in the data, and the unfolding and reweighting process is iterated. It converges after a few steps. Secondly, since the cross section is nowhere explicitly calculated, and all analysis steps are performed equally on both data and MC, it is possible to make mistakes, like e.g. introducing cuts that reject most of the signal events, or using wrong kinematic reconstruction formulae, without affecting the resulting F_2 in an obvious manner. This requires the control of every single step in the unfolding procedure.

The above procedure has to be generalized in this analysis to the case where more than one MC sample is used. It is convenient to renormalize the number of events in MC by the ratio of luminosities,

$$m_i^{\mathrm{MC}} = M_i^{\mathrm{MC}} \cdot \frac{\mathcal{L}^{\mathrm{data}}}{\mathcal{L}^{\mathrm{MC}}}, \tag{8.14}$$

which yields from Eq. (8.13)

$$\Big(F_2^{\mathrm{data}}(x,Q^2)\Big)_i = \frac{M_i^{\mathrm{data}}}{m_i^{\mathrm{MC}}} \cdot \Big(F_2^{\mathrm{MC}}(x,Q^2)\Big)_i. \tag{8.15}$$

A weight w_j is assigned to each MC event, accounting for transforming from MRSA to ALLM97, and for the diffractive fraction according to

$$w_j = \frac{F_2^{\mathrm{MC}}(x,Q^2)}{F_2^{\mathrm{MRSA}}(x,Q^2)} \cdot \mathcal{L}^{\mathrm{data}} \cdot \begin{cases} f(x,Q^2)\,/\mathcal{L}^{\mathrm{RAPGAP}} & \text{(RAPGAP)} \\ [1-f(x,Q^2)]/\mathcal{L}^{\mathrm{DJANGO}} & \text{(DJANGO)}. \end{cases} \tag{8.16}$$

The normalized number of MC events in bin i is then given by $m_i^{\rm MC} = \sum w_j$, where the sum runs over all events reconstructed in that bin. In the first iteration $F_2^{\rm MC} = F_2^{\rm ALLM97}$ is used. For further iterations, a fit of the form of the ZEUS REGGE fit (section 2.9.3.11) is made to the measured F_2 values and used as $F_2^{\rm MC}$ instead.

One of the advantages of the bin-by-bin unfolding method is that the statistical errors are uncorrelated between bins. The statistical error of F_2 is therefore simply given by the quadratic sum of the statistical errors of data and MC:

$$\left(\frac{\Delta F_2}{F_2}\right)_i = \sqrt{\frac{1}{M_i^{\rm data}} + \frac{\sum w_j^2}{(\sum w_j)^2}}. \tag{8.17}$$

Four separate runs of the analysis job are needed to measure F_2 in the whole kinematic range, due to the four different trigger slots and two reconstruction methods. Possible "overlap" between analysis regions, i.e. events that get reconstructed in different bins with the electron and the $e\Sigma$ method, is thus automatically treated correctly.

8.1.2 Binning of the data

In contrast to the usual choice of x and Q^2 as independent variables in F_2 analyses, bins in y and Q^2 are chosen in this analysis in order to make optimum use of the available phase space in the kinematic plane.[2] All the above discussion in terms of x and Q^2 remains valid as well for y and Q^2.

The region of the kinematic plane that can be covered with bins is essentially limited by the geometrical acceptance of the BPC. The grid of bins is identical to the previous analysis [57] in the overlap region between them.[3] At low y, the bin widths in y are chosen to be 1.5 times the y resolution, decreasing to bin widths equal to the resolution at higher y. The Q^2 bins have a width of twice the Q^2 resolution. The bin grid and the x and Q^2 resolutions are shown in Fig. 8.1.

The following bin quality criteria are checked using the MC simulation:

- Before cuts (i.e. for all generated events):

$$\text{geometrical acceptance} = \frac{\#\text{ in fiducial area \& generated in the bin}}{\#\text{ generated in the bin}}. \tag{8.18}$$

  The geometrical acceptance is between 4–14% for most of the bins, bins with 1–4% at the edge of acceptance are also accepted (Fig. 8.2). A low geometrical acceptance typically corresponds to a high statistical error, and those bins are more strongly affected by uncertainties in the alignment, or changes of the fiducial area and event vertex cuts.

  This criterion results in the characteristic shape of the region accessible to the BPC, limited by iso-θ lines.

- After cuts (i.e. for those events passing the selection cuts):

$$\text{acceptance} = \frac{\#\text{ generated \& reconstructed in the bin}}{\#\text{ generated in the bin}}. \tag{8.19}$$

  The acceptance is a measure of migrations out of bins into the surrounding ones. As a rule of thumb, for bins that have a width of $\pm 1\sigma$ in y and Q^2, one expects an acceptance of

[2] Precisely, the bins are parallelogram-shaped bins in x and Q^2. This subtle difference becomes relevant when dealing with radiative events.

[3] The resolution of kinematic variables has not improved very much by using the BPT in addition, because both the x and Q^2 resolution were already dominated by the energy resolution of the BPC (section 6.3.7).

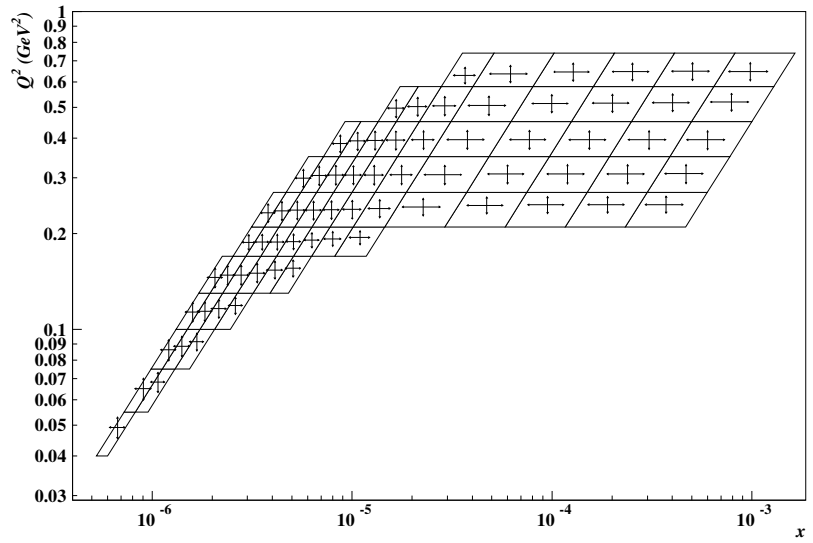

Fig. 8.1: The resolution in x and Q^2 in the bins chosen for the F_2 analysis. For events generated in a bin, the arrows cover $\pm 1\sigma$ of the resolution and are centered at the mean reconstructed x and Q^2.

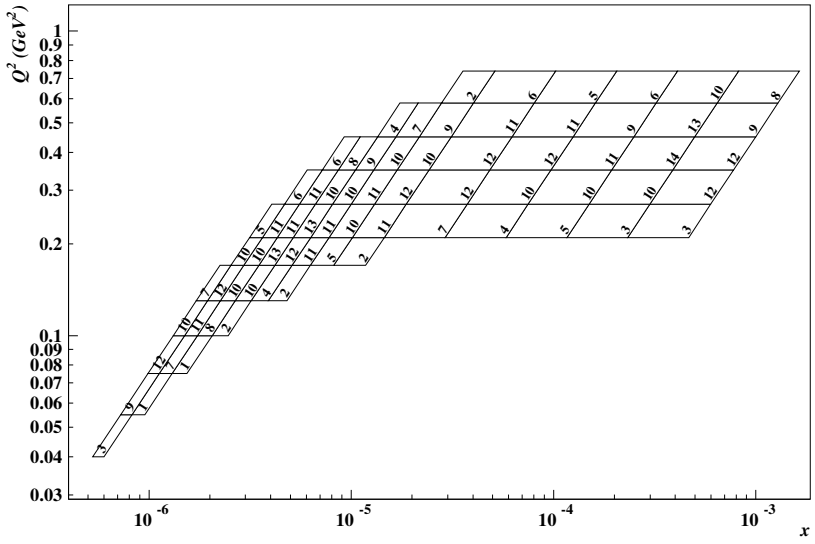

Fig. 8.2: The geometrical acceptance in the bins (in %). See text for the definition.

$(68\%)^2 = 46\%$. For the bins of this analysis, the acceptance varies between 50–70% (Fig. 8.3).

$$\text{purity} = \frac{\#\text{ generated \& reconstructed in the bin}}{\#\text{ reconstructed in the bin}}. \tag{8.20}$$

The purity is a measure of migrations into the bins from outside. For the bins of this analysis, the purity ranges typically between 40–65%. At very low y, it decreases to 30% (Fig. 8.4).

Note that the ratio of acceptance and purity is the element of the diagonal approximation to the transfer matrix in Eq. (8.7).

8.1.3 Estimate of the effect of F_L

Since $F_L^{\text{MC}} = 0$ was chosen at the stage of event generation, the result of the above unfolding procedure is F_2^{data} under the assumption $F_L^{\text{data}} = 0$. However, given that $R = F_L/(F_2 - F_L)$ is known (from a measurement or from a theoretical calculation), the extracted $F_2^{F_L=0}$ can be corrected for $F_L > 0$ afterwards, if the effect of F_L is small:

$$F_2^{F_L>0} = F_2^{F_L=0} \cdot \left(1 - \frac{y^2}{1+(1-y)^2} \cdot \frac{R}{1+R}\right)^{-1}. \tag{8.21}$$

The value of R has never been measured in the BPC kinematic region, so it must be taken from theory. At higher Q^2, one usually relies on F_L as calculated in NLO-pQCD in the framework of a DGLAP fit to the measured F_2. However, as perturbative QCD is not expected to be applicable at Q^2 as low as in this analysis, a different approach is needed.

Two strategies have been used at HERA in the past. In the 1995 BPC analysis, ZEUS used

$$R = k\frac{Q^2}{m_\rho^2} \quad \text{with} \quad k = 0.5. \tag{8.22}$$

In the table of F_2 values, $F_2^{F_L=0}$ and the effect of $F_L \neq 0$ were quoted.

For their 1995 low-Q^2 measurement [140], H1 used R according to the BKS model [76], which can be parameterized in the range of interest here to a very good approximation as

$$R = k\frac{Q^2}{m_\rho^2} \quad \text{with} \quad k = 0.165, \tag{8.23}$$

i.e. H1 used for R a function that is smaller by a factor of 3 than the value used by ZEUS. In the table of F_2 values, $F_2^{F_L=\text{BKS}}$ and the used value of R were quoted.

Both methods are equivalent in the sense that if in the future a measurement of F_L should become available, the published values can readily be corrected to it without loss of information or precision. For this analysis, it was decided to follow the second strategy. Since the parameterization of R provided by the authors of [76] refuses to work below $x < 6 \cdot 10^{-6}$, the approximation is used instead. The effect of assuming F_L^{BKS} instead of $F_L = 0$ is small: in some bins at high y and moderate Q^2, it reaches 2–3%, in the remaining bins it is negligible (Fig. 8.5). This is due to the very low Q^2 in this analysis ($F_L \propto Q^4$ for $Q^2 \to 0$, while $F_2 \propto Q^2$).

However, from a puristic point of view the presence of F_L prevents a measurement of F_2 as long as F_L has not been measured. The actually measured quantity is the double differential cross section, and the only point to make in favor of calling the above procedure a measurement of F_2 is the fact that the effect of F_L is believed to be small.

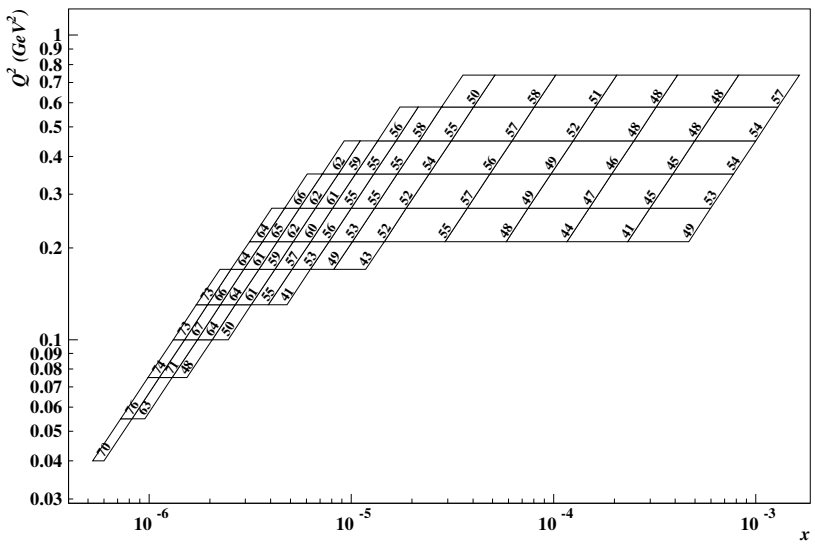

Fig. 8.3: The acceptance in the bins (in %). See text for the definition of acceptance.

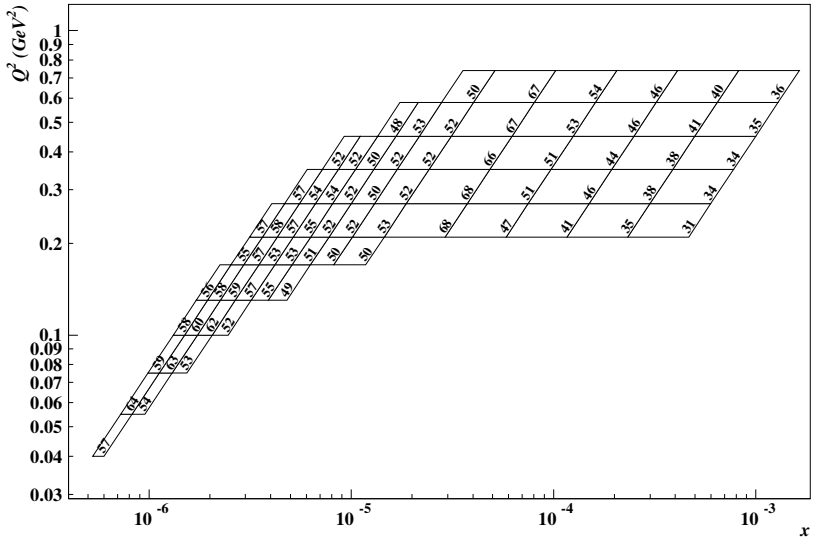

Fig. 8.4: The purity in the bins (in %). See text for the definition of purity.

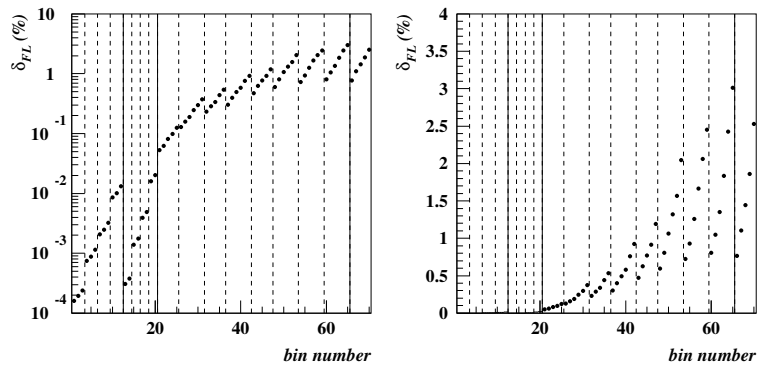

Fig. 8.5: Effect on F_2 from assuming $R = 0.165 \cdot Q^2/m_\rho^2$ (approximation of the BKS model) instead of $R = 0$, plotted vs. bin number. See Fig. 8.6 for the bin numbering scheme.

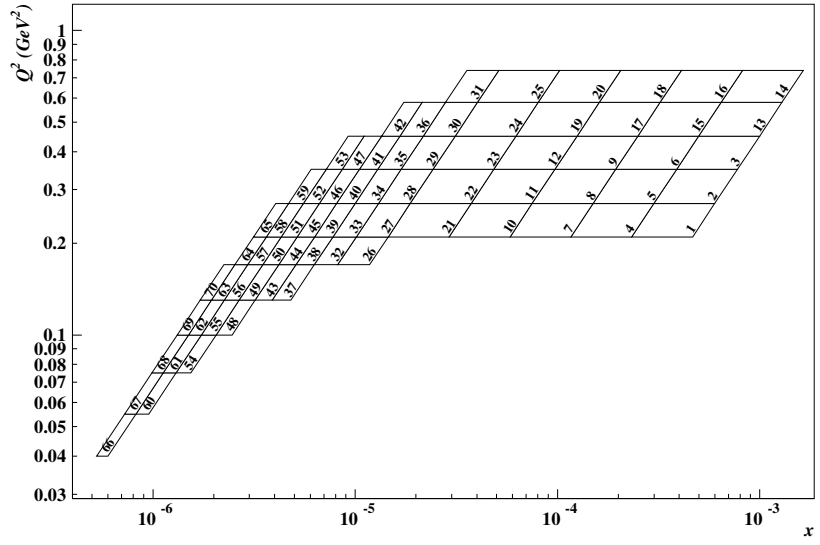

Fig. 8.6: The bin number increases from the low-y prescaled, the low-y and the medium-y region to the high-y region. For each region, it increases from low y to high y, and for each y from low Q^2 to high Q^2.

8.1.4 Estimate of systematic uncertainties

Fifteen systematic checks were performed to study the stability of the results under variations of the detector calibration, alignment and efficiency, of the event selection cuts, and of the mixing ratio between DJANGO and RAPGAP. In each case, one of the aspects is varied, the determination of F_2 repeated and the change in the result noted. That is, the gradient vector

of F_2 with respect to the different checks, ∇F_2, multiplied by the magnitude of the variation, $\Delta\vec{x}$, is determined and taken as a measure of the systematic uncertainty. The total systematic error is calculated as the quadratic sum of the individual contributions, separately for positive and negative ones.

This technique is relatively insensitive to statistical fluctuations, because the F_2 extraction is performed with the same (i.e. a 100% correlated) sample of events, only slightly modified in a certain aspect. Otherwise, the systematic error would unwantedly include a contribution from the statistical error. This can, however, be the case when events migrate out of bins due to variations of the kinematic reconstruction.

The average statistical error (including the statistical error of the number of MC events) is 2.6% per bin, the average systematic error 3.3%, approaching the typical precision of fixed target experiments. In most bins, the systematic error is of similar magnitude as the statistical one, and there is no single dominant contribution to the total systematic error. For the two bins at highest y, the systematic error is dominated by the uncertainty in the fraction of diffractive events, and the systematic error is significantly larger than the statistical one. The uncertainty of the luminosity determination induces an additional overall normalization uncertainty of $\pm 1.8\%$.

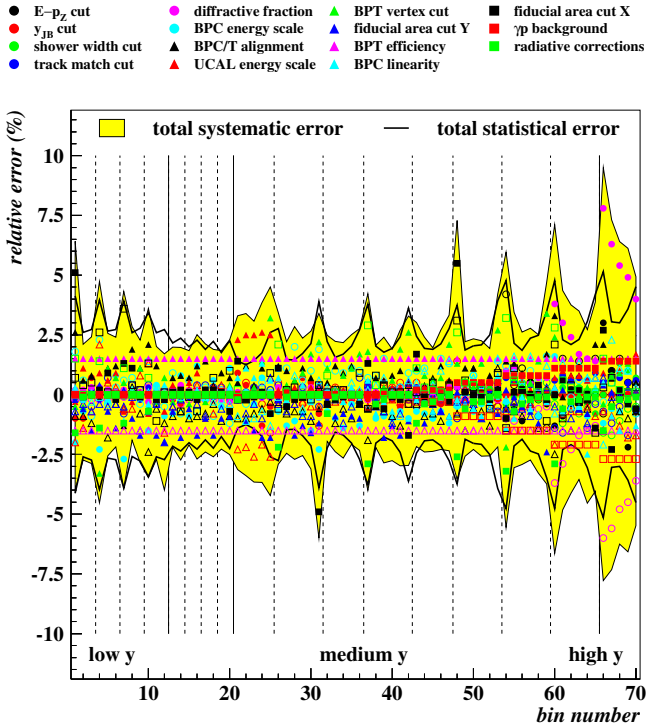

Fig. 8.7: Summary of effects of systematic checks, plotted vs. bin number. The shaded band shows the total systematic error, the thick solid line the total statistical error. Open and filled symbols show the effect of the "down" and "up" direction of the checks on the resulting F_2, which is displayed in more detail in Fig. 8.8.

In order to quantify the systematic error, analysis cuts have been varied in a range reflecting the (limited) arbitrariness of picking a particular cut value; in most cases, beyond the range of the variation known problems would show up, like trigger thresholds, acceptance limits etc. becoming important. Reconstruction parameters have been varied according to the precision to which they are known. In detail, the following checks were performed (the effect on F_2 is given in parentheses, and is also displayed in Figs. 8.7 and 8.8):

- Variation of the $\delta > 30\,\mathrm{GeV}$ cut by $\pm 2\,\mathrm{GeV}$ (mostly below 1.5%, up to 4% at high y).
- Variation of the $y_{\mathrm{JB}} > 0.06/0.004\,\mathrm{GeV}$ cut by $\pm 0.01/0.001$ (up to 1% at moderate y).
- Variation of the shower width cut by $\pm 0.1\,\mathrm{cm}$ (up to 1.5% at low electron energies).
- Variation of the track match cut by $\pm 2\sigma$ (up to 2% at low electron energies).
- Variation of the fiducial area cut in X by $\pm 1\,\mathrm{mm}$ (mostly below 3%, up to 6% in bins with low geometrical acceptance).
- Variation of the fiducial area cut in Y by $\pm 1\,\mathrm{mm}$ (up to 2%).
- Change of the BPT vertex cut from $\pm 90\,\mathrm{cm}$ to $\pm 50\,\mathrm{cm}$ (up to 3% in bins with low geometrical acceptance).

  Excludes events coming from the range in vertex Z that is not well reproduced by MC (section 7.4.2).
- Variation of the BPC energy scale by $\pm 0.3\%$ (mostly 2%, up to 3% at low y).

  Reflects the uncertainty of the BPC energy scale after calibration (section 6.1.1).
- Variation of the BPC energy response by $\pm 1\%$ at $4\,\mathrm{GeV}$, decreasing linearly to $\pm 0\%$ at $27.5\,\mathrm{GeV}$ (up to 2.5% at medium and high y).

  Reflects the uncertainty of the linearity of the BPC energy response (section 6.1.1).
- Variation of the BPC/BPT position by $\pm 200\,\mu\mathrm{m}$ (mostly 1.5%, up to 3.5% in some bins).

  Reflects the uncertainty of the absolute BPC/BPT position after alignment (section 6.1.3).
- Variation of the BPT efficiency by $\pm 1.5\%$ (1.5%).

  Reflects the uncertainty of the BPT tracking efficiency (section 6.1.4).
- Variation of the CAL energy scale by $\pm 3\%$ (up to 2.5% at very high and very low y).

  Reflects the uncertainty of the CAL hadronic energy scale (section 3.2.1).
- Variation of the fraction of diffractive events by $\pm 15\%$ (relative), or by the difference between fractions obtained from $\eta_{\max}$ or δ_{had} and $p_{T,\mathrm{had}}$ (mostly below 1%, up to 8% in the two highest y bins).

  Reflects the remaining uncertainty about the fraction of diffractive events (section 7.2).
- Variation of the subtracted photoproduction background by $+200\%$ and -100% (up to 2.5% at high y).

  Reflects the uncertainty in normalization of subtracted photoproduction from the comparison of photoproduction MC and LUMI-tagged photoproduction events (section 7.3.2).

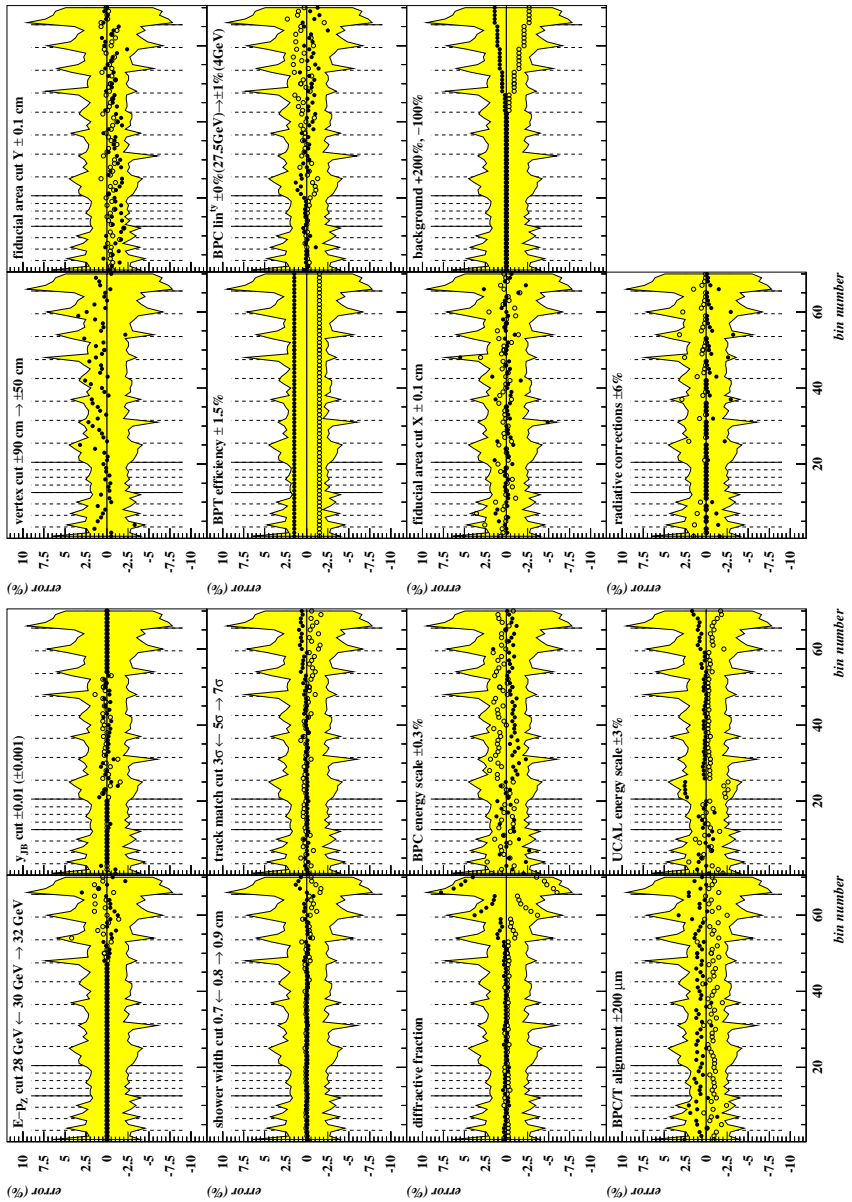

Fig. 8.8: Effect of individual systematic checks, plotted vs. bin number. The shaded band indicates the total systematic error, open and filled circles show the effect of the "down" and "up" direction of the check on the resulting F_2.

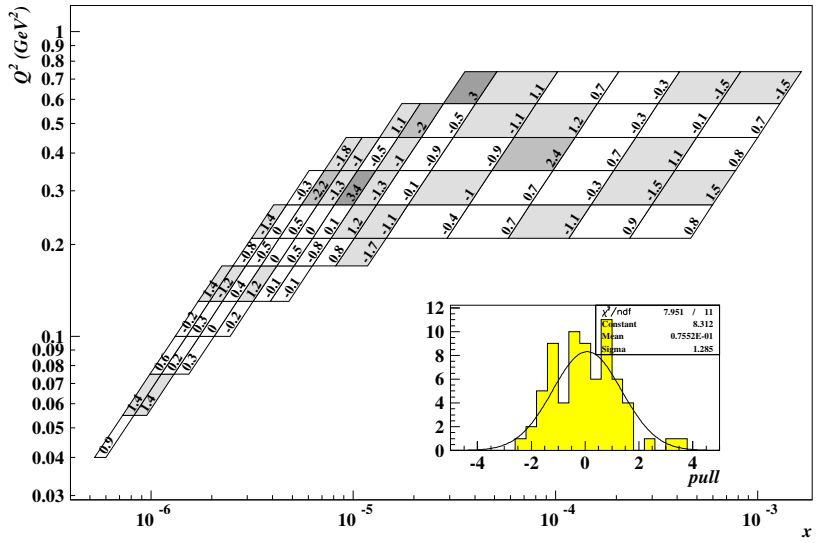

Fig. 8.9: Pull of the measured F_2 with respect to a smooth parameterization, taking into account statistical errors only. In the white bins, F_2 deviates by less than $\pm 1\sigma$ from the parameterization. The inset shows the one-dimensional pull distribution.

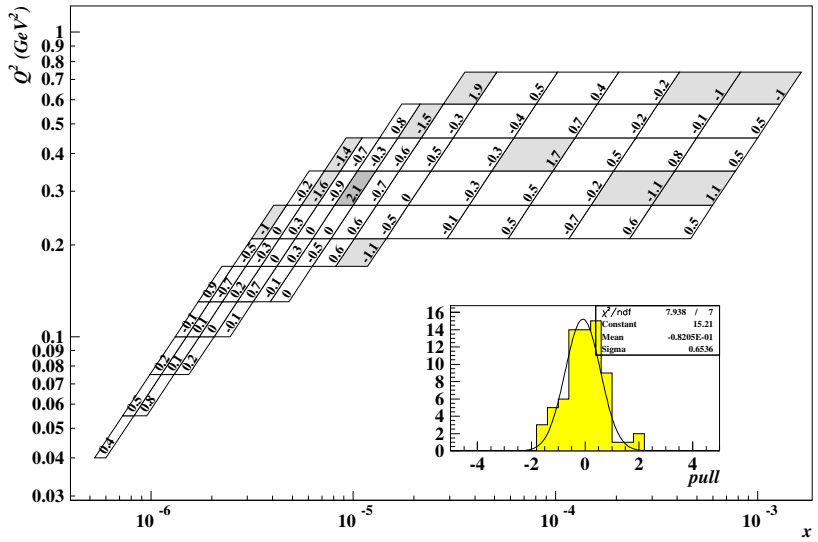

Fig. 8.10: Same as before, but statistical and systematic errors added in quadrature.

- Radiative corrections: reweight F_2 in the Monte Carlo outside the bins of the analysis by $\pm 6\%$, thus varying the amount of unrecognized ISR events migrating into the region of the measurement (up to 3% in some bins).

  This reflects the uncertainty of F_2 at lower Q^2 and higher x than in the analysis, estimated from an analysis of ISR events (appendix B).

Compared to the previous measurement, the overall systematic uncertainty has been reduced by roughly a factor of 2–3. The main improvements lie in a better knowledge of the detectors, a better simulation of the hadronic final state, a more sophisticated estimate of the uncertainty of radiative corrections and less photoproduction background which needs to be subtracted. These improvements reduce the total systematic error by two effects: they allow to decrease the magnitude of some variations, and they render the result less sensitive to variations of other parameters.

The results of some consistency checks were not included in the systematic error. For example, the reconstruction method in the low-y region was changed from $e\Sigma$ to double-angle, and from ZUFO's to CAL-only, and the analysis repeated. No deviations apart from statistical fluctuations were observed (note that the assumed high correlation between original and varied sample is not given here due to the change in reconstruction method). In order to study the possible effect of noise in a worst-case scenario, the analysis was repeated with lower noise cuts (100/150 MeV). The effect on F_2 was negligible with the exception of the two lowest y bins, where effects of up to 10% were observed. This is the effect of the known insufficient noise simulation in the MC.

As a final check, the ZEUS REGGE fit is taken to represent a smooth parameterization of the data and compared to the measured F_2 values (Figs. 8.9 and 8.10). Shown is the pull value, $(F_2 - F_2^{\rm fit})/\Delta F_2$. No accumulations of bins that deviate systematically from the fit are observed. When taking only statistical errors into account, the width of the pull distribution is greater than unity, which indicates the presence of systematic effects. Taking statistical and systematic errors added in quadrature, the width of the pull distribution falls below unity, because the systematic effects are not completely uncorrelated between bins (or have been slightly overestimated).

8.1.5 Results of the measurement

The extracted F_2 values are listed in Table 8.1, and shown in Figs. 8.11 and 8.12 in comparison to the previous analysis [57] and to data from the E665 experiment [141]. Inner error bars represent statistical errors, outer error bars statistical and systematic errors added in quadrature. Also shown is the ZEUS REGGE 97 fit from section 8.2.2.

In general, good agreement with the previous analysis is observed, and the errors have been significantly reduced in the overlap region. At low Q^2 and low x, the new results are systematically lower by about 1σ of the total error than the old points. This effect is most pronounced in the two bins at $Q^2 = 0.11\,\text{GeV}^2$ and $0.20\,\text{GeV}^2$. Most parameterizations that included the 1995 BPC data had problems in accomodating these points, and agree better with the new result. This discrepancy might be attributed to the fact that these bins are strongest affected by the fraction of diffractive events (i.e. by the quality of the simulation of the hadronic final state), and by the amount of statistically subtracted background.

Compared to the 1995 analysis, the new measurement extends toward lower Q^2 (adding three new bins in Q^2), as well as higher and lower x, adding one respectively four new bins in x.

With this analysis, ZEUS has finally reached overlap with the x values of the fixed-target experiment E665. The F_2 values typically agree within the quoted errors. The agreement in the x-shape of F_2 is good at $Q^2 = 0.65\,\text{GeV}^2$, but deteriorates toward lower Q^2. The extrapolation of the ZEUS points with the ZEUS REGGE 97 fit is about 10–15% above the E665 measurements at the lowest Q^2 bins of E665.

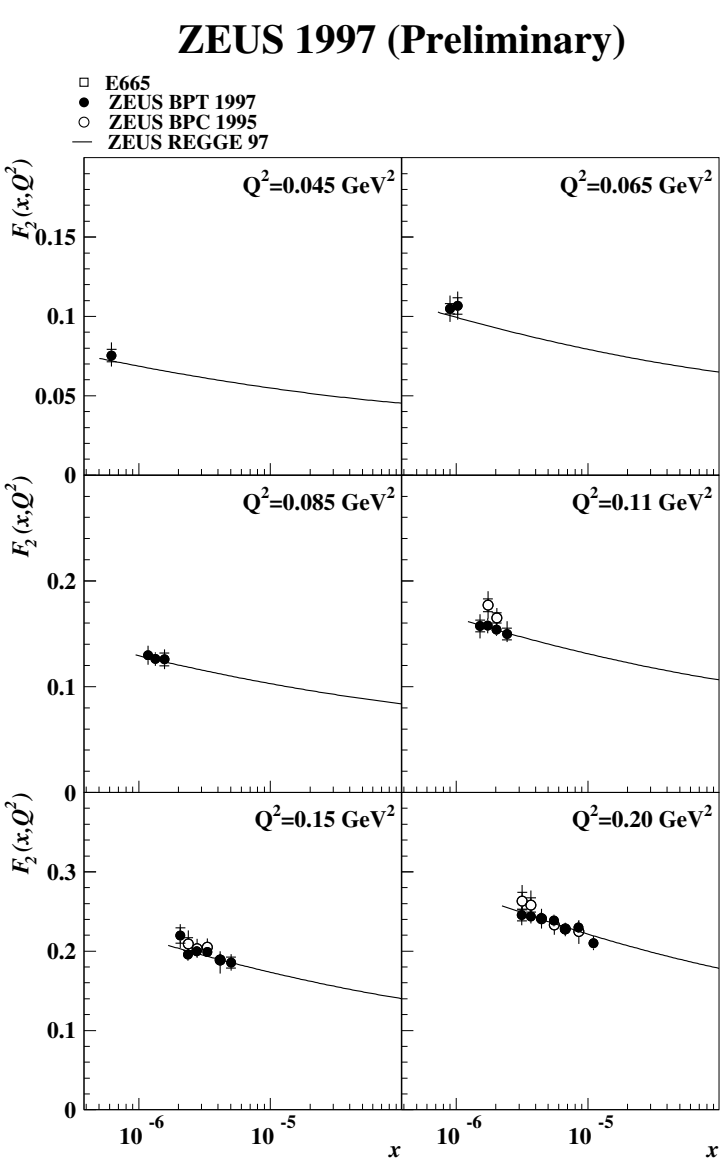

Fig. 8.11: Measured F_2 vs. x in bins of Q^2 (for $0.045\,\mathrm{GeV}^2 < Q^2 < 0.20\,\mathrm{GeV}^2$). Filled circles denote results from this analysis, and open circles the previously published data from 1995. The effect of F_L has been corrected for by using $R = 0.165 \cdot Q^2/m_\rho^2$. Shown as solid line is the ZEUS REGGE 97 fit (see text).

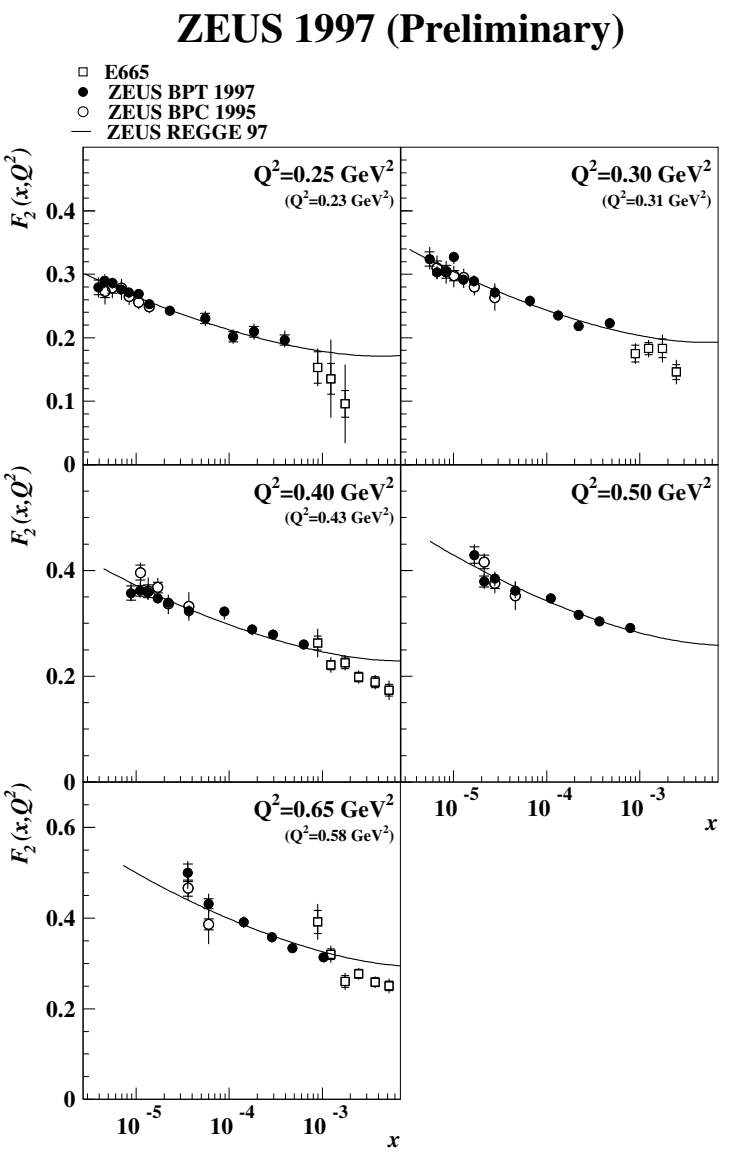

Fig. 8.12: Measured F_2 vs. x in bins of Q^2 (for $0.25\,\mathrm{GeV}^2 < Q^2 < 0.65\,\mathrm{GeV}^2$). As in Fig. 8.11. Open squares show the results from E665. The Q^2 values given in parentheses denote the original Q^2 of the E665 measurements, which have been shifted to the Q^2 of the ZEUS measurement using the ALLM97 parameterization. Normalization uncertainties from both ZEUS and E665 are not included.

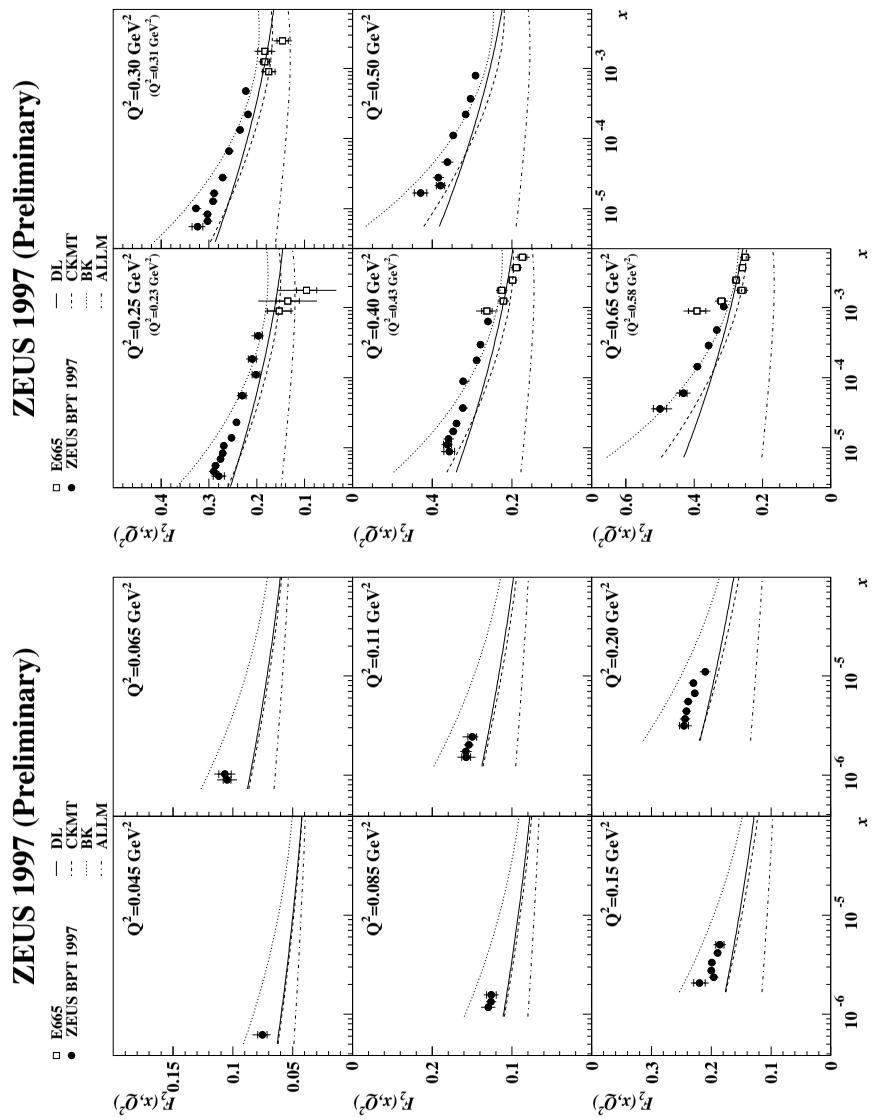

Fig. 8.13: Comparison of the F_2 results to early parameterizations that did not include the 1995 BPC data in the fit. Shown as solid line is the DL (Donnachie and Landshoff) parameterization, the dashed line represents the CKMT (Capella, Kaidalov, Merino and Tran Thanh Van), the dotted line the BK (Badełek and Kwieciński) and the dash-dotted line the ALLM (Abramowicz, Levy, Levin and Maor) parameterization.

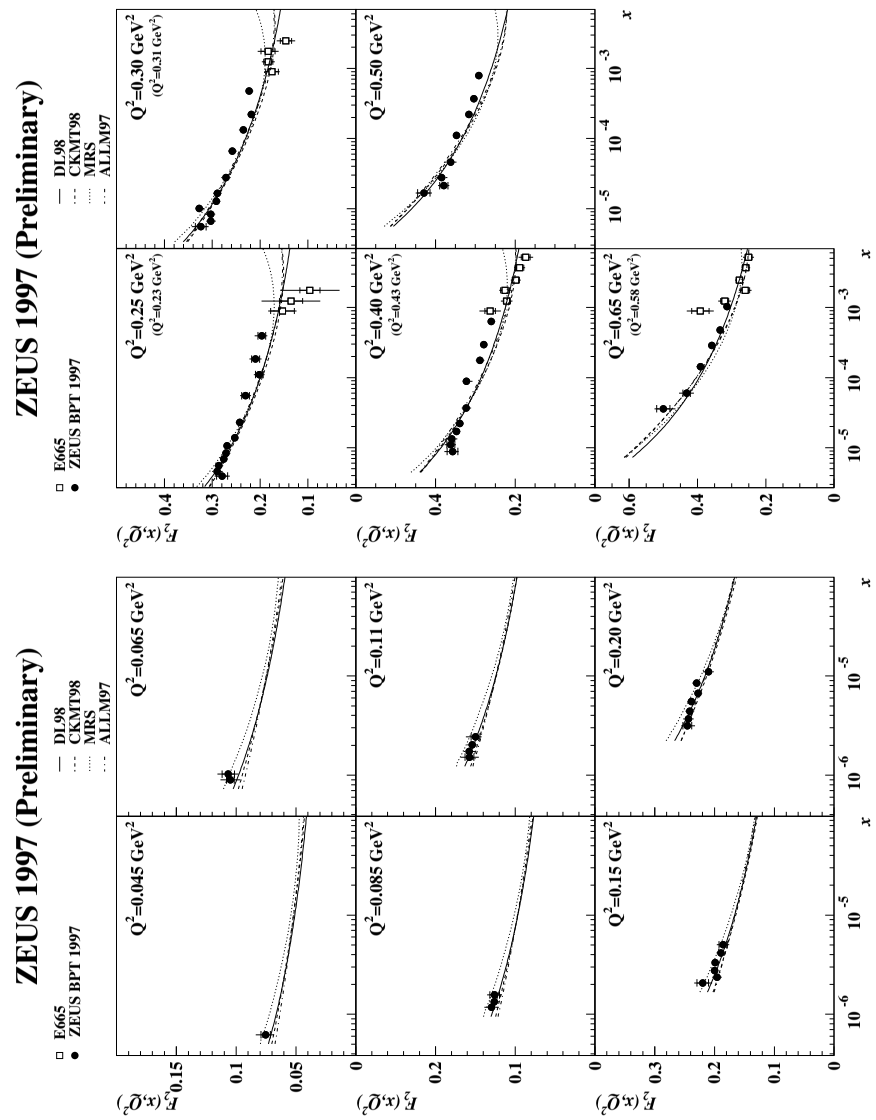

Fig. 8.14: Comparison of the F_2 results to newer parameterizations that included the 1995 BPC data in the fit. Shown as solid line is the DL98 (Donnachie and Landshoff) parameterization, the dashed line represents the CKMT98 (Capella, Kaidalov, Merino and Tran Thanh Van), the dotted line the MRS (Martin, Ryskin and Staśto) and the dash-dotted line the ALLM97 (Abramowicz, Levy, Levin and Maor) parameterization.

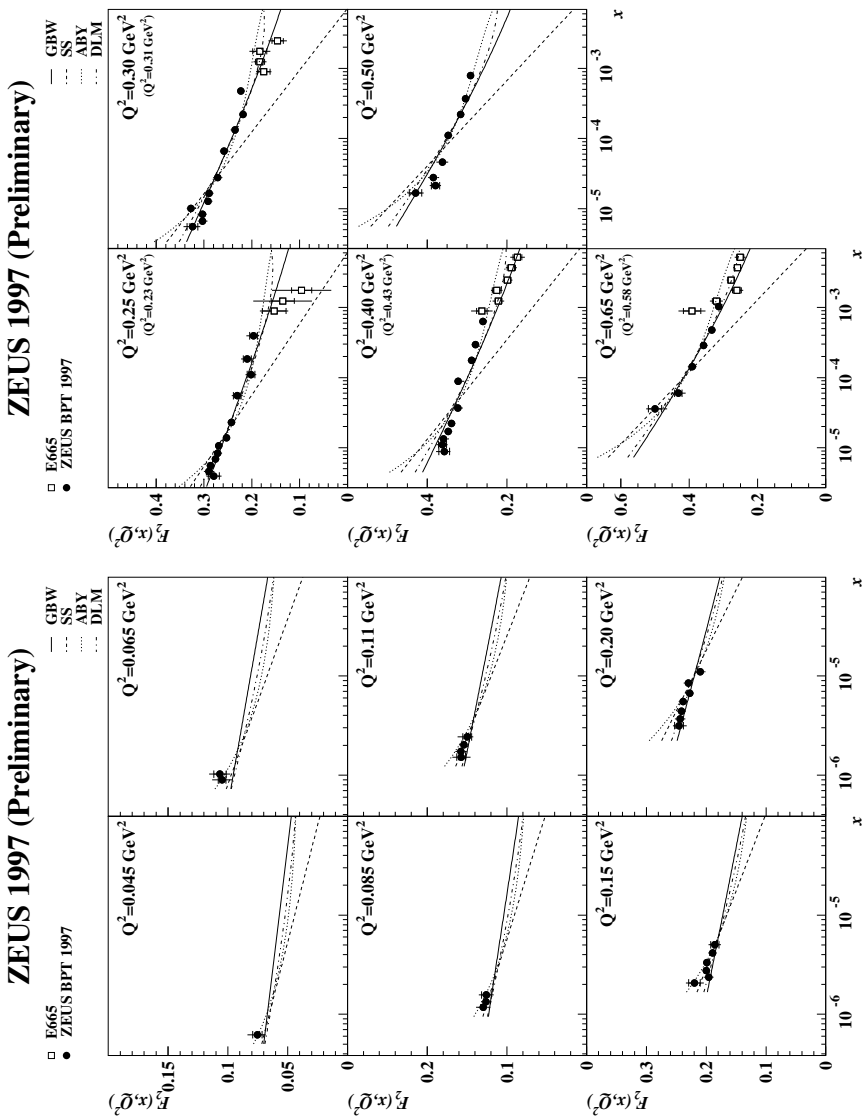

Fig. 8.15: Comparison of the F_2 results to newer parameterizations that included the 1995 BPC data in the fit. Shown as solid line is the GBW (Golec-Biernat and Wüsthoff) parameterization, the dashed line represents the SS (Schildknecht and Spiesberger), the dotted line the ABY (Adel, Barreiro and Ynduráin) and the dash-dotted line the DLM (Desgrolard, Lengyel and Martynov) parameterization.

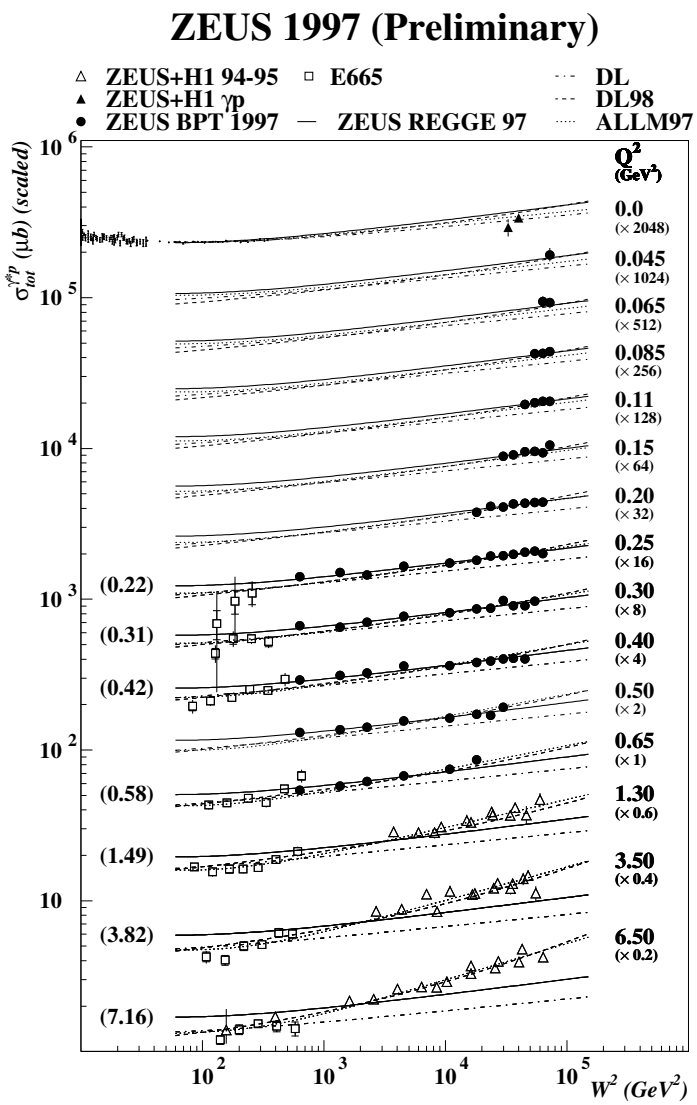

Fig. 8.16: $\sigma_{\rm tot}^{\gamma^* p}$ vs. W^2 in bins of Q^2. Filled circles denote results from this analysis, open triangles are measurements from ZEUS and H1 at higher Q^2, filled triangles are ZEUS and H1 measurements in photoproduction, and open squares show results from E665. Small dots for $Q^2 = 0$ are from low-energy experiments. Numbers in parentheses on the left-hand side are the original Q^2 values of the E665 measurements, which have been shifted to the Q^2 of the ZEUS measurement using the ALLM97 parameterization. Numbers in parentheses on the right-hand side indicate the scale factors for the different Q^2 bins.

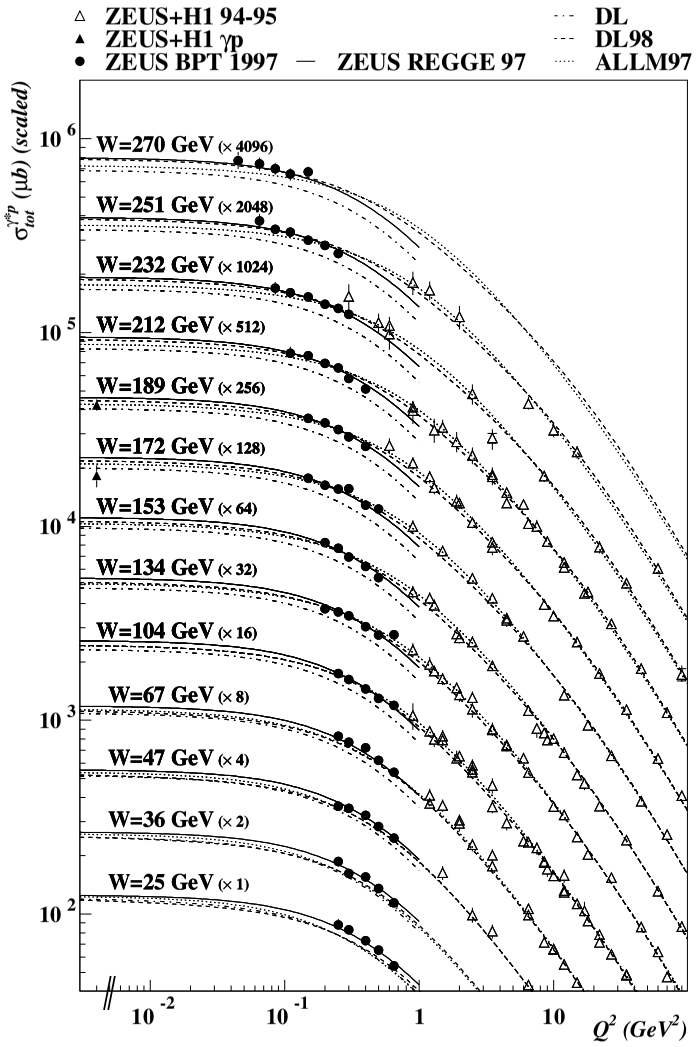

Fig. 8.17: $\sigma_{\rm tot}^{\gamma^* p}$ vs. Q^2 in bins of W. At the low Q^2 of this analysis, the total cross section is nearly independent on Q^2; in contrast, at higher Q^2 it falls approximately like $1/Q^2$, as shown by the ZEUS and H1 measurements, which are indicated by open triangles. This can be exploited to constrain the extrapolation of the cross section to $Q^2 \to 0$, where the two direct measurements from ZEUS and H1 in photoproduction are shown as filled triangles. Numbers in parentheses indicate the scale factors for the different W bins.

ZEUS 1997 (Preliminary)

Q^2 (GeV^2)	x	y	F_2	$\pm$ stat	+ sys	− sys
0.045	$6.21 \cdot 10^{-7}$	0.800	0.0754	0.0039	0.0072	0.0059
0.065	$1.02 \cdot 10^{-6}$	0.700	0.1066	0.0051	0.0076	0.0071
0.065	$8.97 \cdot 10^{-7}$	0.800	0.1049	0.0032	0.0077	0.0077
0.085	$1.56 \cdot 10^{-6}$	0.600	0.1258	0.0060	0.0075	0.0070
0.085	$1.34 \cdot 10^{-6}$	0.700	0.1263	0.0029	0.0055	0.0061
0.085	$1.17 \cdot 10^{-6}$	0.800	0.1297	0.0039	0.0083	0.0081
0.110	$2.43 \cdot 10^{-6}$	0.500	0.1498	0.0056	0.0109	0.0053
0.110	$2.02 \cdot 10^{-6}$	0.600	0.1539	0.0033	0.0053	0.0047
0.110	$1.73 \cdot 10^{-6}$	0.700	0.1578	0.0033	0.0059	0.0065
0.110	$1.51 \cdot 10^{-6}$	0.800	0.1574	0.0056	0.0096	0.0103
0.150	$5.02 \cdot 10^{-6}$	0.330	0.1855	0.0070	0.0078	0.0074
0.150	$4.14 \cdot 10^{-6}$	0.400	0.1891	0.0046	0.0057	0.0041
0.150	$3.31 \cdot 10^{-6}$	0.500	0.1988	0.0037	0.0044	0.0051
0.150	$2.07 \cdot 10^{-6}$	0.800	0.2196	0.0098	0.0107	0.0119
0.150	$2.76 \cdot 10^{-6}$	0.600	0.1998	0.0037	0.0052	0.0058
0.150	$2.36 \cdot 10^{-6}$	0.700	0.1959	0.0045	0.0068	0.0069
0.200	$1.10 \cdot 10^{-5}$	0.200	0.2098	0.0058	0.0072	0.0061
0.200	$8.49 \cdot 10^{-6}$	0.260	0.2300	0.0051	0.0057	0.0045
0.200	$6.69 \cdot 10^{-6}$	0.330	0.2274	0.0046	0.0047	0.0050
0.200	$5.52 \cdot 10^{-6}$	0.400	0.2386	0.0046	0.0057	0.0057
0.200	$4.41 \cdot 10^{-6}$	0.500	0.2413	0.0049	0.0056	0.0055
0.200	$3.68 \cdot 10^{-6}$	0.600	0.2438	0.0057	0.0067	0.0066
0.200	$3.15 \cdot 10^{-6}$	0.700	0.2457	0.0074	0.0066	0.0110
0.250	$3.94 \cdot 10^{-4}$	0.007	0.1962	0.0081	0.0126	0.0078
0.250	$1.84 \cdot 10^{-4}$	0.015	0.2095	0.0083	0.0099	0.0095
0.250	$1.10 \cdot 10^{-4}$	0.025	0.2016	0.0079	0.0087	0.0079
0.250	$5.52 \cdot 10^{-5}$	0.050	0.2303	0.0079	0.0083	0.0080
0.250	$2.30 \cdot 10^{-5}$	0.120	0.2426	0.0034	0.0080	0.0076
0.250	$1.38 \cdot 10^{-5}$	0.200	0.2528	0.0037	0.0056	0.0062
0.250	$1.06 \cdot 10^{-5}$	0.260	0.2692	0.0042	0.0060	0.0064
0.250	$8.36 \cdot 10^{-6}$	0.330	0.2714	0.0048	0.0065	0.0077
0.250	$6.90 \cdot 10^{-6}$	0.400	0.2761	0.0052	0.0054	0.0065
0.250	$5.52 \cdot 10^{-6}$	0.500	0.2865	0.0059	0.0064	0.0073
0.250	$4.60 \cdot 10^{-6}$	0.600	0.2900	0.0071	0.0072	0.0094
0.250	$3.94 \cdot 10^{-6}$	0.700	0.2793	0.0115	0.0106	0.0111
0.300	$4.73 \cdot 10^{-4}$	0.007	0.2227	0.0058	0.0047	0.0061
0.300	$2.20 \cdot 10^{-4}$	0.015	0.2182	0.0058	0.0056	0.0056
0.300	$1.32 \cdot 10^{-4}$	0.025	0.2353	0.0061	0.0067	0.0045
0.300	$6.62 \cdot 10^{-5}$	0.050	0.2580	0.0067	0.0052	0.0070
0.300	$2.76 \cdot 10^{-5}$	0.120	0.2716	0.0034	0.0092	0.0092
0.300	$1.65 \cdot 10^{-5}$	0.200	0.2891	0.0042	0.0082	0.0078
0.300	$1.27 \cdot 10^{-5}$	0.260	0.2913	0.0049	0.0063	0.0077
0.300	$1.00 \cdot 10^{-5}$	0.330	0.3273	0.0063	0.0062	0.0090
0.300	$8.28 \cdot 10^{-6}$	0.400	0.3030	0.0064	0.0081	0.0069
0.300	$6.62 \cdot 10^{-6}$	0.500	0.3032	0.0075	0.0058	0.0077
0.300	$5.52 \cdot 10^{-6}$	0.600	0.3240	0.0111	0.0150	0.0119
0.400	$6.31 \cdot 10^{-4}$	0.007	0.2601	0.0071	0.0063	0.0075
0.400	$2.94 \cdot 10^{-4}$	0.015	0.2786	0.0076	0.0067	0.0061
0.400	$1.76 \cdot 10^{-4}$	0.025	0.2886	0.0080	0.0066	0.0082
0.400	$8.83 \cdot 10^{-5}$	0.050	0.3225	0.0088	0.0055	0.0129
0.400	$3.68 \cdot 10^{-5}$	0.120	0.3232	0.0046	0.0099	0.0118
0.400	$2.20 \cdot 10^{-5}$	0.200	0.3389	0.0058	0.0080	0.0086
0.400	$1.70 \cdot 10^{-5}$	0.260	0.3473	0.0070	0.0087	0.0072
0.400	$1.33 \cdot 10^{-5}$	0.330	0.3589	0.0086	0.0096	0.0106
0.400	$1.10 \cdot 10^{-5}$	0.400	0.3616	0.0099	0.0119	0.0084
0.400	$8.83 \cdot 10^{-6}$	0.500	0.3573	0.0138	0.0148	0.0077
0.500	$7.89 \cdot 10^{-4}$	0.007	0.2914	0.0063	0.0058	0.0064
0.500	$3.68 \cdot 10^{-4}$	0.015	0.3038	0.0061	0.0056	0.0064
0.500	$2.20 \cdot 10^{-4}$	0.025	0.3163	0.0060	0.0067	0.0076
0.500	$1.10 \cdot 10^{-4}$	0.050	0.3470	0.0061	0.0064	0.0079
0.500	$4.60 \cdot 10^{-5}$	0.120	0.3621	0.0063	0.0139	0.0133
0.500	$2.76 \cdot 10^{-5}$	0.200	0.3845	0.0082	0.0102	0.0119
0.500	$2.12 \cdot 10^{-5}$	0.260	0.3790	0.0102	0.0104	0.0088
0.500	$1.67 \cdot 10^{-5}$	0.330	0.4291	0.0154	0.0140	0.0126
0.650	$1.02 \cdot 10^{-3}$	0.007	0.3138	0.0074	0.0062	0.0086
0.650	$4.78 \cdot 10^{-4}$	0.015	0.3339	0.0076	0.0084	0.0090
0.650	$2.87 \cdot 10^{-4}$	0.025	0.3580	0.0080	0.0068	0.0093
0.650	$1.43 \cdot 10^{-4}$	0.050	0.3912	0.0088	0.0090	0.0098
0.650	$5.98 \cdot 10^{-5}$	0.120	0.4316	0.0112	0.0194	0.0182
0.650	$3.59 \cdot 10^{-5}$	0.200	0.5001	0.0194	0.0169	0.0299

Table 8.1: Measured F_2 values with statistical and systematic errors. The effect of F_L has been corrected for by using R from an approximation of the BKS model, $R = 0.165 \cdot Q^2/m_\rho^2$. The bin boundaries in y are 0.005, 0.01, 0.02, 0.04, 0.08, 0.16, 0.23, 0.30, 0.37, 0.45, 0.54, 0.64, 0.74, 0.84; those in Q^2 are 0.040, 0.055, 0.075, 0.10, 0.13, 0.17, 0.21, 0.27, 0.35, 0.45, 0.58, 0.74 GeV^2.

In Fig. 8.13 the data are compared to F_2 parameterizations that were published before the 1995 BPC data were available (DL [62], CKMT [66], BK [70], ALLM [64]), as well as in Figs. 8.14 and 8.15 to parameterizations that already included the 1995 BPC data in their fits (DL98 [63], CKMT98 [67], MRS [71], ALLM97 [65], GBW [75], SS [72,73], ABY [68], DLM [69]). Not shown is the H [74] parameterization.

None of the old parameterizations is able to describe the data. DL and CKMT are too low by about 10–15%, BK is too high by 20% at low x and Q^2 (but agrees well at higher x and Q^2). ALLM is off by a factor of two in some bins. The post-BPC parameterizations all agree with the data relatively well in the limited range of the 1995 measurement, which was to be expected. Therefore, as a measure of the quality of the description of the data, a χ^2 value is calculated for each of the parameterizations. The best description of the data in the medium and high-y regions is obtained by the H and DL98 parameterizations, and the agreement with GBW and CKMT98 is similarly good. None of the other parameterizations is in severe disagreement with the data, the most significant deviations are found for ABY and SS. At low y, ABY and BK describe the data best, and also from DLM and GBW one obtains relatively good results. Here, the other parameterizations have significantly worse χ^2; especially H and SS are far off. Overall, GBW, DLM and DL98 give the best description of the data. A conclusive comparison will, however, have to be postponed until the groups have updated their fits to include the new data.

The measured F_2 values are converted using Eq. (2.60) to a total photon-proton cross section and shown as $\sigma_{\rm tot}^{\gamma^* p}$ vs. W^2 (Fig. 8.16) and $\sigma_{\rm tot}^{\gamma^* p}$ vs. Q^2 (Fig. 8.17). The rise of the cross section with W^2 is slow at $Q^2 < 0.5\,\mathrm{GeV}^2$, but steepens at higher Q^2 values. At the lowest Q^2, the total photon-proton cross section is nearly independent of Q^2; in contrast, at higher Q^2 it falls approximately like $1/Q^2$. This can be exploited to constrain the extrapolation of the cross section to $Q^2 \to 0$.

8.2 Interpretation of the results

In the following, the behavior of F_2 and $\sigma_{\rm tot}^{\gamma^* p}$ as functions of x (respectively W^2) and Q^2 will be studied quantitatively by making physics-motivated fits to the data. These fits will also be used to extract certain quantities of interest. The previous study of the phenomenology of F_2 at low Q^2 performed by the ZEUS collaboration [56] is adopted as a guideline for the set of aspects to be discussed using the precise and enlarged F_2 data sample of this analysis.

8.2.1 Extrapolation of the cross section to photoproduction

GVDM and Regge theory predict approximate factorization of the Q^2 and the W^2 dependence of the cross section at low Q^2. For the Q^2 dependence, the explicit prediction from GVDM is used, taking only the continuum part into account:

$$\sigma_T^{\gamma^* p}(W^2, Q^2) = \left(\frac{m_0^2}{m_0^2 + Q^2}\right) \sigma_{\rm tot}^{\gamma p}(W^2) \qquad (8.24)$$

$$\sigma_L^{\gamma^* p}(W^2, Q^2) = \xi \left(\frac{m_0^2}{Q^2} \ln \frac{m_0^2 + Q^2}{m_0^2} - \frac{m_0^2}{m_0^2 + Q^2}\right) \sigma_{\rm tot}^{\gamma p}(W^2). \qquad (8.25)$$

Using Eqs. (8.24) and (8.25), the data can be extrapolated to $Q^2 = 0$, yielding values for the total photon-proton cross section $\sigma_{\rm tot}^{\gamma p}$. For the sake of simplicity, the Q^2 dependence is taken from the GVDM prediction about σ_T only, i.e. ξ is set to zero at this stage. This will be justified later.

The free parameters of the fit are m_0^2 and the values of $\sigma_{\rm tot}^{\gamma p}(W^2)$ for 13 W bins in the range $25\,\mathrm{GeV} \ldots 270\,\mathrm{GeV}$ (14 parameters in total). The results of the fit are shown in Fig. 8.18 and listed in Table 8.2. For low W, the extrapolation has to bridge a large gap in Q^2, but the errors

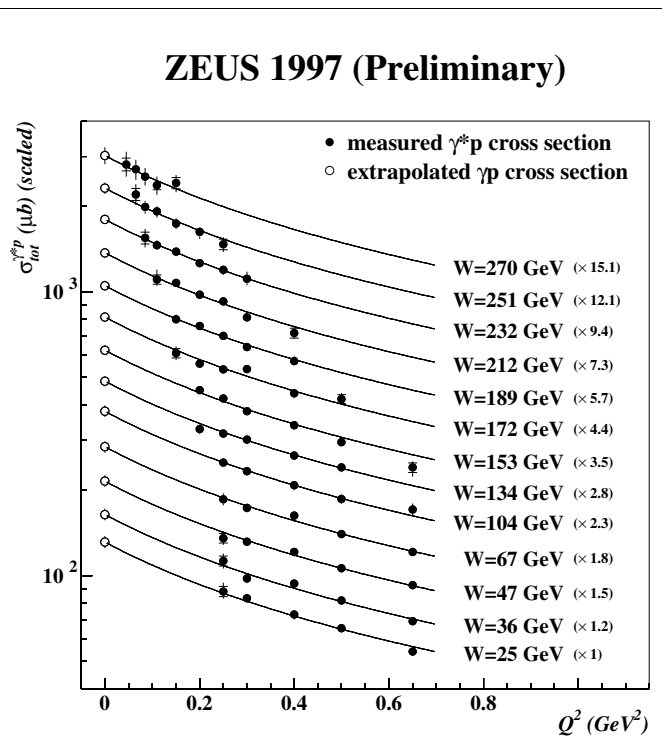

Fig. 8.18: Extrapolation of $\sigma_{\rm tot}^{\gamma^* p}$ as measured by the BPT to $Q^2 = 0$ in bins of W. Filled circles denote measurements of $\sigma_{\rm tot}^{\gamma^* p}$, open circles the extrapolated $\sigma_{\rm tot}^{\gamma p}$. The lines are the result of the fit. Numbers in parentheses indicate the scale factors for the different W bins.

of the measured $\sigma_{\rm tot}^{\gamma^* p}(W^2, Q^2)$ are relatively small; vice versa, for high W the gap is small but the errors are larger. Therefore, the relative error of the extrapolated $\sigma_{\rm tot}^{\gamma p}(W^2)$ values of about 5% is nearly independent of W. The fit has a reasonable $\chi^2/\mathrm{ndf} = 1.3$, taking into account statistical errors only. It yields a value of $m_0^2 = (0.49 \pm 0.02(\mathrm{stat}) \pm 0.04(\mathrm{sys}))\,\mathrm{GeV}^2$ (slightly below $m_\rho^2 = 0.59\,\mathrm{GeV}^2$; this will be discussed later).

The Q^2 dependence assumed in the fit describes the data well. Only in the highest Q^2 bin at $0.65\,\mathrm{GeV}^2$, a slight deviation is observed: points at lower W are below the curve, points at higher W above.

For the systematic error, the measured $\sigma_{\rm tot}^{\gamma^* p}$ values are varied according to the effect of each systematic check, and the fit is repeated. The systematic error is then calculated as the quadratic sum of all variations (separately for positive and negative deviations). The systematic error does not take into account the model-dependence, i.e. the variation of the results when assuming a different Q^2 dependence. This issue will be discussed in section 8.2.2.

The magnitude of σ_L is unknown in this kinematic region. A value of $\xi = 0.171$ is obtained from a fit to ZEUS and H1 data at low and high Q^2 [72,73]. Repeating the fit with $\xi = 0.171$ instead of $\xi = 0$ changes the resulting extrapolated cross sections only within their statistical errors (but has a significant effect on m_0^2). The effect of excluding the points at $Q^2 = 0.65\,\mathrm{GeV}^2$ from the fit is also negligible.

ZEUS 1997 (Preliminary)

W (GeV)	$\sigma_{\rm tot}^{\gamma p}$ (μb)	± stat (μb)	− sys (μb)	+ sys (μb)
25	131.3	2.8	5.6	5.9
36	136.8	2.9	5.5	5.9
47	143.4	3.0	5.6	6.5
67	158.1	3.3	6.5	6.2
104	164.9	2.9	6.9	7.3
134	173.1	2.9	6.4	6.7
153	177.9	3.0	6.2	6.9
172	185.2	3.1	6.4	6.3
189	184.5	3.0	6.1	7.0
212	188.1	2.9	6.1	6.8
232	191.5	2.7	6.6	7.0
251	191.8	2.6	8.3	7.9
270	200.1	3.4	12.9	13.3

Table 8.2: Extrapolated $\sigma_{\rm tot}^{\gamma p}$ values with statistical and systematic errors.

The reason why including or excluding the σ_L term does not affect the result of the extrapolation, although the contribution of σ_L to the total cross section is rather nonnegligible, can be understood from the strong correlation between ξ and m_0^2. This is illustrated by a numerical example in Fig. 8.19. The sum of the σ_T and σ_L terms for a given m_0^2 value can be approximated very well by the σ_T term alone, but with a higher m_0^2 value. The difference between σ_T (using $m_0'^2$) and $\sigma_T + \sigma_L$ (using m_0^2) is below 1% for Q^2 values between 0 and $0.8\,\mathrm{GeV}^2$. Consequently between these scenarios cannot be discriminated, given the precision of the measured $\sigma_{\rm tot}^{\gamma^* p}$; in other words this means that the data have only very little sensitivity to F_L. However, it should be pointed out that there is a price to pay for the simplification of neglecting the σ_L term: it renders the obtained value of m_0^2 meaningless.

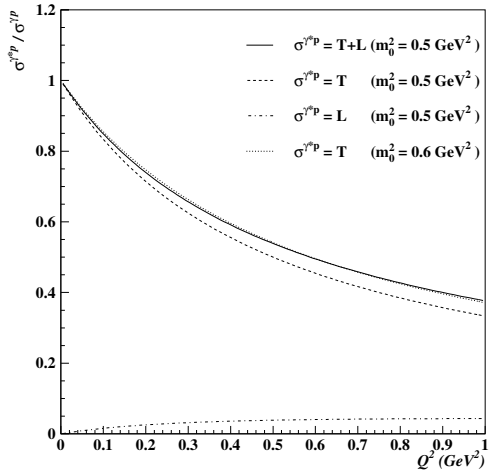

Fig. 8.19: The effect of including or excluding the σ_L term in the extrapolation of $\sigma_{\rm tot}^{\gamma^* p}$. Normalized to $\sigma_{\rm tot}^{\gamma p}$, the solid, dashed and dash-dotted lines show $\sigma_T + \sigma_L$, as well as σ_T and σ_L separately, for $m_0^2 = 0.5\,\mathrm{GeV}^2$. The dotted line is σ_T for $m_0'^2 = 0.6\,\mathrm{GeV}^2$, which approximates $\sigma_T + \sigma_L$ for $m_0^2 = 0.5\,\mathrm{GeV}^2$ very well. The difference is below 1% for Q^2 values between 0 and $0.8\,\mathrm{GeV}^2$.

8.2.2 Energy dependence of the photoproduction cross section

The extrapolated real photon-proton cross section values $\sigma_{\rm tot}^{\gamma p}(W^2)$ are compared in Fig. 8.20 to direct measurements of the photoproduction cross section, i.e. the results from ZEUS and H1 [50, 51] and previous measurements from other experiments at low W [142, 143]. The parameterizations DL98 and ALLM97, as well as two fits of the form

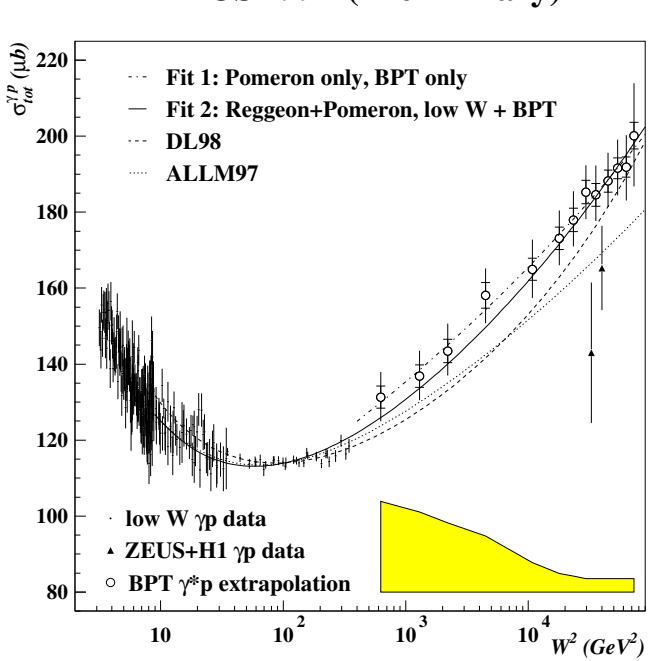

Fig. 8.20: Extrapolated and measured values of $\sigma_{\rm tot}^{\gamma p}$ vs. W^2. Small dots denote cross section measurements at low energies before the advent of HERA. The filled triangles are the two direct measurements from ZEUS ($W = 181\,\mathrm{GeV}$) and H1 ($W = 200\,\mathrm{GeV}$). The open circles are the extrapolations of the BPT $\sigma_{\rm tot}^{\gamma^* p}$ measurements to $Q^2 = 0$. The curves show two different fits to the data (see text) as well as the parameterizations DL98 and ALLM97. The shaded band is an estimate of the model-dependence of the extrapolation.

$$\sigma_{\rm tot}^{\gamma p}(W^2) = A_{\mathbb{R}} \cdot (W^2)^{\alpha_{\mathbb{R}}-1} + A_{\mathbb{P}} \cdot (W^2)^{\alpha_{\mathbb{P}}-1}, \tag{8.26}$$

are overlaid, where $A_{\mathbb{R}}$, $\alpha_{\mathbb{R}}$, $A_{\mathbb{P}}$, $\alpha_{\mathbb{P}}$ are free or fixed parameters, depending on the fit (see below). The systematic errors have been determined in the same way as in section 8.2.1.

The fits yield the following results for $\alpha_{\mathbb{P}}$. From fit 1, where only the pomeron term is used, and only BPT extrapolated cross sections are included in the fit (free parameters are $A_{\mathbb{P}}$ and $\alpha_{\mathbb{P}}$), one obtains

$$\alpha_{\mathbb{P}} = 1.087 \pm 0.004(\mathrm{stat}) \pm 0.008(\mathrm{sys}).$$

From fit 2, where the sum of the pomeron and the reggeon term is used, and both BPT extrapolated cross sections and measurements at low W (but not the ZEUS and H1 measurements at high W) are included in the fit (free parameters are $A_{\mathbb{P}}$, $A_{\mathbb{R}}$ and $\alpha_{\mathbb{P}}$; $\alpha_{\mathbb{R}}$ is fixed at 0.5), the result is

$$\alpha_{\mathbb{P}} = 1.105 \pm 0.001(\mathrm{stat}) \pm 0.007(\mathrm{sys}).$$

These results agree well with the soft pomeron intercept of 1.095 ± 0.02, and are also marginally compatible with each other (note, though, that the systematic errors are correlated between the two values). If $\alpha_{\mathbb{R}}$ is left as a free parameter in fit 2, it is found to be $0.56 \pm 0.02(\text{stat}) \pm 0.02(\text{sys})$.

The extrapolated cross sections are higher than the direct measurements by H1 and ZEUS at $W \approx 200\,\text{GeV}$. This discrepancy has already been observed with the 1995 data, but with less significance due to the larger systematic errors of that measurement. The magnitude of the discrepancy has not changed much. The extrapolations also appear to be slightly higher than expected at the transition to the low W measurements.

Fit 2 describes well the low W measurements and the extrapolated points above $W = 100\,\text{GeV}$, while between 25 GeV and 100 GeV the curve is systematically 0.5–1σ of the total error below the points, and at $W \approx 200\,\text{GeV}$ it is 2σ above the HERA measurements. Fits to both the measured and the extrapolated cross sections cannot be expected to describe both of them perfectly. Around $W = 20\,\text{GeV}$, the fits are strongly constrained by many low energy points with tiny errors, so the most obvious disagreement is observed in the low-W range of the extrapolated values. At $W \approx 200\,\text{GeV}$, the direct measurements would (if included) not affect the fit very much, because of their larger errors and smaller number of points compared to the extrapolations.

Returning to a statement made above, the extrapolation assumes a certain Q^2 dependence and is therefore not model-independent. Any model dependence is expected to be minimized by measuring $\sigma_{\text{tot}}^{\gamma^* p}$ as close as possible to $Q^2 = 0$, and should decrease thus toward higher W, corresponding to lower Q^2 values in this analysis.

An attempt is made to estimate the magnitude of the model-dependence. From each of the parameterizations DL, DL98 and ALLM97, pseudo-measurements of $\sigma_{\text{tot}}^{\gamma^* p}$ values are generated in the bins of the measured data. These values are assigned pseudo-errors that are the same as in data, and the extrapolation is repeated with the pseudo-data sets. The extrapolated values for $\sigma_{\text{tot}}^{\gamma p}$ can be compared to the analytical curve given by the respective parameterization, which they should ideally coincide with. The result is the following: for DL, the extrapolated points reproduce the analytical curve very well, only the point at the lowest W deviates by 1σ of the statistical error. For ALLM97, the extrapolated points are up to 25% below the analytical curve at low W, while at high W they agree well with it. For DL98, the extrapolated points are up to 20% below the analytical curve at low W, and at high W they are by 5% below the curve.

The conclusion is that the extrapolation procedure apparently works properly if there is only one simple pomeron with a fixed intercept. As soon as the pomeron intercept is allowed to depend on Q^2 (like in ALLM97) or an effective Q^2 dependence is introduced by the interplay of two pomerons (DL98), the extrapolation fails to reproduce the correct cross section. Although this numerical experiment cannot be taken as a serious determination of the model-dependence, it may give an indication of its magnitude. The biggest deviation found for DL, DL98 and ALLM97 at each point in W is therefore shown as the shaded band in Fig. 8.20.

As the final step, a combination of the two fits, describing both the W^2 and the Q^2 dependence, is performed according to

$$\sigma_{\text{tot}}^{\gamma^* p}(W^2, Q^2) = \left(\frac{m_0^2}{m_0^2 + Q^2}\right) \left(A_{\mathbb{R}} \cdot (W^2)^{\alpha_{\mathbb{R}}-1} + A_{\mathbb{P}} \cdot (W^2)^{\alpha_{\mathbb{P}}-1}\right). \tag{8.27}$$

This fit is shown in Figs. 8.11, 8.12, 8.16 and 8.17 as ZEUS REGGE 97. It has also been used for the reweighting of the Monte Carlo (section 8.1.1), for a systematic check (section 8.1.4) and for the determination of the uncertainty of F_2 in the region of the ISR analysis (appendix B.5). The parameters of the separate fits are not modified by more than their errors when determined in the combined fit instead.

Taking the ZEUS REGGE 97 fit as a parameterization of purely soft Regge behavior, i.e. a constant and small x-slope of F_2, or equivalently a slow rise of $\sigma_{\text{tot}}^{\gamma^* p}$ with W^2, one observes

that this fit follows the data up to $Q^2 = 0.5\,\text{GeV}^2$, while at $Q^2 = 0.65\,\text{GeV}^2$ the data rise more steeply with W^2 than the fit (Fig. 8.16). This aspect is explored in detail in section 8.2.3.

8.2.3 The slope of F_2

The x dependence of F_2 is measured in terms of λ_{eff}, the logarithmic derivative:

$$\lambda_{\text{eff}} = \frac{d \log F_2}{d \log(1/x)}. \tag{8.28}$$

From the measured F_2 points, λ_{eff} can only be determined as an average over a certain range in x, where it must be assumed to be constant (or varying only little). This translates into the assumption that at low x, or, equivalently, at high W,

$$F_2 \propto \left(\frac{1}{x}\right)^{\lambda_{\text{eff}}} \quad \text{or} \quad \sigma_{\text{tot}}^{\gamma^* p} \propto (W^2)^{\lambda_{\text{eff}}}. \tag{8.29}$$

So, in Regge theory λ_{eff} is closely related to the intercept of the pomeron trajectory, $\alpha_{\mathbb{P}}$, and the assumption that λ_{eff} is constant over a certain range in x translates in Regge language to the requirement that the exchange of one trajectory, i.e. the pomeron, dominates. However, it should be noted that λ_{eff} averages over the exchange of all possible trajectories and therefore also includes a small contribution of reggeon exchange, rendering λ_{eff} slightly smaller than $\alpha_{\mathbb{P}} - 1$. Furthermore, it should be pointed out that the method to determine λ_{eff} from the measured F_2 also remains well-defined if Regge theory does not hold.

The values of λ_{eff} are extracted from the measured F_2 points with a fit of the form $F_2 = a \cdot x^{-\lambda_{\text{eff}}}$. For illustration, the fit is also applied to F_2 values as measured by ZEUS at higher Q^2 values [144]. The results are shown in Fig. 8.21 and listed in Table 8.3. The systematic errors have been determined in the same way as in section 8.2.1. The precision can be compared to Fig. 2.16. Due to the wider range in x covered by this analysis, it is not necessary to rely on additional data from E665 any more. Introducing an additional parameter according to $F_2 = a \cdot x^{-\lambda_{\text{eff}}} + b$ produces randomly fluctuating results, presumably due to the strong correlation of the parameters.

For Q^2 values up to $0.5\,\text{GeV}^2$, the extracted λ_{eff} values are well compatible with a constant value. For greater Q^2, $\lambda_{\text{eff}}(Q^2)$ rises approximately logarithmically with Q^2. Taking the small error of the λ_{eff} value at $Q^2 = 0.65\,\text{GeV}^2$ into account, one observes a kink close to this point and thus the onset of the strong rise of F_2 with x. The observation that the extrapolation of a linear (in $\log Q^2$) fit of the λ_{eff} values at $Q^2 > 2\,\text{GeV}^2$ agrees well with the $Q^2 = 0.65\,\text{GeV}^2$ point may support this interpretation.

Q^2 (GeV^2)	λ_{eff}	$\pm$ stat	$-$ sys	$+$ sys
0.11	0.1206	0.094	0.1730	0.1181
0.15	0.1051	0.041	0.0628	0.0548
0.20	0.1117	0.022	0.0307	0.0202
0.25	0.0950	0.006	0.0116	0.0084
0.30	0.0920	0.005	0.0038	0.0041
0.40	0.0768	0.006	0.0029	0.0053
0.50	0.0852	0.006	0.0042	0.0082
0.65	0.1256	0.010	0.0134	0.0129

Table 8.3: Extracted λ_{eff} values with statistical and systematic errors (for the BPT data only).

Due to the distribution of available data points in the kinematic plane, it is nontrivial to plot a theory curve on top of the measured values. In order to account for the varying range in x that is averaged over, and to cope with the different magnitudes of errors of the measured points, the method already introduced in section 8.2.2 has been adopted here. From a parameterization, a set of pseudo-measurements of F_2 is generated in the bins of the measured data. These values

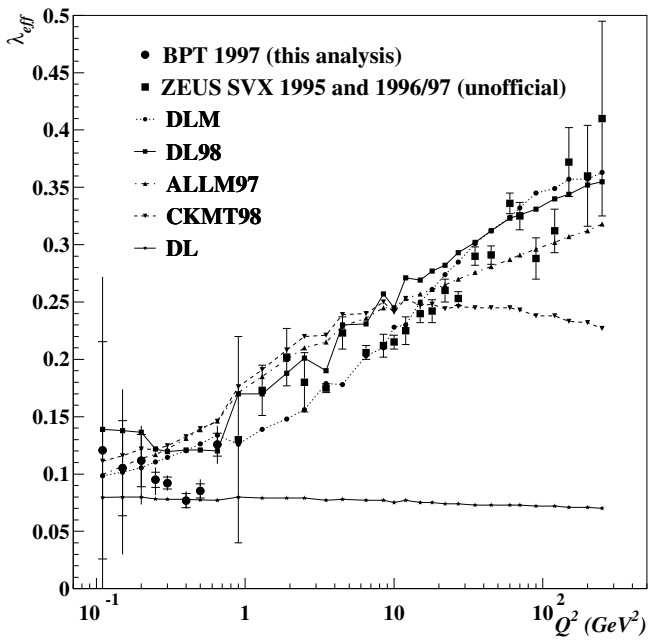

Fig. 8.21: $\lambda_{\rm eff}$, the slope of F_2 with $\log(1/x)$. For the purpose of illustration, $\lambda_{\rm eff}$ has also been extracted from ZEUS data at higher Q^2. The data are compared to the predictions of the DL, DL98, ALLM97, CKMT and DLM parameterizations. These theory curves are actually made from discrete values extracted from pseudo-measurements of the parameterizations, connected by straight lines.

are assigned pseudo-errors that are the same as in data, and are subjected to the same fit. The resulting values can then directly be compared to data.

The DL parameterization predicts a nearly constant value of $\lambda_{\rm eff}$. It gives the best description of the BPT data, but fails completely to follow the rise in $\lambda_{\rm eff}$ at higher Q^2. The more recent DL98 reproduces the shape of the data very well, but is altogether too high over the whole Q^2 range. ALLM97, CKMT98 and DLM do not exhibit a kink at $Q^2 = 0.5\,\mathrm{GeV}^2$ and predict instead a smooth rise of $\lambda_{\rm eff}$, which is clearly incompatible with the measurement. At higher Q^2, the DLM parameterization achieves the best description of the data, while the saturating behavior of CKMT is clearly incompatible with the data.

Chapter 9

Summary

The proton structure functions, $F_2(x,Q^2)$ and $F_L(x,Q^2)$, or, equivalently, the virtual photon-proton cross sections, $\sigma_{\rm tot}^{\gamma^* p}$ and $\sigma_L^{\gamma^* p}$, contain information about the dynamics of quarks and gluons in the proton. They are measured in the deep inelastic scattering (DIS) reaction $e^+p \to e^+X$, where the electron interacts with a quark in the proton which carries a momentum fraction x, by exchanging a photon of virtuality Q^2. The ep collider HERA at DESY in Hamburg, which began routine operation in 1992, has extended the accessible region in the kinematic variables Q^2 and x by two orders of magnitude toward higher Q^2 (for fixed x) and toward lower x (for fixed Q^2) compared to previous fixed target experiments. While in the first years the attention focused on the high Q^2 regime, considerable interest has recently also arisen in measurements at low Q^2. In this region, conventional perturbative calculation techniques in QCD are not expected to be applicable, which makes models based on Regge theory and vector-meson dominance important here. Measurements in this region allow to study the transition to $Q^2 = 0$, i.e. from a virtual to a real photon being exchanged.

In the analysis presented here, the proton structure function F_2 has been measured at very low values of Q^2 using a data sample corresponding to an integrated luminosity of $3.9\,\mathrm{pb}^{-1}$ collected with the ZEUS detector in 1997. The key detector components for this investigation were the Beam Pipe Calorimeter (BPC) and the Beam Pipe Tracker (BPT), a small electromagnetic sampling calorimeter and a tracking device of silicon microstrip detectors, used to detect the scattered electron at small scattering angles and thus at small Q^2. The BPT was installed in ZEUS in 1997 and has been used in a physics analysis for the first time here. Detailed studies were performed in order to achieve a good understanding of this detector. Compared to a previous measurement, performed with the BPC only, the use of the BPT permits significantly better background suppression and better control of the systematic uncertainties, thus allowing the extension of the kinematic region of the measurement toward lower Q^2 as well as toward higher and lower x. Significant improvement has also been achieved in the simulation of the hadronic final state by an optimized mixture of samples of non-diffractive and diffractive Monte Carlo events, generated by the programs DJANGO and RAPGAP, respectively.

The F_2 analysis covers the range $0.045\,\mathrm{GeV}^2 < Q^2 < 0.65\,\mathrm{GeV}^2$ and $6 \cdot 10^{-7} < x < 1 \cdot 10^{-3}$. It reaches down to the lowest x values ever accessed at HERA, and up to the x values of the fixed target experiment E665. In a considerable part of the covered region, F_2 has been measured for the first time. The results have typical statistical errors of 2.6% and systematic errors of 3.3%, thus reaching the typical precision of fixed target experiments.

The structure function F_2 is found to rise slowly toward small values of x; the steepness of the rise is considerably smaller than that found at higher values of Q^2. The F_2 results have been compared to a number of parameterizations based on Regge theory and generalized vector meson dominance, and found to be in reasonable, though not perfect, agreement with most of those which included the previous BPC results. A good description of F_2 has been obtained in a compact form inspired by Regge theory and GVDM. The measured virtual photon-proton cross

sections, $\sigma_{\rm tot}^{\gamma^* p}$, have been extrapolated in a model-dependent way to the cross sections for real photons, $\sigma_{\rm tot}^{\gamma p}$, and are found to be slightly, but systematically, higher than direct measurements of $\sigma_{\rm tot}^{\gamma p}$. The reason for this remains to be resolved in the future. It is possibly related to the model dependence of the extrapolation in Q^2, which is shown to be large at low values of W. The rise of F_2 as a function of x, quantified in the logarithmic derivative $\lambda_{\rm eff}$, has been extracted from the data, and was found to be compatible with a soft behavior for $Q^2 < 0.5\,{\rm GeV}^2$. None of the parameterizations studied is able to give a completely satisfying description of the extracted $\lambda_{\rm eff}$ values.

In 1998, the H1 collaboration has installed the VLQ, a device similar to the combined BPC and BPT, and is currently working on the analysis of the data. The luminosity upgrade of HERA in the year 2000 will demand the removal of BPC and BPT from ZEUS, as well as the removal of the VLQ from H1, and will make further measurements at very low Q^2 impossible. After that, new results in this region can only be expected in the far future, from machines like LEP $\times$ LHC and NLC $\times$ HERA$_p$.

Appendix A

A Simple Model for Diffraction

The modified RAPGAP version that was used to generate diffractive events for the F_2 analysis (section 5.3.2) implements a certain assumption about parton densities in diffractive processes. This assumption is primarily driven by the need to generate a sample of events distributed in x and Q^2 in exactly the same way as the non-diffractive DJANGO sample. However, one can also turn the argument around and take the assumption as a model for diffraction. It then has to be checked if this model can describe measured data.

The model for diffraction makes the intuitive assumption that the parton density functions of the proton are universal, i.e. are the same for diffractive and non-diffractive interactions. The assumed pomeron flux is

$$f_{\mathbb{P}/p} = e^{-6|t|}/x_{\mathbb{P}}^n \cdot N, \tag{A.1}$$

where N is a normalization constant related to the fraction of diffractive events. The pomeron structure function is defined by the requirement of universal PDF's:

$$F_2^{\mathbb{P}}(\beta, Q^2) = F_2(\beta \cdot x_{\mathbb{P}}, Q^2), \tag{A.2}$$

and $F_2(x, Q^2)$ is taken from the ALLM97 parameterization. The requirement that the pomeron has to be colorless implies $q_i(x, Q^2) = \bar{q}_i(x, Q^2)$ for quark distributions in diffractive events, which is approximately met by the MRSA set in the x range where it is used here, because nearly all quarks at low x are sea quarks.

The free parameters of the model are determined from a fit to diffractive structure function data as measured by ZEUS at higher Q^2 [145]. The parameters of the fit are the normalization N (which is allowed to depend on Q^2) and the exponent of $x_{\mathbb{P}}$ in the pomeron flux. For $F_2(x, Q^2)$, the ALLM97 parameterization is taken.

One obtains a good description (Figs. A.1 and A.2) for $N \approx 0.12$ (only weakly dependent on Q^2: $N = 0.13$, 0.12, 0.12, 0.08 for $Q^2 = 8$, 14, 27, 60 GeV^2) and $n = 1.08$. Using $n = 2\alpha_{\mathbb{P}}^{\rm eff} - 1$, this translates into $\alpha_{\mathbb{P}}^{\rm eff} = 1.04$. From the integration over t one expects $\alpha_{\mathbb{P}}^{\rm eff} \approx \alpha_{\mathbb{P}}(0) - 0.03$, i.e. a value of $\alpha_{\mathbb{P}}(0) = 1.07$, in relatively good agreement with the soft pomeron value. It is concluded that this model, although maybe not very well motivated by theory, is at least reasonable enough to justify its use here.

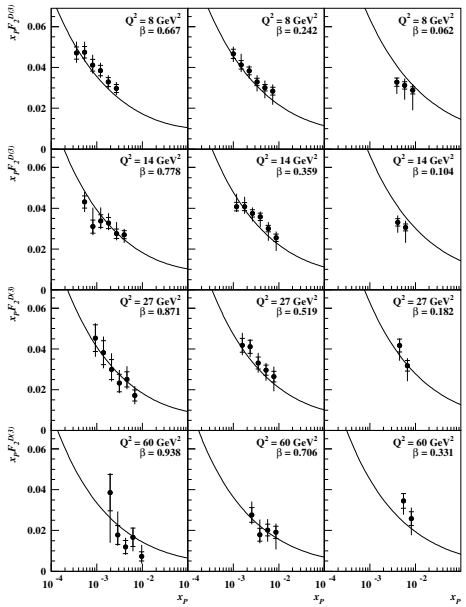

Fig. A.1: $x_{\mathbb{P}} F_2^{D(3)}$ as a function of $x_{\mathbb{P}}$ in bins of β and Q^2, compared to the simple model for diffraction used in event generation for the BPT analysis. For ease of comparison, the arrangement of plots is the same as in [145].

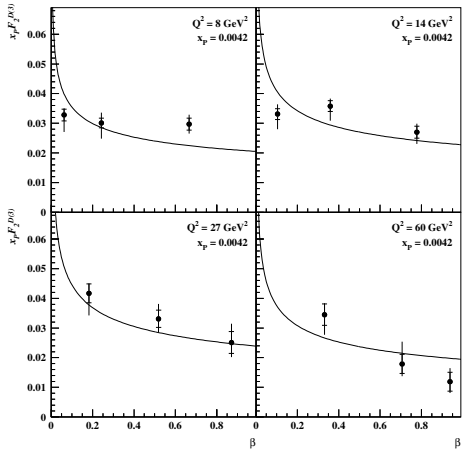

Fig. A.2: $x_{\mathbb{P}} F_2^{D(3)}$ for fixed $x_{\mathbb{P}} = 0.0042$ as a function of β in bins of Q^2, compared to the simple model for diffraction used in event generation for the BPT analysis. For ease of comparison, the arrangement of plots is the same as in [145].

Appendix B

Measurement of the structure function using radiative events

In the context of the F_2 measurement, an additional analysis of events with hard photon radiation in the initial state (ISR) has been performed. The result is limited by large statistical errors, and is not intended to be taken as a measurement, but rather as a feasibility study. However, the results of this study are very useful in order to determine an upper bound of the possible systematic effect of radiative events in the nominal analysis.

B.1 Event selection, reconstruction, and binning of the data

The kinematic variables for each event are reconstructed (like in the low-y region) with the $e\Sigma$ method (section 6.3.6). Unlike in the nominal analysis, they have to be corrected for the effect of ISR [15], using the energy of the radiated photon as reconstructed in the photon calorimeter of the LUMI system.

The trigger path used in the ISR analysis is FLT 32 $\rightarrow$ SLT DIS 2 $\rightarrow$ TLT DIS 21, thus covering the kinematic region between $0.08 < y < 0.37$ (not corrected for ISR) and $0.03 < Q^2 < 0.21\,\mathrm{GeV}^2$, as shown in Fig. B.1. Using radiative events allows to measure F_2 outside the region in the kinematic plane defined by the geometrical acceptance of BPC and BPT, i.e. at higher values of x and smaller values of Q^2. The following offline cuts are applied (most of them are identical to the selection cuts for the medium-y region):

- Like in the nominal analysis, a well-reconstructed electron in BPC and BPT is required:
  - $5.2\,\mathrm{cm} < X < 9.3\,\mathrm{cm}$
  - $-2.3\,\mathrm{cm} < Y < 2.8\,\mathrm{cm}$
  - $X - Y < 10.7\,\mathrm{cm}$
  - $X + Y < 11.2\,\mathrm{cm}$
  - $\sqrt{\left(\sigma_X^2 + \sigma_Y^2\right)/2} < 0.8$
  - $|X_{\mathrm{BPC}} - X_{\mathrm{BPT}}| < 5\sigma$
  - $E'_e > 7\,\mathrm{GeV}$
  - $-90\,\mathrm{cm} < Z_{\mathrm{BPT}}^{\mathrm{vertex}} < 90\,\mathrm{cm}$
  - $|t - \bar{t}| < 3\,\mathrm{ns}$.
- In addition to these cuts, ISR-specific requirements are imposed. The energy measured in the photon calorimeter is required to be in a range where the acceptance of the electron calorimeter for corresponding bremsstrahlung electrons is large (assuming $E_e = E_\gamma + E'_e$).

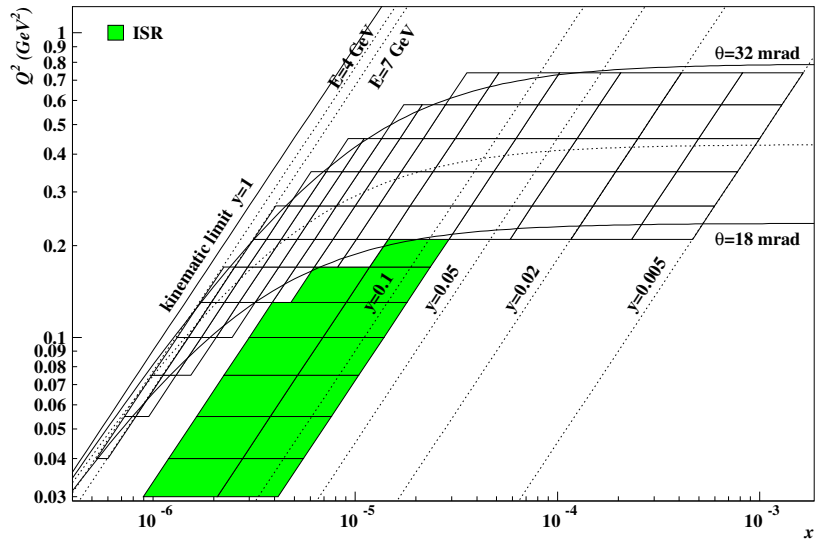

Fig. B.1: The region in the kinematic plane covered by bins in the ISR analysis, compared to the bins used in the nominal analysis. Using radiative events allows to measure F_2 at higher values of x and smaller values of Q^2 than in the nominal analysis.

This allows to suppress bremsstrahlung overlays by a veto on energy deposited in the electron calorimeter (section B.2):

- $9\,\mathrm{GeV} < E_{\mathrm{LUMI}-\gamma} < 18\,\mathrm{GeV}$
- $E_{\mathrm{LUMI}-e} < 3\,\mathrm{GeV}$.

- Assuming that an event originated from ISR, i.e. that the detected photon has been radiated from the electron before the interaction, the sum of their energies should be below the maximum possible energy of the scattered electron (plus a safety margin for resolution effects in both BPC and LUMI-γ):
  - $E'_e + E_{\mathrm{LUMI}-\gamma} < 35\,\mathrm{GeV}$.
- Further suppression of background is achieved by a tight cut on δ':
  - $40\,\mathrm{GeV} < \delta' < 60\,\mathrm{GeV}$.
- A cut on the (ISR-corrected) y_{JB} rejects migrations from lower y:
  - $y_{\mathrm{JB}} > 0.06$.

After all cuts, 575 reconstructed events remain for the analysis. The bins for the ISR analysis are chosen such that purity and acceptance have acceptable values, that the bins have dimensions larger than the resolution in each bin, and that the number of reconstructed events in the data is reasonably high. Typically, acceptance and purity of the ISR bins both range from 45% to 65%. The number of reconstructed events varies between 20 and 60 in each bin.

B.2 Background

In the BPT-ISR analysis, the most important background events are overlays of a normal low-Q^2 DIS event and a bremsstrahlung event, where the electron from the DIS event and the photon from the bremsstrahlung event allow the event to pass the selection cuts. In a refined ISR analysis, this background would have to be simulated by artificially constructed overlay events and statistically subtracted [9]. For the purpose of this analysis, a simpler way is chosen: E_γ is limited to a range where the LUMI$-e$ tagger is known to be highly efficient in tagging a potential bremsstrahlung electron (assuming $E_e = E_\gamma + E'_e$). Rejecting events with a signal in the electron calorimeter then provides a handle to suppress this class of background. The price to pay is the loss of a row of ISR-bins at high y and a loss of statistical precision.

B.3 Comparison of data and MC

Although the large statistical errors prevent a clear statement, the data seem to be well reproduced by the Monte Carlo simulation, as can be seen from Fig. B.2. The simulated events have been reweighted to the same structure function as in the nominal analysis, and DJANGO and RAPGAP have been mixed in the same x-dependent fractions as determined there. No background subtraction has been performed.

B.4 Results of the measurement

The result of the F_2 measurement with radiative events is shown in Fig. B.3 and listed in Table B.1. Only statistical errors are given. Most of them range between 13% and 18%. In view of this large error, the determination of systematic errors is not performed. Those coming from the same sources as in the nominal analysis are expect to give similar, i.e. small contributions. An important additional source of systematic effects in an ISR analysis is the LUMI-γ calorimeter. Extensive studies of its acceptance and energy resolution are necessary in order to understand their effect on the results, as performed e.g. in [100]. In this analysis, the ratio of acceptances in data and MC is simply assumed to be flat and taken to be 0.9 on average, and the MC events are weighted with this factor in order to account for the different acceptance for the radiated photon in data. The energy resolution as simulated by MOZART is assumed to be correct.

Q^2 (GeV^2)	x	y	F_2	$\pm$ stat
0.035	$3.22 \cdot 10^{-6}$	0.120	0.0422	0.0139
0.035	$1.48 \cdot 10^{-6}$	0.260	0.0411	0.0246
0.045	$4.14 \cdot 10^{-6}$	0.120	0.0703	0.0128
0.045	$1.91 \cdot 10^{-6}$	0.260	0.0570	0.0138
0.065	$5.98 \cdot 10^{-6}$	0.120	0.0958	0.0136
0.065	$2.76 \cdot 10^{-6}$	0.260	0.0975	0.0160
0.085	$7.82 \cdot 10^{-6}$	0.120	0.1182	0.0154
0.085	$3.61 \cdot 10^{-6}$	0.260	0.1371	0.0221
0.110	$1.01 \cdot 10^{-5}$	0.120	0.1115	0.0179
0.110	$4.67 \cdot 10^{-6}$	0.260	0.1620	0.0302
0.150	$1.38 \cdot 10^{-5}$	0.120	0.2402	0.0432
0.150	$6.37 \cdot 10^{-6}$	0.260	0.1303	0.0384
0.200	$1.84 \cdot 10^{-5}$	0.120	0.1438	0.0447

Table B.1: Measured F_2 values in the ISR analysis with statistical errors only. Due to the low values of y and the large errors, the effect of F_L has been neglected. The bin boundaries in y are 0.08, 0.16, 0.37; those in Q^2 are 0.03, 0.04, 0.055, 0.075, 0.10, 0.13, 0.17, 0.21 GeV^2.

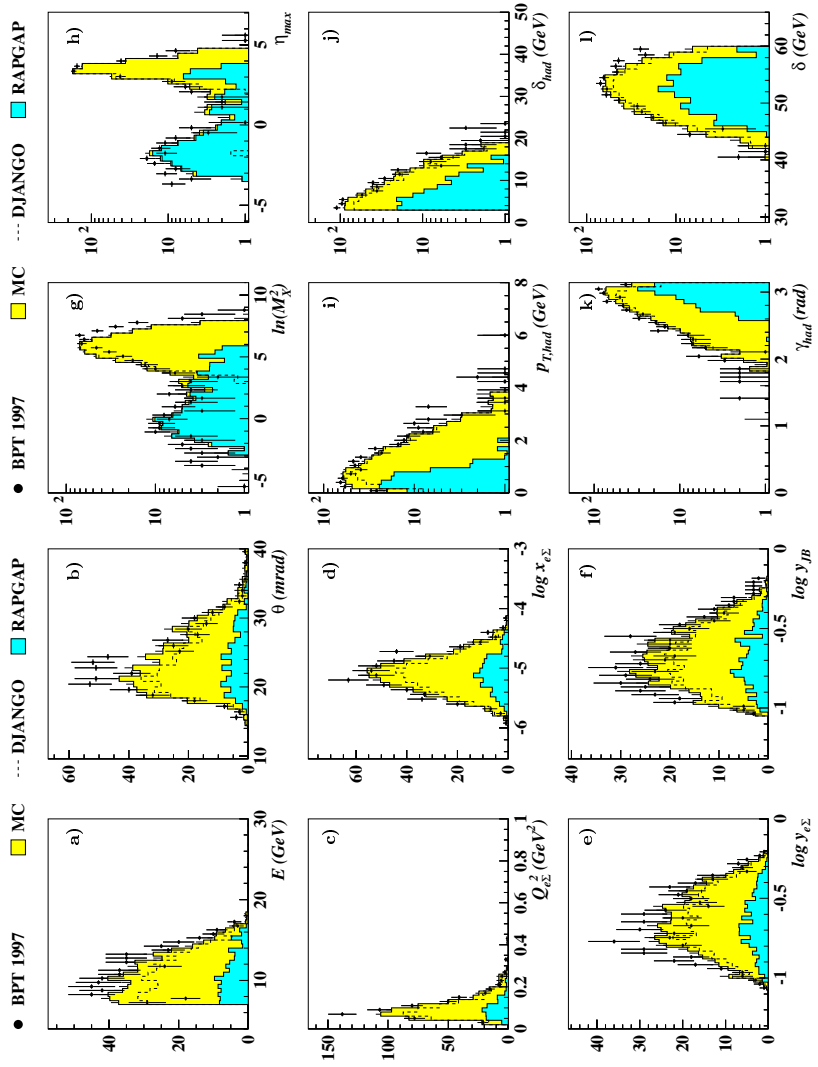

Fig. B.2: ISR analysis. Distributions of reconstructed quantities for data and Monte Carlo simulation. The points denote measured data, the light-shaded histogram is the sum of non-diffractive (DJANGO) and diffractive (RAPGAP) MC, the dark-shaded histogram is RAPGAP alone, and the dashed line is DJANGO alone. The plots a)–l) show the same quantities as in Figs. 7.10 and 7.11. Q^2, x and y have been reconstructed with the $e\Sigma$ method.

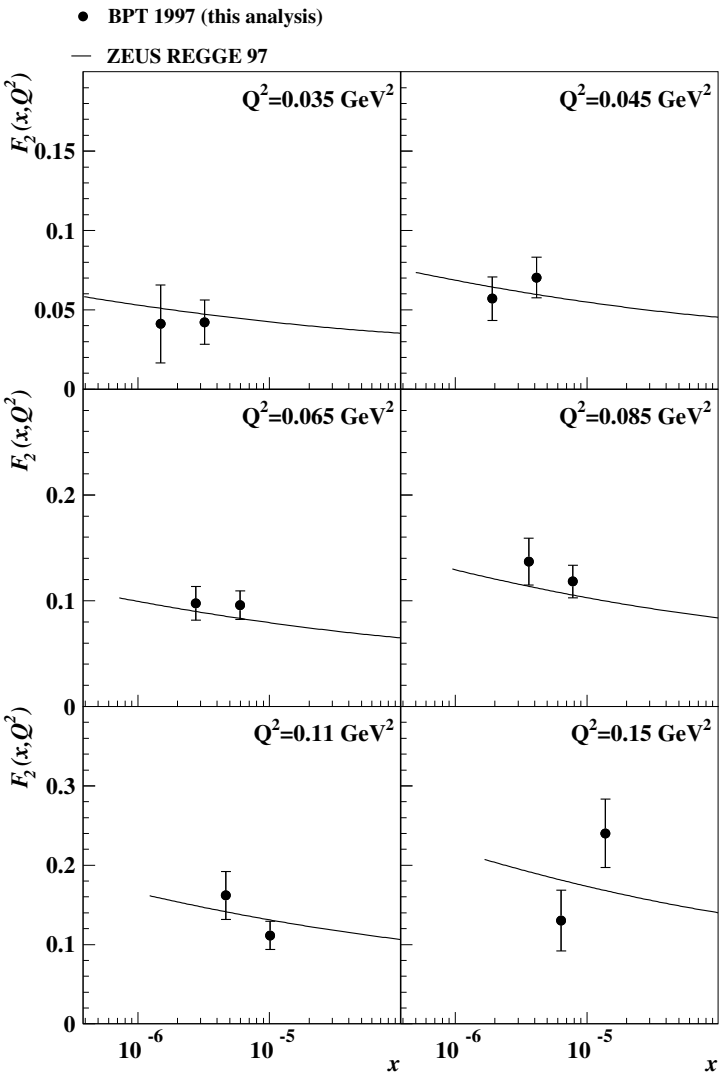

Fig. B.3: F_2 in bins of Q^2 from the ISR analysis. Only statistical errors are shown. The solid line shows the ZEUS REGGE 97 fit, which did not include the measured points shown here. Not shown is the point at $Q^2 = 0.2\,\mathrm{GeV}^2$.

B.5 Uncertainties from radiative corrections in the nominal analysis

Returning to the nominal analysis, this section is devoted to a discussion of the uncertainty of radiative corrections in the F_2 analysis. The ISR analysis will be of use to estimate their magnitude. At HERA, radiative corrections affect the F_2 measurements predominantly at high and moderate values of y, therefore the discussion is limited to the high and medium-y regions and to the electron method.

HERACLES takes into account one-photon radiative corrections, i.e. real photon emission from the lepton line (ISR, FSR, Compton contribution) as well as virtual corrections.

The effect of the latter is calculable in QED and there are no significant uncertainties associated to them. Real photon emission collinear with or close to the outgoing electron is a negligible problem in the case of calorimetric electron energy measurement, because the radiated photon contributes to the measured electron energy, such that the radiation has no net effect.

The remaining source of uncertainty are predominantly ISR events. Here, F_2 at higher x and lower Q^2 affects the measured F_2 due to migration of unrecognized ISR events into the region of the measurement. How far events migrate in the x-Q^2 plane is correlated with the radiated photon energy (Fig. B.4).

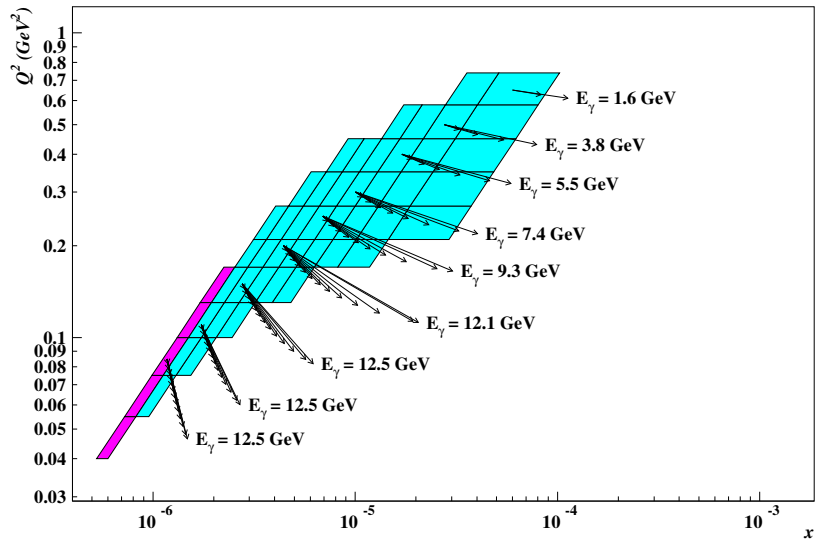

Fig. B.4: Effect of an undetected ISR photon on kinematic variables reconstructed with the electron method. The arrows point from the apparent (i.e. measured) to the true x and Q^2 in steps of E_γ of 1 GeV. The number at the last arrow indicates the highest possible E_γ for which $y_{\rm JB} > 0.06$ and $\delta > 30$ GeV (these cuts are applied in the medium and high-y regions; the detector resolution is neglected here). Each bundle of arrows is representative for a row of bins at the same y.

Making δ and $y_{\rm JB}$ cuts suppresses events where part of the final state (e.g. the ISR photon) has disappeared through the rear beam hole. The condition $y_{\rm JB} > y_{\rm JB}^{\rm min}$ implies

$$E_\gamma < E_e(y_e - y_{\rm JB}^{\rm min}), \tag{B.1}$$

and $\delta > \delta^{\rm min}$ limits the allowed range of E_γ to

$$E_\gamma < E_e - \delta^{\rm min}/2, \tag{B.2}$$

where y_e and $y_{\rm JB}$ are reconstructed y values without taking ISR into account, as in the nominal analysis. These cuts, together with a steeply falling ISR photon energy spectrum, imply that the relevant contribution to the uncertainty due to radiative corrections comes from regions in x and Q^2 close to the point where F_2 is to be measured. The bins at high and moderate Q^2 and low and moderate x are therefore expected to be only very weakly affected by uncertainties about radiative corrections (because F_2 is measured at the same time also "below" these bins), whereas the bins at low Q^2 and high x should see the largest effect (because F_2 "below" is unknown).

To quantify the effect of ISR on the BPT analysis, the BPT-ISR analysis is used to estimate the uncertainty of F_2 below the region of the nominal measurement. From a ZEUS REGGE fit with only one free parameter (the normalization) and all other parameters fixed at their values from the nominal fit (section 8.2.2), the uncertainty of the magnitude of F_2 in the BPT-ISR region is determined to be 6% (this is the statistical error of the normalization as returned by the fit; the systematic error is assumed to be a negligible contribution). The absolute value of the normalization is found to be in good agreement with the nominal fit.

Consequently, as systematic check of radiative corrections, the MC is reweighted to an F_2 that is unchanged for true Q^2 and x inside the bins of the nominal analysis (where it is being measured with high precision) and shifted in normalization by $\pm 6\%$ below this region (where it is only loosely constrained by the BPT-ISR points). F_2 is then unfolded ignoring the partial reweighting of the MC. The result is compared to the nominal measurement, yielding the result of the check as given in section 8.1.4.

Appendix C

Selection Cuts

In the following, the cuts used to select the various data samples in different stages of the analysis are summarized. To explain what variables are exactly used in the cuts, the BPC/BPT reconstruction procedure is summarized here.

The BPT track is reconstructed as a straight line joining two hits in the two BPT planes. The pattern recognition algorithm takes the mean Z vertex of the run and the shower position in the BPC into account.

$Z_{\mathrm{BPT}}^{\mathrm{vertex}}$ is the track extrapolation to the mean X vertex of the run. $X_{\mathrm{BPT}}^{\mathrm{vertex}}$ and $Y_{\mathrm{BPT}}^{\mathrm{vertex}}$ are set to the mean values for the run as measured by the CTD.

θ_X is the angle of the BPT track in the X-Z plane. θ_Y is reconstructed from the shower Y_{BPC} and the BPT vertex. θ_X is corrected for the beam tilt on a run-by-run basis. θ is then given by $\theta = \sqrt{\theta_X^2 + \theta_Y^2}$.

X_{BPT} is the extrapolation of the BPT track to the shower center of gravity in the BPC. This is used for the track matching cut.

X and Y are the distances between the projections of X_{BPT} and Y_{BPC} to the BPC front face and the mean X and Y position of the beam at the Z of the BPC front face. These values are used for the fiducial area cut, which thereby takes into account the actual beam position in the run. This is particularly important due to the limited geometrical acceptance of the BPC which directly enters the measured cross section and may therefore not be a function of the beam position.

C.1 BPC energy calibration

The energy calibration sample is a sample of kinematic peak electrons, selected via $y_{\mathrm{JB}} < 0.04$. The fiducial area cuts are less restrictive than in the final analysis, in order to achieve a calibration that safely works also at the edges of the fiducial area.

- $4.8\,\mathrm{cm} < X < 10.0\,\mathrm{cm}$
  $-2.5\,\mathrm{cm} < Y < 3.0\,\mathrm{cm}$
  $X - Y < 10.9\,\mathrm{cm}$
  $X + Y < 11.4\,\mathrm{cm}$
- $\sqrt{\left(\sigma_X^2 + \sigma_Y^2\right)/2} < 0.8$
- $-90\,\mathrm{cm} < Z_{\mathrm{BPT}}^{\mathrm{vertex}} < 90\,\mathrm{cm}$
- $|X_{\mathrm{BPC}} - X_{\mathrm{BPT}}| < 5\sigma$
- $E_e' > 20\,\mathrm{GeV}$

- $35\,\mathrm{GeV} < \delta < 65\,\mathrm{GeV}$
- $0.005 < y_{\mathrm{JB}} < 0.04$
- $|t - \bar{t}| < 3\,\mathrm{ns}$
- no trigger bits required

C.2 BPC position reconstruction

For the tuning of the electron position reconstruction algorithm, a sample in a wide energy range is used. The cuts are a subset of the cuts for the medium-y region.

- $5.2\,\mathrm{cm} < X < 9.3\,\mathrm{cm}$
  $-2.3\,\mathrm{cm} < Y < 2.8\,\mathrm{cm}$
  $X - Y < 10.7\,\mathrm{cm}$
  $X + Y < 11.2\,\mathrm{cm}$
- $\sqrt{\left(\sigma_X^2 + \sigma_Y^2\right)/2} < 0.8$
- $-90\,\mathrm{cm} < Z_{\mathrm{BPT}}^{\mathrm{vertex}} < 90\,\mathrm{cm}$
- $|X_{\mathrm{BPC}} - X_{\mathrm{BPT}}| < 5\sigma$
- $E'_e > 7\,\mathrm{GeV}$
- $35\,\mathrm{GeV} < \delta < 65\,\mathrm{GeV}$
- $y_{\mathrm{JB}} > 0.06$
- $|t - \bar{t}| < 3\,\mathrm{ns}$
- trigger bit: TLT DIS 17

C.3 BPC and BPT alignment

The selection of events for the alignment is more restrictive than the other sets: the cut on the reconstructed electron position in the BPC is tighter than in the final analysis, in order to avoid possible position biases as much as possible. Also, to become less sensitive to the magnetic field, the range in Y is chosen symmetric around zero. Special cuts are chosen to ensure a very well reconstructed CTD vertex.

- $6.0\,\mathrm{cm} < X < 9.2\,\mathrm{cm}$
  $-2.3\,\mathrm{cm} < Y < 2.3\,\mathrm{cm}$
  $X - Y < 10.7\,\mathrm{cm}$
  $X + Y < 10.7\,\mathrm{cm}$
- $\sqrt{\left(\sigma_X^2 + \sigma_Y^2\right)/2} < 0.8$
- $n_{\mathrm{BPT}}^{\mathrm{hits}} = 2$

- $-90\,\mathrm{cm} < Z_{\mathrm{CTD}}^{\mathrm{vertex}} < 90\,\mathrm{cm}$
  $\sqrt{\left(X_{\mathrm{CTD}}^{\mathrm{vertex}}\right)^2 + \left(Y_{\mathrm{CTD}}^{\mathrm{vertex}}\right)^2} < 0.4\,\mathrm{cm}$
  $n_{\mathrm{CTD}}^{\mathrm{tracks}} \geq 3$
  $\chi^2 / \left(2n_{\mathrm{CTD}}^{\mathrm{tracks}} - 1\right) < 3$
- $E'_e > 15\,\mathrm{GeV}$
- $35\,\mathrm{GeV} < \delta < 65\,\mathrm{GeV}$
- $y_{\mathrm{JB}} > 0.06$
- $|t - \bar{t}| < 3\,\mathrm{ns}$
- no trigger bits required

C.4 BPT efficiency determination

For the efficiency determination, the fiducial area cuts must be the same as applied in the F_2 analysis. A very well reconstructed CTD vertex is needed for a precise prediction for hits in the BPT.

- $5.2\,\mathrm{cm} < X < 9.3\,\mathrm{cm}$
  $-2.3\,\mathrm{cm} < Y < 2.8\,\mathrm{cm}$
  $X - Y < 10.7\,\mathrm{cm}$
  $X + Y < 11.2\,\mathrm{cm}$
- $\sqrt{\left(\sigma_X^2 + \sigma_Y^2\right)/2} < 0.8$
- $-50\,\mathrm{cm} < Z_{\mathrm{CTD}}^{\mathrm{vertex}} < 50\,\mathrm{cm}$
  $\sqrt{\left(X_{\mathrm{CTD}}^{\mathrm{vertex}}\right)^2 + \left(Y_{\mathrm{CTD}}^{\mathrm{vertex}}\right)^2} < 0.4\,\mathrm{cm}$
  $n_{\mathrm{CTD}}^{\mathrm{tracks}} \geq 3$
  $\chi^2_{\mathrm{CTD}} / \left(2n_{\mathrm{CTD}}^{\mathrm{tracks}} - 1\right) < 3$
- $E'_e > 15\,\mathrm{GeV}$
- $35\,\mathrm{GeV} < \delta < 65\,\mathrm{GeV}$
- $|t - \bar{t}| < 3\,\mathrm{ns}$
- no trigger bits required

C.5 High-y region

- $5.2\,\mathrm{cm} < X < 9.3\,\mathrm{cm}$
  $-2.3\,\mathrm{cm} < Y < 2.8\,\mathrm{cm}$
  $X - Y < 10.7\,\mathrm{cm}$
  $X + Y < 11.2\,\mathrm{cm}$
- $\sqrt{\left(\sigma_X^2 + \sigma_Y^2\right)/2} < 0.8$

- $-90\,\mathrm{cm} < Z_{\mathrm{BPT}}^{\mathrm{vertex}} < 90\,\mathrm{cm}$
- $|X_{\mathrm{BPC}} - X_{\mathrm{BPT}}| < 5\sigma$
- $4.4\,\mathrm{GeV} < E'_e < 7.2\,\mathrm{GeV}$
- $30\,\mathrm{GeV} < \delta < 65\,\mathrm{GeV}$
- $y_{\mathrm{JB}} > 0.06$
- $|t - \bar{t}| < 3\,\mathrm{ns}$
- trigger bit: TLT DIS 22

C.6 Medium-y region

- $5.2\,\mathrm{cm} < X < 9.3\,\mathrm{cm}$
  $-2.3\,\mathrm{cm} < Y < 2.8\,\mathrm{cm}$
  $X - Y < 10.7\,\mathrm{cm}$
  $X + Y < 11.2\,\mathrm{cm}$
- $\sqrt{\left(\sigma_X^2 + \sigma_Y^2\right)/2} < 0.8$
- $-90\,\mathrm{cm} < Z_{\mathrm{BPT}}^{\mathrm{vertex}} < 90\,\mathrm{cm}$
- $|X_{\mathrm{BPC}} - X_{\mathrm{BPT}}| < 5\sigma$
- $E'_e > 7\,\mathrm{GeV}$
- $30\,\mathrm{GeV} < \delta < 65\,\mathrm{GeV}$
- $y_{\mathrm{JB}} > 0.06$
- $|t - \bar{t}| < 3\,\mathrm{ns}$
- trigger bit: TLT DIS 17

C.7 Low-y region

- $7.2\,\mathrm{cm} < X < 9.3\,\mathrm{cm}$
  $-2.3\,\mathrm{cm} < Y < 2.8\,\mathrm{cm}$
  $X - Y < 10.7\,\mathrm{cm}$
  $X + Y < 11.2\,\mathrm{cm}$
- $\sqrt{\left(\sigma_X^2 + \sigma_Y^2\right)/2} < 0.8$
- $-90\,\mathrm{cm} < Z_{\mathrm{BPT}}^{\mathrm{vertex}} < 90\,\mathrm{cm}$
- $|X_{\mathrm{BPC}} - X_{\mathrm{BPT}}| < 5\sigma$
- $E'_e > 20\,\mathrm{GeV}$
- $35\,\mathrm{GeV} < \delta < 65\,\mathrm{GeV}$
- $0.004 < y_{\mathrm{JB}} < 0.1$
- $|t - \bar{t}| < 3\,\mathrm{ns}$
- trigger bits: TLT DIS 17 or 23

C.8 Low-y prescaled region

- $5.2\,\mathrm{cm} < X < 9.3\,\mathrm{cm}$
  $-2.3\,\mathrm{cm} < Y < 2.8\,\mathrm{cm}$
  $X - Y < 10.7\,\mathrm{cm}$
  $X + Y < 11.2\,\mathrm{cm}$
- $\sqrt{\left(\sigma_X^2 + \sigma_Y^2\right)/2} < 0.8$
- $-90\,\mathrm{cm} < Z_{\mathrm{BPT}}^{\mathrm{vertex}} < 90\,\mathrm{cm}$
- $|X_{\mathrm{BPC}} - X_{\mathrm{BPT}}| < 5\sigma$
- $E'_e > 20\,\mathrm{GeV}$
- $35\,\mathrm{GeV} < \delta < 65\,\mathrm{GeV}$
- $0.004 < y_{\mathrm{JB}} < 0.1$
- $|t - \bar{t}| < 3\,\mathrm{ns}$
- trigger bits: FLT 52 $\rightarrow$ SLT DIS 2 $\rightarrow$ TLT DIS 18

C.9 ISR analysis

- $5.2\,\mathrm{cm} < X < 9.3\,\mathrm{cm}$
  $-2.3\,\mathrm{cm} < Y < 2.8\,\mathrm{cm}$
  $X - Y < 10.7\,\mathrm{cm}$
  $X + Y < 11.2\,\mathrm{cm}$
- $\sqrt{\left(\sigma_X^2 + \sigma_Y^2\right)/2} < 0.8$
- $-90\,\mathrm{cm} < Z_{\mathrm{BPT}}^{\mathrm{vertex}} < 90\,\mathrm{cm}$
- $|X_{\mathrm{BPC}} - X_{\mathrm{BPT}}| < 5\sigma$
- $E'_e > 7\,\mathrm{GeV}$
- $|t - \bar{t}| < 3\,\mathrm{ns}$
- $9\,\mathrm{GeV} < E_{\mathrm{LUMI}-\gamma} < 18\,\mathrm{GeV}$
- $E_{\mathrm{LUMI}-e} < 3\,\mathrm{GeV}$
- $E'_e + E_{\mathrm{LUMI}-\gamma} < 35\,\mathrm{GeV}$
- $40\,\mathrm{GeV} < \delta' < 60\,\mathrm{GeV}$
- $y_{\mathrm{JB}} > 0.06$
- trigger bit: TLT DIS 21

References

[1] E. Rutherford, Phil. Mag. **21** (1911) 669.

[2] ZEUS Collaboration, J. Breitweg et al., Measurement of the Proton Structure Function F_2 at Very Low Q^2 and Very Low x, contributed to: International Europhysics Conference on High Energy Physics, Tampere (1999).

[3] Ch. Amelung (for the ZEUS Collaboration), Measurement of the Proton Structure Function F_2 and of the Total Photon-Proton Cross Section $\sigma_{\rm tot}^{\gamma^* p}$ at Very Low Q^2 and Very Low x, in: Proceedings of the 7th International Workshop on Deep Inelastic Scattering and QCD, ed. J. Blümlein and T. Riemann, DESY, Zeuthen (1999), Nucl. Phys. **B** (Proc. Suppl.) **79** (1999) 176.

[4] Ch. Amelung (for the ZEUS and H1 Collaborations), Status of Measurements and Interpretation of Total Real and Virtual Photon-Proton Cross Sections, to be published in: Proceedings of the International Conference and VIII Blois Workshop on Elastic and Diffractive Scattering, Protvino (1999), `hep-ex/9911005`.

[5] T. Doeker, A. Frey and M. Nakao, Electron Position Reconstruction—Update of the ELECPO Routines, ZEUS Note 94-123.

[6] Ch. Amelung, Electron Position Reconstruction in ZEUS: Further Update of the ELECPO Package (Based on 1995 Data), ZEUS Note 96-093.

[7] Ch. Amelung, Electron Position Reconstruction in ZEUS: Another Update of the ELECPO Package (Based on 1995/96 Data), ZEUS Note 97-053.

[8] A. Weber, Der Silizium-Spurdetektor BPT für kleinste Elektron-Streuwinkel in ZEUS: Alignment mit Teilchenspuren, Diplomarbeit, Universität Bonn (1998), BONN-IB-98-18 (in German).

[9] I. Weber, Diplomarbeit, Universität Bonn, in preparation.

[10] R.W. McAllister and R. Hofstädter, Phys. Rev. **102** (1956) 851.

[11] M.R. Yearian and R. Hofstädter, Phys. Rev. **110** (1958) 552.

[12] SLAC-MIT Collaboration, E.D. Bloom et al., Phys. Rev. Lett. **23** (1969) 930.

[13] SLAC-MIT Collaboration, M. Breidenbach et al., Phys. Rev. Lett. **23** (1969) 935.

[14] Particle Data Group, C. Caso et al., Eur. Phys. J. **C 3** (1998) 1.

[15] G. Wolf, The Kinematics of Deep Inelastic Scattering in the Presence of Initial State Radiation, DESY Report 97-047.

[16] R.P. Feynman, Phys. Rev. Lett. **23** (1969) 1415.

[17] C.G. Callan and D.J. Gross, Phys. Rev. Lett. **22** (1969) 156.

[18] J.D. Bjorken, Phys. Rev. **179** (1969) 1547.

[19] J.D. Bjorken and E.A. Paschos, Phys. Rev. **185** (1969) 1975.

[20] M. Gell-Mann, The Eightfold Way: A Theory of Strong Interaction Symmetry, Caltech Report CTSL-20 (1961).

[21] Y. Ne'eman, Nucl. Phys. **26** (1961) 222.

[22] M. Gell-Mann, Phys. Lett. **8** (1964) 214.

[23] G. Zweig, CERN Report TH-401 (1964).

[24] G. Zweig, CERN Report TH-412 (1964).

[25] C.H. Llewellyn-Smith, Phys. Rep. **C 3** (1972) 261.

[26] J.C. Collins, D.E. Soper and G. Sterman, in: Perturbative Quantum Chromodynamics, ed. A.H. Mueller, World Scientific, Singapore (1989).

[27] G. Altarelli, R.K. Ellis and G. Martinelli, Nucl. Phys. **B 157** (1979) 461.

[28] W.A. Bardeen, A.J. Buras, D.W. Duke and T. Muta, Phys. Rev. **D 18** (1978) 3998.

[29] V.N. Gribov and L.N. Lipatov, Sov. J. Nucl. Phys. **15** (1972) 438.

[30] L.N. Lipatov, Sov. J. Nucl. Phys. **20** (1975) 96.

[31] G. Altarelli and G. Parisi, Nucl. Phys. **B 126** (1977) 298.

[32] Y.L. Dokshitzer, Sov. Phys. JETP **46** (1977) 641.

[33] K. Prytz, Phys. Lett. **B 311** (1993) 286.

[34] G. Wolf, HERA Physics, DESY Report 94-022.

[35] B.L. Ioffe, Phys. Lett. **B 30** (1969) 123.

[36] L.N. Hand, Phys. Rev. **129** (1963) 1834.

[37] F.J. Gilman, Phys. Rev. **167** (1968) 1365.

[38] J.J. Sakurai, Phys. Rev. Lett. **22** (1969) 981.

[39] J.J. Sakurai and D. Schildknecht, Phys. Lett. **B 40** (1972) 121.

[40] I.F. Ginzburg and V.G. Serbo, Phys. Lett. **B 109** (1982) 231.

[41] M. Froissart, Phys. Rev. **123** (1961) 1053.

[42] A. Martin, Nuovo Cimento **42** (1966) 930.

[43] G.F. Chew and S.C. Frautschi, Phys. Rev. Lett. **8** (1962) 41.

[44] A. Donnachie and P.V. Landshoff, Phys. Lett. **B 296** (1992) 227.

[45] UA8 Collaboration, R. Bonino et al., Phys. Lett. **B 211** (1988) 239.

[46] UA8 Collaboration, A. Brandt et al., Phys. Lett. **B 297** (1992) 417.

[47] ZEUS Collaboration, M. Derrick et al., Phys. Lett. **B 315** (1993) 481.

[48] H1 Collaboration, T. Ahmed et al., Nucl. Phys. **B 429** (1994) 477.

[49] J.-R. Cudell, K. Kang and S.K. Kim, Phys. Lett. **B 395** (1997) 311.

[50] ZEUS Collaboration, M. Derrick et al., Z. Phys. **C 63** (1994) 391.

[51] H1 Collaboration, S. Aid et al., Z. Phys. **C 69** (1995) 27.

[52] M. Botje, QCD Fits to ZEUS and Fixed Target F_2 Data, ZEUS Note 98-062.

[53] A. Cooper-Sarkar, R. Devenish and A. de Roeck, Int. J. Mod. Phys. **A 13** (1998) 3385.

[54] H. Abramowicz and A. Caldwell, HERA Collider Physics, DESY Report 98-192, submitted to Rev. Mod. Phys.

[55] ZEUS Collaboration, M. Derrick et al., Z. Phys. **C 72** (1996) 399.

[56] ZEUS Collaboration, J. Breitweg et al., Eur. Phys. J. **C 7** (1999) 609.

[57] ZEUS Collaboration, J. Breitweg et al., Phys. Lett. **B 407** (1997) 432.

[58] A.D. Martin, R.G. Roberts, W.J. Stirling and R.S. Thorne, Eur. Phys. J. **C 4** (1998) 463.

[59] CTEQ Collaboration, H.L. Lai et al., Global QCD Analysis of Parton Structure of the Nucleon: CTEQ5 Parton Distributions, MSU-HEP-903100, `hep-ph/9903282`.

[60] M. Glück, E. Reya and A. Vogt, Z. Phys. **C 67** (1995) 433.

[61] M. Glück, E. Reya and A. Vogt, Eur. Phys. J. **C 5** (1998) 461.

[62] A. Donnachie and P.V. Landshoff, Z. Phys. **C 61** (1994) 139.

[63] A. Donnachie and P.V. Landshoff, Phys. Lett. **B 437** (1998) 408.

[64] H. Abramowicz, E.M. Levin, A. Levy and U. Maor, Phys. Lett. **B 269** (1991) 465.

[65] H. Abramowicz and A. Levy, The ALLM Parameterization of $\sigma_{\rm tot}^{\gamma^* p}$—An Update, DESY Report 97-251.

[66] A. Capella, A.B. Kaidalov, C. Merino and J. Tran Thanh Van, Phys. Lett. **B 337** (1994) 358.

[67] A.B. Kaidalov and C. Merino, Eur. Phys. J. **C 10** (1999) 153.

[68] K. Adel, F. Barreiro and F.J. Ynduráin, Nucl. Phys. **B 495** (1997) 221.

[69] P. Desgrolard, A. Lengyel and E. Martynov, Eur. Phys. J. **C 7** (1999) 655.

[70] B. Badełek and J. Kwieciński, Phys. Lett. **B 295** (1992) 263.

[71] A.D. Martin, M.G. Ryskin and A.M. Staśto, Eur. Phys. J. **C 7** (1999) 643.

[72] D. Schildknecht and H. Spiesberger, Generalized Vector Dominance and Low x Inelastic Electron-Proton Scattering, BI-TP 97/25.

[73] H. Spiesberger, private communication.

[74] D. Haidt, Double log Behavior of F_2 at Low x and Low Q^2, in: Proceedings of the 7th International Workshop on Deep Inelastic Scattering and QCD, ed. J. Blümlein and T. Riemann, DESY, Zeuthen (1999).

[75] K. Golec-Biernat and M. Wüsthoff, Phys. Rev. **D 59** (1999) 014017.

[76] B. Badełek, J. Kwieciński and A. Staśto, Z. Phys. **C 74** (1997) 297.

[77] HERA – A Proposal for a Large Electron-Proton Colliding Beam Facility at DESY, DESY Report HERA 81-10 (1981).

[78] G.-A. Voss and B.H. Wiik, The Electron-Proton-Collider HERA, Ann. Rev. Nucl. Part. Sci. **44** (1994) 413.

[79] ZEUS Collaboration, M. Derrick et al., The ZEUS Detector, Status Report, DESY Report (1993).

[80] H. Bethe and W. Heitler, Proc. Roy. Soc. **A 146** (1934) 83.

[81] J. Krüger, The Uranium Scintillator Calorimeter for the ZEUS Detector at the Electron-Proton Collider HERA, Habilitationsschrift, Universität Hamburg (1992), DESY Report F35-92-02.

[82] R. Schattevoy, Optimierung, Validation und Analyse der ZEUS-Ereignisselektion unter besonderer Berücksichtigung der Kalorimetrie, Dissertation, Universität Bonn (1994), BONN-IR-94-08 (in German).

[83] R. Hall-Wilton, N. McCubbin, P. Nylander, M. Sutton and M. Wing, The CTD Tracking Resolution, ZEUS Note 99-024.

[84] P. de Jong, Status of the Uranium Calorimeter Reconstruction Programme, ZEUS Note 91-036.

[85] G.F. Hartner, Y. Iga, J.B. Lane, N.A. McCubbin and M. Wing, VCTRAK (3.07/04): Offline Output Information, ZEUS Note 97-064.

[86] G.F. Hartner, VCTRAK Briefing: Program and Math, ZEUS Note 98-058.

[87] U. Fricke, BPRECON User's Guide and Reference, ZEUS Note 98-081.

[88] D.C. Williams, BPTRECON User's Guide and Reference, ZEUS Note 98-038.

[89] `http://www-zeus.desy.de/ZEUS_ONLY/analysis/Phantom/index.html`.

[90] `http://www-zeus.desy.de/ZEUS_ONLY/analysis/Runlib/index.html`.

[91] Z. Qian et al., Comp. Phys. Comm. **45** (1987) 283.

[92] HBOOK Reference Manual;
`http://wwwinfo.cern.ch/asdoc`.

[93] L.A.T. Bauerdick, O. Derugin, D. Gilkinson, M. Kasemann and O. Manczak, ZARAH: The Central Computing Facility for the ZEUS Experiment, DESY Report 95-236-B.

[94] CERNLIB Reference Manual;
`http://wwwinfo.cern.ch/asd/cernlib.html`.

[95] F. James and M. Roos, Comp. Phys. Comm. **10** (1975) 343;
`http://wwwinfo.cern.ch/asdoc`.

[96] PAW Reference Manual;
`http://wwwinfo.cern.ch/asd/paw/index.html`.

[97] ZEUS Collaboration, M. Derrick et al., Z. Phys. **C 69** (1996) 607.

[98] A. Frey, Messung der Protonstrukturfunktion $F_2(x, Q^2)$ in radiativer ep-Streuung mit dem ZEUS-Detektor, Dissertation, Universität Bonn (1996), BONN-IR-96-03 (in German).

[99] R. Kerger, Messung der Protonstrukturfunktion $F_2(x, Q^2)$ in tiefinelastischer ep-Streuung für Q^2 von 0.75 bis 20.0 GeV^2 mit ZEUS-Daten aus der Meßperiode 1995, Diplomarbeit, Universität Bonn (1997), BONN-IB-97-13 (in German).

[100] A. Bornheim, Messung der Protonstrukturfunktionen F_2 und F_L in radiativer ep-Streuung mit dem ZEUS-Detektor, Dissertation, Universität Bonn (1999), in print (in German).

[101] B. Surrow, Measurement of the Proton Structure Function F_2 at Low Q^2 and Very Low x with the ZEUS Beam Pipe Calorimeter at HERA, Dissertation, Universität Hamburg (1998), DESY-THESIS-1998-004.

[102] A. Caldwell, S. Ritz, Q. Zhu and R. Klanner, A Silicon Tracker for BPC and a Possible Upgrade to BPC III, ZEUS Note 96-044.

[103] E. Barberis et al., Nucl. Instr. Methods **A 364** (1995) 507.

[104] E. Weiss, private communication.

[105] A. Pellegrino, private communication.

[106] R. Brun et al., GEANT 3.13, CERN Report DD/EE/84-1 (1987);
`http://wwwinfo.cern.ch/asd/geant/index.html`.

[107] J. Tickner, Proton Structure Functions at Low Q^2, Ph.D. thesis, Oxford University (1997).

[108] J. Tickner, The BPCAL Monte Carlo, unpublished software.

[109] H. Bichsel, Rev. Mod. Phys. **60** (1988) 663.

[110] C.F. von Weizsäcker, Z. Phys. **88** (1934) 612.

[111] E.J. Williams, Phys. Rev. **45** (1934) 729.

[112] V.M. Budnev et al., Phys. Rep. **C 15** (1975) 181.

[113] K. Charchula, G.A. Schuler and H. Spiesberger, Comp. Phys. Comm. **81** (1994) 381;
`http://www.desy.de/~hspiesb/djangoh.html`.

[114] H. Jung, Comp. Phys. Comm. **86** (1995) 147;
`http://www-h1.desy.de/~jung/rapgap.html`.

[115] A. Kwiatkowski, H. Spiesberger and H.-J. Möring, Comp. Phys. Comm. **69** (1992) 155;
`http://www.desy.de/~hspiesb/djangoh.html`.

[116] L. Lönnblad, Comp. Phys. Comm. **71** (1992) 15.

[117] T. Sjöstrand, Comp. Phys. Comm. **39** (1986) 347.

[118] T. Sjöstrand and M. Bengtsson, Comp. Phys. Comm. **43** (1987) 367.

[119] T. Sjöstrand, Comp. Phys. Comm. **82** (1994) 74.

[120] G. Ingelman, LEPTO 6.1, in: Proceedings of the 1991 Workshop on Physics at HERA, ed. W. Buchmüller and G. Ingelman, DESY, Hamburg, Vol. 3 (1992) 1366.

[121] H.U. Bengtsson and T. Sjöstrand, Comp. Phys. Comm. **46** (1987) 43.

[122] H. Plothow-Besch, Comp. Phys. Comm. **75** (1993) 396;
`http://wwwinfo.cern.ch/asdoc`.

[123] `http://www-zeus.desy.de/ZEUS_ONLY/analysis/Amadeus/index.html`.

[124] B.D. Burow, FUNNEL: Towards Comfortable Event Processing, in: Computing in High Energy Physics, Rio de Janeiro (1995) 59.

[125] I. Bohnet, U. Fricke, B. Surrow and K. Wick, Radiation Damage Effects in the Beam Pipe Calorimeter at ZEUS, in: Proceedings of the 6th International Conference on Advanced Technology and Particle Physics, Villa Olmo (1998).

[126] W.R. Nelson et al., The EGS4 Code System, SLAC Report 265 (1985).

[127] D.C. Williams, 1997 BPT Alignment, ZEUS Note 98-078.

[128] A. Weber, Alignment of the Beam Pipe Tracker (BPT) for the 1997 Running Period Using Particle Tracks, ZEUS Note 98-069.

[129] K. Piotrzkowski, private communication.

[130] A. Savin, Study of Calorimeter Noise in the 1996 Data, ZEUS Note 98-007.

[131] G. Briskin, Diffractive Dissociation in *ep* Deep Inelastic Scattering, Doctoral thesis, University of Tel Aviv (1998), DESY-THESIS-1998-036.

[132] `http://www-zeus.desy.de/~ntuning/ZEUS_ONLY/zufo_new.html`.

[133] J. Grosse-Knetter, Corrections for the Hadronic Final State, ZEUS Note 98-031.

[134] S. Bentvelsen, J. Engelen and P. Koijman, Reconstruction of x, Q^2 and Extraction of Structure Functions in Neutral Current Scattering at HERA, in: Proceedings of the 1991 Workshop on Physics at HERA, ed. W. Buchmüller and G. Ingelman, DESY, Hamburg, Vol. 1 (1992) 23.

[135] F. Jacquet and A. Blondel, in: Proceedings of the Study of an *ep* Facility for Europe, ed. U. Amaldi, DESY Report 79/48, Hamburg (1979) 391.

[136] U. Bassler and G. Bernardi, Nucl. Instr. Methods **A 426** (1999) 583.

[137] `http://www-zeus.desy.de/~schlenst/lumi.html`.

[138] A. Quadt and O. Ruske, A New Method to Measure Vertex Distributions, ZEUS Note 98-036.

[139] A. Quadt and O. Ruske, private communication.

[140] H1 Collaboration, C. Adloff et al., Nucl. Phys. **B 497** (1997) 3.

[141] E665 Collaboration, M.R. Adams et al., Phys. Rev. **D 54** (1996) 3006.

[142] D.O. Caldwell et al., Phys. Rev. Lett. **40** (1978) 1222.

[143] S.I. Alekhin et al., CERN Report HERA 87-01 (1987).

[144] R. Deffner, Dissertation, Universität Bonn, in preparation.

[145] ZEUS Collaboration, J. Breitweg et al., Eur. Phys. J. **C 6** (1999) 43.

Acknowledgments

Viele Menschen am Physikalischen Institut in Bonn und am DESY in Hamburg haben dazu beigetragen, diese Arbeit zum Erfolg zu führen. Ihnen möchte ich an dieser Stelle danken für eine schöne und interessante Doktorandenzeit.

Zuvorderst meinem Doktorvater Erwin Hilger gilt mein tief empfundener Dank. Die Jahre, die ich als Praktikant, Diplomand und Doktorand in seiner Bonner ZEUS-Gruppe verbringen durfte, werden mir in bester Erinnerung bleiben. Ihm verdanke ich die Anregung zu einer sehr interessanten und vielseitigen Arbeit, die er mich mit großer Freiheit verfolgen ließ, die er gleichzeitig aber mit viel Interesse und Anteilnahme begleitete.

Uli Katz hat durch sorgfältiges Korrekturlesen viele große und kleine Fehler entdeckt, ihm sowie Jim Crittenden und Alexander Kappes verdanke ich zahlreiche wertvolle Hinweise. Robert Kerger hat dafür gesorgt, daß auch das Leben neben der Physik nicht zu kurz kam, Adi Bornheim war in allen Fragen rund um F_2 hilfsbereit und hilfreich, und in Gesprächen mit Ainas Weber habe ich viel über das BPT-Alignment gelernt.

Ihnen und ebenso den übrigen aktuellen und verflossenen Mitgliedern der Bonner ZEUS-Kalorimeter-Gruppe, Thomas Doeker, Ariane Frey, Michael Geerts, Boris Hinzen, Thomas Machholz, Ralf Ossowski, Matthias Pfeiffer, Julian Rautenberg, Oliver Strangfeld und Ingo Weber sei für das freundliche Arbeitsumfeld gedankt. Bei der Erfüllung meiner Aufgaben als Systemverwalter unserer Workstations und PC's war Thomas Kokott stets ein hilfsbereiter und kompetenter Ansprechpartner.

Ganz besonders gilt mein Dank meiner Frau und meinen Eltern, deren Liebe und Vertrauen mich durch alle Höhen und Tiefen begleitet und unterstützt haben.

Many people in Bonn and Hamburg contributed to the success of this work. I would like to take the opportunity to say "thank you" for a superb time as a diploma student and doctoral candidate.

Many thanks go to Ulli Fricke and Vincenzo Monaco for their friendly collaboration in the F_2 analysis. Our coordinators, Arnulf Quadt, Rik Yoshida and Antonio Pellegrino, pushed the analysis forward by many helpful questions and suggestions. Robert Klanner, Marco Costa and David Williams watched and guided my first steps in the BPT business. Allen Caldwell, Camille Ginsburg and Ken Long helped to bring the EPS paper in good shape. James Tickner, Bernd Surrow and Teresa Monteiro kindly explained details of their work to me. Hubert Spiesberger and Hannes Jung patiently gave explanations about DJANGO and RAPGAP and beyond.

For some of the figures I am grateful to Arnulf Quadt (Fig. 2.15), Ainas Weber (Figs. 4.5 and 6.8), Antonio Pellegrino (Fig. 4.7), Nils Gendner (Figs. 4.8 and 4.9), Corinna Catterall (Fig. 5.4) and David Williams (Fig. 6.9).

High energy physics experiments are of enormous size and complexity, and therefore require the collaboration of many people. I have enjoyed to be a member of the ZEUS collaboration during my diploma and doctoral time. The results presented in this report could only be obtained by relying on hardware and software work done by many colleagues, and their contribution is highly appreciated. I was grateful to be given the opportunity to represent the ZEUS collaboration in presenting the results of my and our work at international conferences.

Diese Arbeit wurde aus Mitteln des Bundesministeriums für Wissenschaft und Forschung in Deutschland gefördert.